

# Analysis of Anisotropic Jovian Electron Events

Dissertation  
zur Erlangung des Doktorgrades  
der Mathematisch-Naturwissenschaftlichen Fakultät  
der Christian-Albrechts-Universität  
zu Kiel

vorgelegt von  
Phillip Dunzlaff

Kiel

November 2012

1. Gutachter : Prof. Dr. Bernd Heber

2. Gutachter : Dr. Horst Fichtner

Tag der mündlichen Prüfung : 07. Februar 2013

Zum Druck genehmigt : 07. Februar 2013

---

**Der Dekan**

# Contents

<b>Contents</b>	<b>1</b>
<b>1 Introduction</b>	<b>5</b>
<b>2 The Sun and Heliosphere</b>	<b>9</b>
2.1 The Solar Wind . . . . .	9
2.2 The Heliosphere and its Boundaries . . . . .	15
<b>3 The Jovian System in the Heliosphere</b>	<b>21</b>
3.1 The Planet Jupiter . . . . .	21
3.2 The Jovian Magnetosphere . . . . .	22
<b>4 Transport of Charged Particles in Interplanetary Space</b>	<b>27</b>
4.1 Particles in Magnetic Fields . . . . .	27
4.2 The Random Walk . . . . .	30
4.3 The Fokker-Planck Equation for Space Plasmas . . . . .	31
4.4 Special Cases of the Master Equation . . . . .	35
<b>5 Instrumentation, Trajectories, and Methods</b>	<b>39</b>
5.1 Measurements of Charged Particles . . . . .	39
5.2 Ulysses . . . . .	41
5.3 Pioneer 10/11 . . . . .	46
5.4 The Concept of Anisotropy . . . . .	49
5.5 Pitch-Angle Coverage of the KET Experiment . . . . .	53
5.6 The Lomb-Scargle Algorithm . . . . .	54
5.7 Correlations of Timeseries . . . . .	58
<b>6 “Quiet-Time“ Jovian Electrons in the Heliosphere</b>	<b>61</b>
6.1 The Pre-Ulysses Era . . . . .	61
6.2 Ulysses – Conquering the Third Dimension . . . . .	65
6.3 On the Focusing of Jovian Electrons . . . . .	66
<b>7 How is the Jovian Clock Ticking?</b>	<b>71</b>
7.1 The Clock Model . . . . .	72

7.2	The Disc Model . . . . .	72
7.3	The Anomaly Model . . . . .	73
7.4	Re-Analysis of Ulysses Data . . . . .	74
7.5	Ulysses Outbound Observations . . . . .	81
7.6	Results from the Pioneer spacecraft . . . . .	85
7.7	Interpretation and Consequences . . . . .	88
<b>8</b>	<b>Analysis of Jovian Jets</b>	<b>91</b>
8.1	Jovian Jets Observed by Ulysses . . . . .	91
8.2	Investigation of Anisotropies . . . . .	93
8.3	Jovian Jets And ICMEs . . . . .	98
8.4	Detection of the 10 h Periodicity . . . . .	107
8.5	Reinvestigation of the 1992 Time Period . . . . .	108
8.6	Ulysses' Second Flyby . . . . .	118
8.7	Jovian Jets Observed by Pioneer 10 . . . . .	131
8.8	Overview of the Pioneer Events & the 10 h Modulation . . . . .	133
8.9	Short Lived Events in the Pioneer Data . . . . .	134
8.10	A Series of Events Seen by Pioneer 10 . . . . .	135
8.11	Observation of "Reverse" Jovian Bursts? . . . . .	140
<b>9</b>	<b>A FPE Based Jovian Electron Burst Transport Model</b>	<b>147</b>
9.1	Setup of the Simulation . . . . .	147
9.2	Propagation in a Homogeneous Fluxtube . . . . .	150
<b>10</b>	<b>Summary &amp; Outlook</b>	<b>161</b>
<b>A</b>	<b>The System III (1965) Coordinate System</b>	<b>165</b>
<b>B</b>	<b>Numerical Solution of the Transport Model</b>	<b>167</b>
B.1	Numerical Setup . . . . .	168
B.2	The Discretization of the Transport Equation . . . . .	177
B.3	Convergence & Stability Considerations . . . . .	179
B.4	Testing the Code . . . . .	184
	<b>Bibliography</b>	<b>191</b>

# Zusammenfassung

Die Jupitermagnetosphäre stellt neben der Sonne und der galaktischen kosmischen Strahlung eine bedeutende Quelle von energiereichen, geladenen Teilchen im Sonnensystem bzw. der Heliosphäre dar. Der Schwerpunkt der vorliegenden Arbeit liegt auf der Komponente der sogenannten "Jupiterelektronen", Elektronen im Energiebereich von  $\sim 1$  bis  $> 40$  Megaelektronenvolt (MeV). Diese Teilchenpopulation wurde erstmals durch die Pioneer 10 und 11 Raumsonden in den frühen 1970ern beobachtet.

Im Rahmen dieser Arbeit wurde eine Analyse von MeV-Elektronen Meßdaten der Ulysses und Pioneer 10/11 Raumsonden in der Magnetosphäre des Jupiters durchgeführt. Durch die Anwendung von statistischen Methoden und Zeitreihenanalysen konnte neben der bekannten – mit der Rotation des Planeten verknüpften – 10 h Modulation des Energiespektrums eine weitere periodische Variation nachgewiesen werden. Während erstgenannte, unter dem Stichwort "Jovian Clock" bekannte Modulation Gegenstand einer Anzahl wissenschaftlichen Artikel ist, wird in der vorliegenden Arbeit erstmals eine ausführlichere Beschreibung und insbesondere ein Vergleich zwischen den Ulysses und Pioneer Ergebnissen dargestellt.

Der umfangreichste Teil dieser Arbeit widmet sich der Analyse von "Jovian Jets" anhand von Meßdaten der Raumsonden Ulysses und Pioneer 10/11. Diese Ereignisse, erstmals 1993 anhand von Ulysses-Daten beschrieben, zeichnen sich im Vergleich zur übrigen Population von Jupiterelektronen durch einen plötzlichen Anstieg und Abfall der Elektronenzählraten bei einer gesamten Ereignisdauer von höchstens einigen Stunden in Verbindung mit einer deutlichen Richtungsanisotropie des Teilchenflusses aus. Bei einigen dieser Ereignisse kann eine zeitliche Modulation des Energiespektrums der Elektronen mit der Rotationsperiode des Jupiter von  $\sim 10$  Stunden gefunden werden, wie sie innerhalb der Jupitermagnetosphäre vorherrschend ist. Die Anwendung einer "dreidimensionalen" Spektralanalyseverfahren erwies sich als den bisher verwendeten Methoden bzgl. des Nachweises dieser Modulation überlegen. Insbesondere konnte die 10 h Periodizität erstmalig bei einem Abstand vom Jupiter von deutlich über 1 AU (Astronomische Einheit) nachgewiesen werden, entsprechend einer Erweiterung der bisherigen Nachweisgrenze um den Faktor  $\sim 1.5$ .

Eine Anwendung dieser Analysemethoden auf die Meßdaten der Pioneer 10 Raumsonden ergab eine gute Übereinstimmung mit den Ulysses Daten. Insbesondere konnte gezeigt werden, dass die als "Jovian Bursts" bezeichneten Ereignisse als "Jovian Jets" aufgefasst werden können.

Die Entwicklung sowie Anwendung eines die Anisotropie (bzw. des magnetischen Anstellwinkels) dieser Jupiter-Ereignisse berücksichtigenden Transportmodells wurde vorgestellt. Die Berücksichtigung des Anstellwinkels bei der Ausbreitung von Jupiterelektronen führt zur der Annahme, dass die Beobachtung von Jovian Jets eine direkte Folge der Injektion von Elektronen nahe der Jupitermagnetosphäre ist.

## Abstract

The Jovian magnetosphere, besides the Sun and galactic cosmic radiation, is a considerable source of energetic particle in the solar system. The focus of this work is on so-called “Jovian electrons”, i.e. electrons of about  $\sim 1$  to  $> 40$  MeV. This particle population was first observed by the Pioneer 10 and 11 spacecraft in the early 1970s.

Within the scope of this work is an analysis of MeV electrons measured by the Ulysses and Pioneer 10/11 spacecraft in the Jovian magnetosphere. Due to the application of statistical and time series analysis methods it was possible to identify another quasi-periodic variation of the energy spectrum beside the famous “Jovian clock” related to the Jovian periodicity of 10 h. While the latter observation is extensively discussed in the corresponding literature, the work at hand provides a more detailed discussion of the second quasi-periodic variation based on the analysis and comparison of Ulysses and Pioneer data.

The main part of this work is dedicated to the analysis of “Jovian jet” events. These events – discussed for the first time in 1993 by Ulysses data – are characterized by sharp increases and decreases of flux and a duration of not more than a few hours. Furthermore, these events are accompanied by significant directional anisotropies of the particles. Some events also show evidence for the presence of the Jovian 10 h periodicity in the energy spectrum similar to the observations inside the magnetosphere. The application of a “three-dimensional” spectral analysis method was found to be superior to previously used methods with respect to the identification of the 10 h modulation. In particular, it was possible to detect the 10 h periodicity well beyond a distance of 1 AU (Astronomical Unit) from Jupiter, increasing the previous detection limit by a factor of  $\sim 1.5$ .

An application of these methods to the Pioneer 10 data revealed a good agreement with Ulysses data. In particular, it could be shown that larger bursts of Jovian electrons named “Jovian jets” can be interpreted as being composed of Jovian jet events.

The development of a pitch-angle dependent numerical transport model for Jovian electron events is presented. The consideration of the pitch angle in the propagation of Jovian electrons lead to the interpretation that the observation of Jovian jets are a direct consequence of the injection of electrons near the Jovian magnetosphere.

# Chapter 1

## Introduction

Since the earliest days of mankind, people may have watched the impressive and mysterious night sky. During the *neolithic revolution*, the transition from hunting and gathering to agriculture (around 10000 B.C.), people found that the annual movement of the celestial bodies seem to be closely related to life on Earth, e.g. it was recognized that the rise and descend of the *Plejads* marked the beginning of spring and autumn, and therefore the time for sowing and harvest. These *cosmic-terrestrial* relations challenged mankind's imagination and religiousness and constellations of stars were attributed to religious and mythological traditions or even to things of every-day experience. However, it was found that some of the stars on the celestial sphere seem to have no fixed position with respect to their neighbors but are wandering more or less independently. These stars were called *planets*<sup>1</sup> and in the classical antiquity they were identified with deities of the Greek or Roman pantheon. The brightest planet that can be observed during the whole night was named after the mightiest god of the roman pantheon: *Jupiter*, the king of the gods, and the god of the sky and thunder.

Indeed, after the invention of the telescope (credited to Hans Lippershey) and early studies by Galileo Galilei and others, it became evident that the planet Jupiter is the biggest body beside the Sun in the solar system. For the next 300 years, ground-based optical observations revealed a lot of information about the planet. For instance, the four Galilean moons were the first objects found to orbit another planet. Much attention was payed to the evolution and dynamics of the Jovian atmosphere, in particular the Great Red Spot, an extremely stable giant storm located in the planet's south equatorial belt known to have existed since it was first observed in the 17<sup>th</sup> century.

In the 1950s Jupiter came into the focus of the young science of radio astronomy, when Burke and Franklin (1957) discovered nonthermal radio emissions from Jupiter. These decimetric and decametric radio emissions were then interpreted as synchrotron radiation emitted by relativistic electrons gyrating around magnetic lines of force and led to the postulation of a Jovian magnetic field, analogous to the magnetic field of the Earth first measured in 1958 by Explorer 1 and later coined "magnetosphere" by

---

<sup>1</sup>From the Greek *πλανήτης* for wanderer.

the Austrian-born astrophysicist Thomas Gold (Gold, 1959) to define the region where the magnetic field of the Earth controls the motions of fast charged particles.

With the launch of the Sputnik I satellite in 1957, the *in situ* exploration of the solar system began. Since the 1970s, eight spacecraft came close to Jupiter, beginning with Pioneer 10 (1973), followed by its twin-spacecraft Pioneer 11 (1974), the two Voyager spacecraft (both 1979), Ulysses (1992, and a distant flyby in 2004), the Cassini spacecraft *en route* to Saturn (2000) and New Horizons on its way to the dwarf planet Pluto (2007). All these spacecraft used Jupiter as a “springboard” to their final destinations, e.g. the outer solar system or the poles of the Sun in case of Ulysses, but nevertheless collected an amount of scientific data. The only spacecraft to orbit Jupiter was the Galileo spacecraft. Launched in 1989, it investigated Jupiter from 1995 to 2003, obtaining immense information about the Jovian system, e.g. the configuration of the magnetosphere and the Jovian moons.

The focus of this thesis is on the investigation and interpretation of so-called Jovian electrons, i.e. electrons of energies of several MeV emerging from the Jovian magnetosphere. Beginning with the literally pioneering work of Chenette et al. (1974), the Jovian electron source turned out to be an important tool to study the dynamics of magnetospheres and the structure of the heliospheric magnetic field and its spatial and temporal variations. In the context of this work, two issues are of accentuated interest: (i) The existence of short-lived anisotropic bursts of Jovian electrons called “Jovian jets” that can be observed in the heliosphere not too far away from Jupiter. While these events suggest a good magnetic connection between the observing spacecraft and the Jovian magnetosphere, they are frequently found at locations not favored by the mean magnetic field predictions to establish those connections. (ii) Inside the Jovian magnetosphere, a sustainable modulation of the energy spectrum of the MeV electrons is observed underlying a periodicity related to the synodic periodicity of the planet ( $\approx 10$  h). This phenomenon, coined “Jovian clock”, still lacks an conclusive explanation, not at least because of the somewhat counterintuitive fact that the spectral modulation seems not to be a spatial effect in a sense that it depends on the observers position in the magnetosphere but is a global effect. Interestingly, the spectral modulation of Jovian electrons can also sometimes be discovered outside the magnetosphere in the interplanetary medium during “bursts” or “Jovian jets”<sup>2</sup>, i.e. prominent Jovian electron enhancements accompanied by directional anisotropies of the particles.

The intent of this thesis is the study of the Jovian jet phenomenon with respect to the interplanetary conditions based on data analysis of the Ulysses and Pioneer 10/11 spacecraft in conjunction with a mathematical model to describe the propagation of Jovian electrons up to now successfully applied to solar event particles. For this task, an adequate knowledge of the particle source, i.e. Jupiter’s magnetosphere is of importance. Therefore a reinvestigation of the “Jovian clock“ is part of this work.

Chapters 2 and 3 are dedicated to a description of the heliospheric environment

---

<sup>2</sup>The term “Jovian jet” in the sense as it will be used here was first coined in 1992 by researcher working on Ulysses data.



and the magnetosphere of Jupiter will be discussed as far as it is of importance for this work. The first issue covers the interplanetary magnetic field and the solar wind as well as large scale structures like corotating interaction regions and coronal mass ejections. Furthermore, the energetic particle populations (e.g. galactic cosmic rays) will be discussed. The second issue addresses the structure and dynamics of the Jovian magnetosphere and the particle populations observed in this environment in its inner, middle and outer regions.

Chapter 4 focuses on the physical/mathematical framework of charged particle propagation in the heliosphere leading to the discussion of the transport equation that will be used in this work to model the pitch-angle dependent transport of Jovian electrons. The Fokker-Planck equation as the fundamental equation for the description of charged particle propagation in a non-homogenous magnetic field will briefly be described followed by the discussion of two special cases of this equation: The focused transport equation (also known as Roelof's equation) and the Parker equation.

Chapter 5 deals with methods of charged particle measurements in the space environment and a description of the spacecraft whose data had been used in this work (Ulysses and Pioneer 10/11). Furthermore, the concept of anisotropy in the context of the measurement of charged particles will be described.

The subsequent chapter gives an overview of the fundamental results of the observation of Jovian electrons in the heliosphere to provide an adequate background for the understanding of the Jovian electron source. The influence of magnetic mirroring of charged particle coming from the outer region of the heliosphere will also be discussed.

In chapter 7, the results of a re-investigation of Ulysses data in the Jovian magnetosphere will be presented. Beside the well-known "Jovian clock", another quasi-periodic modulation of electrons was identified in the Ulysses data. A comparison with Pioneer data confirms the existence of this modulation that was found to be related to the planet's magnetospheric current sheet.

The most voluminous part of this work is chapter 8 dealing with the analysis of Jovian jets detected by Ulysses and Pioneer 10. As mentioned above, Jovian jets often occur at locations not favored by the nominal Parker field. The influence of interplanetary mass ejections is discussed as a possible source for the large temporal deviations of the local magnetic field. Based on the methods elaborated in chapter 5, the pitch-angle distribution of Jovian jets will be studied for some examples to answer the question if Jovian jet events show evidence for a significant backscattering of particles. This important question is a prerequisite for the justification of the transport model. Another important problem pursued in this chapter is the detectability of Jupiter's rotation period of 10 h in the energy spectrum and counting rates of Jovian electron at considerably distances from the planet. By applying a three-dimensional version of the Lomb-Scargle spectral analysis it was possible to find clear evidence for the 10 h periodicity as far away as 1.2 AU from the planet. While this observations shifts the distance at which Jupiter's signature was detected by a factor of  $\sim 1.5$ , evidence for the presence of the 10 h periodicity even at 2.2 AU will be discussed. Spurred by these results, the Pioneer 10 data close to the Jovian magnetosphere were

analyzed with respect to Jovian jets. This investigation revealed that the "Jovian bursts" found by Chenette et al. (1974) can be identified as composition of events very similar to the "Jovian jets" Ferrando et al. (1993) described to account for the Ulysses observations.

The following chapter 9 contains the application of the transport equation to the pitch-angle dependent Jovian electron transport. It could be shown that the anisotropy of Jovian jets is a direct consequence of the pitch-angle dependent transport under the assumption of typical mean free paths. Furthermore the phenomenon of the 10 h periodicity is discussed. In good agreement with the observations, the model predicts that the 10 h periodicity is accompanied by a certain level of particle anisotropy.

The two appendixes at the end of this work provide a short recapitulation of the System III (1965) coordinate system for Jupiter's magnetosphere and a mathematical description of the algorithm used to solve the transport equation.

# Chapter 2

## The Sun and Heliosphere

Who has seen the wind?  
Neither I nor you: but when  
the leaves hang trembling  
The wind is passing thro'

---

Christina Rossetti

### 2.1 The Solar Wind

The Sun's energy is produced by nuclear fusion of hydrogen to helium in the core and is transported via radiation and convection to the Sun's outer layers. The visible surface of the Sun is the so-called photosphere. The Sun itself is a magnetic star, i.e. in a rather simplified approach, the Sun can be imagined as a gigantic bar magnet, producing a dipole-like magnetic field. It is believed, that the Sun's magnetic field is generated by strong currents in the solar interior (dynamo effect). Right above the photosphere, only separated by the relatively thin chromosphere, the corona is located. The solar corona can be treated as a part of the Sun's atmosphere and is of highest interest for space physics, because it is the source of the solar wind, a continuous flow of charged particles away from the Sun. Moreover, the solar wind drags the Sun's magnetic field into outer space, leading to the formation of the structure of the heliosphere with all its consequences to the propagation of charged particles in the solar system.

#### The Corona – Source of the Solar Wind

The solar corona defines the uppermost layer of the Sun's atmosphere, made of primarily hydrogen and helium, with a density significantly lower than in the photosphere. While the Sun's visible surface, the photosphere, has a temperature of  $\sim 6000$  K, the corona's temperature is of the order of  $10^6$  K. This is a puzzling fact, because the question arises how the corona can be hotter than the photosphere (Prölls, 2001).

This problem, however, had not been solved satisfactory up to know, although several theories had been developed including heating by magnetic reconnection or by waves (Meyer-Vernet, 2007; Aschwanden, 2009). Fig. 2.1 shows two photographs of the solar corona at extreme ultraviolet wavelengths taken by the SOHO satellite. Regions of different brightness can be identified over the all latitudes. The prominent bright areas in equatorial regions are so-called “active regions”, i.e. regions of enhanced solar activity like flares or coronal mass ejections. Close to the poles of the Sun, regions that appear to be darker than the equatorial region can be found. These regions are dominated by open magnetic field lines, allowing for an effective outflow of solar wind plasma. Consequently, the density of hot plasma is much lower than at low or medium latitudes. This is the reason why they are darker than their equatorial counterparts, where the magnetic field lines are closed.

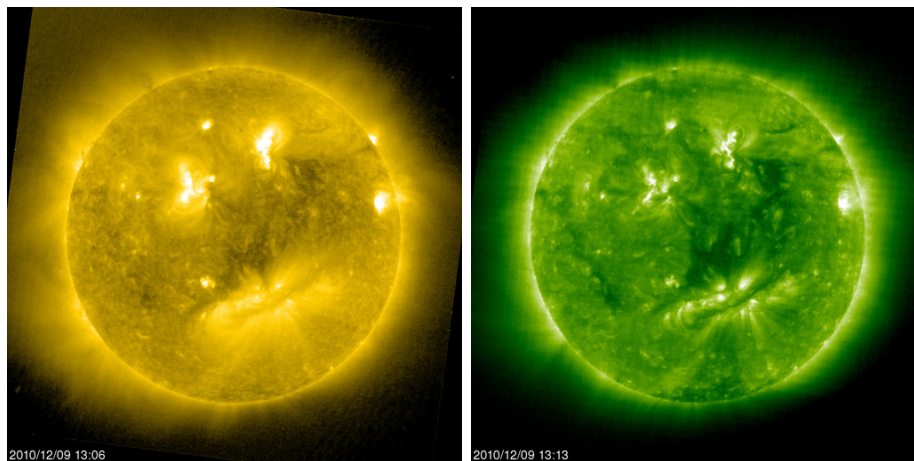


**Figure 2.1:** The photography on the left shows the solar corona at the emission wavelength of Fe XV (284 Ångstroms) taken by the EIT instrument aboard SOHO on 9.12.2010. A clear pattern of active regions can be identified. The photography on the right was taken on the same day but at the wavelength of Fe XII, corresponding to 195 Ångstroms. The dark spots on the Sun’s surface are coronal holes. Taken from <http://soho.nascom.nasa.gov>.

In the late 1950s, E. N. Parker, based on hydrodynamic calculations, postulated that the corona is not static, but underlies a permanent expansion, manifested by a steady outflow of coronal material into the solar system (Parker, 1958). Four years later, when the American spacecraft Mariner 2 was launched to its interplanetary trajectory, Parker’s postulation was ultimately confirmed by the detection of an interplanetary continuous flow of protons away from the Sun, known since then as the solar wind.

## The Solar Wind and the Interplanetary Magnetic Field

The properties of the solar wind are under investigation for decades after its discovery in the early 1960's, both in the ecliptic as well as at mid and high latitudes (see e.g. the references in Meyer-Vernet, 2007) and the summary of the results of the Helios mission by Schwenn and Marsch (1990). Long term observations near the ecliptic plane and at higher latitudes revealed that the solar wind plasma can principally be divided into two different types: The slow solar wind with a mean speed of  $\sim 400$  km/s and the fast solar wind with a mean speed of  $\sim 800$  km/s. The origin of the slow solar wind are the regions of closed magnetic fields, i.e. bright regions of the corona, while the fast solar wind emerges from coronal holes. The fast solar wind is primarily a feature of higher solar latitudes as can be seen in Fig. 2.2, showing measurements of the solar wind speed as a function of latitude obtained by the spacecraft Ulysses during its trajectory almost perpendicular to the ecliptic plane (McComas et al., 2000). As can be seen, the regions of slow solar wind are limited to a band not broader than  $\pm 45^\circ$ . However, in equatorial regions an alternating flow of fast and slow solar wind can be detected. The reason for this is the fact that coronal holes may extend down to equatorial regions, so that the fast and slow solar winds are observed variably.

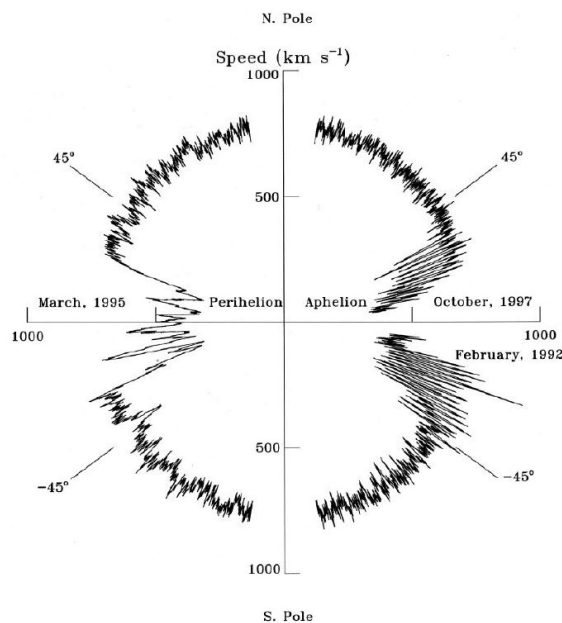


**Figure 2.2:** Dependence of the solar wind speed as a function of latitude measured by the SWOOPS experiment aboard Ulysses. Taken from <http://swepam.lanl.gov/Figures/Figure01.JPG>.

As stated above, the Sun has a magnetic field. This has important consequences on the structure of the interplanetary medium. The conductivity of the interplanetary

medium can be treated as almost infinite, i.e. there are no permanent large scale electric fields. As a consequence, the magnetic field is “frozen“ in the solar wind plasma, as can be derived from Maxwell’s equation and the Newton-Lorentz equation for the case of an infinite conductivity. This frozen-in condition results in the fact that plasma parcels attached to a magnetic field line will be attached to this field line forever. This concept will now be illustrated for solar wind parcels emerging from a fixed longitude on the solar surface while the Sun rotates around their spin axis. The

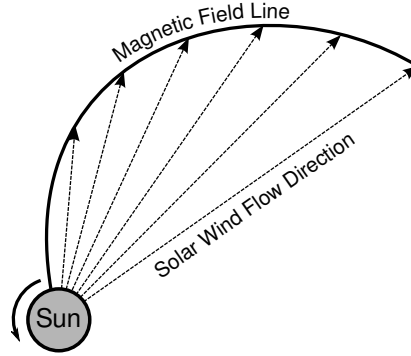


**Figure 2.3:** The shape of the Parker spiral in the heliographic plane as seen from north. The solar wind particles propagate radially away from the corona. The Sun rotates with the angular speed of  $\Omega$  and since the magnetic field is attached to the solar wind plasma due to the “frozen in” condition, the typical shape of the Parker spiral evolves.

solar-centric distance of a solar wind particle is simply given by

$$r(t) = r_0 + u_{sw} \cdot \Delta t, \quad (2.1)$$

where  $r_0$  is the distance of the particle’s source (i.e. the corona) with respect to the center of the Sun. The solar wind speed is given by  $u_{sw}$ <sup>1</sup> and  $\Delta t$  is the time after the particle was injected. However, since the magnetic field lines are “frozen in”, they are attached to the solar wind. As a consequence, the interplanetary magnetic field forms an Archimedian spiral, also known as Parker spiral

$$r(\varphi) \approx -\frac{u_{sw}}{\Omega} (\varphi - \varphi_0) \quad \varphi < \varphi_0, \quad (2.2)$$

as it is shown in Fig. 2.3. Here,  $\Omega$  is the angular speed of the Sun,  $\varphi$  is the longitude and  $\varphi_0$  the longitude of the footpoint of the magnetic field line. The components and the magnitude of the interplanetary magnetic field can be derived from the frozen-in

<sup>1</sup>Throughout this work,  $u$  will refer to the speed of solar wind particles while  $\vec{v}$  denotes the velocity of energetic (test) particles.

theorem (Prölss, 2001) and read

$$B_r = B(r_0) \left(\frac{r_0}{r}\right)^2 \quad (2.3)$$

$$B_\vartheta = 0 \quad (2.4)$$

$$B_\varphi = -B(r_0) \frac{\Omega r_0}{u_{sw}} \left(\frac{r_0}{r}\right), \quad (2.5)$$

and

$$B = B(r_0) \sqrt{1 + \left(\frac{\Omega r}{u_{sw}}\right)^2} \left(\frac{r_0}{r}\right)^2, \quad (2.6)$$

where  $r_0$  is an arbitrary distance from the Sun with  $r > r_0$ . As a result of the radial outflow of the solar wind, the Parker field has no latitudinal component, i.e. the three dimensional shape of a Parker spiral is simply a cone resembling an ice-cream cornet.

While the solar wind drags the magnetic field lines away from the Sun, the original dipole of the solar magnetic field becomes highly stretched. In particular, in equatorial regions a surface is found where the polarity of the magnetic field changes its sign rapidly. Due to Ampère's law,  $\oint \vec{B} \cdot d\vec{l} = \mu_0 \int \vec{J} \cdot d\vec{A}$ , this requires the existence of a current at these boundary. This boundary is called the heliospheric current sheet. Due to the inclination of the Sun's magnetic field and the finite propagation time of the solar wind, the current sheet has the shape similar to that of the skirt of a swirling ballerina, an image coined by Alfvén (1977). The existence of the heliospheric current sheet, i.e. a region of flipping polarity, has important influence on the propagation of charged particles in the heliosphere as for example discussed by Strauss et al. (2012) and references therein.

### Corotating Interaction Regions

In the previous section it is already mentioned that there are basically two types of solar wind streams, i.e. the slow ( $\sim 400$  km/s) and the fast solar wind ( $\sim 800$  km/s). If a coronal hole, i.e. the source region of the fast solar wind, extends to equatorial regions, an interaction region develops. Because of the rotation of the Sun and the stability of the interaction regions up to several months, an observer encounters this interaction region recurrently every  $\sim 26$  days. Therefore, these interaction regions are called corotating interaction region (CIRs). Fig. 2.4 shows schematically the interaction of a slow and a fast solar wind stream emerging from the Sun at different latitudes. While the solar wind propagates radially away from the Sun, the fact that the Sun rotates leads to the consequence that the fast solar wind runs into the slow one. However, the fast solar wind can not overtake the slow solar wind because of the frozen-in condition of the interplanetary magnetic field. Therefore, a compressing region develops at the boundary between the two different streams. At heliographic distances of 2-3 AU, the magnetosonic speed has decreased to values that are frequently below the difference of the speed of the fast and slow solar wind streams (Burlaga, 1974). As a consequence,

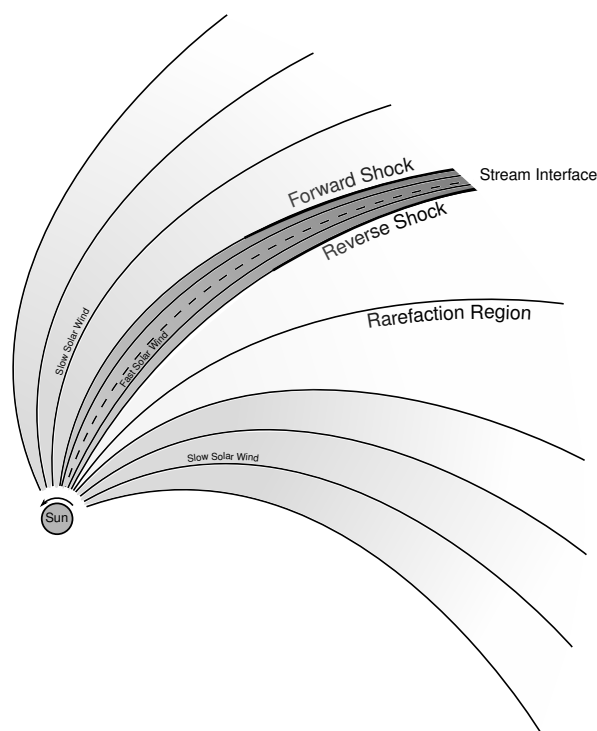


**Figure 2.4:** The interaction of two solar wind streams with different speeds leads to the evolution of a corotating interaction region. The different shades illustrate the different levels of plasma density.

a forward and a backward shock pair evolves bounding the compression region. This shock pair is the source of CIR associated energetic particles, that gain their energies of up to several MeV by shock acceleration (Mason et al., 1999).

The boundary between the slow and the fast solar wind plasmas is the so-called stream interface (SI), indicated by the dashed curve in the Figure. The SI is a quite sharp boundary ( $< 10^4$  km) and is defined by a decrease in density of the plasma by a factor of 2 and a small increase of the solar wind speed and an increase of the plasma's kinetic temperature by a factor of 2 (Burlaga, 1974; Wimmer-Schweingruber et al., 1997). Since magnetic field lines can not penetrate each other, the SI is not only a boundary separating two distinct plasmas, but also magnetic field lines. As a consequence, CIRs are effective barriers for the propagation of energetic particles in the heliosphere as has been pointed out e.g. for Jovian electrons by Conlon and Simpson (1977), Conlon (1978) or Dunzlaff (2007).

## Solar Flares

While CIRs are recurrent events, two principal classes of transient events are observed in the heliosphere. The first type of event to mention are solar flares. The formation



of solar flare events is caused by magnetic reconnection, i.e. a change in the magnetic field topology, at the Sun's surface. During reconnection, magnetic energy is converted to kinetic energy, i.e. charged particles are accelerated at the reconnection site, what is typically associated with the release of electromagnetic radiation, and propagate along the Parker spiral. Solar flare accelerated particles are used as test particles for the investigation of transport parameters, i.e. diffusion coefficients and the corresponding mean free paths, in the heliosphere (Dröge, 2004; Dröge and Kartavykh, 2009).

### Coronal Mass Ejection

The term Coronal Mass Ejection (CME) denotes the explosive-like release of large amounts of coronal material into interplanetary space (Aschwanden, 2009). These CMEs, often associated with large flare events, are also the result of energy releases on large scales. Compared to solar flare events, CMEs carry their own magnetic field, leading to disturbances of the mean Parker field as they propagate away from the Sun where they are called Interplanetary Coronal Mass Ejections (ICMEs). Typical signatures for the detection of ICMEs at the orbit of the Earth are anomalously low plasma temperatures, bidirectional fluxes of superthermal electrons and energetic ions of coronal origin as well as the observation of enhanced helium abundances and unusual ionization states of heavier ions (von Steiger and Zurbuchen, 2003; Du et al., 2010). A subclass of CMEs are magnetic clouds, making up 30% of the ICME population and are characterized by a smooth rotation of the magnetic field forming a flux rope structure. Because of their size and transient character, CMEs are known to cause temporal disturbances in the surrounding IMF.

## 2.2 The Heliosphere and its Boundaries

The heliosphere is defined as the space influenced by the Sun and the solar wind and separates the solar wind plasma from the interstellar medium (ISM) (e.g. Potgieter, 2010). The shape of the heliosphere is determined by the counterplay of the pressure of the solar wind emerging from the Sun and the pressure of the ISM. The solar wind and the attached interplanetary magnetic field is an obstacle for the ISM. As a consequence, the ISM is decelerated to subsonic speeds, given that it initially traveled with super-sonic speed. This question is still under debate and it is, therefore, not clear if the bow shock exists, although a recent study by McComas et al. (2012) suggest the non-existence of a bow shock but merely a "bow wave".

The termination shock is the region where the solar wind plasma becomes subsonic and the heliopause constitutes the interface between the interplanetary magnetic field and the magnetic field of the ISM, since these magnetic fields can not penetrate each other. Assuming that the ISM constantly hits the heliosphere from one direction, the heliospheric tail develops, i.e. the heliosphere is significantly stretched in one direction, similar to planetary magnetospheres. A sketch illustrating the shape of the heliosphere

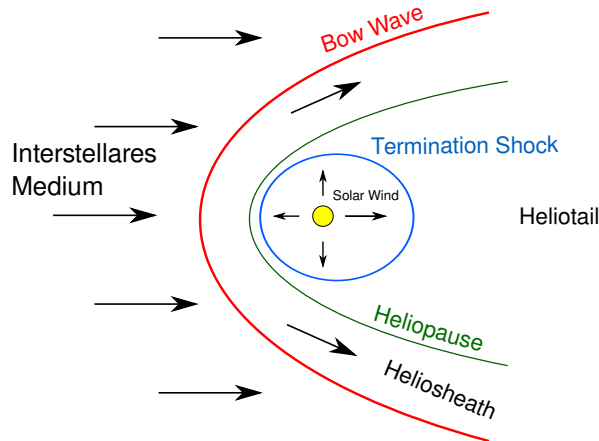


**Figure 2.5:** Sketch of the heliosphere. The heliopause separates the solar wind from the ISM while the solar wind itself already becomes subsonic at the termination shock. The layer between the heliopause and the termination shock is called heliosheath. The sketch is not to scale.

is shown in Fig. 2.5.

## Galactic Cosmic Rays

The observation of galactic cosmic rays started at the beginning of the 20<sup>th</sup> century, right after the discovery of natural radioactivity. In 1912, V. Hess started a balloon campaign to investigate the ionization of air due to the terrestrial radiation as a function of altitude. However, contrary to what was expected, he discovered that the ionization rate increased with increasing distance from sea level and concluded that the source of this *Höhenstrahlung*<sup>2</sup> is extraterrestrial. After the invention of the Geiger-Müller detector, it finally turned out that cosmic rays consists of charged particles and not of electro-magnetic rays. Nowadays, cosmic rays (and/or their secondary particles) are under permanent investigation by a fleet of spacecraft, either at Earth's orbit or on interplanetary trajectories, and a network of neutron monitors on the Earth's surface. In the literature, the term galactic cosmic rays (GCRs) generally addresses energetic particles that come from outside the heliospheric boundaries, while "cosmic rays" is commonly used as a generic term for solar energetic particles as well as energetic planetary particles like Jovian electrons. The galactic cosmic ray population mainly consist of protons and heavier nuclei ( $\sim 98\%$ ), while only  $\sim 2\%$  is made of electrons. The large majority of the positively charged cosmic ray component is made of protons ( $\sim 87\%$ ). The fraction of helium nuclei is about 12%, while the remaining part (1%) is made of

<sup>2</sup>A proper translation is "high-altitude radiation". The term "cosmic rays" was proposed in 1925 by R. A. Millikan and its literal translation "*Kosmische Strahlung*" is now commonly used in the German language.

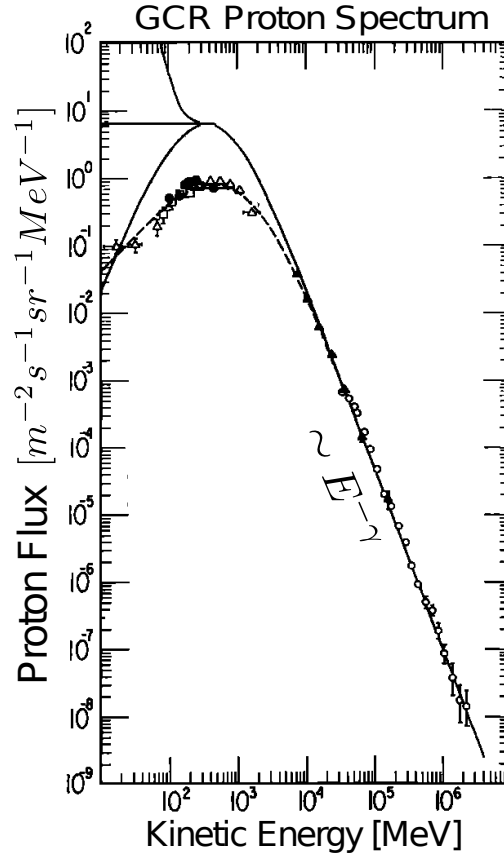


**Figure 2.6:** The GCR proton spectrum from 10 MeV up to  $10^7$  MeV. Beyond  $10^4$  MeV, the energy spectrum can be well described by a power law with spectral index  $\gamma$ . The symbols represent measurements, the dashed line corresponds to the near-Earth modulated spectrum, the solid curves the derived interstellar spectrum. Taken from Fulks (1975), modified.

nuclei of heavier elements like iron or carbon (Longair, 1992). The energy spectrum of GCR protons measured at Earth's orbit is shown in Fig. 2.6, which has been taken from Fulks (1975). On a double-logarithmic scale, the plot shows the proton flux as a function of energy in a range of energy from 10 MeV up to  $10^7$  MeV. The symbols correspond to measured data while the dashed line is a fit to the data. The solid curves are the derived interstellar spectrum. As can be seen, for energies above  $\sim 10^4$  MeV, the energy spectrum can be described by a power law (Longair, 1992) of the form

$$N(E)dE = KE^{-\gamma}dE, \quad (2.7)$$

where  $N(E)dE$  is the differential flux,  $K$  is a constant,  $E$  is the energy and  $\gamma$  is the so-called spectral index, that determines the slope of the spectrum. The energy spectrum of GCRs is strongly affected by the configuration of the heliosphere, i.e. the

interplanetary magnetic field and the solar wind, as the particles travel from the border of the heliosphere towards the inner regions of the solar system. The variation of the transport parameters is mainly caused by the solar cycle, i.e. a period variation of the Sun's magnetic configuration. The galactic origin of GCRs and their acceleration mechanism is in discussion since their first observation. However, within the last decades it turned out that there is strong evidence that GCRs are primarily accelerated at the moving shock front of supernova remnants (Ginzburg and Syrovatskii, 1964; Longair, 1994; Aharonian and the HESS consortium, 2006; Büsching and Potgieter, 2008) or by the rotational energy of millisecond pulsars (Büsching et al., 2008).

## The Solar Cycle

The overall configuration of the solar corona and the photospheric magnetic field of the Sun is not in a steady-state condition. Indeed, the Sun underlies a periodic variation of about 11 years. This variation is called the solar cycle and has first been observed

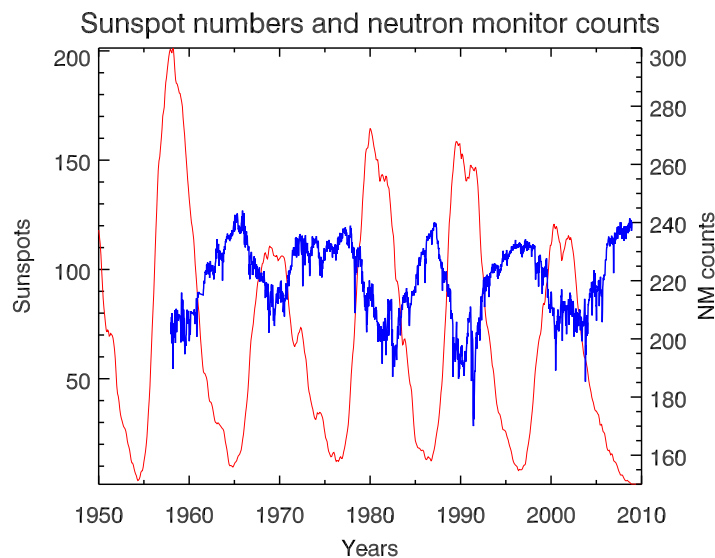


**Figure 2.7:** This Figure shows the sunspot number and neutron monitor counts from 1950 and 1957, respectively to 2010. A clear anti correlation between these quantities is visible, suggesting a dependence of the galactic cosmic rays flux at Earth's orbit from the configuration of the Sun and the interplanetary magnetic field.

by investigations of sunspots, i.e. regions of a significantly increased magnetic field strength near the solar surface. It turned out that the number of sunspots visible on the solar surface shows minima and maxima with a periodicity of  $\sim 11$  years. This 11 years solar cycle is accompanied by a global reconfiguration of the Sun's dipole field, i.e. a reversal of the magnetic field polarity in the two hemispheres. As it takes 11 years

to switch the sense of polarity of the Sun, after 22 years the orientation of the Sun's magnetic field is the same again. This polarity reversal is related to changes in the solar wind properties and the occurrence of coronal disturbances like flares or CMEs. The time period when a maximum of sunspots is observed is called solar maximum and is characterized by a slow solar wind speed profile from low to highest latitudes and a maximum of the occurrence of flares and CMEs, while during solar minimum these events are at a minimum and both slow and fast solar wind streams are observed. Like the heliospheric current sheet, the actual polarity of the Sun's magnetic field has influence on the propagation of GCRs. This is illustrated in Fig.2.7, showing the sunspot number as well as neutron monitor counts as a measure for the GCR flux at Earth. As can clearly be seen, the GCR flux is at minimum during solar maximum, i.e. when the sunspot number is high and vice versa. It is also evident that the maxima of the neutron monitor counts are alternating peak-like and plateau-like. This behavior is related to drift effects, caused by the polarity of the Sun (e.g. Potgieter, 2008).



# Chapter 3

## The Jovian System in the Heliosphere

If you have seen one  
magnetosphere, you haven't  
seen them all.

---

James A. Van Allen

The Jovian system is doubtlessly one of the most complex and dynamical astronomical object accessible to in-situ and ex-situ observations. This chapter is dedicated to a brief description of Jupiter and its magnetosphere as far as it is necessary to understand the observations and discussion presented in the chapter dealing with the dynamics of high energetic particles hosted in the magnetosphere, especially with respect to the  $\sim 10$  h modulation of MeV electrons. A comprehensive discussion of all aspects of the Jovian magnetosphere, as well as the planet itself and its moons can be found in Gehrels and Matthews (1976), Dessler (1983) and Bagenal et al. (2004).

### 3.1 The Planet Jupiter

Jupiter is the fifth member of the planets orbiting the Sun, located between Mars and Saturn at a mean distance from the Sun of about 5.2 AU. The orbital period is 11.86 years, i.e. the average orbital speed is  $\sim 13$  km/s. Like all other planets, Jupiter is located very close to the plane of the ecliptic. Concerning mass, radius, Jupiter is definitely the largest planet in the solar system with an equatorial radius of  $71492 \pm 4$  km (Seidelmann et al., 2007), i.e. more than 11 times that of Earth, and a mass of  $1.89 \cdot 10^{27}$  kg, i.e. about 318 Earth masses. An important feature of the Jovian magnetosphere described in the following section is the very fast rotation of the body with a period of  $\sim 9\text{h}55'29.704''$  (Yu and Russell, 2009). Compared to the rocky planets Mercury, Venus, Earth, and Mars, Jupiter is a so called gas giant like Saturn. That means, Jupiter is not primarily made of solid matter, but mainly consists of hydrogen and helium (more

than 87%) and traces of other gases like methane and ammonia. The atmosphere of the planet is dominated by the presence of highly dynamical cloud ribbons at all latitudes streaming at different speeds leading to turbulence and circulation patterns (Fig. 3.1). The most prominent of which is the famous Great Red Spot, a stable



**Figure 3.1:** Jupiter as seen by Pioneer 10 in December 1973 during the spacecraft's flyby. The cloud ribbon and the Great Red Spot can be seen as well as the shadow of one of Jupiter's moons.

structure probably lasting for hundreds of years, located in the southern hemisphere. The interior of Jupiter can be divided into three main regions, namely a helium-poor hydrogen layer at the top of the planet, followed by a helium-rich envelope of metallic hydrogen and finally a dense core of a still uncertain composition. However, it is assumed that a convection-driven dynamo in the electrically conducting regions of the planet's interior leads to the generation of the internal Jovian magnetic field (Busse, 1979), responsible for Jupiter's giant magnetosphere described in the following section.

## 3.2 The Jovian Magnetosphere

Beside Venus and Mars, all planets of the solar system are hosts of an intrinsic magnetic field. The cavity generated by this magnetic field is called magnetosphere. It is believed that the magnetic fields of Jupiter is generated by a dynamo operating in the interior of the planets (Neubauer, 1991). Fig. 3.2 shows a comparison of the sizes of the magnetospheres of Mercury, Earth, Saturn and Jupiter. As can clearly be seen, the Jovian magnetosphere is by far the largest one in the solar system with subsolar magnetopause distances varying from 45-100  $R_J$  ( $1R_J = 71492$  km) as it was deduced from spacecraft observations (Khurana et al., 2004), reflecting the large variability of the Jovian magnetosphere in response to changing solar wind conditions. Fig. 3.3 shows an illustration of Jupiter's magnetosphere. The solar wind, coming from the left side, is decelerated to subsonic speeds when encountering the magnetosphere, resulting in the formation of the bow shock and the magnetosheath. The boundary between the interplanetary medium and the magnetosphere is defined by the magnetopause. In



equatorial regions, a current sheet is formed as a result of outwards streaming plasma dragging the magnetic field lines. Since the observations of the Jovian magnetosphere by the Pioneer and Voyager spacecraft, it is common to divide Jupiter's magnetic field into three distinct regions, namely the inner, middle and outer magnetosphere. Each of which is characterized by special properties concerning the magnetic field and plasma environment.

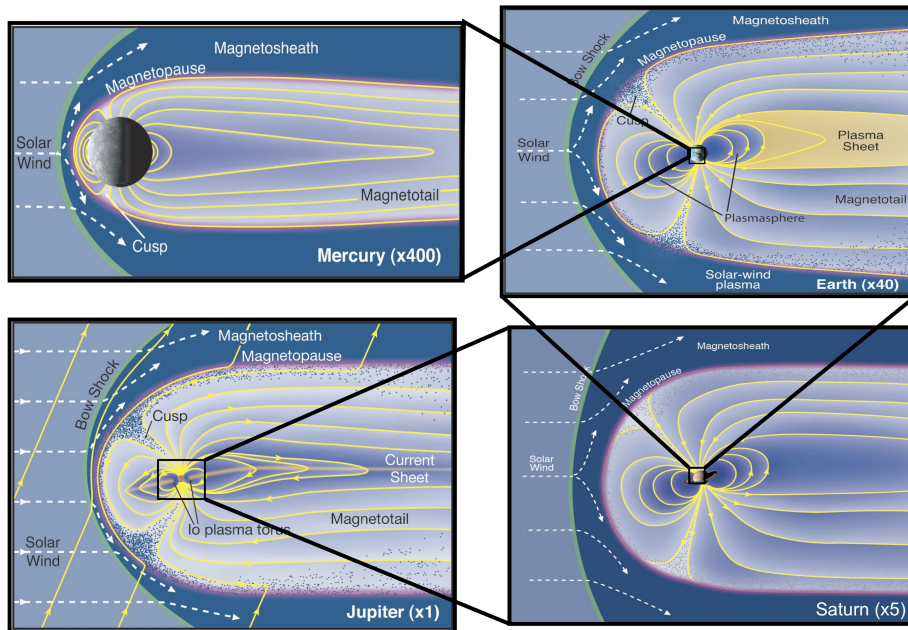


**Figure 3.2:** Comparison of the sizes of magnetospheres of Mercury, Earth, Saturn and Jupiter. The Jovian magnetosphere is by far the largest planetary magnetic field in the heliosphere. Taken from <http://lasp.colorado.edu/mop/resources/graphics/JSEM.jpg>.

## The Inner Magnetosphere

The inner magnetosphere is the region that is strongly dominated by the internally produced field and extends up to distances of about  $6 R_J$ , i.e. roughly the orbit of the satellite Io. The inner magnetosphere is typically treated as a current-free region and is known to be the source of the plasma in the magnetosphere and is the host of the inner radiation belts of the planet (Garrett et al., 2005). Observations made by the Voyager spacecraft (Broadfoot et al., 1981) revealed that the innermost of the four Galilean moons, Io, is the primary source of plasma in the Jovian magnetosphere. The reason for this are the strong tidal forces induced by Jupiter acting on the moon

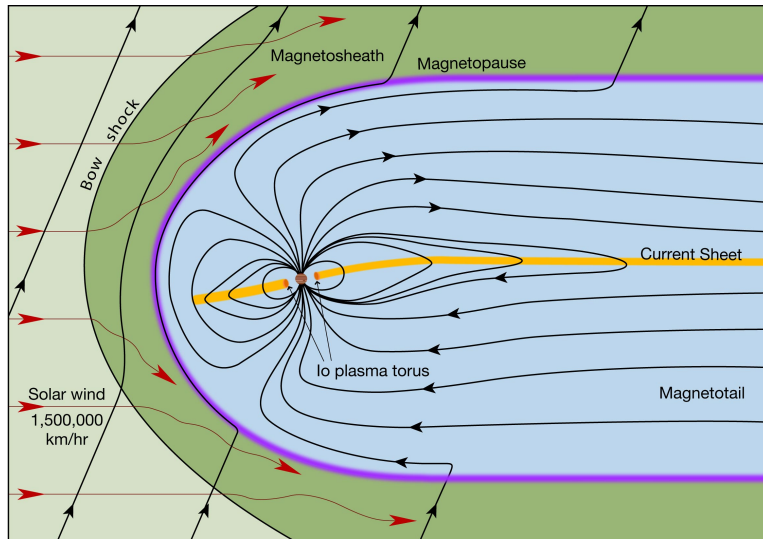


**Figure 3.3:** A more detailed view of the Jovian magnetosphere. The inner and middle regions of the magnetosphere are strongly dominated by the moon Io and the magnetospheric current sheet. The outer region is very variable as it is strongly affected by the conditions of the solar wind acting on the magnetosphere.

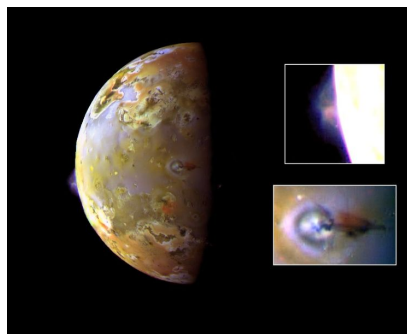


**Figure 3.4:** Photography of the Galilean moon Io, the most volcanic body in the solar system. The insets show volcanic eruptions on the moon's surface. The ejected material is ionized by radiation and becomes an important source of plasma in the Jovian magnetosphere.

leading to tidal heating of Io (McEwen et al., 2000). As a result, Io is found to be the most volcanic object in the solar system (see Fig. 3.4), injecting 1 ton/s into the magnetosphere. This material, mainly consisting of sulfur and oxygen, creates the so-called Io plasma torus located between  $5.2 R_J$  and  $\sim 10 R_J$  until it is ionized by electron impacts and charge exchange (Thomas et al., 2004, and references therein). Because of centrifugal forces, this plasma is convected away from the planet, leading to

the formation of a current sheet dominating the middle regions of the magnetosphere.

### The Middle Magnetosphere

The middle magnetosphere is strongly affected by the presence of an azimuthal current sheet as a result of the outflowing iogenic plasma. Similar to the formation of the heliospheric current sheet, the plasma drags the magnetic field lines leading to a significant deformation of the dipole-like field. In equatorial regions, a surface is found where the radial component of the magnetic field changes its sign, resulting in a current system because of the non-vanishing integral  $\oint \vec{B} \cdot d\vec{l}$  across this region (Ampère's law). The magnetic dipole is tilted by  $\sim 9.6^\circ$  with respect to the planet's spin normal  $\vec{\omega}$ . Consequently, a spacecraft located near the rotational equator, experiences two changes in polarity in a Jovian revolution, while a spacecraft located at higher magnetic latitudes remains in the same magnetic polarity sector. The latitudinal excursion of a spacecraft with respect to the nominal magnetic equator is approximately given by

$$\vartheta_m = 9.6^\circ \sin(\lambda_{III} - 110^\circ) + \vartheta, \quad (3.1)$$

where  $\vartheta$  is the jovigraphic latitude of the spacecraft and  $\lambda_{III}$  its System III (1965) longitude. The factor  $9.6^\circ$  corresponds to the magnetic tilt angle. Since the tilt angle is tilted towards  $\lambda_{III} \approx 200^\circ$ , the magnetic and jovigraphic equators intersect at  $\lambda_{III} = 110^\circ$  and  $\lambda_{III} = 290^\circ$ . Therefore, the phase angle in Eqn. 3.1 is  $110^\circ$ . See Appendix A for further discussion.

### The Outer Magnetosphere

The outer magnetosphere is a highly irregular region between the middle magnetosphere and the magnetopause. The extension of the outer magnetosphere, and therefore that of the magnetosphere as a whole, is subject of significant variations depending on the conditions of the interplanetary medium, in particular the pressure of the solar wind and the polarity of the IMF. Consequently, the sunward extension of the magnetosphere may change significantly in response to varying IMF conditions. While the current sheet is normally well established in the middle magnetosphere, it can barely be recovered in the outer region of the magnetosphere as a result of the unsteady and irregular conditions. As stated above, the radius of the magnetosphere lies between  $\sim 45$  and  $\sim 100 R_J$ .



# Chapter 4

## Transport of Charged Particles in Interplanetary Space

But now I have come to believe that the whole world is an enigma, a harmless enigma that is made terrible by our own mad attempt to interpret it as though it had an underlying truth.

---

Umberto Eco - Foucault's Pendulum

In this chapter the theoretical framework of transport theories for particles in a space plasma will be discussed. After a short recapitulation of single particle motion in homogeneous magnetic fields, a short outline of the derivation of the Fokker-Planck equation will be given as well as a discussion of some of its special applications commonly used in space science.

### 4.1 Particles in Magnetic Fields

The equation of motion of a charged particle in a magnetic field is given by the Newton-Lorentz equation

$$\gamma m_0 \frac{d\vec{v}}{dt} = q (\vec{v} \times \vec{B}), \quad (4.1)$$

where  $m_0$  is the rest mass of the particle,  $q$  its charge,  $\vec{v}$  the velocity and  $\vec{B}$  an external, uniform and static magnetic field. The factor  $\gamma$  is the Lorentz factor, i.e. Eqn. (4.1) takes into account the motion of particles with relativistic energies as it is the case for Jovian electrons or GCR protons of several hundreds to thousands of MeV. From Eqn. (4.1) it follows, that a particle with a non-zero velocity component perpendicular

to the magnetic field vector experiences a force pointing in the direction given by the cross product of  $\vec{v}$  and  $\vec{B}$ . As a consequence, the particles perform orbital motions around their corresponding magnetic field lines. The magnetic field line in the center of the circle described by the motion of the particle is called the guiding center. If the particle also has a component parallel to the magnetic field, the total velocity is given by the orbital motion around the guiding center and a motion parallel to the field line. This results in a helical orbit of the particle around the magnetic field line as is illustrated in Fig. 4.1. The magnetic field, i.e. the guiding center is indicated by the red line. The helix shows the gyromotion of the particle along the magnetic field line. The total velocity  $\vec{v}$  is the result of the motion along the magnetic field line ( $\vec{v}_{\parallel}$ )

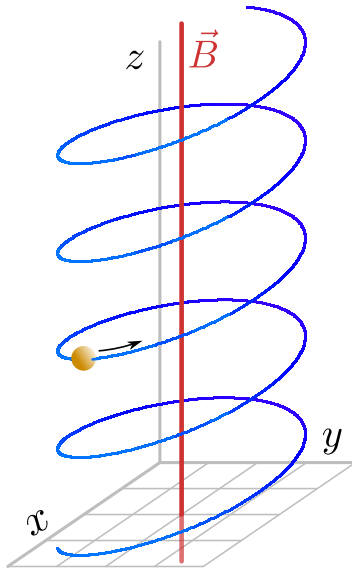


**Figure 4.1:** Helical orbit of a charged particle (orange dot) in a uniform magnetic field (red line). The particle moves with a speed  $v_{\parallel}$  along the  $z$ -axis while it spirals around its guiding center with a speed  $v_{\perp}$ . The pitch angle cosine  $\mu$  is defined as the ratio between the parallel velocity component and the total velocity, i.e.  $\mu = v_{\parallel}/v$ .

and perpendicular to it ( $\vec{v}_{\perp}$ ). An important parameter is the pitch angle of the particle and is defined as the angle between  $\vec{v}_{\parallel}$  and  $\vec{v}$  and is given by

$$\cos \vartheta = \frac{|\vec{v}_{\parallel}|}{|\vec{v}|}. \quad (4.2)$$

However, it turned out to be useful not to mention the pitch angle  $\vartheta$  itself but the so-called pitch-angle cosine  $\mu$ , i.e.

$$\mu = \cos \vartheta. \quad (4.3)$$

The gyroradius of the particle, i.e. the distance from the guiding center is given by (cf. Longair, 1992) as

$$r = \frac{\gamma m_0 |\vec{v}| \sqrt{1 - \mu^2}}{|q\vec{B}|}. \quad (4.4)$$

From Eqn. (4.4) it follows that the gyroradius of a particle not only depends on the magnetic field strength, but also on its mass. As a consequence, electrons and protons propagating with the same speed have considerable different gyroradii. Since the mass of a proton is about 1836 times that of an electron, its gyroradius is 1836 larger due to the linear relationship in Eqn. (4.4).

## Magnetic Mirrors

If there is a (weak) gradient in the magnetic field  $\vec{B}$  parallel to the lines of force, a particle propagating along this magnetic field gradually changes its pitch angle as a result of the conservation of the magnetic momentum (Boyd and Sanderson, 1969), i.e.

$$\frac{W_{\perp}}{B} = \text{const.}, \quad (4.5)$$

where  $W_{\perp} = (1 - \mu^2)mv^2/2$  is the energy of the particle related to its motion perpendicular to  $\vec{B}$ . Because of the invariance of the magnetic moment, it follows that

$$(1 - \mu^2)/B = \text{const.}, \quad (4.6)$$

what readily leads to

$$\mu_2 = \sqrt{1 - \frac{B_2}{B_1}(1 - \mu_1^2)} \quad (4.7)$$

as an expression for the pitch angle cosine at  $B_2$  when the particle started at  $B_1$  with pitch angle  $\mu_1$ . The mirror points, i.e. the magnetic field strength at which the pitch angle cosine of the particle is zero and the particle starts to move in the opposite direction is calculated to

$$B_2 = \frac{B_1}{1 - \mu_1^2} \quad \text{with } |\mu_1| \leq 1. \quad (4.8)$$

Those mirror points in magnetic field configurations are e.g. found in the dipole field of a planetary magnetosphere, where the field strength increases towards the poles. In this case, the particles are bouncing between the poles of the dipole. Another situation is the Parker field where cosmic rays traveling from the outer heliosphere towards the Sun experience an increasing magnetic field strength, leading to an increase of the pitch angle. The opposite is true for particles injected near the solar surface, e.g. solar flare particles. As these particles propagate away from the Sun, their pitch angles will decrease with decreasing field strength.

## 4.2 The Random Walk

At the beginning of the last section it has been assumed that the magnetic field is uniform in space and time and fluctuating fields are absent, i.e.  $\vec{B}(t) = \vec{B}_0$ . In this case, the motion of a particle is completely described by the equation of motion (Eqn.( 4.1)). Even if non-uniform magnetic fields like magnetic bottles are introduced, the path of a single particle is still determined if its position in phase space is known at a given time if the drift motion of the particle is considered. However, in most cases the magnetic field is imposed by small scale irregularities. In this case, the magnetic field may be written as

$$\vec{B} = \vec{B}_0 + \delta\vec{B}, \quad (4.9)$$

where  $\delta\vec{B}$  represent irregularities in the magnetic field caused e.g. by turbulence and  $\vec{B}_0$  is the background magnetic field. Therefore, the average  $\langle\delta\vec{B}\rangle = 0$  by definition. When irregularities are present in the magnetic field, the trajectory of a particle is not longer completely determined in the classical sense, i.e. the exact position in phase space of the particle at time  $t_1$  can not exactly determined if its position was known at time  $t_0$ , because the exact form of  $\delta\vec{B}$  is not predictable. However, the position of the particle at time  $t_1$  is related to a probability to find the particle in a certain phase-space interval. The mathematical treatment of this is founded on the concept of diffusion or random walk as described in the following.

The basic concept of diffusion is well known from everyday experiences. Imagine, for example, a drop of ink falling into a glass of water. The inkdrop will immediately start to spread and finally the ink will be homogeneously distributed in the water. The reason for this is diffusion or random walk of the ink particles (colloids) caused by persistent irregular collisions of the particles with the water molecules. This observation was first described by R. Brown in 1827 when studying pollen particles in water under the microscope. However, it was A. Einstein (Einstein, 1905), who gave a mathematical expression of this so-called Brownian motion. In the case of ink particles, this points to the question for the probability distribution  $W(x, t, x_0)$ , which governs the probability that a particle may be found in the interval  $x, x + dx$  at time  $t$  when the position of the particle was  $x_0$  at time  $t_0$ . For the one dimensional case, this leads to the diffusion equation

$$\frac{\partial W}{\partial t} = D \frac{\partial^2 W}{\partial x^2}, \quad (4.10)$$

where  $D$  is the (constant) diffusion coefficient. This equation has the general solution

$$W(x, t, x_0) = \frac{1}{\sqrt{4\pi Dt}} e^{-(x-x_0)^2/4Dt}. \quad (4.11)$$

A measure for the diffusion coefficient is the mean square displacement of the particles defined by

$$\langle(\Delta x)^2\rangle = \langle(x(t) - x(0))^2\rangle, \quad (4.12)$$



where  $x(0)$  is the initial position of the particle and  $x(t)$  the position of the particle at time  $t$ . If one assumes that the mean square displacement of the particle due to scattering is proportional to the time,

$$\langle(\Delta x)^2\rangle \sim t^\alpha, \quad (4.13)$$

$\alpha = 1$  refers to normal (Markovian) diffusion. This implies, that the particles do not have a "memory", i.e. their position at the next time step does only depend on the position at the current time and is totally independent on the positions at past times<sup>1</sup>. For  $\alpha = 2$ ,  $\langle(\Delta x)\rangle = vt$ , i.e. there is no diffusion but simple streaming of the particles at speed  $v$ . The spatial diffusion coefficient can now be defined as

$$D = \lim_{t \rightarrow \infty} \frac{\langle(\Delta x)^2\rangle}{2t}, \quad (4.14)$$

and has the famous solution  $D = \frac{kT}{f}$  for the Brownian motion of a free particle in a liquid as derived by Einstein (1905), where  $T$  is the temperature and  $k$  is Boltzmann's constant and  $f$  the friction coefficient. That means, it is possible to derive an expression how a particle ensemble, expressed by the probability function in phase space, will evolve in time without the necessity to know the precise realization of the fluctuations if their statistical behavior is known good enough (see also Chandrasekhar, 1943).

For charged particles propagating in interplanetary or cosmic magnetic fields, however, the derivation of diffusion coefficients is much more complicated because of the special geometry defined by the magnetic field and the various forms of turbulence and waves being present. Furthermore, besides stochastic forces acting on the particle, there are also systematic effects acting on the particles. This leads to the Fokker-Planck equation and will be discussed in the following section as far as it is important for this work.

### 4.3 The Fokker-Planck Equation for Space Plasmas

Because of the stochastic nature of diffusion processes and the large number of particles under consideration it is often inconvenient to trace the path of a single particle<sup>2</sup> but it is common to introduce the phase space density  $f$ . The phase space density is defined that the integral over a given phase space interval is the probability to find a particle there. In particular,

$$\int_{-\infty}^{\infty} \int_{-\infty}^{\infty} f(\vec{x}, \vec{v}, t) d\vec{x} d\vec{v} = 1, \quad (4.15)$$

<sup>1</sup>This is basically the definition of a Markov-chain, i.e. the particles do not remember past timesteps. A famous example is the Galton board.

<sup>2</sup>However, due to increasing computation power and sophisticated mathematical concepts, several approaches were made to track the single particle motion of energetic particles in interplanetary space in terms of stochastic differential equations (SDEs), see e.g. Strauss et al. (2011).

i.e. the particle must be located somewhere in the phase space.

The temporal evolution of the phase space density  $f$  of a particle ensemble can be described by the relativistic Vlasov equation (Boyd and Sanderson, 1969)

$$\frac{\partial f}{\partial t} + \vec{v} \frac{\partial f}{\partial \vec{x}} + \dot{\vec{p}} \frac{\partial f}{\partial \vec{p}} = Q(\vec{x}, \vec{p}, t), \quad (4.16)$$

where  $p$  is defined by Eqn. (4.1).  $Q$  denotes time dependent sources (or sinks) of particles, i.e. the injection location of solar flare particles or the Jovian magnetosphere. Choosing a phase space coordinate system  $x_\sigma = (p, \mu, \phi, x, y, z)$ , where  $p$  is the momentum,  $\mu$  the pitch-angle cosine,  $\phi$  the gyroangle and  $x, y, z$  the spatial coordinates, one obtains

$$\frac{\partial f}{\partial t} + v\mu \frac{\partial f}{\partial z} - \frac{q}{|q|} \frac{\partial f}{\partial \phi} + \frac{d(mv\mu)}{dt} \frac{\partial f}{\partial(mv\mu)} + \frac{1}{p^2} \frac{\partial}{\partial x_\sigma} (p^2 g_{x_\sigma} f) = Q(\vec{x}, \vec{p}, t), \quad (4.17)$$

where  $g_{x_\sigma}$  refers to the random fluctuations of the magnetic field in terms of a generalized force<sup>3</sup>. The term just before the fluctuating part is not included in Schlickeiser (2002) and introduces systematic changes in the pitch angle of the particles due to systematic changes in the magnetic field as discussed in Section 4.1.

As stated above, the concrete possible realizations of the fluctuations are not important but their statistical properties they share. That means, one is interested in the mean value of all possible realizations and defines

$$\langle f \rangle = F. \quad (4.18)$$

Rearranging Eqn. (4.17) by using  $F$  and substituting the individual realization of the generalized force terms by their statistical representation, i.e. a diffusion coefficient, one finally obtains (Schlickeiser, 2002)

$$\frac{\partial F}{\partial t} + v\mu \frac{\partial F}{\partial z} - \frac{q}{|q|} \frac{\partial F}{\partial \phi} + \frac{d\mu}{dt} \frac{\partial F}{\partial \mu} - \frac{1}{p^2} \frac{\partial}{\partial x_\sigma} \left( p^2 D_{x_\sigma x_\nu} \frac{\partial F}{\partial x_\nu} \right) = Q(\vec{x}, \vec{p}, t), \quad (4.19)$$

called the Fokker-Planck equation, where Einstein's sum convention was used. The coefficients  $D_{x_\sigma x_\nu}$  are the Fokker-Planck coefficients and are defined by

$$D_{x_\sigma x_\nu} = \int_0^t ds \langle \bar{g}_{x_\sigma}(t) \bar{g}_{x_\nu}(s) \rangle. \quad (4.20)$$

Here, the bars indicate that the generalized force terms are calculated along unperturbed orbits (Jokipii, 1971; Schlickeiser, 2002). As pointed out by Bieber and Matthaeus (1997), this notation is equivalent to Eqn. (4.14).

<sup>3</sup>This generalized force term is similar to the fluctuating force term  $g$  in Langevin's equation  $m \frac{dv}{dt} = -fv + g(t)$ , describing the force acting on a particle with speed  $v$  underlying a systematic force  $-fv$  (where  $f$  represents friction) and a fluctuating part  $g(t)$ .

## The Diffusion Coefficients

As a charged particle travels along a magnetic field line  $B_0$  imposed by fluctuations it undergoes permanent small changes of its pitch angle. If the single changes of the pitch angle are sufficiently small, this can be described by diffusion. The corresponding pitch-angle diffusion coefficient  $D_{\mu\mu}$  is calculated by Eqn. (4.20). In this case (Shalchi, 2009), the generalized force term is the temporal derivation of the pitch angle, i.e.

$$D_{\mu\mu} = \int_0^\infty dt \langle \dot{\mu}(t) \dot{\mu}(0) \rangle. \quad (4.21)$$

In quasi-linear theory (QLT), where unperturbed particle trajectories are considered to derive diffusion coefficients,  $D_{\mu\mu}$  is given by (e.g. Earl, 1974; Hatzky, 1996; Agueda, 2008)

$$D_{\mu\mu} = \frac{\nu(\mu)}{2} (1 - \mu^2), \quad (4.22)$$

with the scattering frequency

$$\nu = \nu_0 |\mu|^{q-1}, \quad (4.23)$$

and

$$\nu_0 = \frac{6v}{2\lambda_{\parallel}(1 - \sigma^2)(q - 2)(q - 4)}. \quad (4.24)$$

The factor  $(1 - \mu^2)$  results from the usage of the pitch-angle cosine as a variable and from the mathematical treatment of diffusion on a sphere (Perrin, 1928). The quantity  $\sigma$  corresponds to the so-called helicity and is a measure for the relation of left-handed and right-handed polarized waves (e.g. Bieber et al., 1987). The helicity, however, will not be considered in the calculations presented in this work, i.e.  $\sigma = 0$ , assuming equal fractions of left-hand and right-handed polarized magnetic fluctuations. The quantity  $q$  is the spectral index of the magnetic field fluctuations,  $v$  is the speed of the particles and  $\lambda_{\parallel}$  is the parallel mean free path and will be defined in Eqn (4.27).

However, it was found to be useful to introduce another parameter in the pitch-angle scattering coefficient  $h$  to take into account an isotropic scattering term beside the  $\mu$ -dependent scattering (Kunow et al., 1991; Hatzky, 1996). The modified Fokker-Planck coefficient now reads

$$D_{\mu\mu} = \frac{\nu_0}{2} (|\mu|^{q-1} + h) (1 - \mu^2) \quad (4.25)$$

Fig. 4.2 shows four examples of the shape of  $D_{\mu\mu}$  for variations of the parameters  $q$  and  $h$ . Note that for  $q \geq 2$ , the two pitch-angle hemispheres are totally decoupled, i.e. particles in the hemisphere  $\mu \in (0, 1]$  are not able to propagate to the hemisphere  $\mu \in [-1, 0)$  and vice versa (Earl, 1974), resulting in a completely coherent transport of the particles. As shown e.g. by Earl (1974) and Shalchi (2009), the pitch-angle diffusion coefficient and the spatial parallel diffusion coefficient are related via

$$\kappa_{\parallel} = \frac{v^2}{8} \int_{-1}^{+1} d\mu \frac{(1 - \mu^2)^2}{D_{\mu\mu}}. \quad (4.26)$$

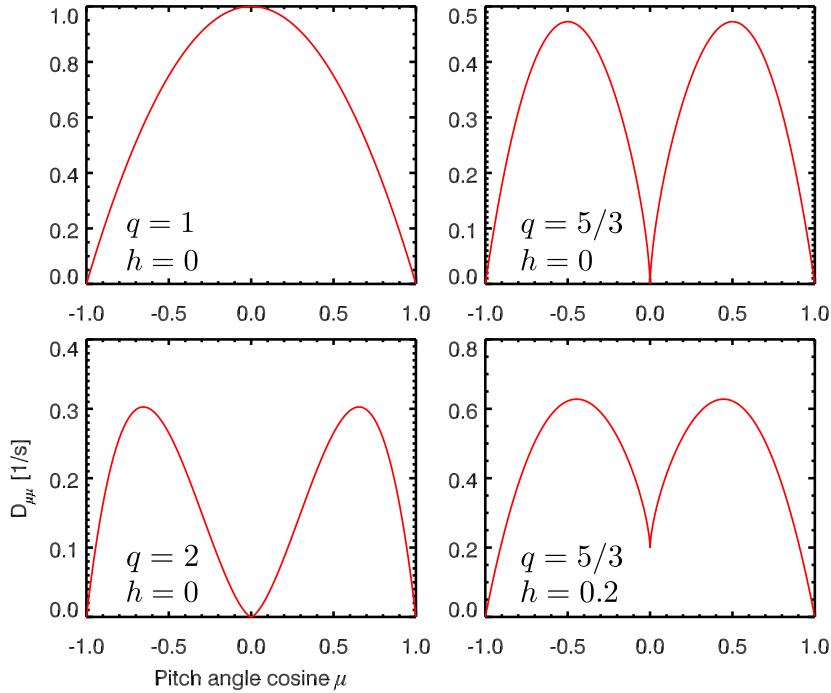


**Figure 4.2:** The Fokker-Planck coefficient  $D_{\mu\mu}$  for different values of  $q$  and  $h$ . Note the so-called resonance gap at  $\mu = 0$  for  $q \neq 1$ .

That means, diffusion in the pitch angle domain leads to a diffusion of particles in real space. While the derivation of this expression is not trivial, the qualitative result is intuitive: The scattering of particles in the pitch-angle domain leads to small changes in the particle's pitch angle  $\Delta\mu$ , leading directly to a change in the particle's parallel speed, i.e.  $\Delta v_{\parallel} = \Delta\mu v$ . An important parameter in this context is the so-called mean free path  $\lambda_{\parallel}$ . The mean free path is defined by

$$\lambda_{\parallel} = \frac{3}{v} \kappa_{\parallel}. \quad (4.27)$$

This expression is derived in analogy to the kinetic theory of gases (cf. section 6.5.6 in Meschede, 2010). In cosmic ray physics, the mean free path is not the distance a particle traveled between two single scattering events, but is the mean distance covered by the particle until its pitch angle has changed by  $90^\circ$ . The scattering of particles perpendicular to the nominal magnetic field is fairly more complex than the treatment of parallel scattering. What are the possible processes, that lead to a net displacement of a charged particle perpendicular to the mean field? This is a complicated and highly discussed topic. However, perpendicular diffusion is commonly treated as a combination of several effects leading to a displacement of a particle perpendicular to a defined  $\vec{B}_0$ :

*”The process of perpendicular diffusion is thus a combination of field line random walk, backscatter from parallel diffusion, and transfer of particles across field lines owing to the magnetic field’s perpendicular complexity.”* (Bieber et al., 2004).

The first and second point is actually perpendicular propagation across the mean field  $B_0$ , while the particle’s guiding center still propagates parallel to the local magnetic field. The third issue, however, deals with the motion of the guiding center across the mean/local magnetic field, i.e. the particle may move from one magnetic field line to the other as a result of perpendicular inhomogeneities in the neighboring magnetic field line.

## 4.4 Special Cases of the Master Equation

In the following, two special cases of Eqn. (4.19) will be discussed. The first case considers the pitch-angle dependent propagation of charged particles along the Parker spiral including systematic changes of the pitch angle. This equation is the transport equation used in this work to study the pitch-angle dependent propagation of Jovian electrons and is in use to model the propagation of solar flare particles. The second case assumes pitch-angle isotropy, but includes spatial diffusion in three dimensions, convection, drift effects as well as adiabatic energy changes, known as Parker’s equation.

### Focused Transport

The first step in the derivation of a focused transport equation is the treatment of the effect of the diverging interplanetary magnetic field on the pitch angle of the particles, i.e. on the term  $\frac{d\mu}{dt}$  in Eqn (4.19) under the consideration of the heliospheric magnetic field. This term can be written as (Roelof, 1969; Hatzky, 1996)

$$\frac{d\mu}{dt} = \frac{v}{2L}(1 - \mu^2), \quad (4.28)$$

where  $L = -B/(\partial B/\partial z)$  is the so-called focusing length, a function depending on the distance from the Sun and a measure for the strength of the focusing due to the diverging magnetic field. Introducing this expression in Eqn (4.19) and neglecting diffusion perpendicular to the magnetic field line as well as energy changes, the new equation reads

$$\frac{\partial f}{\partial t} + \underbrace{\mu v \frac{\partial f}{\partial z}}_{\text{Advection}} + \underbrace{\frac{v(1 - \mu^2)}{2L} \frac{\partial f}{\partial \mu}}_{\text{Focusing}} = \underbrace{\frac{\partial}{\partial \mu} \left( D_{\mu\mu} \frac{\partial f}{\partial \mu} \right)}_{\text{Diffusion}} + Q(z, \mu, t), \quad (4.29)$$

where it is assumed that the particle ensemble is gyrotropic, i.e. there is no gradient in  $\phi$ . This equation is called Roelof’s equation or focused transport equation (Roelof, 1969) and is the fundamental transport equation being used to investigate

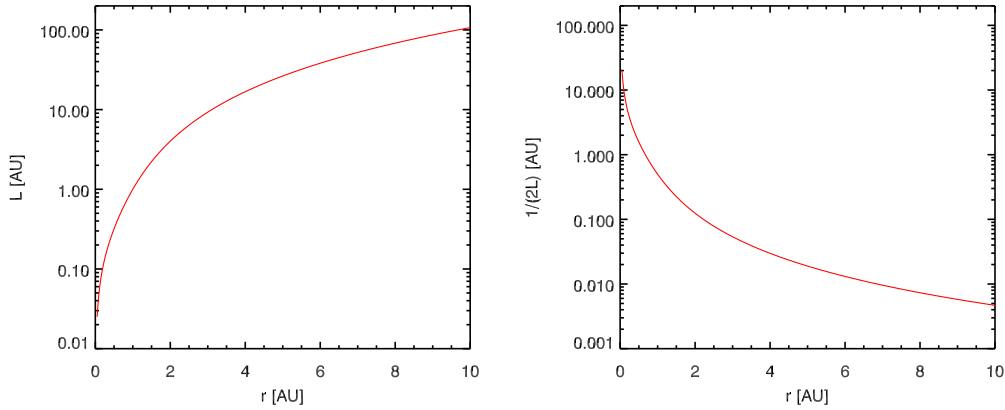


**Figure 4.3:** The panel panel shows the parameter  $L$  as a function of radial distance from the Sun, the right panel shows the quantity  $1/(2L)$  as a function of distance.

the anisotropic propagation of solar flare particles along the Parker spiral and includes convection, focusing and pitch-angle diffusion and the presence of particle sources. Changes in the particles momentum/energy are neglected in this model.

Before another special case of the general transport equation will be discussed, it is necessary to pay some attention to the process of focusing. According to Boyd and Sanderson (1969), we discuss an inhomogeneous magnetic field and assume that the magnetic field remains almost constant along the distance the particle moved until it had completed a full gyration orbit. This distance, denoted  $d_g$ , needs to be sufficiently smaller than the typical distance over which the magnetic field changes significantly, i.e. the focusing length  $L$ , so we may write

$$d_g \ll L. \quad (4.30)$$

Let us now consider a 7 MeV electron in a magnetic field of 5 nT, corresponding to a radial distance from the Sun of  $\sim 1$  AU. The gyroradius of the particle is given by

$$r = \frac{\gamma m_e v_{\perp}}{eB}, \quad (4.31)$$

where  $m_e$  is the rest mass of the electron and  $e$  its charge. The speed of the particle is about  $0.997 \cdot c$ , therefore  $\gamma \approx 13$ . With  $m_e = 9.1 \cdot 10^{-31}$  kg and  $e = 1.602 \cdot 10^{-19}$  C we find

$$r \approx 4417 \text{ km.}$$

The angular gyrofrequency  $\Omega = v_{\perp}/r$  can now be expressed as

$$\Omega = \frac{eB}{\gamma m_e}, \quad (4.32)$$

and with  $\nu = \Omega/2\pi$  we obtain a gyrofrequency  $\nu \approx 10$  Hz, i.e. the particle performs 10 full orbits in a second. Assuming that  $v_{\parallel} = c$ , we find

$$d_g \approx 0.1s \cdot c,$$

i.e. a value of  $d_g$  of about 30000 km or  $\sim 10^{-4}$  AU. Comparing this result with  $L(1 \text{ AU}) \approx 1 \text{ AU}$ , the length scale over which the heliospheric magnetic field changes significantly is much larger than the distance of a 7 MeV electron traveled within 0.1 s.

We conclude that the focusing term in the transport equation is valid for relativistic electrons, as long as the field is static inhomogeneous and not time varying or superimposed by electric fields and the magnetic moment is an adiabatic invariant (Jackson, 1962, p. 421)<sup>4</sup>. In addition, energy losses of the electrons by synchrotron emission that change the particle's relativistic mass can totally be neglected in heliospheric applications and is only of interest for planetary magnetospheres (on longer time scales) or more exotic environments like magnetic white dwarfs or pulsars as pointed out by Ho (1986).

## Spatial Diffusion

While in the latter transport model the pitch angle was an important variable, it is often not necessary to take care about the evolution of the pitch angle. This is the case when a particle ensemble is considered which initial pitch-angle distribution is (almost) isotropic and under the assumption that the pitch-angle distribution would not change significantly with time. The propagation of GCRs as well as Jovian electrons is commonly treated under the assumption that the pitch angle of the particles are equally distributed in the pitch-angle domain, i.e.  $\partial f/\partial\mu = 0$ . Consequently,  $f$  is not a function of  $\mu$ . The corresponding three-dimensional transport equation including spatial diffusion, drifts as well as adiabatic changes of the particle's momentum had been derived by (Parker, 1965) from the Fokker-Planck equation and reads

$$\frac{\partial f}{\partial t} = \underbrace{\nabla \cdot (\kappa^S \cdot \nabla f)}_{\text{Diffusion}} - \underbrace{(\vec{u}_{sw} + \vec{v}_d) \cdot \nabla f}_{\text{Convection \& Drift}} + \underbrace{\frac{1}{3}(\nabla \cdot \vec{u}_{sw}) \frac{\partial f}{\partial \ln p}}_{\text{Adiab. Losses}} + Q(\vec{x}, p, t). \quad (4.33)$$

The new terms in this equation are the following:

**Diffusion** The three dimensional spatial diffusion is expressed by a tensor  $\kappa^S$ , containing the diffusion coefficients along and perpendicular to the magnetic field.

**Convection & Drift** Parker's equation takes into account that the background medium in which the test particles propagate is moving with the solar wind speed

---

<sup>4</sup>In the presence of a static magnetic field, the speed and kinetic energy of a particle remains constant, so does  $\gamma$ . In a time varying magnetic field, the particle can gain energy (Betatron effect) and  $\gamma$  is no longer a constant.

$u_{sw}$ . A vivid case is the the inkdrop in water. If the water is at rest with respect to the laboratory frame, the center of the ink drop will not move while the ink diffuses. If the water is moving, as in the case of a flowing river, a net displacement of the center of the inkdrop occurs. The coefficient  $\vec{v}_d$  denotes the sum of the drift velocities resulting from the gradient and curvature drift the particles experience in the Parker field.

**Adiabatic Energy Losses/Changes** This term takes into account the fact that the solar wind is radially flowing away from the Sun, while GCRs undergo diffusion in this medium. This effect is similar to the loss of internal energy particles experience when it does work in expanding its volume (Longair, 1992).

Parker's Equation had successfully been applied to several problems of the transport of GCRs and Jovian electrons in the heliosphere and the galaxy, e.g. by Heber et al. (2006).



# Chapter 5

## Instrumentation, Trajectories, and Methods

Beep, beep, beep!

---

Sputnik I

In the previous chapter the theoretical basics of particle transport in the heliospheric magnetic field had been described. If one wants to perform measurements of the particle in space, sophisticated detector systems are necessary to obtain adequate information of the physical properties. In what follows, the principles of the detection of charged particles will be described followed by an overview of the instrumentation flown on Ulysses and the Pioneers.

### 5.1 Measurements of Charged Particles

The detection of energetic charged particles, e.g. GCRs or particles trapped in planetary magnetospheres, is based on the interaction of these particle with matter they penetrate. The principal physical interactions between an incident particle and the material are ionization losses and inelastic scattering processes. To quantify the energy losses a particle experiences, several detectors were developed. In what follows, the main features of the detector types that are commonly used in space borne experiments to detect energetic charged particles, especially that being used for the design of the charged particle instruments used in this study are described (cf. Sierks, 1988; Longair, 1992; Grupen, 1993; Heber, 1997).

**Solid State Detectors** Solid state detectors are based on the ability of charged particle to ionize the material (i.e. the target) they penetrate, leading to the production of electron-hole pairs (Kittel, 2004). Typical materials for solid state detectors are the semiconducting elements Silicon (Si) and Germanium (Ge), because ordinary insulators are too impure for this purpose since many of the free

electrons and holes are lost in the imperfections in the structure of the target. If an energetic particle knocks out an electron of the semiconductor, it moves to the conducting band and leaves a hole, i.e. an unoccupied state, in the valence band. If the semiconductor is attached to a voltage source, realized by connecting a pair of electrodes at the edges of the detector, the electrons are swept away by the electric field and can be registered as a current pulse. Since the amount of the produced electron-hole pairs are proportional to the energy of the charged particle (typically  $10^5/\text{MeV}$ ), this allows an estimation of the energy of the particle, but not its sign of charge nor the charge number.

**Cherenkov Detectors** To distinguish between ions and electrons, Cherenkov detectors are used. Cherenkov detectors are based on the observation that a particle moving through a medium at a velocity higher than the speed of light in that medium, i.e.  $c_n = c/n$ , where  $c$  is the speed of light in a vacuum and  $n$  is the index of refraction in the medium), it emits so-called Cherenkov radiation. On its way through the medium, the charged particle polarizes the molecules of the medium, which, in response, emit electromagnetic radiation that can be detected by photomultipliers attached to the medium. A particle with a velocity  $v < c_n$  it does not polarize the medium along its track, i.e. no radiation is emitted. This has an important impact on the determination of the type of the incident particle, because an electron with a kinetic energy  $E$  has a much higher velocity than a proton at the same energy. Therefore, the energy of electrons necessary to produce Cherenkov radiation is much lower than for protons, i.e. it is possible to distinguish between electrons and protons in a wide range of energy by the Cherenkov radiation produced by the particles. Typical materials for Cherenkov detectors are aerogel or lead fluoride (PbF) with refraction indexes of  $n = 1.065$  and  $n = 1.8$ , respectively.

**Scintillation Detectors** Scintillation detectors consist of a transparent crystal, usually NaJ or organic compounds. When hit by an energetic charged particle, the medium fluoresces when free electrons produced by ionization fall back to the valence band. This emitted radiation is measured by a sensitive photomultiplier tube. Because of their limited energy resolution compared to solid state devices but fast response, scintillation detectors are nowadays used as anticoincidences guarding the particle telescope.

It is clear that the use of a single detector is often insufficient to obtain a reasonably complete set of information (e.g. energy, type, direction) on the measured particles. Therefore, the sophisticated combination of several different detectors to an instrument is required, leading to different instrumental designs, dependent on the scientific purpose of the instrument. In Section 5.2, the mode of operation of the Kiel Electron Telescope, the contribution of the University of Kiel to Ulysses, will briefly be described since this work mainly makes use of the data obtained by this instrument (in conjunction with other instruments).

## 5.2 Ulysses

### Mission Overview

Although the idea of exploring the heliosphere at high solar latitudes is as old as the age of space exploration itself (Simpson et al., 1959), it was not before the mid-seventies when work began on a mission to explore the solar poles. This mission was initially designed as a twin spacecraft mission named "International Solar Polar Mission" (ISPM) and was re-named to Ulysses after several changes in the design of the mission and the budget allowance and was finally launched as a single spacecraft mission in October 1990. The primary aims of the mission were the following:

- The study of the three-dimensional properties of the interplanetary magnetic field and the solar wind, including studies of the composition of the solar wind to understand its origin at different latitudes and the investigation of waves, shocks, discontinuities and the interaction of different solar wind streams.
- The investigation of galactic cosmic rays (including Jovian electrons), and solar energetic particles.
- Improvement of the understanding of interplanetary dust in the solar system.

### Trajectory

Ulysses was launched in October 1990 and followed an in-ecliptic path towards Jupiter where the spacecraft was deflected by the gravitational field of the giant planet to achieve its final orbit, a highly inclined ( $\sim 80^\circ$ ) Keplerian orbit around the Sun. Fig. 5.1 shows the trajectory of Ulysses including the in-ecliptic trajectory segment up to the year 2001. The aphelion distance was determined by the orbit of Jupiter, the perihelion was chosen to be  $\sim 1.3$  AU for thermal reasons. The orbital period is  $\sim 6.4$  years, i.e. roughly half a solar cycle. When the spacecraft's instrumentation was finally switched-off in mid 2009, it completed three full orbits including a second, more distant Jupiter approach ( $> 0.8$  AU) in 2003/04.

### Instrumentation

To achieve the goals of the mission described above, Ulysses was equipped with 9 instruments. Those being relevant for this work are the following:

**VHM/FMG** The magnetometer aboard Ulysses, described in detail by Balogh et al. (1992), consists of two separate instruments. The Vector Helium Instrument (VHM) is based on the magnetometers already flown on the Pioneer 10/11 and ISEE3 spacecraft and exploits the observation that the effectiveness of optical pumping is affected by the presence of an ambient magnetic field. The Fluxgate Magnetometer (FGM) consists of three single axis ring-core fluxgate sensors.

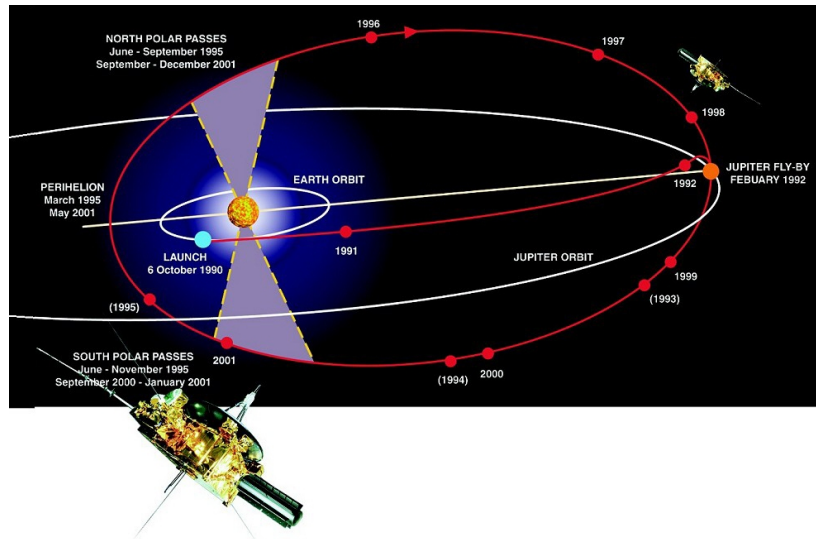


**Figure 5.1:** The in-ecliptic trajectory and orbit of Ulysses around the Sun. The Jupiter flyby occurred in Feb. 1992 and about 1.5 years later, in summer 1994, the spacecraft passed the Sun's south pole and crossed the ecliptic plane in March 1995. Roughly 12 years after the Jupiter flyby, the spacecraft came again close to the planet in 2003/04. <http://ulysses-ops.jpl.esa.int/ulysses>.

The combination of these instruments allows measurements of the interplanetary magnetic field and the magnetic field of Jupiter with high precision. For interplanetary spacecraft missions it is common to use the RTN-coordinate system<sup>1</sup> for the representation of the magnetic field vector. The R component is along the connection from the Sun to the spacecraft. The T component is the result of the cross product of the solar rotation axis and R. The N component is the cross product of R and T.

**SWICS and SWOOPS** The Solar Wind Ion Composition Spectrometer (SWICS) was designed to measure the elemental and charge composition, the temperature as well as the velocity of solar wind particles (Gloeckler et al., 1992) and consists of three separate units. The measuring principle makes use of a combination of electrostatic deflection, post-acceleration and time-of-flight and energy measurements. The Solar Wind Observations Over the Poles of the Sun instrument (Bame et al., 1992) was also designed to measure the solar wind properties in the heliosphere, e.g. the solar wind velocity.

**COSPIN** The Cosmic Ray and Solar Particle Investigation (COSPIN) instrument group consists of the Kiel Electron Telescope (KET), the High Energy Telescope (HET), the High Flux Telescope (HFT), the Low Energy Telescope (LET) and

<sup>1</sup>Radial-Tangential-Normal.

the Anisotropy Telescope (AT) as described by Simpson et al. (1992a). The purpose of COSPIN is the measurement of high energetic particles in a wide range of energy in the interplanetary medium. The KET and HET will be described further in the following sections.

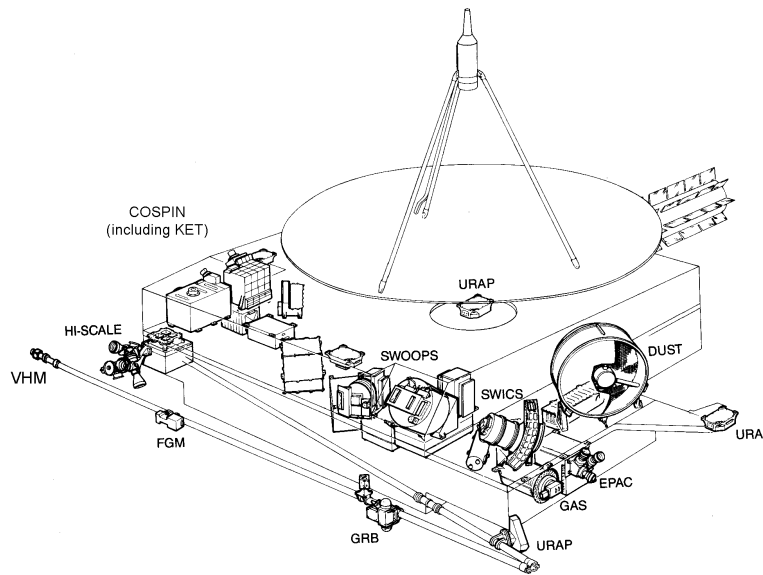


**Figure 5.2:** Sketch of the spacecraft Ulysses including the locations of scientific payload. The dish antenna on top of the spacecraft's body provides up- and downlink communication between the ground control and Ulysses. The power source, a RTG (radioisotope thermoelectric generator), is located on the right upper side locations of the sketch. [http://ccar.colorado.edu/asen5050/projects/projects\\_2001/aponte/Ulysses.htm](http://ccar.colorado.edu/asen5050/projects/projects_2001/aponte/Ulysses.htm).

### The Kiel Electron Telescope (KET)

The KET consists of a combination of two semiconductor detectors D1 and D2, two Cherenkov detectors C1 and C2 and three scintillator devices used as anticoincidences. Fig. 5.3 shows a schematic illustration of the KET and the respective detectors. D1, C1 and D2 form the entrance telescope to obtain information on the energy loss  $dE/dx$  of the particles in the two semiconductor detectors in combination with C1 to separate electrons from nucleons as described in Section 5.1. The D2 detector is followed by the Cherenkov detector C2 used as a calorimeter to determine the energy of particles stopping there. The Cherenkov detectors are attached to photomultipliers (PM) to read out the Cherenkov light. The opening angle of the instrument's aperture is  $44.6^\circ$  and is surrounded by the anticoincidence A to make sure that no particles are

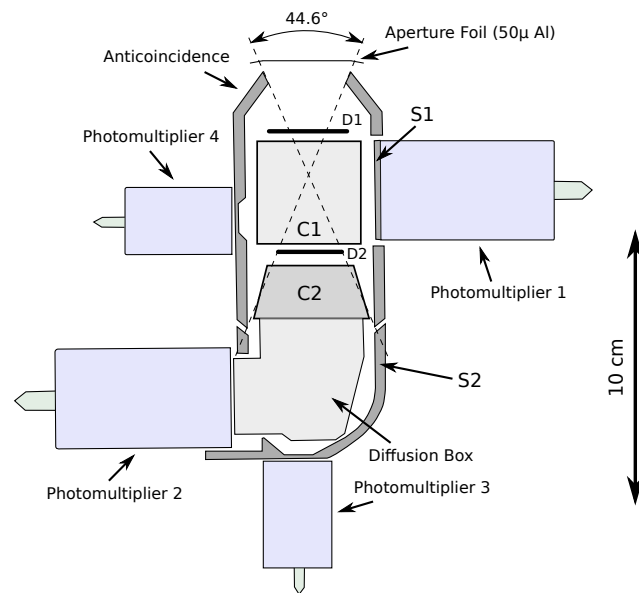


**Figure 5.3:** Sketch of the detector system of the Kiel Electron Telescope. The opening angle of the entrance telescope is  $44.6^\circ$  and is made of two solid state detectors D1 and D2 and the Cherenkov detector C1. D2 is followed by the Cherenkov detector C2 used as a calorimeter. The KET is surrounded by anticoincidence detectors to prevent particles from being registered that do not enter the instrument through the aperture.

registered that do not enter the telescope through the aperture. The same is true for the anticoincidences S1 and S2. S2 is also used to detect particles with energies high enough to leave C2. The measuring principle will now be explained for some energy channels described in Heber (1997): An electron that penetrates the instrument and triggers D1, C1 and D2 but not C2, i.e. it either loses its energy in D2 or has not enough energy to produce Cherenkov radiation is assigned to the E4 channel, counting electrons in the energy range from 2.5-7 MeV. An electron with energy  $> 7$  MeV will also trigger the adjacent C2 detectors and will be assigned to the E12 channel, counting electrons from 7–  $\sim 500$  MeV. If the energy of the particle is still high enough to trigger the scintillator S2, it will be counting as a E300 electron with an energy  $> 500$  MeV. Because this particle also triggers S2 it is not possible to determine whether the electrons entered the KET through the aperture cone or backwards because of the finite processing time of the electronics. Considering protons, the Cherenkov detectors are used to discriminate them from electrons as illustrated for the case of the P32 proton channel counting electrons between 5.4 and 23.1 MeV. Protons of these energies trigger D1 and D2 but not C1 or C2, because their energy is too small to produce Cherenkov radiation and stop before they reach S2. To discriminate protons

from  $\alpha$ -particles or if the energy of electrons and protons is high enough to trigger D1, C1, D2, C2 and S2, it is necessary to separate these particles by the introduction of energy thresholds for the respective detectors and is described in great detail by Sierks (1988). The energy channels of primary interest are the E4 and E12 electron channels, counting particles in a range of energy from 2-7.5 and  $> 7.5$  MeV. A complete table of the KET's energy channels may be found in Heber (1997).

An issue that needs some discussion is the response of the instrument with respect to the incidence angle of the incoming particle, because of its importance for the estimation of the pitch-angle coverage as discussed in section 5.5. The theoretical foundations of the effectiveness of a detector system are discussed in Sullivan (1971) and was compared with the calibration experiments by Sierks (1988). However, no such measurements had been performed for the E4 channel that is of major interest in the context of this work. However, we follow the arguments of Hatzky (1993) and assume that the response of the E4 channel is comparable with the response of channel E12, for which measurements are available. Fig. 5.4 shows the theoretical response

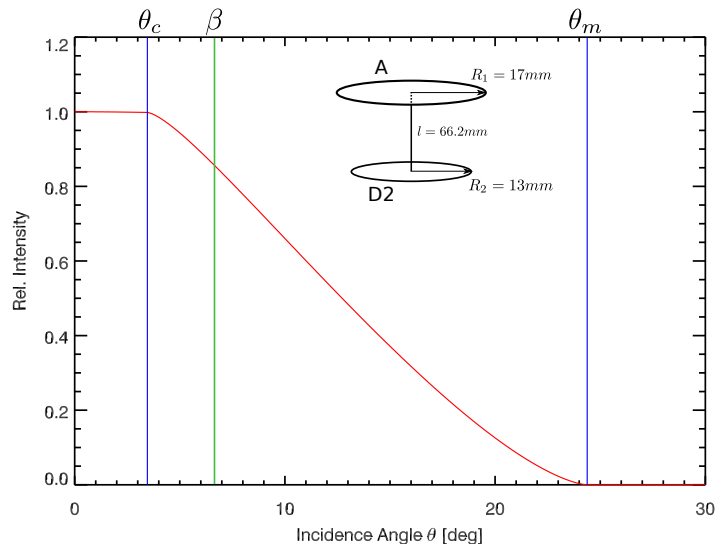


**Figure 5.4:** Normalized theoretical response function (red curve) for the E4/E12 channels derived from the formula given by Sullivan (1971). The response stays fairly constant up to the angle  $\theta_c$  and becomes zero at  $\theta_m$ . The green line ( $\beta \approx 6.7^\circ$ ) indicates the angle at which the integrals of the left and right part of the response functions are equal. The inset shows the dimensions of the aperture and the D2 detector.

function of the E4/E12 channels according to the formula given by Sullivan (1971). The response function is determined by the geometrical properties of the detector elements defining the channel. In the case of the E4/E12 channels, the aperture cone A (radius=17 mm) and the D2 detector (radius=13 mm) must be taken into account. The distance between the elements is 66.2 mm. As can be seen, the response function

stays fairly constant up to the  $\theta_c$ . up to this angle, D2 lies completely in the “shadow” of the aperture cone. The response function then decreases as a function of the incidence angle and becomes zero at  $\theta_m$ . Beyond this incidence angle, a particle can not reach D2. The green line at  $\beta \approx 6.7^\circ$  indicates the angle at which the integrals of the left and right parts of the response function are equal. For the calculation of the pitch-angle coverage (Section 5.5), an effective half-opening cone of  $15^\circ$  had been chosen. This interval covers approx. 90% of the integral over the complete response function.

## 5.3 Pioneer 10/11

### Mission Overview

The NASA missions Pioneer 10 and 11 were launched in March 1972 and April 1973, respectively. Similar to Ulysses, these spacecraft were the first man-made objects to proceed to regions in the heliosphere that had not been explored in situ before at this time, i.e. the solar system beyond the orbit of Mars and the Asteroid Belt. The main objectives of two twin spacecraft read as follows:

- In situ measurements of the interplanetary magnetic field, the solar wind and galactic cosmic rays.
- Investigation of the asteroid belt located between Mars and Jupiter.
- Exploration of the magnetic field and particle population in the Jovian magnetosphere (Pioneer 10/11) and the magnetic field of Saturn (Pioneer 11 only).
- Investigation of the boundaries of the heliosphere.

### Trajectory

The pre-Jupiter trajectory of the two Pioneer spacecraft was similar to Ulysses’ trajectory and is shown in Fig. 5.6. After the Jupiter flyby, the spacecraft followed different paths towards the outer heliosphere: While Pioneer 10 directly moved outwards, Pioneer 11 was deflected back to the inner heliosphere in order to approach Saturn in September 1979.

### Instrumentation

Like Ulysses, the Pioneers were spacecraft with a broad set of scientific instruments to allow fairly complete measurements of magnetic field, plasmas and energetic particles. Of interest for this study are the following instrument groups.



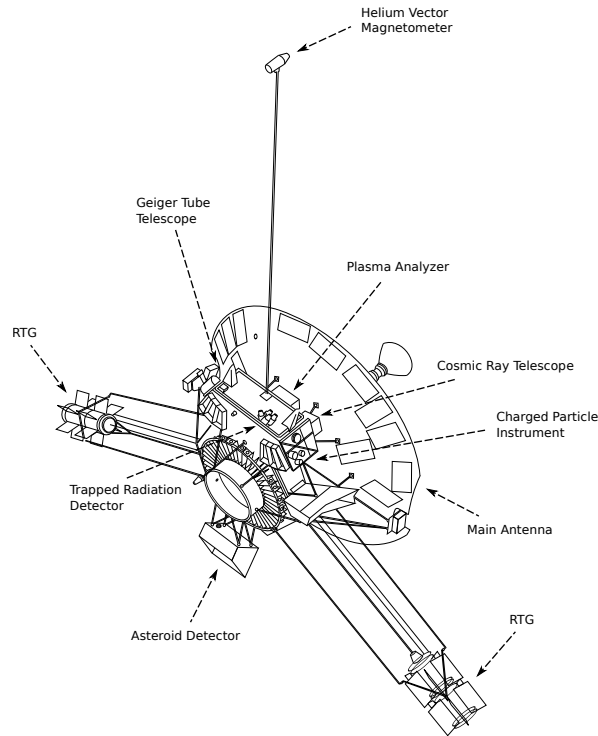


**Figure 5.5:** Sketch of the Pioneer 10/11 spacecraft and most of the scientific instruments. Author's work but adapted from <http://www.physics.uiowa.edu/newsletter/2003/pa03-alumni.html>.

**Magnetometer** The magnetic field measurements aboard the Pioneer spacecraft were performed by a Helium Vector Magnetometer, similar to the one used for the Ulysses mission.

**Plasma Analyzer** The plasma analyzer was designed to measure solar wind properties in the heliosphere.

**Energetic Particle Instruments** The Pioneers carried a couple of instruments to measure the properties of energetic particles in the interplanetary medium and in the magnetospheres of Jupiter and Saturn. These instruments are the Charged Particle Instrument (CPI), the Cosmic Ray Telescope (CRT), the Geiger Tube Telescope (GTT), and the Trapped Radiation Detector (TRD). In this work, the data obtained by the CPI (also called University of Chicago Instrument) is used.

The Chicago Instrument consists of four individual instruments, namely the Main Telescope (CPI/MT), the Low Energy Telescope (CPI/LET), an Electron Current Detector (CPI/ECD) and a fission cell. The instruments flown on Pioneer 10 and 11 were almost identical and are briefly described by Lentz et al. (1973), Chenette et al. (1974) and McCarthy and Ogallagher (1975). In this work, the data obtained

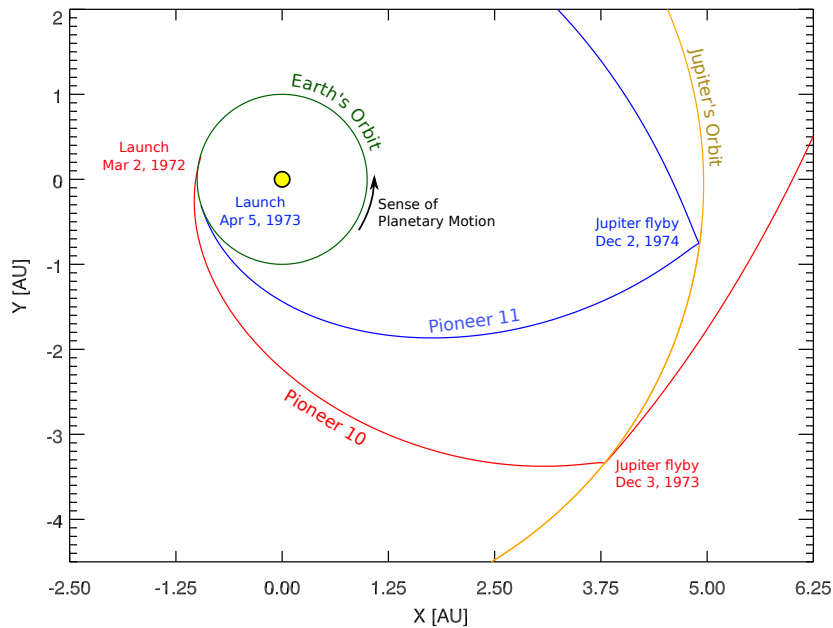


**Figure 5.6:** Trajectories of the Pioneer 10 and 11 spacecraft up to 1975 (P10) and 1977 (P11) as seen from the North. The orbits of the Earth and Jupiter are indicated as well as the dates of the launches and Jupiter encounters. While Pioneer 10 directly left to the outer heliosphere after the flyby, Pioneer 11 returned to the inner heliosphere in order to approach Saturn.

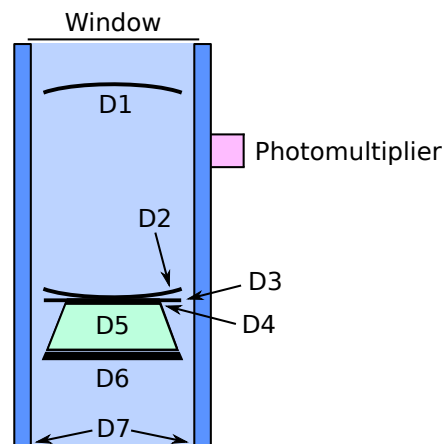


**Figure 5.7:** Sketch of the CPI/MT. The single detectors are indicated by  $D_n$ , where  $n$  is the number of the respective detector.

by the MT are used. A sketch of the instrument is shown in Fig. 5.7. The MT is a multi-element telescope, utilizing solid state detectors, a CsI scintillator (D5) and a

plastic scintillator used as an anticoincidence guard (D7). Particles of different species and energies are discriminated by a combination of coincidence and anticoincidence requirements and are assigned to so-called id's, i.e. energy and species-dependent channels. In the case of Jovian electrons, the id4 and id5 logics are of importance, counting electrons with energies from 2-7 MeV and 6-28 MeV, respectively. For the id4, the coincidence logic reads  $D1D2D4(\overline{D5 \text{ or } D7})$  (abbreviated as  $D4N5$ ). The id5 channel requires a particle to trigger the logic  $D1D2D4D5(\overline{D6 \text{ or } D7})$  (i.e.  $D5N6$ ), i.e. electrons with energies high enough to trigger the CSI scintillator D5 are counted as id5 electrons. However, the id4 and id5 channels are also sensitive to protons and heavier ions with energies of several tens of MeV. In this work, two sets of CPI data are used. The first data set contains omnidirectional counting rates of the CPI/MT at a time resolution of 15 minutes obtained from NSSDC<sup>2</sup>. The second data set, containing a subset of the CPI/MT data in a 30 minutes resolution, but with sectorized counting rates for the id4 logic as it is the case for the E4 channel of the KET aboard Ulysses, was provided by R. B. McKibben (University of New Hampshire, USA).

## 5.4 The Concept of Anisotropy

It is often not only desired to know how many particles were counted by an instrument in a given time interval, but one also wants to know where the particles are coming from. This information may be related to the viewing direction of the instrument (directional anisotropy) or related to the magnetic field at the time of measurement, providing information on the pitch-angle anisotropy.

To establish communication between the spacecraft and the ground control, it is necessary that the antenna of the spacecraft is always pointing to Earth. If the spacecraft is spin stabilized (as it is the case for Ulysses and Pioneer 10/11), i.e. it rotates perpendicular to the axis pointing to Earth (cf. Fig. 5.8), the rotation of the spacecraft allows to scan the circle defined by this motion with a particle telescope. This means, it is not only possible to attribute a measured particle with the time of measurement but also with the viewing direction of the instrument at that given time.

The formal definition of anisotropy with respect to the magnetic field is given by

$$\vec{A}(\vec{x}, E, t) = 3 \cdot \frac{\int_{-1}^{+1} I(\vec{x}, E, t, \mu) \mu d\mu}{\int_{-1}^{+1} I(\vec{x}, E, t, \mu) d\mu} \cdot \hat{e}_B, \quad (5.1)$$

where  $I$  is the intensity as a function of energy,  $\mu$  is the pitch-angle cosine and  $\hat{e}_B$  is the unit vector of the magnetic field passing through the spacecraft.

### Flux-Reconstruction Using a Fourier Series

Several methods are in use to give a numerical expression for the anisotropy depending on the purpose and the available data set. A method to determine the degree of the

<sup>2</sup>[ftp://nssdcftp.gsfc.nasa.gov/spacecraft\\_data/pioneer/](ftp://nssdcftp.gsfc.nasa.gov/spacecraft_data/pioneer/)

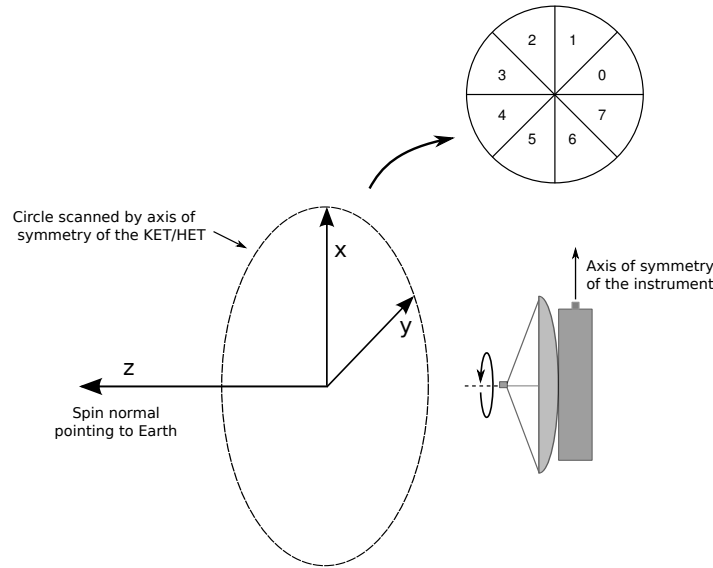


**Figure 5.8:** Sketch of a spinning spacecraft. The antenna is always pointing towards Earth while the spacecraft rotates around this axis. An instrument with a viewing direction perpendicular to the spin axis scans a complete circle once in a spacecraft's revolution.

anisotropy frequently encountered is to fit a Fourier series to the data. The formal definition of the Fourier series (Arfken, 1985) reads

$$f(x) = \frac{a_0}{2} + \sum_{n=1}^{\infty} a_n \cos nx + \sum_{n=1}^{\infty} b_n \sin nx, \quad (5.2)$$

with the Fourier coefficients  $a_0$ ,  $a_n$  and  $b_n$ . However, it is more practical to use either sine or cosine and a finite set of terms (Hatzky, 1993). Therefore, after introducing a necessary phase angle information, the cosine series may now be written as

$$j(\phi) = A_0(1 + A_1 \cos(\phi - \phi_1) + A_2 \cos(2(\phi - \phi_2)) + \dots). \quad (5.3)$$

Here,  $j(\phi)$  is the flux at a phase angle  $\phi$  and  $\phi_n$  is the phase of the respective cosine term. A useful restriction is to set  $n = 2$ , i.e. only the first and second harmonics are considered. The Fourier series can now be fitted to a data set, where  $A_0$ ,  $A_1$ ,  $A_2$  and the corresponding phase angles  $\phi_1$  and  $\phi_2$  are free parameters. The parameters  $A_1$ ,  $A_2$  are expressions for the degree of first and second order anisotropy, while  $A_0$  represents the offset, i.e. the isotropic part of the distribution. To understand the physical meaning of the Fourier series and their coefficients in the context of a space plasma, three examples of their application are given in Fig. 5.9. The first case, panel a), shows a purely isotropic distribution, i.e.  $dj/d\phi = 0$ . In this case, there is no net streaming of particles from one preferred direction. The panel in the middle shows

a first order anisotropy of particles, i.e. there is a net flux of particles coming from the left in this case as it is the case for solar particle events or Jovian electron jets. The angle  $\phi_1$  indicates the phase angle of Eqn. (5.3), i.e. the axis of symmetry and is identical to the magnetic field line. For comparison, a circle representing an isotropic distribution is added. Panel c) shows the case of a second-order anisotropy. Here, the particles come from two preferred directions. Again,  $\phi_2$  indicates the offset of the phase angle. The physical meaning of this distribution is that there is a bi-directional streaming (dumbbell distribution) of particles as it is observed in magnetic clouds, a subset of coronal mass ejection events. Particles ensembles trapped in the dipole field of a planetary magnetosphere can also be described by a second-order anisotropy. In this case, the two flux minima are the result of the lose cone of the magnetic bottle configuration.

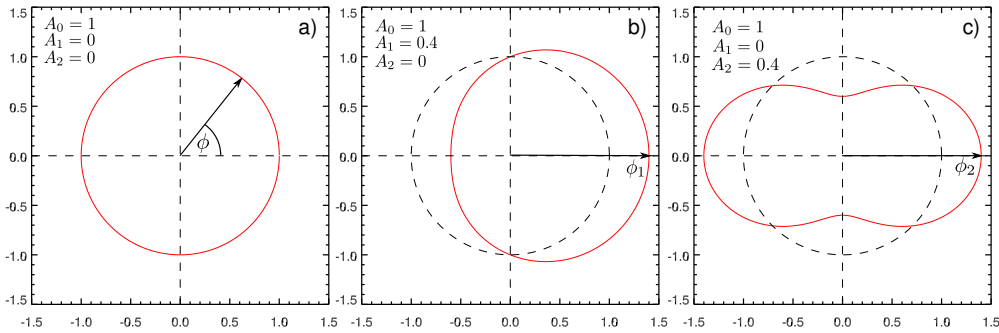


**Figure 5.9:** Examples of three different sets of coefficients of the cosine series as polar plots. Panels a) shows a purely isotropic distribution, a first-order anisotropy is shown in a) and b) while c) shows a second order anisotropy.

Another, more straightforward method to estimate the degree of anisotropy is to compare the fluxes of two hemisphere with the total flux, i.e.

$$A = 3 \left( \frac{f_{\mu>0} - f_{\mu<0}}{f_{\mu>0} + f_{\mu<0}} \right), \quad (5.4)$$

what is a simplified version of Eqn. (5.1), when  $f_{\mu<0}$  and  $f_{\mu>0}$  denote the flux from the hemisphere with positive or negative pitch angle, respectively.

### Application to Spacecraft and the Projection of the Magnetic Field

To apply the concepts described in the previous section on the real-world situation of a spinning spacecraft, knowledge of the position of the spacecraft with respect to Earth and the Sun (or the ecliptic plane) is necessary to calculate the correct orientation of the spin plane and the alignment of the spin sectors. In addition, in many cases it is desired not only to have sectorized count rates, but additionally a projection of

the magnetic field vector on the spin plane to compare the sector distributions of the particle with the magnetic field directly.

For the case of Ulysses, the spin plane is defined as the plane orthogonal to the direction vector of Earth and the spacecraft, where  $\vec{z}$  is the normal vector pointing to Earth and is given by  $\vec{z} = \vec{r}_e - \vec{r}_p$ , where  $\vec{r}_e$  and  $\vec{r}_p$  are the positions of Earth and the spacecraft. This vector  $\vec{z}$  is one vector of a right-handed coordinate system defining the orientation of the sector. The second vector,  $\vec{y}$ , is found by  $\vec{y} = \vec{r}_e \times \vec{r}_p$ , i.e.  $\vec{y}$  is perpendicular to the plane spanned by the Sun, the Earth and the spacecraft. The third component,  $\vec{x}$ , completes a right-handed system by  $\vec{x} = \vec{y} \times \vec{z}$ . This vector is identical with the beginning of the first sector of the sector system, because once per spacecraft revolution a “sun pulse” spinning with the spacecraft delivers the time when the instrument detects the Sun, defining the beginning of the first sector. For a spacecraft located in the ecliptic, the beginning of the first sector is parallel to the ecliptic plane. At higher latitudes, however, this is not always true. That means, the beginning of the first sector has to be determined by taking into account the projection of the direction vector from the spacecraft to the Sun on the spin plane. As a consequence of this definition of the sector orientation, it is important to consider if the spacecraft is in a position West or East from the connection line Sun-Earth. If the spacecraft is located in an eastern position with respect to the line connecting the Sun and Earth, the vector  $\vec{y}$  is pointing northwards and southwards in the case of a western position due to the cross-product  $\vec{y} = \vec{r}_e \times \vec{r}_p$ . Since the defined coordinate system has to be right-handed, the orientation of  $\vec{x}$  changes with  $\vec{y}$ . Given this new coordinate system defined by the vectors  $\vec{z}, \vec{y}, \vec{x}$ , it is possible to calculate the projection of the magnetic field vector onto the spin plane. For the Ulysses’ spacecraft, data of the magnetic field projected on the spin plane is already available at the Ulysses Data Center <sup>3</sup>. Therefore it was only necessary to perform this transformation to the relative position of Jupiter to relate the measured anisotropies with the magnetic field and the position of the planet.

For the Pioneer 10/11 spacecraft, however, these data are not available. Therefore, it was necessary to derive them from the given trajectory and magnetic field data. In addition, the definition of the sector geometry is slightly different from Ulysses. The sense of the spacecraft’s spin looking from Earth is counterclockwise, and the start of the first sector is within a few degrees parallel to the ecliptic and the orientation of the eight sector segments is fixed with respect to the sense of the orbital motion of the planets. (R. B. McKibben, private communication).

---

<sup>3</sup><http://helio.esa.int/ulysses/>

## 5.5 Pitch-Angle Coverage of the KET Experiment

The binning of a spacecraft's spin plane allows a principal investigations of anisotropies if a particle telescope is mounted perpendicular<sup>4</sup> to the spacecraft's spin axis. While a simple comparison of parallel and antiparallel particle fluxes with respect to an axis of symmetry, e.g. the magnetic field, is often sufficient to derive an estimation of the anisotropy, a more sophisticated analysis of the pitch-angle intervals being actually covered by a sector bin is necessary.

In what follows, functional dependencies between the viewing direction of the KET and the elevation of the magnetic field with respect to the spin plane will be derived in an iterative way. Let us consider for the moment a hypothetical particle telescope with an infinitely small view cone spinning around an axis. The inclination of the magnetic field,  $\eta$ , lies within a range  $\eta \in [-90^\circ, 90^\circ]$ , so that  $\eta = 0^\circ$  means that the magnetic field vector is orthogonal to the spin axis. In this case, the pitch angle cosine  $\mu$  that corresponds to the current viewing direction of the telescope is given by

$$\mu = \vec{e}_I(\alpha - \alpha_0) \cdot \vec{e}_B(\eta), \quad (5.5)$$

where  $\vec{e}_I$  is the unit vector of the telescope's viewing direction and  $\vec{e}_B(\eta)$  the inclination of the magnetic field vector with respect to the spin plane and  $\alpha$  is the current rotational angle of the telescope and  $\alpha_0$  the azimuth angle of the magnetic field on the spin plane. Clearly, this resembles the formal definition of the pitch-angle cosine if one carries out the dot product:

$$\mu = \cos(\alpha') \cos(\eta) \quad \alpha' = \alpha - \alpha_0 \quad (5.6)$$

The pitch-angle cosine interval covered by such an instrument is shown in Fig. 5.10 for several elevation angles  $\eta$  of the magnetic field vector. As expected, a full pitch-angle coverage is provided only if  $\eta = 0$  and decreases as  $\eta$  increases. However, such a telescope would not be very useful and the (effective) opening angle of a real world instrument must be taken into account. The effective half width of the view cone of the E4 channel is  $\sim 20^\circ$  (Sierks, 1988; Hatzky, 1993) and therefore the instrument detects not only particles in an infinitely small pitch-angle interval but in a rather wide range. Let the half opening angle of the instrument be defined by  $\phi_0$ , then all points within the cone are defined by two angles  $\phi$  (polar angle) and  $\chi$  (azimuthal angle), where  $\phi \leq \phi_0$  and  $\chi \in [0, 2\pi]$ . The pitch angle covered by the set of variable  $\eta, \alpha', \phi, \chi$  is given by (Hatzky, 1993)

$$\mu = \cos(\eta) \cos(\alpha') \cos(\phi) - \cos(\eta) \sin(\alpha') \cos(\chi) \sin(\phi) + \sin(\eta) \sin(\chi) \sin(\phi). \quad (5.7)$$

As can be seen, this formula simplifies to Eqn. (5.6) if  $\phi = 0$ . With this knowledge and the information on the orientation of the mean magnetic field vector during the

---

<sup>4</sup>This requirement is fulfilled for the KET (R. Müller-Mellin, private communication). The CPIs aboard the Pioneers, however, have an inclination  $< 90^\circ$  with respect to the spin axis pointing to Earth and require a slightly more complicated calculation.

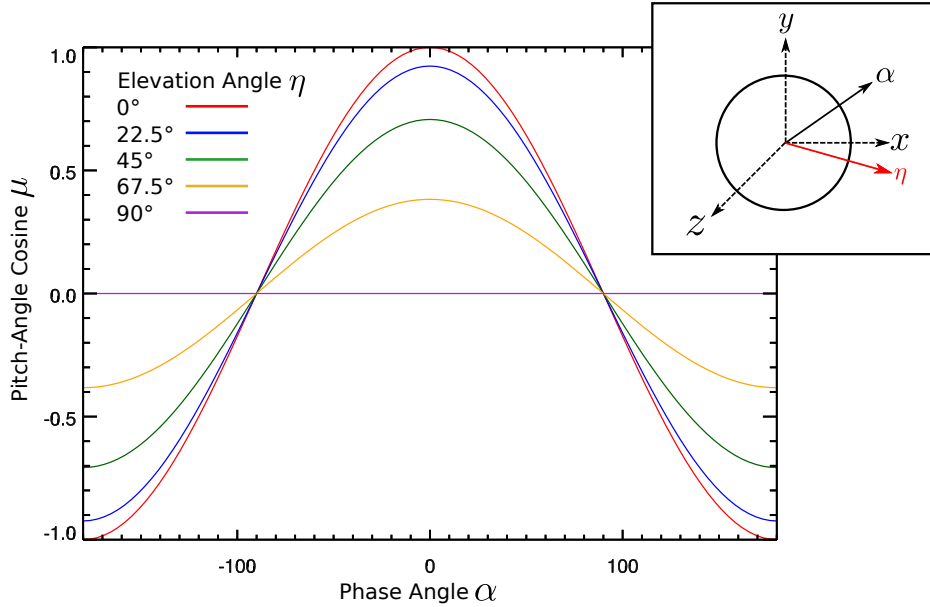


**Figure 5.10:** The pitch-angle cosine scanned by a particle telescope with an infinitely small view cone as a function of the phase angle. Calculation for several elevation angles of the magnetic field vector with respect to the spin plane are shown. As can be seen, the pitch-angle interval covered by the instrument within a full rotation is a function of the elevation angles in a way that large elevation angle lead to bad pitch-angle coverages. The inset in the upper right corner illustrates the geometry. The spin plane is represented by the circle, the vector of the instrument’s phase angle is parallel to the spin plane.

instrument’s integration time, it is possible to derive the pitch-angle coverage for any position of the instrument. An important point already obvious from Eqn. (5.6) is the fact that a full pitch-angle coverage is only given if  $\eta = 0^\circ$ . In the most disadvantageous case  $\eta = \pm 90^\circ$ , the pitch-angle interval is limited to  $\mu \leq |\sin(\phi_0)|$  for all values of  $\alpha'$ . The pitch-angle coverages for the eight segments of the KET (and HET) were computed for the entire mission lifetime of Ulysses and submitted to the Ulysses data system.

## 5.6 The Lomb-Scargle Algorithm

The detection of periodic variations in data is a common task in all disciplines of science. A well known method to analyze data with respect to periodicities is the Fourier transform (FT). Basically, the FT is the transformation of a signal (the time series) in the time domain, say  $f(t)$ , to the frequency domain,  $f(\omega)$ . Based on the representation of the time series in the frequency domain it is possible to determine the periodicities present in the data. However, measured data are discrete values, i.e.



they are not continuous but made of single data points separated by distinct time steps  $\Delta t$  and have a finite duration. This requires a modification of the FT called the discrete Fourier transform (DFT). The most commonly used implementation of the DFT is the Fast Fourier Transformation (FFT), providing an efficient algorithm to compute the frequency domain of a time series (Press et al., 1992).

However, the DFT/FFT is only fully applicable to evenly spaced data sets. In experimental physics, this is not always assured. The time series may be influenced by instrumental blackouts or external reasons that corrupt an equally spaced time series, e.g. the diurnal limitations of astronomical observations. An algorithm to find periodicities in a set of unevenly sampled data was proposed by Lomb (1976) and developed further by Scargle (1982). The spectral power  $P$  of the Lomb-Scargle periodogram as a function of  $\omega = 2\pi f$  is given by

$$P(\omega) = \frac{1}{2\sigma^2} \left( \frac{\left( \sum_j (h_j - \bar{h}) \cos(\omega(t_j - \tau)) \right)^2}{\sum_j \cos^2(\omega(t_j - \tau))} + \frac{\left( \sum_j (h_j - \bar{h}) \sin(\omega(t_j - \tau)) \right)^2}{\sum_j \sin^2(\omega(t_j - \tau))} \right), \quad (5.8)$$

where  $\bar{h}$  and  $\sigma^2$  denote the mean and the variance of the measured data points  $h_j$  and  $t_j$  is the time. The parameter  $\tau$  is introduced to make sure that the spectral power is independent of shifting along the time axis and is computed by

$$\tau = \frac{1}{2\omega} \arctan \left( \frac{\sum_j \sin(2\omega t_j)}{\sum_j \cos(2\omega t_j)} \right). \quad (5.9)$$

The presence of noise beside the real periodicities in the data may introduce further peaks in the periodogram. Based on statistical considerations it is possible (Press et al., 1992) to derive levels of significance which are computed by

$$z = -\ln \left( 1 - (1 - FAP)^{1/N} \right), \quad (5.10)$$

where  $FAP$  is the false-alarm probability,  $N$  is the number of independent frequencies and  $z$  is the spectral power level that corresponds a given  $FAP$ . A  $FAP$  value of 0.01 means that the probability that a peak in the periodogram at  $z(FAP)$  is real is 99%. The number of independent frequencies  $N$  is typically taken to be  $N = n/2$ , where  $n$  is the number of data points, given that the data are equally spaced. However, it is important to note that Eqn. (5.10) is only valid for white noise superimposed on the data (Press et al., 1992). It was pointed out by Paularena (1996) that this assumptions leads to unrealistic false-alarm levels e.g. for the analysis of solar wind data. This concern is comprehensible if one takes into account that the source of the solar wind and the interplanetary magnetic field, i.e. the solar surface or the corona, is a highly irregular and dynamical pattern of structures in a wide range of spatial and temporal scales, where the assumption of totally uncorrelated noise is not necessarily given. Since GCRs propagate in the interplanetary magnetic field, it is assumed that

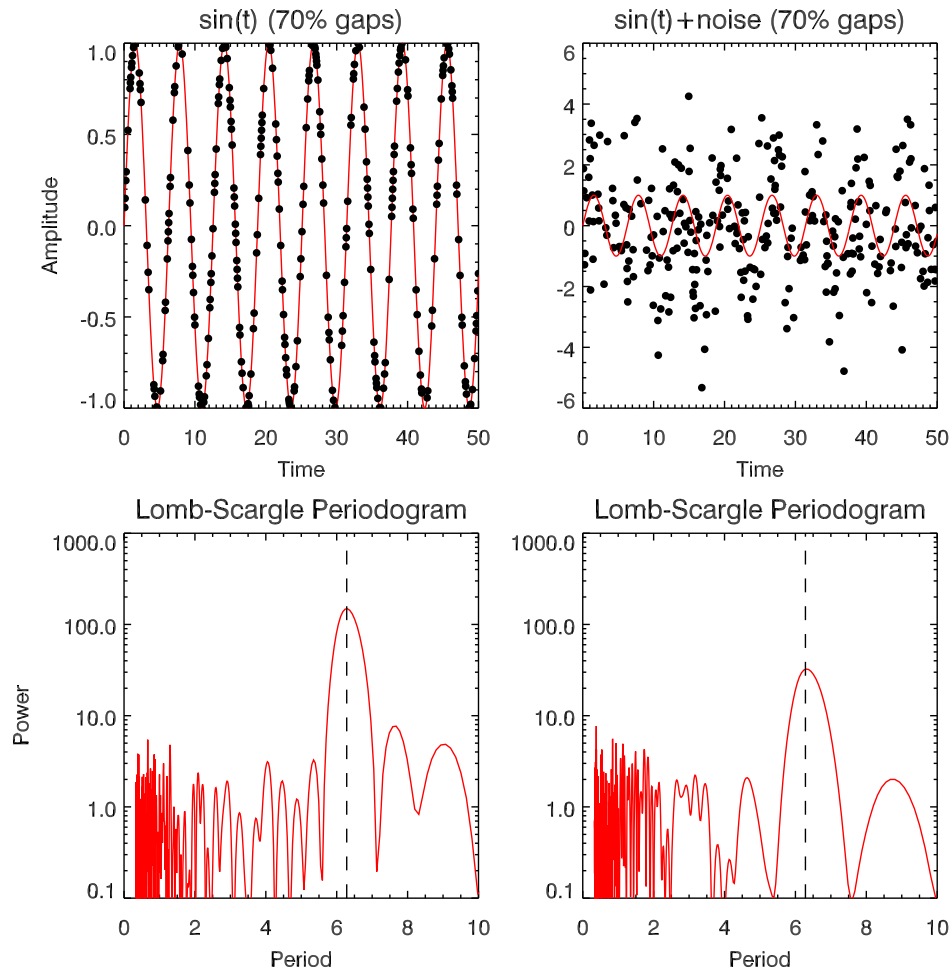


**Figure 5.11:** Result of the Lomb-Scargle analysis for a sinusoid. The upper left panel shows a sine function with a data coverage of 30% (black dots). The result of the Lomb-Scargle analysis is shown in the left bottom panel. The expected period at  $P = 2\pi$  can clearly be seen. The right panel shows the same as the left panel but for additional white noise superimposed on the sinusoid. While the time series shows no periodicity to the eye, the Lomb-Scargle analysis still recovers the periodicity of the sinusoid.

Eqn. (5.10) should also be used with caution for these data. Another limitation of the estimation of significance levels is the question of the actual number of independent frequencies. As stated above, the  $N$  is determined by the number of data points for the case of equally spacing. If the time series is irregular, there is no simple expressions for  $N$  and Monte-Carlo techniques may be taken into account (Dilmaghani et al., 2007). In addition, any preprocessing of data, e.g. smoothing affects the number of independent frequencies and therefore reduces the reliability of Eqn. (5.10) (Hernandez, 1999). In what follows, an example is given for a) a sinusoid with unevenly sampling and b) a

sinusoid with unevenly sampling and noise. The left panels of Fig. 5.11 shows the time series of a sine function with a data coverage of 30% (black dots) and the corresponding sinusoid with no data gaps (red curve) and the resulting Lomb-Scargle periodogram. As can be seen, a clear peak at  $P = 2\pi$  can be identified, corresponding to the period of the input function. Note that there are several smaller peaks that are caused by the unevenly sampled data and by the effect of power leakage due to the finite sampling interval. The right panels show the same information, but now white noise, i.e. noise with a zero mean and a standard deviation of one is added to the signal with data gaps in the form of  $\sin(t) + 1.5 \cdot \text{noise}$ . While a periodic variation of the time series is barely visible to the eye, the Lomb-Scargle periodogram still recovers a clear peak at the expected period. Note that the power level of the peak at  $P = 2\pi$  decreased significantly with respect to the peaks related to the random fluctuations and the influences mentioned above.

Popular implementations of the Lomb-Scargle algorithm<sup>5</sup> do not allow the user to specify what frequencies will be evaluated. Instead of that, the array of evaluated frequencies is defined by

$$f_i = f_{i-1} + 1/(k_{os} \cdot (\max(t) - \min(t))), \quad (5.11)$$

with

$$f_0 = 1/(k_{os} \cdot (\max(t) - \min(t))), \quad (5.12)$$

as the starting frequency. The constant  $k_{os}$  is the so-called oversampling factor and  $t$  is the time. That means that the set of frequencies depends on the length of the time interval, i.e. slightly different time intervals do not share the same set of frequencies. While this is barely an awkward limitation in most cases, in some situations it may be desired to evaluate a user-defined array of frequencies. In the chapter on Jovian jets in the interplanetary medium (chapter 8), a Lomb-Scargle based time-series analysis is not only performed in the traditional way of plotting frequency vs. power for a defined time interval, but also as a “sliding” spectral analysis allowing a three dimensional investigation of a time interval (A. Kopp, private communication). This resembles the waterfall displays used in modern passive sonar stations (Friedman, 2006), although the assignment of abscissa and ordinate are exchanged. This allows a convenient tracking of the temporal evolution of the wave power contained in a fixed frequency interval. For this purpose, a modified version of the Lomb-Scargle algorithm was developed, allowing the user to specify a well defined set of frequencies. The principle of the sliding Lomb-Scargle is visualized in Fig. 5.12. Given a time interval, a subinterval of width appropriate for the frequencies of interest, is analyzed and the resulting power spectrum is assigned to the center of the subinterval. The subinterval is then shifted piecewise and the Lomb-Scargle analysis is repeated for these data. This algorithm is reiterated until the end of the full time interval is reached. Finally, the resulting matrix (*time*  $\times$  *period*) is then displayed in a color-coded way.

---

<sup>5</sup>For example the `lwp_test()` function of the IDL software package based on Press et al. (1992).

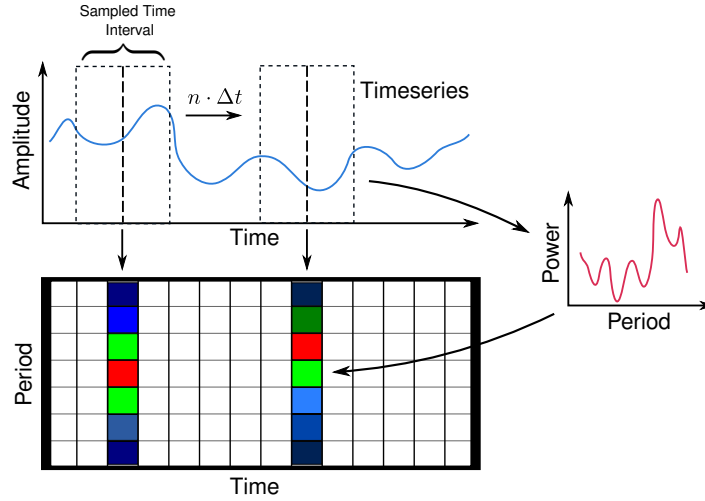


**Figure 5.12:** This sketch illustrates the method of the sliding Lomb-Scargle algorithm. For each subinterval, which centroids are separated by  $\Delta t$ , of the complete timeseries, the Lomb periodogram will be computed. The resultant power of each periodogram is then plotted as a function of time and period: The abscissa represents the time, the ordinate the period and the power is represented in a color-coded way.

## 5.7 Correlations of Timeseries

The correlation analysis deals with the task of finding (recurrent) similarities of timeseries. The auto correlation of a timeseries  $X(t)$  is given by

$$r_{XX}(t, t+u) = \frac{\text{Cov}(X(t), X(t+u))}{\sqrt{\text{Var}[X(t)]\text{Var}[X(t+u)]}}, \quad (5.13)$$

where Cov is the covariance and Var the variance of  $X$  as a function of  $t$  and  $t$  plus a lag  $u$ . That means, a copy of the timeseries is shifted in time with respect to the original timeseries and  $r_{XX} \in [-1, 1]$  is a measure of the correlation between  $X(t)$  and  $X(t+u)$ . Complete correlation is given if  $r_{XX} = 1$ , while  $r_{XX} = -1$  indicates complete anticorrelation. A result of  $r_{XX} = 0$  states a complete uncorrelation. If  $u = 0$ , it is clear that  $r_{XX}$  is always equal to 1. While a white noise signal is uncorrelated for  $u \neq 0$ , a timeseries showing a periodicity will show significant (anti) correlation depending on  $u$ . A trigonometric function, e.g.  $\cos(\frac{2\pi}{P}t)$ , will show a complete correlation for  $u = n \cdot P$  with  $n \in \mathbb{N}$ , because of the identity

$$\cos\left(\frac{2\pi}{P}t\right) = \cos\left(\frac{2\pi}{P}(t+n \cdot P)\right). \quad (5.14)$$

It is often not only desired to investigate a timeseries with respect to itself, but to compute the cross correlation of two timeseries  $X_1$  and  $X_2$  at different lags. Analogous

to the auto correlation function, the cross correlation is defined by

$$r_{12}(t, t + u) = \frac{\text{Cov}(X_1(t), X_2(t + u))}{\sqrt{\text{Var}[X_1]\text{Var}[X_2]}}, \quad (5.15)$$

where  $r_{12} \in [-1, 1]$  is a measure of the correlation of two timeseries as a function of lag  $u$ .

Alternatively to the parametric correlation analysis (Pearson correlation analysis), nonparametric correlation methods may be used (Sprent and Smeeton, 2007). One of these methods is the so-called Spearman rank correlation, being identical to Pearson's correlation, except that the original data are replaced by their ranks (Press et al., 1992, chapter 16.4). Ranked data have the advantage that their actual value is not of importance, but their position within the ranking of the data, making nonparametric analysis techniques generally more robust than their parametric counterparts. Even more nonparametric is the correlation analysis elaborated by Kendall (see also Press et al., 1992, chapter 16.4), because this method only takes into account the relative ordering of ranks. In chapter 7, and implementation of the algorithm for the computation of Kendall's correlation coefficient described by Bandt (2005) will be used to study the energy spectra of MeV electrons in the Jovian magnetic field. The algorithm consists of two steps: The first step is to calculate the so-called Order Structure Matrix  $b$ , which is defined as the comparison of the data point  $X(s)$  with points  $X(t)$  with  $1 \leq s, t \leq N$ , where  $N$  is the number of data points of the time series  $X$ , i.e.

$$b_{s,t} = \begin{cases} 1 & \text{if } X_s \geq X_t \\ 0 & \text{if } X_s < X_t \end{cases} \quad (5.16)$$

The second step is to calculate Kendall's correlation coefficient

$$\tau^d(k) = \frac{1}{N} \sum_{t=1}^{N-k-d} b_{t,t+d} \wedge b_{t+k,t+k+d}, \quad (5.17)$$

where  $\wedge$  means logical equivalence ( $a \wedge b = 1$  if  $a = b$ , otherwise zero) and  $k$  is the shift with respect to the original time series. The parameter  $d$  related values of  $b$  that are  $d$  steps apart. The auto and cross correlation function will be applied to the investigation of the temporal evolution of particles in the Jovian magnetosphere and in the IMF with respect to the 10 h periodicity.



# Chapter 6

## “Quiet-Time“ Jovian Electrons in the Heliosphere

Wer je die flamme umschritt  
Bleibe der flamme trabant!

---

Stefan George

This chapter is dedicated to a recapitulation of both observations and modeling approaches to Jovian electrons, allowing a better understanding of the results of the following chapters. Moreover, the effect of mirroring (i.e. defocusing) on charged particles travelling from the outer heliosphere towards the inner regions will be discussed.

### 6.1 The Pre-Ulysses Era

The Pioneer 10 and 11 spacecraft were the first man-made objects to explore the regions beyond the Asteroid belt (see Fig. 5.6 for the trajectories). Launched in 1972 and 1973, respectively, the spacecraft made valuable scientific investigations for more than 20 years. One of the most important results for the field of heliospheric astroparticle physics was the identification of the Jovian magnetosphere as a copious source of energetic electrons. Starting with the pioneering work of Chenette et al. (1974), it soon turned out that Jovian electrons can be observed almost everywhere in the inner heliosphere. Fig. 6.1 shows a plot of the counting rates of electrons in the range from 3-6 MeV from early 1972 to mid 1976 observed by Pioneer 10. The symbols on top ( $\blacktriangle$ ) indicate the distance of Pioneer 10 from the Sun. As can clearly be seen, a flux increase is observed as the spacecraft came closer to Jupiter with a maximum during the closest approach. From this observation it was concluded that energetic electrons constantly escape from the Jovian magnetosphere and propagate in the heliosphere. This finding was confirmed by measurements of Pioneer 11 one year later and the two Voyager spacecraft approaching Jupiter in 1979. Jovian electrons were also identified as the

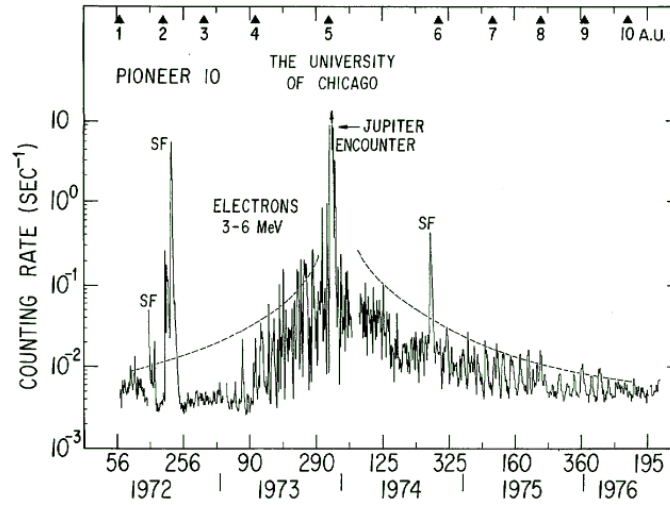


**Figure 6.1:** Counting rates of 3-6 MeV electrons measured by Pioneer 10 from 1972 to 1976. A clear increase of the electron flux is observed with a peak at the closest approach to Jupiter in December 1973. As the spacecraft moved away from the planet, the counting rates decreased. This is a clear indication that the Jovian magnetosphere is a source of energetic electrons that can be measured over wide distances in the heliosphere. The letters “SF” mark solar flares, i.e. these electrons are of solar and not of Jovian origin. Taken from Pyle and Simpson (1977).

source of so-called “quiet-time“ electrons at Earth’s orbit as convincingly elaborated by Teegarden et al. (1974), who showed that every  $\sim 13$  months a recurrent increase of energetic particles at Earth’s orbit can be observed. This effect, now founded on an observational basis of several decades (cf. Kanekal et al., 2003), can be made plausible by keeping in mind that charged particle propagation is most effective parallel to the magnetic field, i.e. parallel to the Parker spiral. Due to the sidereal motion of the Earth ( $T_8^{sid.} = 365.25$  days) and Jupiter ( $T_2^{sid.} = 4331.572$  days) around the Sun the synodic period of Jupiter (with respect to Earth) can easily be obtained by subtracting the sidereal angular speeds, i.e.

$$\omega_2^{syn.} = \omega_8^{sid.} - \omega_2^{sid.} \quad \Rightarrow \quad T_2^{syn.} = \left( \frac{1}{T_8^{sid.}} - \frac{1}{T_2^{sid.}} \right)^{-1} \approx 399 \text{ d.}$$

Consequently, Jupiter and Earth are located on the same Parker spiral every 399 d or 13 months, resulting in an enhanced electron flux at Earth. This is shown in Fig. 6.2 showing counting rates of MeV electrons measured by the IMP-8 satellite orbiting the Earth. A recurrent variation of the electron flux is evident with a periodicity of 13 months. The inset on the right gives a geometrical explanation of the observations.

Furthermore, the Jovian electron flux was found to be interrupted by the occurrence of CIRs as discussed e.g. by Chenette (1980) who showed that the electron flux stays



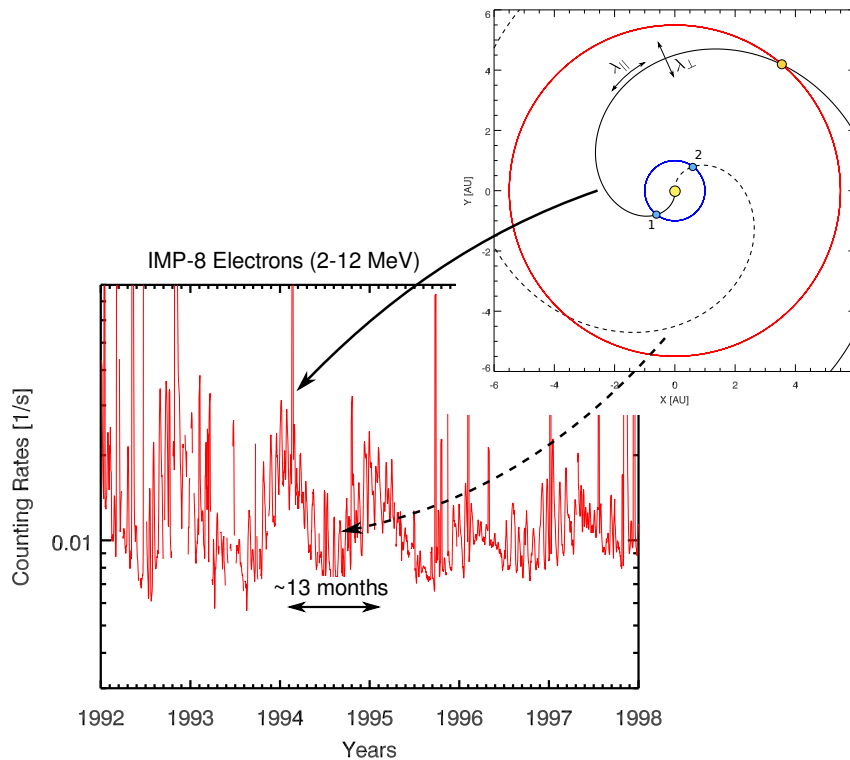


**Figure 6.2:** This Figure illustrates the 13 months periodicity of Jovian electrons observed at Earth’s orbit. If Earth and Jupiter are magnetically connected by the same Parker field line (1), enhanced electrons fluxes are observed. The opposite is observed during times when the magnetic connection is inappropriate (2) the electron flux is at minimum. This ”Jovian season“ is clearly visible in the bottom left Figure showing MeV electron measurements of the IMP-8 satellite orbiting the Earth.

at the background value as long as Jupiter and the spacecraft are separated by the structure. The reason for this is the reduced diffusion coefficient inside the CIR. In particular the stream interface plays an important role as pointed out by Dunzlaff (2007), who showed that the minimum of the electron flux is generally in coincidence with the occurrence of the stream interface at the spacecraft, manifested by either a gradual decrease of the flux right after the forward shock or a rapid disappearance of the flux at the stream interface. An example is shown in Fig. 6.3. From top to bottom this plot shows the solar wind speed, the magnetic field strength, the flux of protons with energies of 0.9-1.2 MeV, counting rates of protons with energies of 2.7-5.4 MeV as well as the counting rate of 2.5-7 MeV electrons. An abrupt decrease of the flux is observed in coincidence with the arrival of the stream interface (SI), i.e. time intervals (3) and (4) in the Figure. Therefore, an observer at Earth’s orbit sees a long-term variation due to the orbital motion of the Earth and Jupiter as well as a short-term

variation of  $\sim 27$  days due to the rotation of the Sun<sup>1</sup>. The Jovian electron source

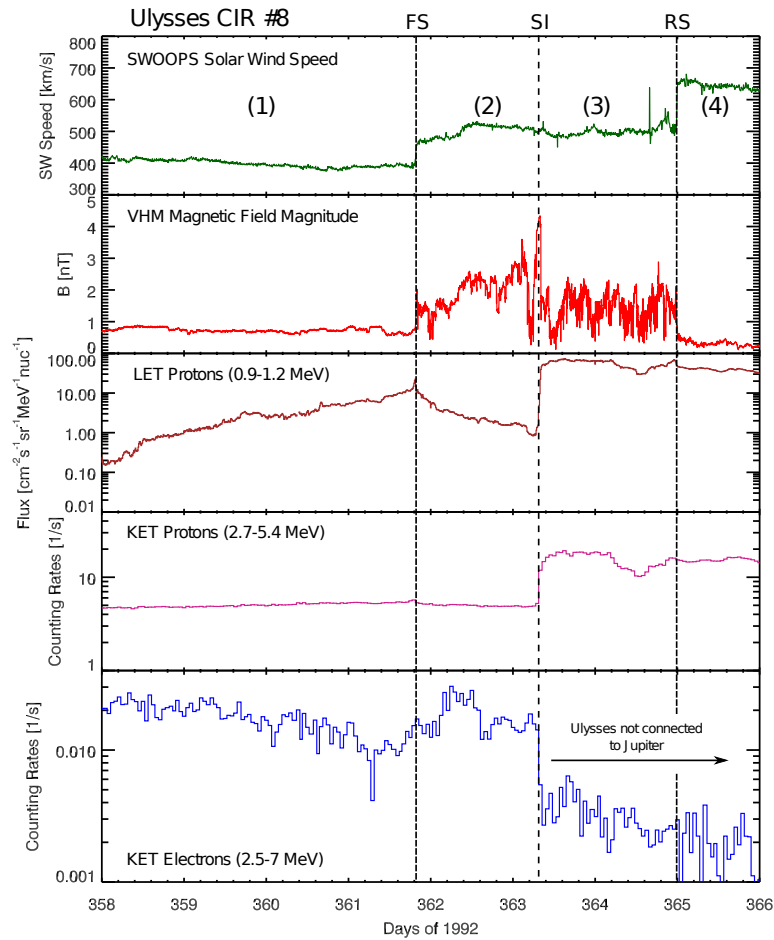


**Figure 6.3:** An impressive example of the role of CIRs as diffusion barriers is the CIR #8 observed by Ulysses during the last days of 1992 in a similar illustration as discussed by Dunzlaff (2007). A clear forward and reverse shock can be identified by jumps in the solar wind speed and the magnetic field strength. The peaks in the low energetic protons suggest shock acceleration. KET data showing 2.5-7 MeV electrons are shown in the bottom panel. An abrupt decrease of the flux is observed in coincidence with the arrival of the stream interface (SI), indicating that Ulysses and Jupiter were more or less magnetically disconnected.

is not only the major contribution to the population of MeV electrons in the inner heliosphere: As Pioneer 10 proceeded to the outer regions of the heliosphere it was

<sup>1</sup>A spacecraft like Ulysses or the Pioneers, traveling mainly radial with respect to the Sun, observes a 26-day periodicity, i.e. the sidereal periodicity of the Sun.

shown (Lopate, 1991) that Jovian electrons can still be identified up to distances from the Sun of  $\sim 25$  AU.

Based on the observational data, propagation models for Jovian electrons were derived from the general Fokker-Planck equation (Conlon, 1978). For the sake of finding an analytical solution, the model neglected effects like adiabatic energy losses and drifts but included spatial diffusion and convection and reads

$$\frac{\partial f}{\partial t} = \frac{\partial}{\partial x_i} \left( \kappa_{i,j} \frac{\partial f}{\partial x_j} - u_i f \right), \quad (6.1)$$

where  $x_i$  and  $x_j$  with  $i, j = [1, 2, 3]$  are the spatial coordinates and  $\kappa_{i,j}$  the corresponding diffusion coefficients, while  $u_i$  is the solar wind speed. Nevertheless, the model, describing particle diffusion in a moving medium, was applied with great success to the measurements and realistic diffusion coefficients were derived from fitting long-term particle fluxes as well as short-term modulation related to CIRs. Typical values found for  $\kappa_{\parallel}$  and  $\kappa_{\perp}$  are  $5 \cdot 10^{22}$  cm<sup>2</sup>/s and  $5 \cdot 10^{20}$  cm<sup>2</sup>/s, respectively. Here,  $\kappa_{\perp}$  primarily refers to the perpendicular diffusion in the ecliptic plane since the Pioneers did not enter higher latitudes; the task of finding the value for  $\kappa_{\perp}$  out of the ecliptic was handed over to Ulysses<sup>2</sup>.

## 6.2 Ulysses – Conquering the Third Dimension

The highly inclined orbit of Ulysses offered the unique opportunity to study the heliospheric environment, including Jovian electrons, at high latitudes. These measurements allowed important insights in the three-dimensional structure of the IMF and propagation of energetic particles. At the same time, numerical solutions of Parker’s transport equation became available due to increased computer power, enhancing the understanding of particle propagation in the heliosphere.

The comparison of observational data (cf. Heber et al., 2007) with numerical results was performed e.g. by Ferreira (2005) and Zhang et al. (2007), covering a time interval of observations of about 7 years. Average diffusion coefficients derived from Ulysses measurement are in good agreement with previous results, e.g. the parallel diffusion coefficient  $\kappa_{\parallel}$  was found to be  $1 \cdot 10^{23}$  cm<sup>2</sup>/s, while  $\kappa_{\perp,r} = \kappa_{\perp,\theta} = 5 \cdot 10^{20}$  cm<sup>2</sup>/s near the ecliptic. However, it was shown that  $\kappa_{\perp,r}$  and  $\kappa_{\perp,\theta}$  are fairly different from each other at higher latitudes, i.e.  $\kappa_{\perp,\theta}$  was found to exceed the value of  $\kappa_{\perp,r}$  by a factor of 13, i.e. a significant increase towards the poles is required to fit the observations. Further studies concerning the spatial and temporal dependence of the heliospheric diffusion tensor were put forward, e.g., by Sternal et al. (2011), Strauss et al. (2011), and Strauss et al. (2012).

---

<sup>2</sup>It is common to split the perpendicular diffusion term in two terms: One for the radial perpendicular diffusion  $\kappa_{\perp,r}$  and one for the latitudinal diffusion coefficient  $\kappa_{\perp,\theta}$ .

### 6.3 On the Focusing of Jovian Electrons

This work mainly deals with the pitch-angle dependent transport of Jovian electrons. While for solar energetic particles the effect of focusing was found to be of importance, the reverse effect, i.e. the mirroring of particle coming from the outer regions of the heliosphere is barely discussed in the literature. The Parker transport model, in particular, used as a standard equation for the modeling of charged particle transport does not take into account these effects. Therefore, the influence of the nominal interplanetary magnetic field on systematic changes of the pitch angle of Jovian electrons will be discussed. The magnitude of the magnetic field strength as a function of radial distance  $r$  is given by

$$B = B_0 \frac{r_0^2}{r^2} \sqrt{1 + (\beta r)^2}, \quad (6.2)$$

where  $\beta = -\Omega_s/u_{sw}$ . Here,  $\Omega_s$  is the angular speed of the Sun and  $u_{sw}$  is the solar wind speed. The length of the Parker spiral, i.e. an Archimedian spiral,  $s$ , is given by (Bronstein et al., 2001)

$$s(\varphi) = \frac{a}{2} \left( \varphi \sqrt{\varphi^2 + 1} + \sinh^{-1} \varphi \right), \quad (6.3)$$

where  $\varphi$  is the azimuth angle and  $a = v/\Omega_s$ , i.e. the ratio of speed of a particle moving away from the source radially and the angular speed of the source, i.e. the Sun. With  $r = \frac{u_{sw}}{\Omega_s} \varphi$  (cf. Eqn 2.2), the latter equation can be expressed as a function of radial distance and reads

$$s(r) = \frac{1}{2\beta} \left( \beta r \sqrt{1 + (\beta r)^2} + \sinh^{-1}(\beta r) \right). \quad (6.4)$$

The length of the spiral between two points  $r_1$  and  $r_2$  follows readily:

$$\hat{s} = s(r_2) - s(r_1). \quad (6.5)$$

The time a particle needs to propagate from  $r_1$  to  $r_2$  is given by  $t = \hat{s}/v_{\parallel}$ , where  $v_{\parallel}$  is the velocity component parallel to the magnetic field line under the assumption that the particle does not change its initial pitch angle during the propagation (cf. Fig. 6.4). This is, however, oversimplified since particles are generally affected by focusing or defocusing as well as pitch-angle diffusion. Therefore, a next step will include the effect of defocusing a particle experiences when it travels from the outer heliosphere towards the inner heliosphere.

Assuming a nominal Parker field, the equation

$$\mu(r) = \sqrt{1 - (1 - \mu_0^2) \left( \frac{r_0^2}{r^2} \right) \frac{\sqrt{1 + \beta^2 r^2}}{\sqrt{1 + \beta^2 r_0^2}}}, \quad (6.6)$$

can be derived as an expression for the pitch-angle cosine at  $r$ , when the particle had

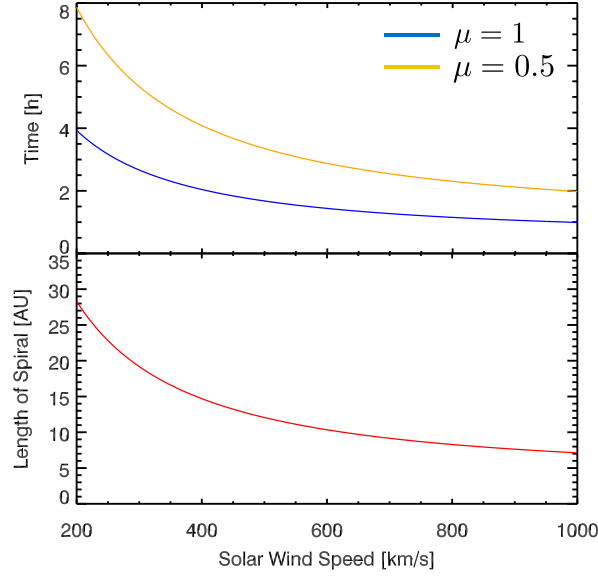


**Figure 6.4:** The length of the Parker spiral from  $r_1 = 1$  AU to  $r_2 = 5.2$  AU as a function of solar wind speed (bottom) and the corresponding travel time of a highly relativistic particle (top panel) for the case that  $\mu = 1$ , i.e. ( $v_{\parallel} \approx c$ ) (blue curve) and for  $\mu = 0.5$ , i.e. ( $v_{\parallel} \approx 0.5c$ ).

an initial pitch-angle cosine  $\mu_0$  at distance  $r_0$ . This equation is independent of the actual magnetic field strength, because only the gradient of the magnetic field along  $r$  determines the focusing/defocusing. The solar wind speed, however, still enters the equation via the parameter  $\beta = \Omega_S/v_{sw}$ . Fig. 6.5 shows the evolution of the pitch-angle cosine as a function of radial distance from the Sun for the case of several different initial pitch angle cosines for a solar wind speed  $v_{sw} = 400$  km/s. The mirror point, i.e. the distance where the motion of the particle changes its direction are the points where  $\mu = 0$ . From this plot it becomes evident that only a relatively small fraction of Jovian electrons are able to reach the orbit of the Earth, if no diffusion occurs. As can be seen, only particles with initial pitch-angle cosine greater than  $\geq 0.9$  are not mirrored back before they arrive at regions close to Earth's orbit.

Charged particles, however, undergo scattering in the interplanetary magnetic field, thus masking the effect of defocusing to some extent. Earl (1974) mathematically described the counter play of focusing and diffusion and found the modified diffusion equation

$$\frac{\partial f}{\partial t} + \frac{\kappa_{\parallel}}{L} \frac{\partial f}{\partial z} = \kappa_{\parallel} \frac{\partial^2 f}{\partial z^2}. \quad (6.7)$$

Here,  $\frac{\kappa_{\parallel}}{L}$  has the meaning of a convection term resulting in a net shift of the particle ensemble. The magnitude of this convection term determines the influence of focusing on the particles. Assuming a parallel diffusion coefficient  $\kappa_{\parallel} = 10^{22}$  cm<sup>2</sup>/s at 5 AU (i.e.  $L \approx 30$  AU according to Fig. 4.3) one obtains a  $\kappa_{\parallel}/L$  ratio of  $\approx 1.5 \cdot 10^{-5}$  AU/s.

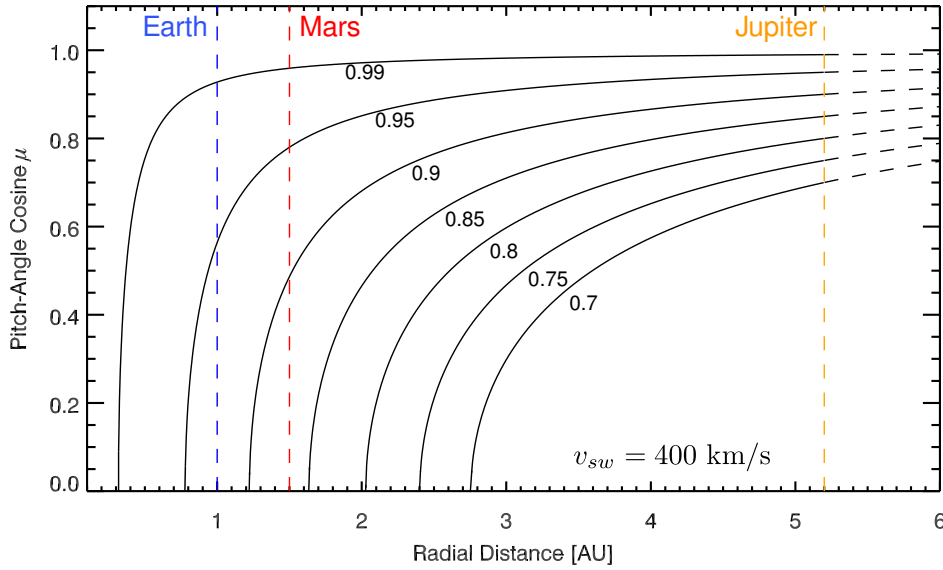


**Figure 6.5:** The pitch-angle cosines as a function of radial distance from the Sun for several initial pitch angle cosines  $\mu_0$ . The numbers at the black curves correspond to the initial pitch angle cosine at Jupiter. If the propagation of Jovian electrons along the interplanetary magnetic field is only determined by focusing/defocusing, only particles with initial pitch-angle cosines well above 0.9 make it to the orbit of the Earth before they are mirrored back. The solar wind speed has been set to  $v_{sw} = 400$  km/s.

Keeping the diffusion coefficient but now taking a focusing length of  $L = 0.25$  AU (corresponding to a distance from Sun of 0.5 AU) the ratio is  $\approx 1.8 \cdot 10^{-3}$  AU/s, i.e. considerably larger.

It follows immediately that the  $\frac{\kappa_{||}}{L}$  ratio is not only a function of distance from the Sun but also of the solar cycle since the parallel diffusion coefficient is found to be related to the solar cycle (e.g. Potgieter, 2008). During solar minimum conditions, the mean free paths of energetic particles are generally larger than during solar maximum and scale with the inverse of the magnetic field strength. The focusing length, however, does not depend on the magnetic field strength but only on its gradient and can therefore be assumed to be constant throughout the solar cycle (neglecting variable solar wind speeds). Consequently, the diffusion/focusing ratio depends on the solar cycle. While diffusion is manifested as a random walk of particles, focusing only acts in one direction. According to Fig.6.5, focusing makes it more difficult for particles coming from the outer heliosphere to be transported to regions close to the Sun. Diffusion of the particles, however, allows a fraction of the particles to be pitch-angle scattered to values of  $\mu$  that allow a propagation towards the inner heliosphere that would not be possible without scattering. Assuming a constant shape of the focusing length as a function of the distance from the Sun but a solar-cycle dependent mean free path it

can thus be argued that during solar minimum a smaller fraction of Jovian electrons may reach region close to the Sun than during solar maximum conditions.

It is interesting to note that Eraker and Simpson (1979) already suggested that mirroring (i.e. defocusing) may play a role in the modulation of Jovian electrons close to the Sun ( $\leq 0.5$  AU) to account for the somewhat surprising observations of negative electron flux gradients between the orbit of Mercury and the Earth.

Somewhat more recently, the influence of diverging or converging magnetic field was discussed by Schlickeiser and Shalchi (2008) for weak adiabatic focusing (i.e. the focusing length  $L$  is considerably longer than the mean free path of the particles) and introduced a modified version of the diffusion-convection equation taking into account focusing.





# Chapter 7

## How is the Jovian Clock Ticking?

Time is what prevents  
everything from happening at  
once.

---

John A. Wheeler

In chapter 3, the basic characteristics of the Jovian magnetosphere are described. In this chapter, a special feature will be discussed, namely the periodic spectral modulation of Jovian electrons in the planet's magnetosphere related to the  $\sim 10$  h rotation period. A reinvestigation of Ulysses' KET/HET data will be presented in order to describe a possible mechanism for the generation of the spectral modulation of Jovian electrons inside the Jovian magnetosphere. Besides the enormous size of the magnetosphere, the observations of the spacecraft that visited Jupiter also revealed the presence of a complex plasma environment on almost all energy scales and periodicities from seconds up to the rotational period of the planet and beyond. Probably the most famous periodicity to be found in the energetic particle populations is that related to the spin period of the planet ( $\sim 10$  h), first discovered by Chenette et al. (1974). These workers, investigating MeV-electron fluxes measured by Pioneer 10 during the spacecraft's approach towards the planet, pointed out that the Jovian magnetosphere is a strong source of MeV electrons. While this was already a surprising finding, they also found that these so-called Jovian electrons temporarily show a period spectral modulation in the interplanetary medium with the rotation period of the planet. When Pioneer 10 entered the Jovian magnetosphere, the 10 h modulation was present most of the time during the inbound and outbound trajectory of the spacecraft. Based on this finding, three models were derived in order to explain the observations and are described in what follows (cf. Schardt and Goertz, 1983).

## 7.1 The Clock Model

Based on measurements of 6-30 MeV electrons obtained by the University of Chicago Instrument aboard Pioneer 10, McKibben and Simpson (1974) investigated the temporal variations of the counting rates. They concluded that the observed variations are caused by a global modulation of the magnetosphere with the (synodic) period of the planet being only a function of time, but not of position. This finding was also supported by Voyager 1 & 2 observations (Schardt et al., 1981) of relativistic electrons in and near the Jovian magnetosphere. In 1992, Simpson et al. (1992b) confirmed the previous findings by the interpretation of data obtained by the HET and KET instruments aboard Ulysses during the spacecraft's flyby maneuver at Jupiter, where no significant phase shift of the spectral modulation expected from the spacecraft's trajectory was observed when the spacecraft passed from the Sunward hemisphere to the dusk side, being interpreted as an indication for a "clock"-like behavior of MeV electrons in the magnetosphere. Expressing the charged particle flux measured by a stationary<sup>1</sup> spacecraft as function of longitude  $\lambda$ , magnetic latitude  $\varphi_m$ , and time  $t$ , the total derivative reads

$$\frac{df(\lambda, \varphi_m, t)}{dt} = \frac{\partial f}{\partial t} + \dot{\lambda} \frac{\partial f}{\partial \lambda} + \dot{\lambda} \frac{\partial f}{\partial \varphi_m} \frac{\partial \varphi_m}{\partial \lambda}, \quad (7.1)$$

where  $\dot{\lambda} = \Omega$  is the angular speed of the planet. For the clock model, all terms but the first disappear, i.e.

$$\frac{df(\lambda, \varphi_m, t)}{dt} = \frac{\partial f}{\partial t}, \quad (7.2)$$

as a result of independence of position.

## 7.2 The Disc Model

According to the anomaly model, the disc model, proposed by van Allen et al. (1974) and Northrop et al. (1974), the observed modulation is related to the actual position of the spacecraft with respect to the magnetic latitude. This model is based on the tilt of the magnetic dipole with respect to the planet's rotational axis leading to a rotational modulation of the electron flux with the distance to the magnetosphere's current sheet (see bottom panel of Fig. 7.1). In contrast to the clock model, the disc model predicts that the temporal variation of the MeV electron flux depends on the relative position of the spacecraft with respect to the current sheet. Therefore, the flux variation predicted by the disc model can be written as

$$\frac{df(\lambda, \varphi_m, t)}{dt} = \dot{\lambda} \frac{\partial f}{\partial \varphi_m} \frac{\partial \varphi_m}{\partial \lambda}. \quad (7.3)$$

---

<sup>1</sup>In a sense that the motion of the spacecraft is small compared to the rotation of the planet.

However, the disc model came into trouble when Pioneer 11 explored relatively high magnetic latitudes during outbound and found the MeV-electron flux to be not much lower than in equatorial regions.

### 7.3 The Anomaly Model

Using Pioneer 10 and 11 magnetic field data, Dessler and Hill (1975) argued that a longitudinal asymmetry of the magnetic field strength near the surface of Jupiter extends along the footprint connection of the ionosphere with the magnetosphere, and results in the 10 h periodicity of energetic particles due to the indirect influence of higher order magnetic multipoles (Grodent et al., 2008, and references therein) being present in the inner magnetosphere. This so-called magnetic anomaly (or active sector) causes an azimuthal asymmetry of the high energetic particle population in the outer regions of the magnetosphere corotating with the planet (see also Vasyliunas and Dessler, 1981) as sketched in the top panel of Fig. 7.1. Using Eqn. (7.1), the flux is only a function of longitude:

$$\frac{df(\lambda, \varphi_m, t)}{dt} = \dot{\lambda} \frac{\partial f}{\partial \lambda}. \quad (7.4)$$

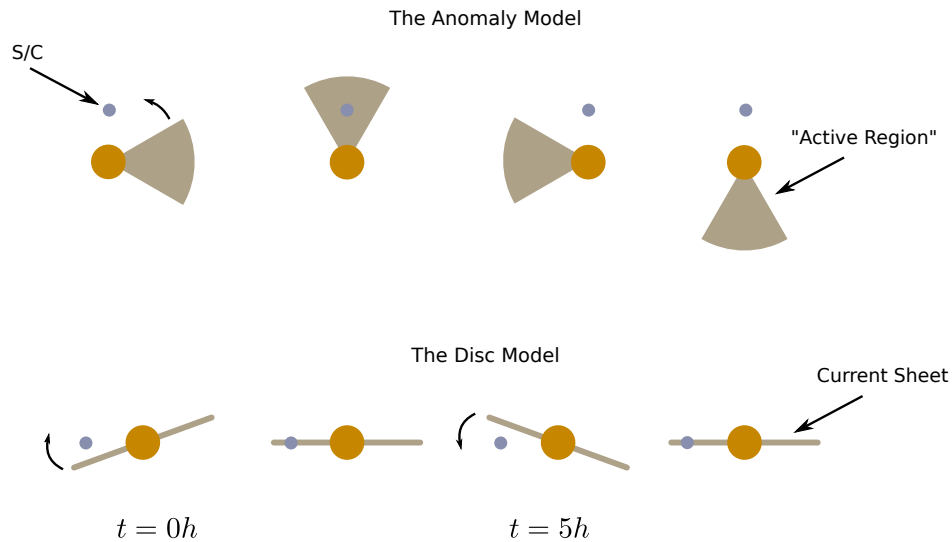


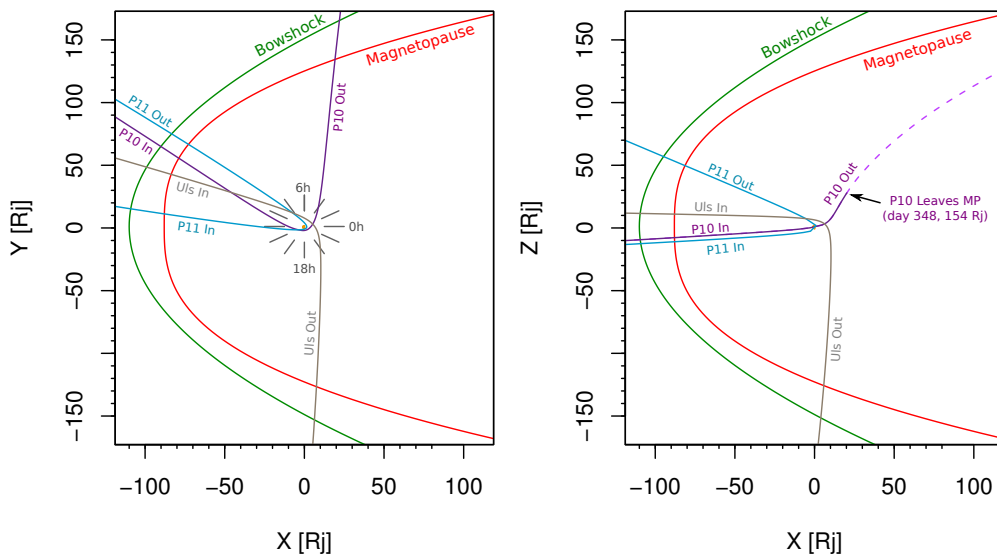
**Figure 7.1:** Graphical illustration of the anomaly (top) and the disc model (bottom). The spacecraft is indicated by the blue dot. As can be seen, the anomaly model can explain a 10 h periodicity while the disc model predicts a 5 h periodicity.

It was noted (Vasyliunas, 1975; Schardt et al., 1981) that the spectral index of energetic electrons is maximal when the system III (1965) longitude range  $\lambda_{III} = 240^\circ -$

310° faces the subsolar point. For an explanation of the system III (1965) coordinate system, the reader is referred to Appendix B in Dessler (1983) or Appendix A of this work. Somewhat recently, the asymmetry model has taken into account by Carbary et al. (2007) in order to describe observed spin-period effects of charged particles in the Kronian magnetosphere.

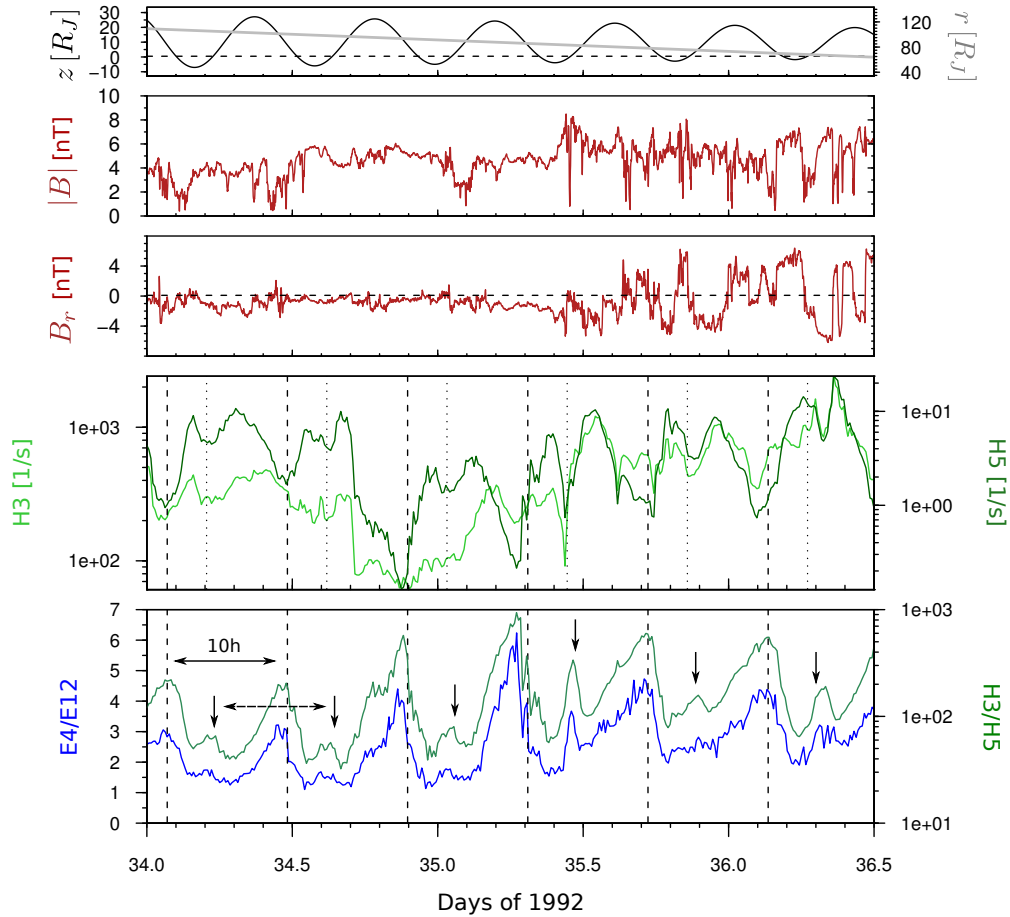
## 7.4 Re-Analysis of Ulysses Data

Fig. 7.2 shows the trajectory of Ulysses and Pioneer 10/11 for the time of their Jupiter flybys in a coordinate system in which the x-axis is the Sun-Jupiter line points away from the Sun, the z-axis is directed northwards, perpendicular to the orbital plane of the planet, and the y-axis completes a right-handed system. As can be seen, all three spacecraft entered the magnetosphere in the post-dawn sector at low latitudes. Their outbound trajectories, however, were quite different from each other. While Pioneer 10 was deflected towards the dawn side of the planet at moderate latitudes, the trajectory of Pioneer 11 after the closest approach is characterized by a high-latitude path towards the post-dawn sector towards the inner solar system. Ulysses entered the magnetosphere in the northern hemisphere and left the magnetosphere in the southern dusk-side hemisphere at very high latitudes as can be seen in Fig. 7.2. In what follows,



**Figure 7.2:** Trajectories of Pioneer 10/11 and Ulysses during their Jupiter encounters. For illustration, the Jovian magnetosheath/bowshock (green line) as well as the magnetopause (red line) is shown for the first or last encounter with the boundary during inbound or outbound path of Ulysses, respectively. The shapes of the bowshock and magnetopause are derived from the equations given by Joy et al. (2002).

the Ulysses and the Pioneer data will be discussed for the time intervals of the inbound and outbound paths starting with a presentation of the respective timeseries.



**Figure 7.3:** Ulysses measurements taken in the outer magnetosphere during the inbound pass. The top panels shows the nominal distance from the Jovian current sheet (black) and the distance from the planet (grey) in units of Jovian radii, followed by the magnetic field's magnitude and radial component. The two bottom panels display counting rates of HET's H3 and H5 channel, as well as the H3/H5 and E4/E12 ratios. For the sake of clarity, KET counting rates are not shown here, as they resemble the HET data in a good manner. The 10 h periodicity is indicated by the dashed solid lines, the minor peaks by the black arrows. The dotted lines refer to the local minima in the counting rates and are related to the minor peaks in the ratios. See text for further explanations.

Fig. 7.3 shows an overview of magnetic field and KET/HET data measured by Ulysses between day 34 and 36.5, i.e. just after the transition of the spacecraft from the interplanetary medium into the magnetosphere until the temporary switch-off of the KET, being in coincidence with the region generally called the outer magnetosphere.

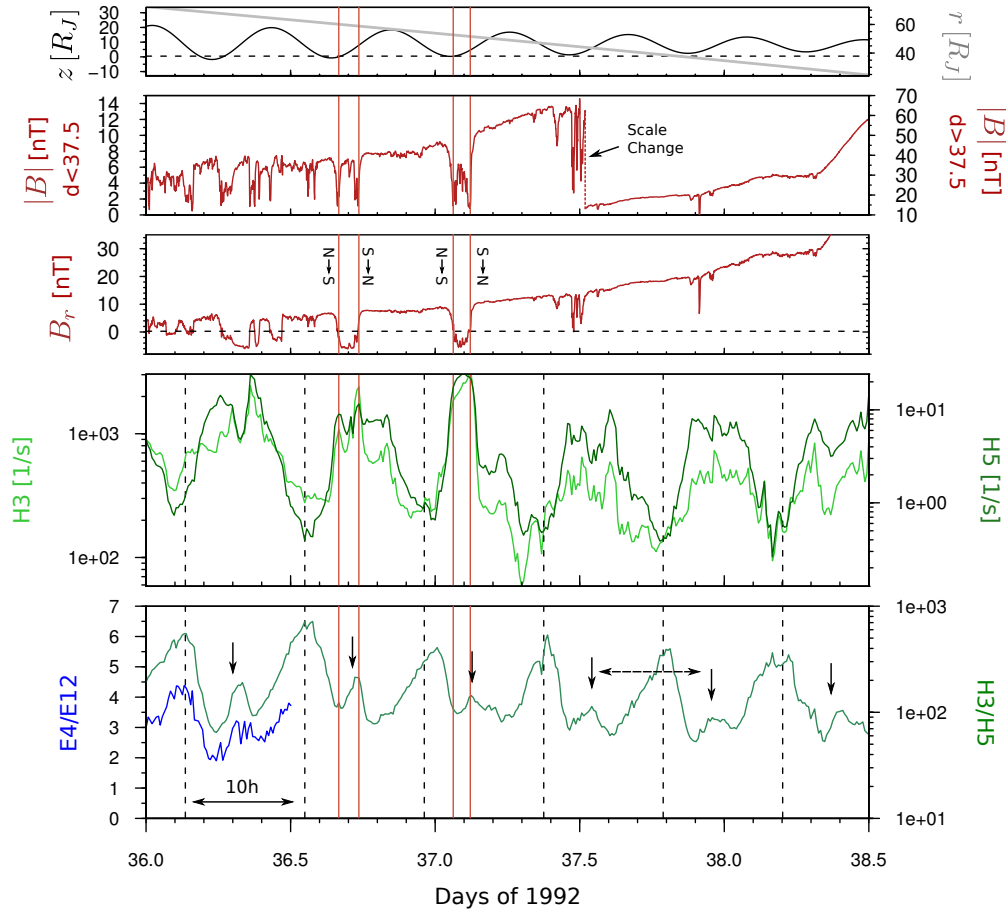


**Figure 7.4:** Same as the previous Figure, but for the time interval from day 36.0 to 38.5. The black dashed lines indicate the major peaks and the black arrows the minors being in phase with Fig. 7.3. As the spacecraft approaches the planet, the magnet field becomes more and more structured ( $>$  day 36.5) and four current sheet traversal can be identified (Krupp et al., 1993). These transitions are indicated by the red solid bars and are characterized by a drop in the magnetic field strength  $|B|$  and an inversion of the direction of the radial component  $B_r$ . Note that the minor peaks are in good correlation with the spacecraft's traversal across the current sheet from South to North. Pay attention to the scale change in  $|B|$  at day 37.5.

According to Simpson et al. (1992b) the H3 and H5 channels of the HET were used. These channels, primarily intended for counting protons in a range of energy from 24-31 and 68-92 MeV, are also sensitive to electrons from 3-5 and 10-16 MeV, respectively. The benefit of using these channels instead of dedicated electron channels is a better prevention of instrumental overflow. During the spacecraft traversal through Jupiter's magnetosphere, H3 and H5 predominantly counted electrons.

Considering the magnetic field data, no clear structure is evident, indicating a highly disturbed orientation of the field in the outer magnetosphere. An investigation of the E4/E12 and H3/H5 ratios, however, reveals a consistent pattern of recurrent variations of the energy spectrum with a periodicity of 10 h as indicated by the dashed solid lines being aligned with the maxima of the ratio. The markers are 9h55min apart from each other. Comparing the temporal evolution of the ratios with the corresponding counting rates of the HET instrument, it becomes evident that both quantities are anti-correlated, i.e. the counting rates tend to increase when the ratio decrease and vice versa. This finding had already been discussed in previous publications, e.g. by Simpson et al. (1992b). However, besides the large peaks, denoted as “major peaks” in the following, peaks of much smaller amplitudes can be identified in the timeseries and are indicated by the black arrows in the bottom panels. An interesting feature of these “minor” peaks is the fact that they occur when the flux level is generally high, but during local minima, i.e. during short-term decreases of the electron counts. This behavior strongly resembles the major peaks. The dotted lines in the panel showing the HET counting rates are positively shifted by 3.25 h with respect to the dashed lines and indicate the local counting rate minima. This shift will be further quantified in the following section when the data will be further discussed with respect to timeseries analysis methods. Nevertheless, it can be noted that the phase difference between the major and minor peaks is not a symmetric behavior since this would imply a phase shift of  $\sim 5$  h. Comparing the occurrence of the minor peaks with the distance from the nominal current sheet<sup>2</sup>, one observes that they generally occur when the spacecraft is located close to the current sheet, i.e. not at high magnetospheric latitudes.

The subsequent Fig. 7.4 covers the time interval from day 36-38.5. During this time, the spacecraft was mainly located in the middle magnetosphere and the presence of the Jovian current sheet can clearly be seen by the four current sheet crossings indicated by the red solid lines (dates taken from Krupp et al. (1993)). These two pairs of crossings from the Northern hemisphere to the South and back are roughly 10 h apart. While these events indicate full current sheet crossings as can be seen by the inversions of the direction of the radial component  $B_r$ , at least three current sheet approaches can be observed as the spacecraft approaches the planet, e.g around day 37.5. These events are characterized by sudden increases in the magnetic field magnitude and radial component, although the polarity does not change. The charged particle data plotted in this Figure are again the counting rates of the HET H3 and H5 channels as well as their ratio and the ratio of the KET E4 and E12 channels. Due to the prevention of possible damages, the photomultiplier of the KET were switched off on day 36.5, i.e. the instrument was not in full operational mode. The dashed solid lines and the arrows indicating the major and minor peaks respectively, are in phase with the markings of Fig. 7.3. Comparing the minor peaks and the magnetic field data during the two pairs of current sheet crossings, an interesting observation is the fact that the peaks are

---

<sup>2</sup>As will be discussed later, the nominal and the actual location of the Jovian current sheet may differ significantly.

in very good coincidence with the spacecrafts crossing from the Southern magnetic hemisphere towards the Northern hemisphere. This suggests that the minor peaks are a spatial effect in more ways than one. On the one hand, the correlation with the current sheet implies that these events are confined to the magnetic equator. On the other hand, an intrinsic longitudinal asymmetry of the electron distribution must be present, since it is unreasonable to assume that the spacecraft should measure different charged particle properties depending on the sense of motion across the current sheet, given that the particles are almost equally distributed around the sheet. These “minor peaks” in the MeV-electron spectrum were previously only mentioned as a side note in Anagnostopoulos et al. (1998) when investigating the temporal behavior of ions close to Jupiter without taking into account magnetic field measurements. The next section will elaborate the findings presented here in more detail, before the Pioneer 10/11 data will be analyzed with respect to the insights drawn from the Ulysses measurements.

### Time Series Analysis of Ulysses Inbound Data $> 60 R_J$

The first analysis technique applied to the HET/KET data during the spacecraft’s inbound passage will be the Lomb-Scargle periodogram that has been described in chapter 5. Fig. 7.5 shows the result of the Lomb analysis of the E4/E12 (left) and H3/H5 (right) ratios during the time interval from day 34 to 36.5. The abscissa represents the period, i.e the reciprocal of the frequency, and the ordinate the corresponding wave power. Clear peaks at 5 and 10 h can be identified in the periodograms. While the prominent 10 h peak doubtlessly refers to the “clock” mechanism, there is reason to assume that the second peaks is related to the minor peaks. As can be seen in the plots showing the time series of the KET and HET data, the difference between the major peaks is  $\sim 10$  h. The same is true for the minor peaks, while the gap between the majors and minors is about 3.25 h. That means, two independent 10 h periodicities are observed. However, the sum of two sines of equal frequency but different phase results in a single sine function of the same frequency, because

$$\sin(\alpha + \varphi_0) + \sin(\alpha + \varphi_1) = 2 \sin\left(\alpha + \frac{\varphi_0 + \varphi_1}{2}\right) \underbrace{\cos\left(\frac{\varphi_0 - \varphi_1}{2}\right)}_{\text{constant}}. \quad (7.5)$$

On the other hand, the observed temporal behavior can be described by

$$\sin(2\pi f x) + \sin^2(2\pi f(x - \varphi)) = \sin(2\pi f x) + \frac{1}{2}(1 - \cos(2(2\pi f(x - \varphi))))), \quad (7.6)$$

leading to the superposition of a sine with frequency  $f$  and a cosine with frequency  $2f$ . Depending on the phase difference  $\varphi$  and amplitude, the resulting curve shows major peaks with shifted minor peaks. Based on this result, the 5 h peak in the spectrogram can be explained in this terms.

Some more attention is required in interpreting the results of the inbound Lomb-Scargle analysis. The additional frequency found in the spectrum beside the expected



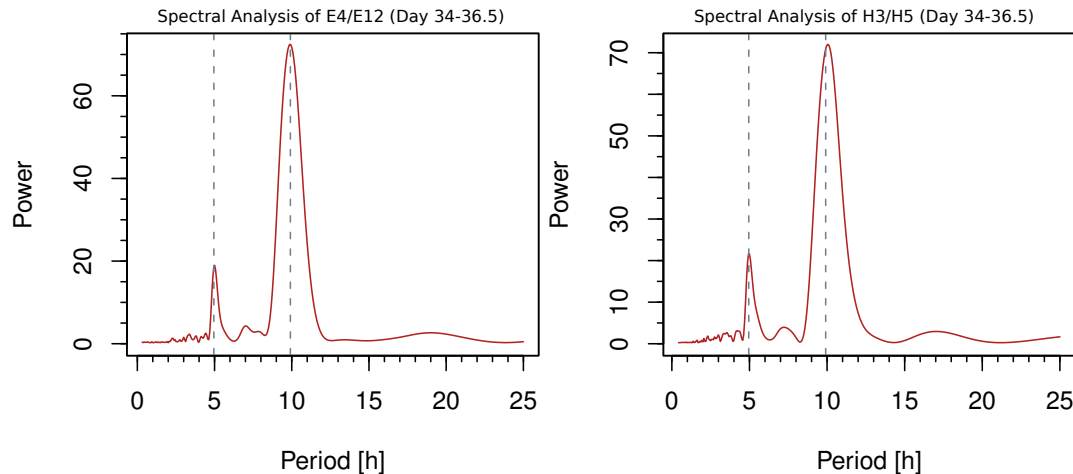


**Figure 7.5:** Lomb-Scargle analysis of the E4/E12 (left) and the H3/H5 ratio (right), during the time period when Ulysses was located in the outer magnetosphere during the spacecraft’s inbound pass. As can be seen, the spectral analysis reveals the existence of a 10 h periodicity, as well as a prominent peak at 5 h for both instruments.

10 h periodicity occurs at 5 h, i.e. two times the principal frequency. While the spectral analysis of a pure sine function leads to a single frequency, the analysis of a non-sinusoidal function leads to a set of additional frequencies besides the fundamental one. The sawtooth function, for instance, is represented by the Fourier series

$$y(x) = \frac{2}{\pi} \sum_{n=1}^{\infty} (-1)^{n+1} \frac{\sin(2\pi n f x)}{n}. \quad (7.7)$$

As can be seen, beside the fundamental frequency  $f$ , odd and even harmonics  $n \cdot f$  with amplitudes  $A_n \propto 1/n$  are present and necessary for the construction of the function. To investigate the question how much wavepower is due to the presence of the minor peaks, two tests were applied.

(i) In a first step, the time intervals including the minor peaks were defined and the corresponding data removed from the time series. If  $T_c$  denotes the full time interval,  $T_g$  contains those subintervals, i.e.  $T_g \subset T_c$ . The next step consists of a reconstruction of these artificial data gaps using splines (Press et al., 1992) and adding white noise.

(ii) Instead of filling the data gaps by using splines, all elements of  $T_g$  were set to a constant value, i.e.  $t = 1$  for all  $t \in T_g$ .

The corresponding time series and the results of the Lomb-Scargle analysis is shown in Fig. 7.6. As can be seen, for both methods to eliminate the minor peaks, the wavepower at  $\sim 5$  h is reduced. However, the signal does not fully disappear. This is an expected result, because the curve resulted from method (i) is still no pure sine and for method (ii) similar arguments as for the sawtooth function apply. The Fourier

series of the function

$$y(x) = \begin{cases} \sin(x) & \text{if } \sin(x) > 0 \\ 0 & \text{if } \sin(x) \leq 0 \end{cases} \quad (7.8)$$

reads

$$y(x) = \frac{1}{\pi} + \frac{1}{2} \sin(x) - \frac{2}{\pi} \sum_{n=1}^{\infty} \frac{1}{4n^2 - 1} \cos(2nx), \quad (7.9)$$

i.e. additional frequencies at  $2 \cdot n$  with amplitudes  $A_n \propto 1/(4n^2 - 1)$  occur. The

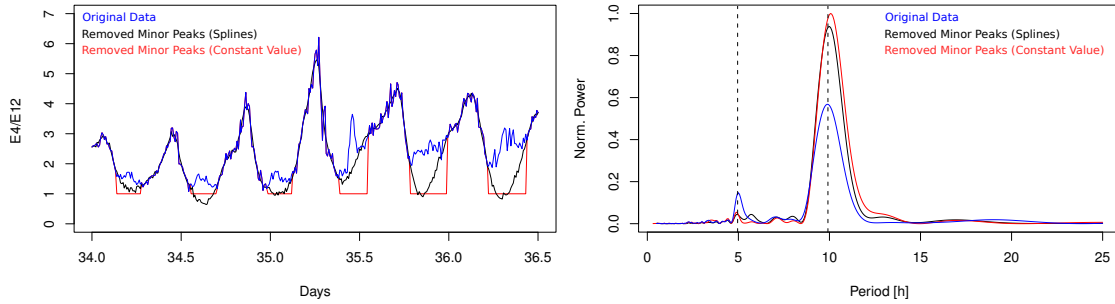


**Figure 7.6:** Left: The original time series of the E4/E12 ratio is shown by the blue curve. For the other curves, the minor peaks were removed and substituted by a spline fit + noise (black) and a constant value (red). Right: The result of the Lomb-Scargle analysis applied to the three data sets. The wavepower at 5 h decreased for the two modified data sets.

lack of a well pronounced 5 h periodicity or a significantly decreased amplitude, respectively, support the conclusion that the additional peak in the periodogram of the original data is mainly due to the presence of the minor peaks. To verify this result, a correlation analysis was applied to the data sets. Fig. 7.7 shows the result of an auto correlation analysis of H5 and H3 data measured between day 34 and 36, i.e. during the spacecraft's path through the outer magnetosphere. The abscissa shows the time lag<sup>3</sup> in hours and the ordinate the corresponding  $r$ -value. It can be seen that the 10 h variation of the counting rates can be recovered in this analysis of H5, as indicated by the recurrent peaks of positive or negative correlation coefficients every 10 h, marked by the solid and dashed vertical lines. However, further peaks can be observed between those related to the prominent 10 h variation, tagged by the dotted vertical lines. These peaks occur  $\sim 3.25$  h before and after the larger 10 h peaks. This time difference corresponds to the time interval between the double peaks of the principal flux enhancements, giving further evidence that this is a systematic effect. The analysis of H3, however, shows no clear modulation like H5. This suggests, that

<sup>3</sup>Although the nominal time resolution of the data is 10 mins, the actual length of the sampling intervals may vary. To take this into account, the mean accumulation time was used to calculate the lag sequence.

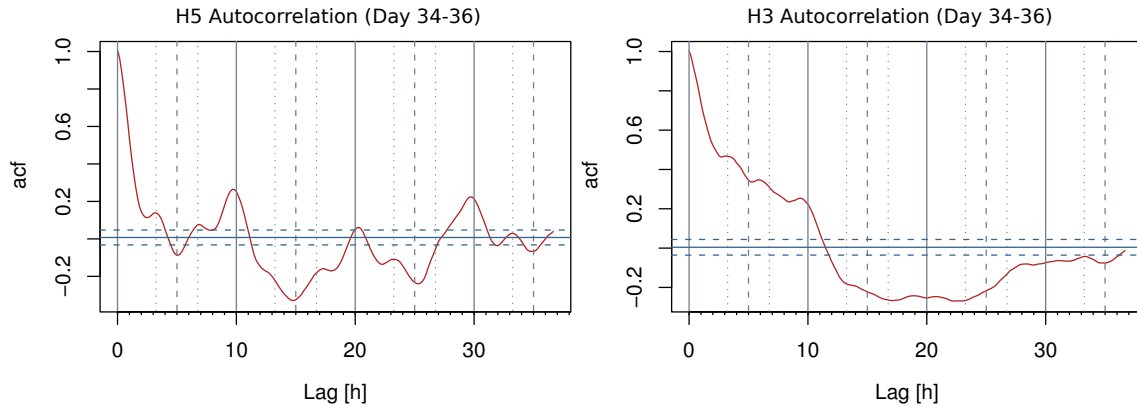


**Figure 7.7:** Left: The autocorrelation of H5 indicates the  $\sim 10$  h periodicity (solid vertical lines), but also a second temporal variation as shown by the dotted vertical lines. These peaks are shifted by  $\pm 3.25$  h with respect to the major 10 h peaks. Here, a confidence level of 50% is shown (dashed horizontal lines). Right: Same analysis, but for H3. No clear modulation is present, suggesting that the spectral rocking is mainly due to the higher energy channel.

the spectral rocking is mainly related to periodic variations of H5, i.e. the channel of higher energies, as well as a larger stationarity of the H5 channel. Indeed, visually investigating the H3 and H5 counts in Figs. 7.3 and 7.4, the H5 channel tends to be better pronounced with respect to the amplitude of its temporal variations.

Considering the electron spectral index, the H3/H5 and E4/E12 ratio were analyzed using the ordinal correlation method discussed in chapter 5. As can be seen in Fig. 7.8, the HET and KET data from day 34-36.5 not only show the presence of the primal 10 h periodicity, but also a periodic pattern of secondary peaks. The peaks are phase shifted by  $\pm 3.25$  h with respect to the 10 h peaks.

As noted before, the major peaks in the spectral index of the electrons is expected when  $\lambda_{III} = 240 - 310^\circ$  faces the subsolar point. Since at least in the outer magnetosphere, the minor peaks trail the major peaks by 3.25 h, this directly suggest that the minor peaks are also confined to a defined longitudinal range.

## 7.5 Ulysses Outbound Observations

Since the Pioneer 11 mission, it is known that the 10 h spectral rocking (the major peaks) can also be observed at high magnetic latitudes. This finding has impressively be confirmed by Ulysses during its unique trajectory at very high magnetospheric latitudes after the closest approach (Simpson et al., 1993). The minor peaks, however, attributed to the current sheet as shown above, are expected to be absent during Ulysses departure far from the planet. An overview of the outbound passage from day

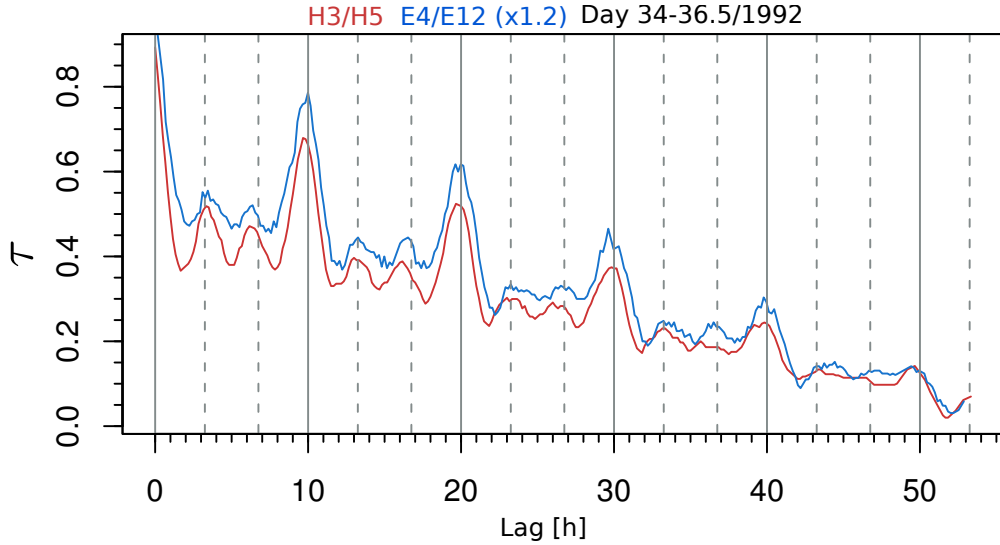


**Figure 7.8:** Kendall's correlation function with delay  $d = 5$  for the H3/H5 (red) and E4/E12 (blue) ratios. Both curves indicate the 10 h periodicity as well as side peaks shifted 3.25 h or 10-3.25 h with respect to the 10 h peaks (gray dotted lines). This finding is in good agreement with the result of the analysis of the H5 counting rates.

40 to 45 is shown in Fig. 7.9 in the same format as the previous Figures.

Comparing the counting rates of H3 and H5 from day 40 to approx. 42 with the distance from the magnetic equator  $z[R_J]$ , it becomes evident that the electron flux is controlled by the proximity to the current sheet, as it has also been reported from low energy particle observations (Lanzerotti et al., 1993), although no actual crossings of the sheet are observed. For days 40-42, a clear identification of periodic patterns in the H3/H5 ratio is hard, however, the large peak at day 40.3 is in phase with the 10 h ticks of the inbound time interval.

From day 42 to mid-43 Ulysses visited a region identified as a high latitude boundary layer (HLBL) of energetic particles at high latitudes by Krupp et al. (1999) and further elaborated by Anagnostopoulos et al. (2001) and Marhavilas et al. (2004) (The existence of such a layer was already speculated by Fillius et al. (1975)<sup>4</sup>). The investigation of the HET counting rates in this time period reveals that the general flux level in this layer is higher than the flux minima from day 40 to  $\sim 42$ , i.e. the green area in Fig. 7.9. As can be seen, the minimum electron flux (related to the maximal distance to the magnetic equator) before day 42 is significantly lower than the flux after day 42. Assuming that the current sheet is the only reservoir of particles in the magnetosphere, one would expect that the general flux level, especially the minima

<sup>4</sup> "... the Pioneer 11 data imply a latitude profile that initially decreases from a maximum at the equator, goes through a minimum, and then increases to a greater maximum at higher latitudes before dropping off again."

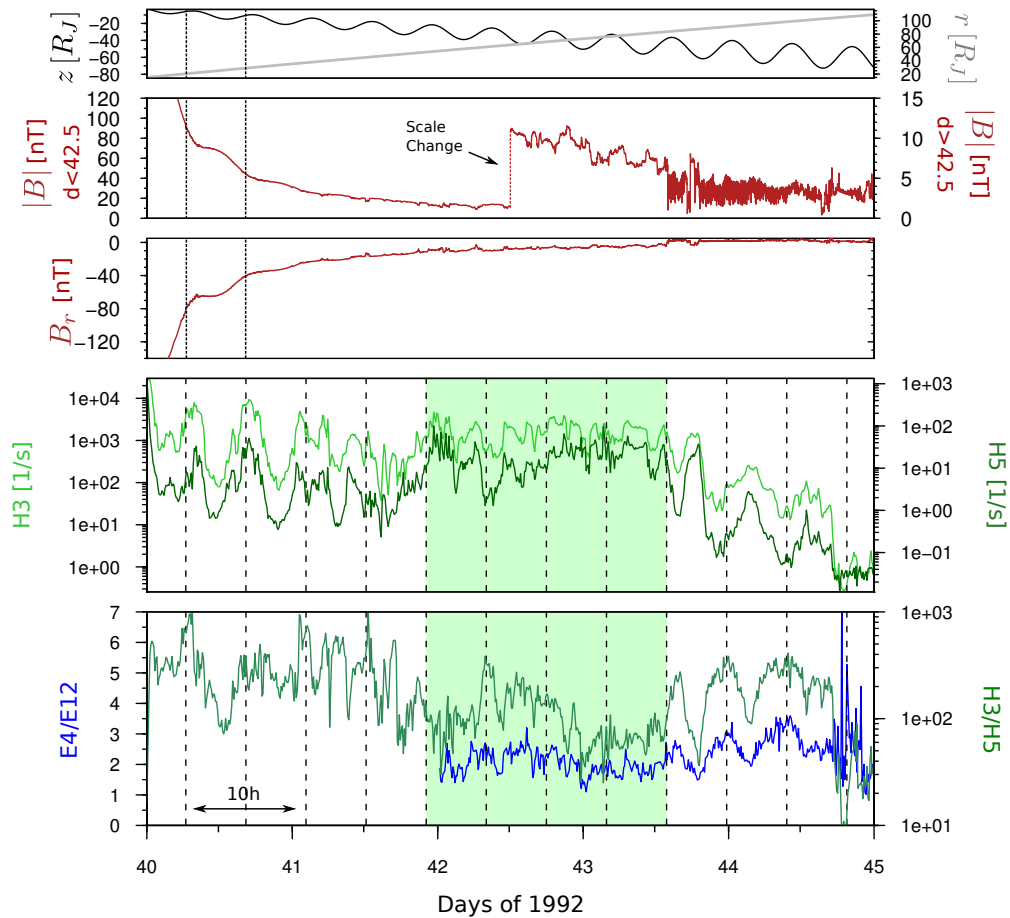


**Figure 7.9:** After the closest approach, Ulysses rapidly descended to Southern latitudes. Three regions can be distinguished during this time period: The first region from day 40-42 is characterized by a 10 h pattern in the counting rates, but an unstructured behavior of the energy spectra. The time profile of the counting rates is related to the proximity to the current sheet. The second time period was identified as the so-called High Latitude Boundary Layer (green shaded area), a region of enhanced particle density. Right after the passage of this layer, the 10 h rocking of the energy spectrum reappears in conjunction with an anticorrelation variation of the counting rates. Note that during this time, the 10 h ticks of the inbound still match the peaks during the outbound passage.

decrease with increasing distance from the planet. However, the opposite is observed. This is an important finding because it confirms that the HLBL is also populated by relativistic electrons of several MeV. With the spacecraft's entrance into the magnetosheath around day 44, the counting rates decrease with increasing distance from the planet. Simultaneously, the counting rates as well as the H3/H5 and E4/E12 ratio

show a well pronounced 10 h periodicity. By comparing the dashed vertical lines with the time profiles of the counting rates before and after the high latitude boundary layer, we find a phase shift of  $\sim 5$  h in the data: The current sheet associated flux increases are correlated with a) the distance to the current sheet and b) the phase of the 10 h periodicity indicated by the arrows. After day 44, however, the arrows are in phase with the counting rate minima. The flux ratio, on the other hand, is anticorrelated with the counting rate maxima. This modulation is not a direct effect of the proximity to the current sheet, because Ulysses was already located in the magnetosheath at a distance  $< 40R_J$  from the magnetic equator and a radial distance of  $> 60R_J$ . Comparing the nominal distance from the magnetic equator with the counting rates or the spectral index, it is hard to judge by eye whether these quantities are positively or negatively correlated (or uncorrelated) as can be seen in Fig. 7.10, showing from top to bottom the distance from the magnetic equator in Jovian radii, the H6/H7 ratio and the H7 counting rates. This Figure covers the time interval from day 43.9 to 44.7. While the counting rates and the spectral index are reasonably anticorrelated (the linear correlation coefficient is  $r(\lg H7, \lg(H6/H7)) = -0.742$ ), there is no reasonable correlation between the distance from the nominal magnetic equator and the counting rates and the spectral index. The calculated correlation coefficients are  $r(\lg H6/H7, Z_{dpl}) = 0.3129$  and  $r(\lg H7, Z_{dpl}) = -0.039$ , respectively. However, it may be argued that the counting rate maxima are related to the closest approach to the HLBL, because an enhanced particle flux was found there, what would require a significant phase shift between the motion of the nominal magnetic equator and the periodic up and down motion of the high latitude boundary layer. The energy spectrum is found to be hardest when the flux is minimal during this time period, being in principal agreement with the spectral index in the HLBL. In particular the E4/E12 ratio in Fig. 7.9 indicates a smaller spectral index inside the HLBL than outside. This interpretation is closely related to the suggestions of Marhavilas et al. (2004), even if there is no indication for such a modulation in the respective time interval in the HI-SCALE ion data. On the other hand, the major peaks during inbound are associated with the excursions of the spacecraft to higher magnetic latitudes (Anagnostopoulos et al., 1998), i.e. a softening of the spectrum is observed when Ulysses approaches the HLBL. This is a critical point, because Simpson et al. (1992b) found the rocking of the spectrum to be in phase during inbound and outbound, while the response of the spectral index to the approach to the HLBL is opposite. Assuming that the up and down motion of the HLBL is coupled with the up and down motion of the magnetic equator, i.e. the modulation of the spectral index observed by spacecraft is spatial, it is not directly clear how this explains that the spectral variation of Jovian electrons does not depend on the hemisphere or local time inside or outside the magnetosphere. We tentatively suggest a HLBL which motion is not directly related to the cyclic up and down motion of the magnetic equator, but responds somewhat globally to the rotation of the “active” region of Vasyliunas and Dessler (1981).

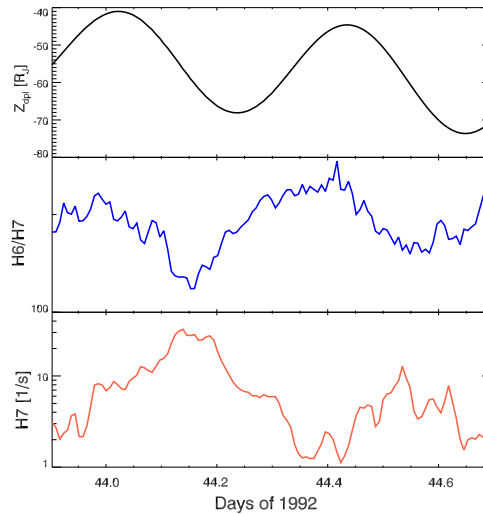


**Figure 7.10:** From top to bottom: the distance from the magnetic equator in Jovian radii, the H6/H7 ratio and the H7 counting rates. While the counting rates and the spectral index are anticorrelated, there is a phase shift between the nominal distance from the magnetic equator ( $Z_{dpl}$ ) and the counting rates and the spectral index.

## 7.6 Results from the Pioneer spacecraft

After having shown that a second periodic modulation in the spectral index (and counting rates) beside the famous “clock” phenomenon can be identified in the Ulysses data, suggesting a connection to the current sheet, the question is if the Pioneer 10/11 data show the same kind of modulation. For the analysis we make use of the id4 (2-7 MeV) & id5 (6-28 MeV) electron channels introduced in chapter 5.

Fig. 7.11 shows Pioneer 10 measurements in the same format as the previously shown Ulysses data. The shown time interval spans from day 331.5 to 336 in 1973, i.e. from the entry into the magnetosphere up to a distance from the planet of about 40 Jovian radii. At a first glance, the periodic rocking of the spectral index (i.e. the id4/id5 ratio) is clearly visible being anti-correlated with the counting rates. The dashed vertical lines are 9h55m apart and indicate the 10 h variation. While this is well known, local minima in the counting rates of channel id5 can also be identified on top of the global maxima. These minima are indicated by dotted lines. These markers are also 9h55m apart, but phase shifted by 3.25 h with respect to the dashed lines. Note, however, that these “valleys” are somewhat weaker pronounced than the ones observed by Ulysses. Comparing the counting rates with the associated spectral index, consistent evidence for minor peaks is barely visible over the full time interval. However, at least a couple of enhancements of the id4/id5 ratio that can be treated as minor peaks are visible. The first one occurs around day 333.4, followed by a well pronounced peak 10 h later on day 333.8. Two more minor peaks may be identified at

day 334.04 and 334.45.

To further analyze the data, the following Fig. 7.12 shows the results of correlation analysis of the Pioneer 10 electron data. Here, the time period under investigation had been splitted into two sub intervals. The first one spans the interval from day 332 to 333.5, the second one from day 333.5 to 336. The panels on top refer to the first

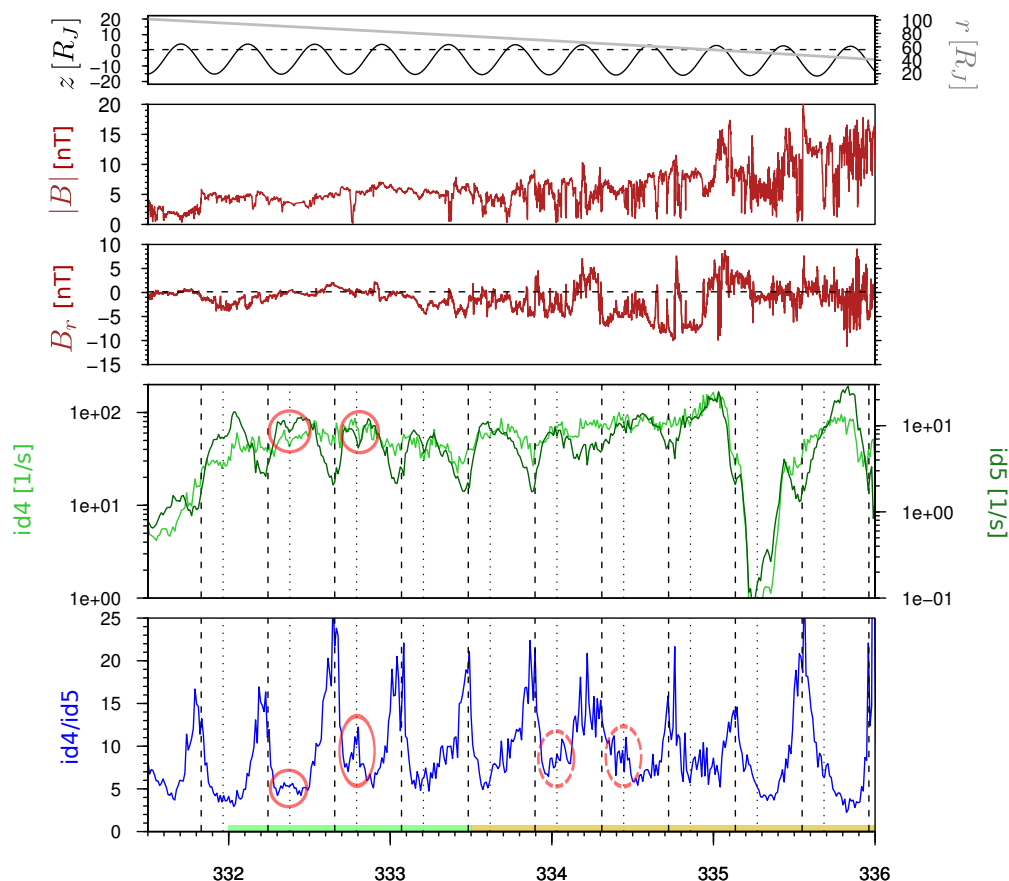


**Figure 7.11:** Measurements of Pioneer 10 in the same format as the Ulysses plots. The shown time interval spans from day 331.5 to 336 in 1973, i.e. from the entry into the magnetosphere up to a distance from the planet of about 40 Jovian radii. The large peaks in the spectral index are indicated by the dashed lines which are 9h55m apart. The dotted lines trail the dashed ones by 3.25 h. The green and yellow boxes on the bottom indicate the time intervals used for the correlation analysis. The solid circles mark local minima in the flux and minor peaks in the spectral index. The dashed circles denote the questionable events.

time interval, the bottom panels to the second. While the 10 h periodicity can be well identified in the id5 and id4/id5 data for both time intervals, there is evidence for the presence of minor peaks during the first time interval.



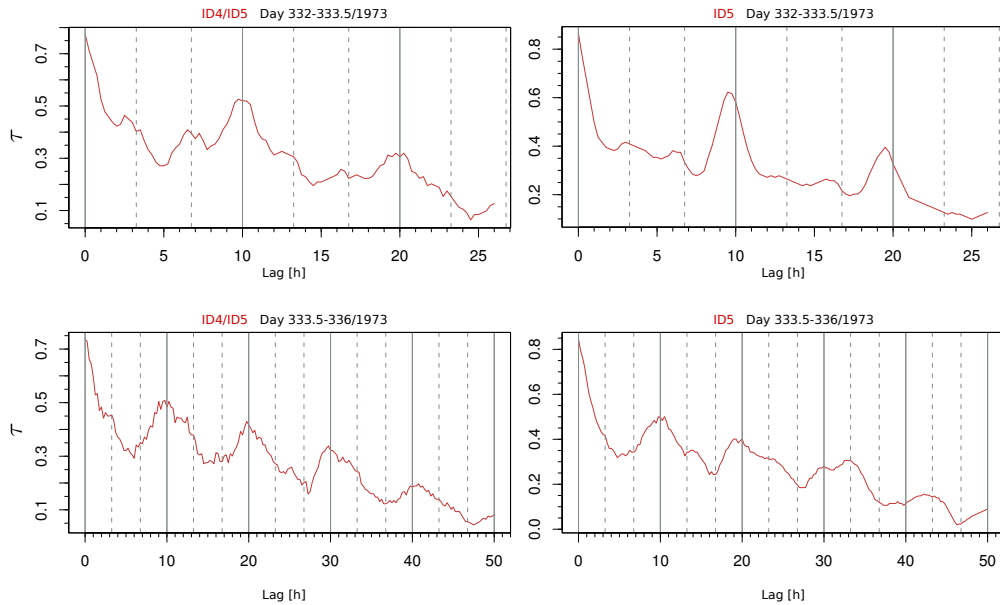


**Figure 7.12:** Kendall's correlation analysis for the Pioneer 10 id4/id5 ratio (left) and the id5 channel (right) for the two time intervals (top and bottom) defined in the previous Figure. The major 10 h peaks can well be identified. However, there is also some evidence for the existence of minor peaks shifted 3.25 h with respect to the majors in the first time interval. These peaks are much less pronounced than those found in the Ulysses data, reflecting the visual impression of Fig. 7.11. During the time interval from day 333.5 to 336, there is no satisfying evidence for minor peaks.

The same methods applied to the Ulysses and Pioneer 10 data were also used for an investigation of the Pioneer 11 data during the spacecraft's Jupiter flyby. Fig. 7.13 shows the same quantities as the corresponding Pioneer 10 data, i.e. the magnitude and  $B_R$  component of the magnetic field, the id4 and id5 counting rates as well as their ratio as a proxy to the spectral index. The magnetic field shows periodic approaches to the Jovian current sheet in good correlation with the nominal distance of the spacecraft to the magnetic equator (black curve in the top panel). While there is evidence for the presence of the well known 10 h modulation in the counting rates as well as in the spectral index (indicated by the dashed vertical lines), there is no indication for minor peaks. The dotted lines in the Figure denote the points in time where the minor peaks are expected according to the Ulysses and Pioneer 10 data. In agreement with this visual impression, the corresponding correlation analysis of the id4 counting rate shown in Fig. 7.14 reveals no evidence for the existence of minor peaks in the data.

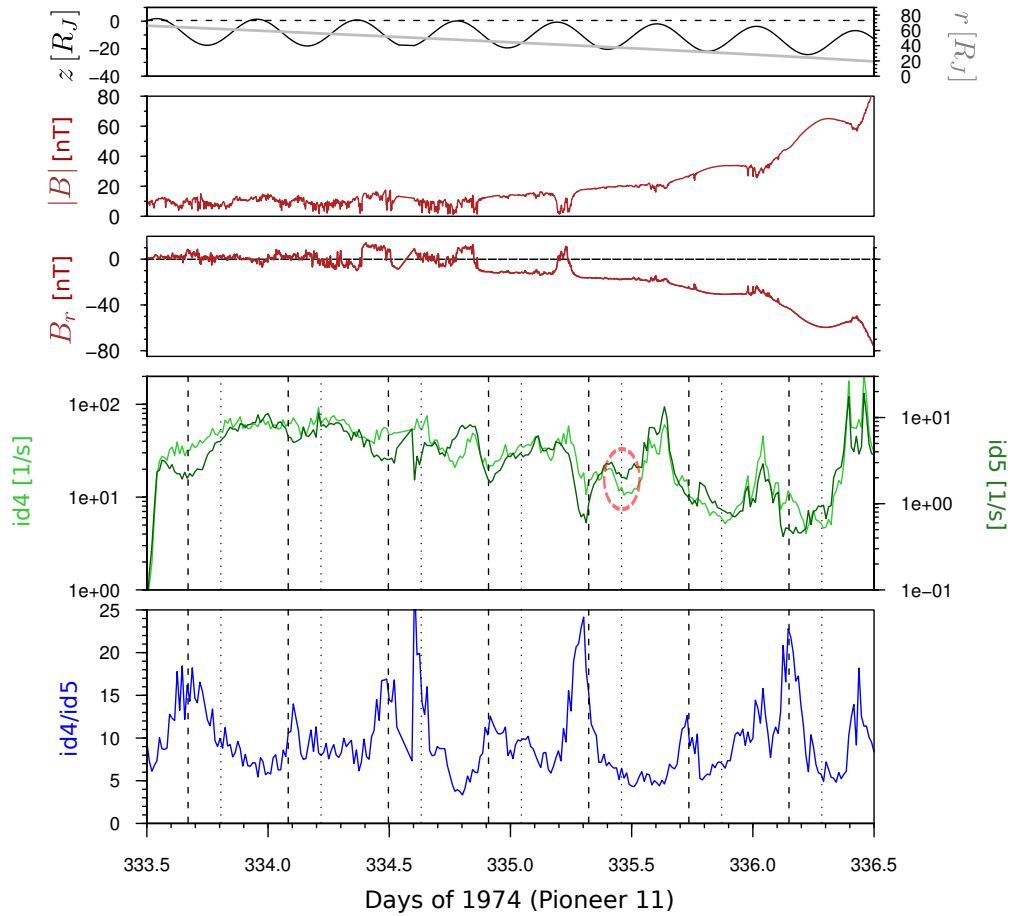


**Figure 7.13:** Same as Fig. 7.11 but for inbound trajectory of Pioneer 11 from day 333.5 to 336.5 in 1974. While there is evidence for the major 10 h periodicity, no evidence for minor peaks can be found in the data. Note, however, the counting rate depression just on day 335.5 marked by the dashed circle. This local minima occurs at the predicted time and resembles Ulysses and Pioneer 10 observation but is not accompanied by a local maxima of the  $id4/id5$  ratio.

## 7.7 Interpretation and Consequences

The purpose of this chapter was twofold: The KET/HET data had been reanalyzed with respect to previous results from the HI-SCALE instrument (Marhavilas et al., 2004) aboard Ulysses with respect to the “clock” phenomenon of MeV electrons in the Jovian magnetosphere. On the other hand, the finding of a second, less well pronounced periodic modulation was discussed. The analysis of the Ulysses data strongly suggests a connection to the magnetospheric current sheet, i.e. particles located at low magnetic latitudes. Furthermore, a comparison with the spacecraft’s transition across the current sheet revealed the existence of a longitudinal asymmetry with a maximum

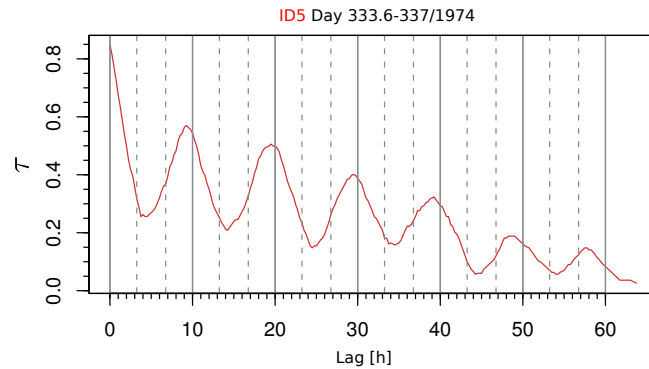


**Figure 7.14:** Kendall's correlation analysis for the id5 energy channel of Pioneer 11. Apparently, no evidence for minor peaks is present in the data.

of the spectral index between  $\lambda_{III} = 40 - 80^\circ$ . An re-investigation of the Pioneer 10 and 11 data with respect to this finding showed that there is evidence for this kind of modulation in the Pioneer 10 data, albeit not as well pronounced as in the case of Ulysses and not for the entire inbound trajectory. For the case of Pioneer 11, no indications for minor peaks could be found in the data. Why is this the case? To elaborate this question, the trajectories of the three spacecraft as a function of System III longitude and distance from the magnetic current sheet will be investigated. Fig. 7.15

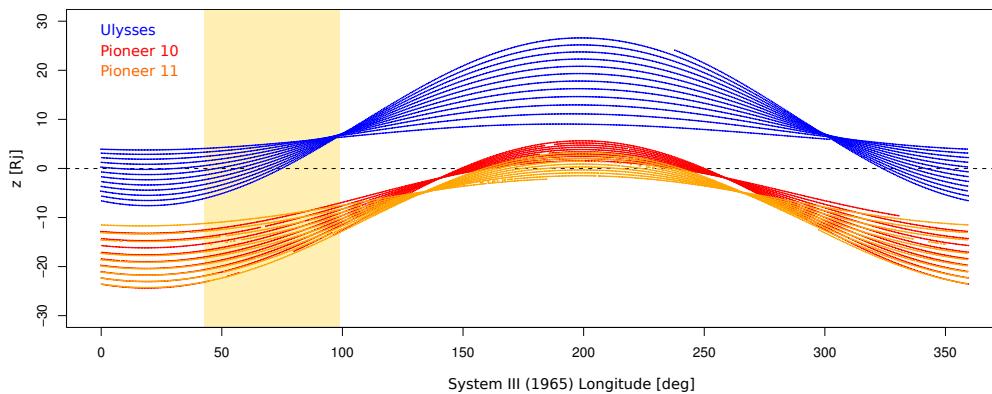


**Figure 7.15:** This Figure shows the distance from the Jovian current sheet (in Jovian radii  $R_J$ ) as a function of System III (1965) longitude for Ulysses, Pioneer 10 and 11. As can be seen, Ulysses was much closer located to the magnetic equator when the minor peaks in the spectral index are expected than the Pioneers. The yellow area indicates the approximate interval during which the minor peaks occur including their rise and decay.

shows the distance from the magnetospheric current sheet (in Jovian radii) of Ulysses and the two Pioneers as a function of the System III (1965) longitude for the inbound

trajectories. The distance from the sheet was computed by  $z = r \sin(\theta)$ , where  $r$  is the distance from the planet and  $\theta$  the spacecraft's latitude, i.e.  $z$  is the distance normal to the current sheet. The yellow area indicates the approximate interval during which the minor peaks occur including their rise and decay. Comparing the traces of the three spacecraft it becomes evident, that Ulysses stayed close to the current sheet during times, the longitudinal region in which the minor peaks of the spectral index are expected. The Pioneers, on the other hand, were relatively far away from the sheet during the same interval of longitudes. This observation offers an explanation for the difference in the three data sets. The Pioneers probably were too far away from the (nominal) current sheet to see a clear presence of the minor peaks that are a feature of low magnetic latitudes.

# Chapter 8

## Analysis of Jovian Jets

To be absolutely certain about something, one must know everything or nothing about it.

---

Henry A. Kissinger

The observation of planetary particle events started in the mid-1960s with the finding of keV electrons accelerated at the terrestrial bow shock traveling upstream with respect to the solar wind flow direction. Since then, upstream events of positively charged particles and/or electrons are a well-known feature of the interaction between the terrestrial magnetosphere and the interplanetary magnetic field (e.g. Klassen et al., 2008, 2009). These events are generally characterized by rapid increases and decreases of flux as well as streaming directions that frequently deviate from the magnetic field orientation predicted by the Parker model of the IMF. During the approach of spacecraft towards the planet Jupiter, ion events strongly resembling those observed at Earth were observed (e.g. Krimigis, 1992; Haggerty and Armstrong, 1999). “Jovian jets”, as they will be discussed in the following, are a subset of what may be called planetary particles sources. These events are generally of much higher energies (MeV) than the typical energies of upstream electron events, but share similar properties.

### 8.1 Jovian Jets Observed by Ulysses

In contrast to the finding of a mostly isotropic Jovian electron population in interplanetary space, Ferrando et al. (1993) reported the observation of 35 so-called Jovian electron jets<sup>1</sup> (in the following abbreviated as “Jovian jets” or simply “jets”). While the isotropic part of the Jovian electron population may have already left the magnetosphere without a significant pitch angle anisotropy, these Jovian electron jets are

---

<sup>1</sup>Note that the term “Jovian jet” is also used by planetologist to characterize features of Jupiter’s atmosphere (see e.g. Sánchez-Lavega et al., 2008).

events of short duration (from some minutes up to several hours) and generally show strong particle anisotropies along the magnetic field. An analysis of the Jovian electron flux performed by McKibben et al. (2007) during the second, more distant Jupiter encounter in 2003-2004 revealed a total number of 15 events. The main features of Jovian jets discussed in the cited studies can be summarized as follows:

- The magnetic field observed during Jovian jets is aligned with the viewing direction from the spacecraft to Jupiter.
- Compared to the background Jovian electron flux, the time profiles of Jovian jets are characterized by relatively sharp increases and decreases in flux.
- A significant anisotropy of the particles with respect to the magnetic field is observed during jet events.
- Most jets require a strong deviation from the nominal Parker line of the interplanetary magnetic field, i.e., a temporary deviation from the expected magnetic field is observed in order to magnetically connect the Jovian magnetosphere and the observer.
- Ferrando et al. (1993) noted that the 10 h periodicity of Jupiter's rotation can be recovered during the jet events up to distances of 0.5 AU from the planet. Beside the fact that the local magnetic field vector points to Jupiter, this is another striking evidence that the observed electrons are of Jovian origin.
- McKibben et al. (2007) noted the absence of protons of several MeV during the Jovian jets beside two events.
- There is no clear correlation between flux intensity or anisotropy with respect to distance from the source.
- As it was pointed out by Ferrando et al. (1993) and McKibben et al. (2007), one of the main problems in understanding Jovian electron jets is the deviation from the nominal Parker spiral, especially perpendicular to the ecliptic plane, and the usually sharp time profiles of the events.

Fig 8.1 shows the trajectory of Ulysses (blue curve) during the first and second Jupiter approach, respectively. The coordinate system is a jovicentric one and is defined in a way that the negative x-axis connects the Sun and Jupiter. The axis unit is Jovian radii ( $1 R_J \approx 71492$  km).

In total, 36 jets were observed before and after the flyby of the Ulysses spacecraft in February 1992. Five jets were observed before the flyby and 31 events after the spacecraft had already left the ecliptic plane on its way to the solar South pole. The most distant jet was observed 0.8 AU away from the planet. Note that distance refers to the straight line distance between the spacecraft and Jupiter and is therefore not necessarily the distance along the magnetic field lines.

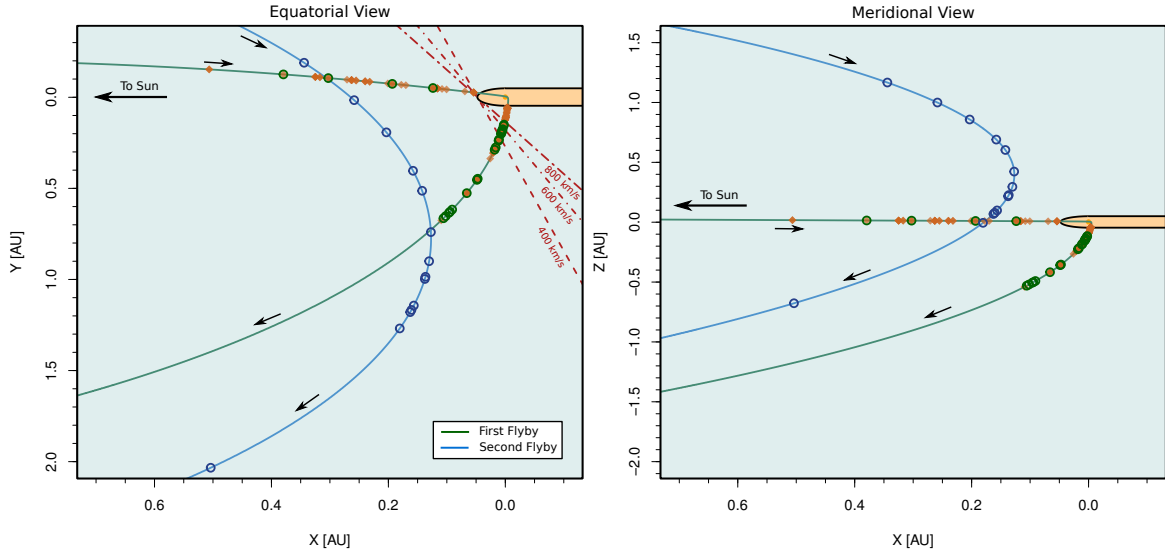


**Figure 8.1:** Trajectory of Ulysses during the first Jupiter flyby in 1991/92 (green curve) and during the second flyby 2003/04 (blue curve) in a Jovicentric coordinate system. The Jovian magnetosphere is indicated assuming a Sunward expansion of  $100 R_j$ . The open circles correspond to the observations of Jovian jets, the orange diamonds to Jovian upstream events (Haggerty and Armstrong, 1999). The dashed red lines in the equatorial view indicate nominal Parker spirals for different solar wind speeds approximated by straight lines.

## 8.2 Investigation of Anisotropies

From the observation of solar events it is well known that particles injected at the Sun may be backscattered as they propagate towards the outer heliosphere as a result of diffusion. However, almost scatter-free propagation of particles is also known, i.e. their motion along the magnetic field line is essentially ballistic. A similar analysis for Jovian jet events has not yet been performed. This question, however, if Jovian jet electrons are affected by pitch-angle diffusion in a way that they may be scattered across  $\mu = 0$  is an important one: how do Jovian jets link to the isotropic Jovian electron population? If Jovian jets show evidence for a significant backscattering, i.e. isotropization and consequently the transition from pitch-angle scattering to full spatial diffusion, this can be seen as a hint that jets contribute to the "quiet time" electron flux observed by spacecraft.

In the following, Jovian jets are analyzed with respect to the temporal evolution of the fraction of particles observed in the pitch-angle half-space pointing to Jupiter and those detected in sectors covering the opposite pitch-angle half-sphere. In order to do so, the techniques described in section 5.5 were applied to the magnetic field data and compared with the counting rates of the eight sector bins of the KET instrument. To obtain a maximum of information, pitch-angle coverages of the specific sectors and

their counting rates as a function of time are plotted. To search for systematic increases or decreases in a sector's counting rates, the temporal evolution of the counting rates during the jet are compared with a baseline derived from the mean value of the counting rates before or after the event. In the following, some examples of events that show considerable, weak or even no evidence for backscattered particles. Fig. 8.2 shows the eight sector counting rates (blue curves) for day 350/2003. The sudden increase of counting rates in sectors 1,2, and 3 starting at 350.7 indicates the occurrence of a Jovian jet. Here, the counting rates are normalized to the respective individual sector. The dark grey shades that belong to each sector represent the pitch-angle interval covered by a sector at a given point in time. The light gray shades additionally take into account the influence of a finite opening angle of the particle telescope. The left ordinates of the panels labeled "PAC" (pitch-angle coverage) indicate the pitch-angle cosine. Comparing the pitch-angle coverage with the corresponding electrons counts, it becomes evident that the electrons come from the positive pitch-angle hemisphere. Investigating the sectors covering the negative (i.e. opposite) pitch-angle domain, there is no evidence for an increase of electrons. To guide the eye, for a time interval before and after the jet, the mean values of the counting rates (black line) and the  $2\sigma$  levels (i.e. two times the standard deviation, plotted in red) were added to the plot. The lack of an electron enhancement in this pitch-angle hemisphere suggests that no particle where scattered across  $\mu = 0$ .

Fig. 8.3 shows the opposite case. Around day 62.5/1992, significant electron increases are evident. However, in this case all sectors simultaneously show an enhanced particle flux. While the majority of particles is observed in sector 7, covering the negative pitch-angle domain close to  $\mu = 1$ , the sectors scanning the positive pitch-angle hemisphere, e.g. sector 3 shows an increase well above the  $2\sigma$  level. This suggests a scattering of electrons coming from Jupiter across  $\mu = 0$ , i.e. they propagate back to Jupiter. This is an important observation, because it shows that the Jovian jet electrons underlay pitch-angle scattering, i.e. they change their initial pitch angle so that the electron ensemble tends to an isotropic state. It is an interesting observation that all flux profiles in Fig. 8.3 are closely correlated. An increase in the flux coming from Jupiter is accompanied by an increase in the backscattering electron population. This observation can be interpreted by assuming that the amount of backscattered particles is proportional to the amount of particles injected into a bundle of magnetic field lines at Jupiter<sup>2</sup>. On the other hand, this observation does not directly suggest a major influence of time on the degree of backscattered particles. In a simple model, the ratio of particles flux  $j$  propagating parallel and anti parallel,

$$r = \frac{\dot{j}_p - \dot{j}_a}{\dot{j}_p + \dot{j}_a}, \quad (8.1)$$

should tend to zero with time if no further injection of particles takes place. On the other hand, a near steady-state condition would result in a constant value of  $r$  in Eqn. (8.1).

---

<sup>2</sup>This implicitly states that the scattering coefficient is not a function of the absolute flux level.



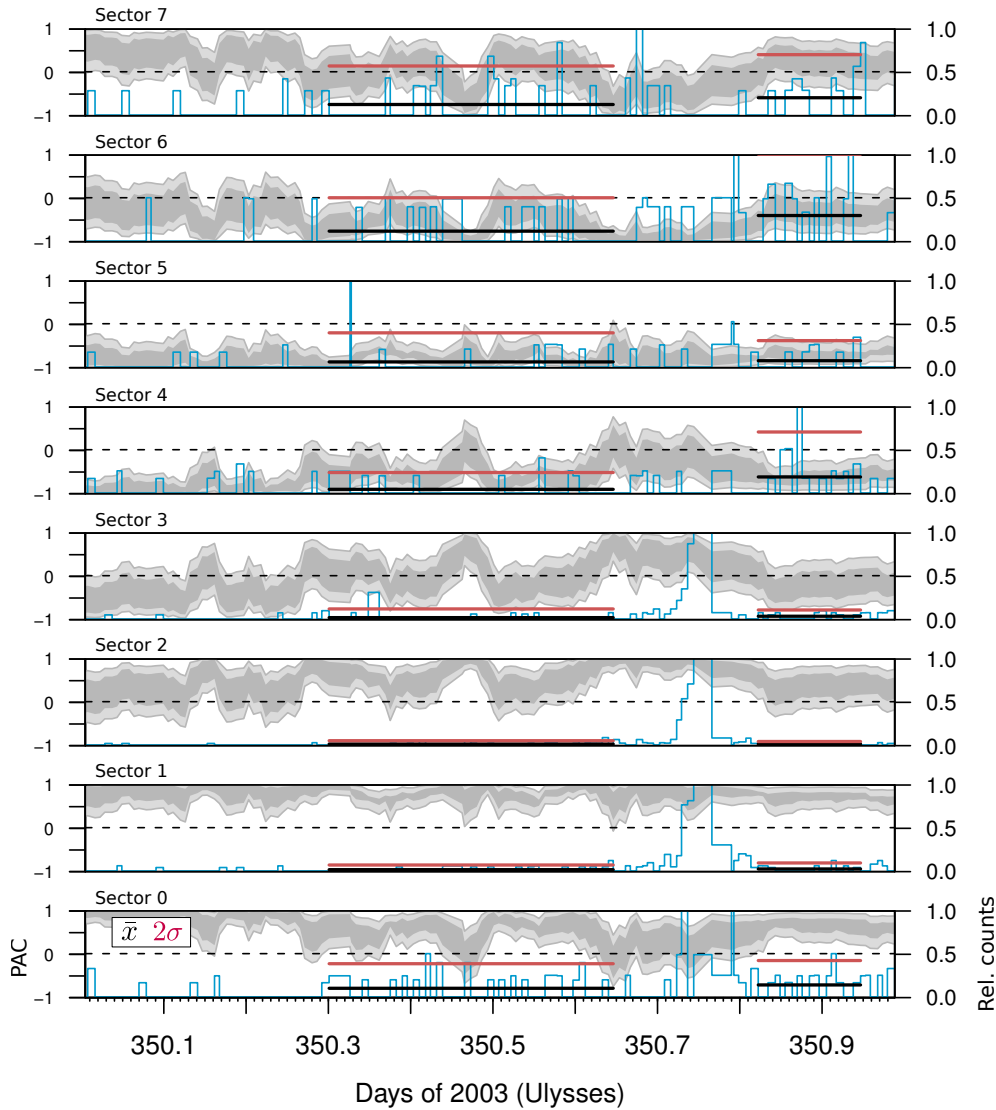


**Figure 8.2:** This example shows an event where no evidence for backscattered electrons can be found. The eight sectors of the KET belong to distinct panels. The gray shaded areas span the pitch-angle space covered by each sector and correspond to the left ordinate (PAC). The black lines indicate the respective mean values of the counting rates, the red one the  $2\sigma$  level. The counting rates in this plot are normalized separately to the maximal counting rate in each sector.

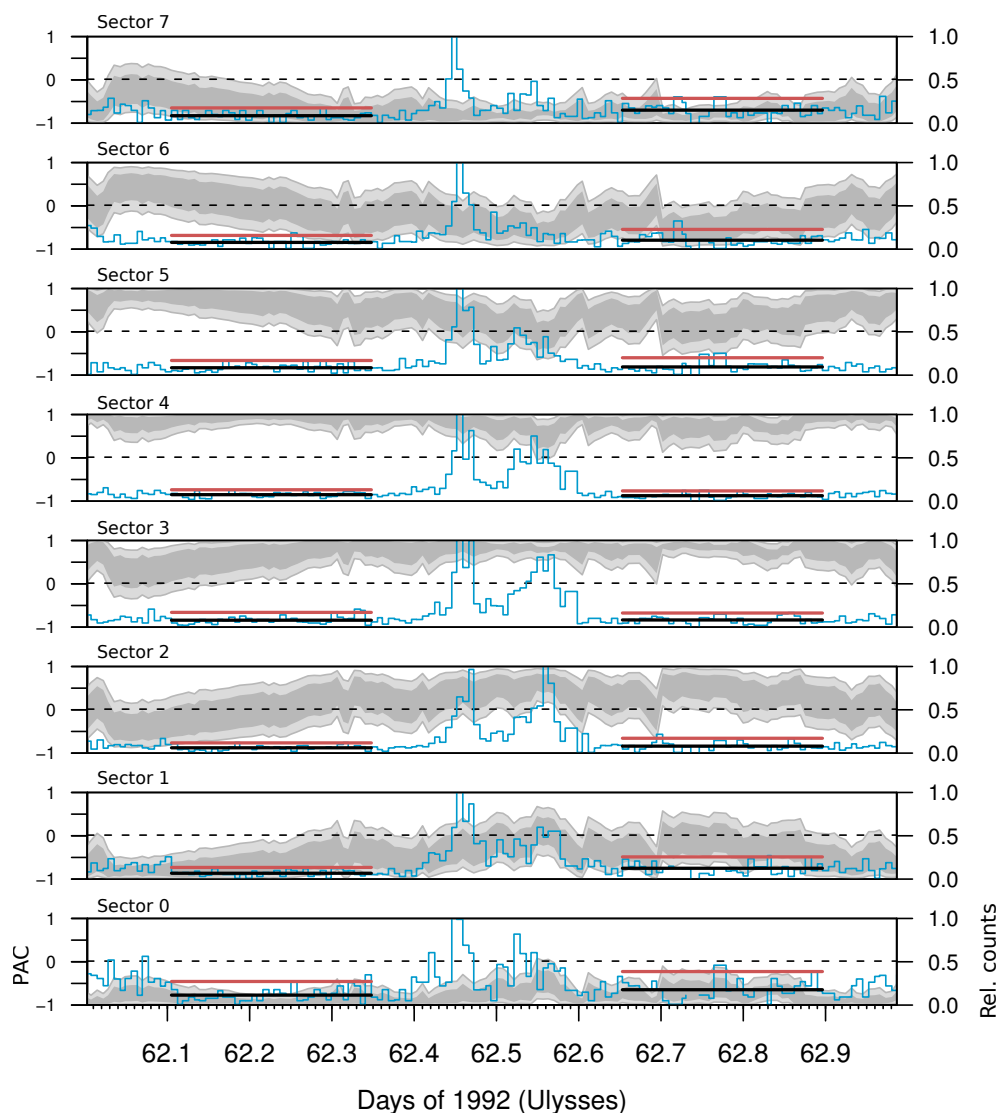


**Figure 8.3:** Similar to Fig. 8.2, this plot shows the pitch-angle coverage and the corresponding normalized sector counts. All sectors show an increase of electron flux. Consequently, the parallel and anti-parallel magnetic field direction is populated by particles, suggesting a backscattering of electrons.

The visual presentation of the pitch-angle coverage of the eight sectors illustrates the fact that the pitch angle space sampled by a specific sector may strongly vary with time. This can be seen in Fig. 8.2. While sector 3 mainly samples the negative pitch-angle hemisphere at the beginning of day 350, around the time of the observation of the jet, the magnetic field has turned in a way that the pitch-angle space scanned by sector 3 is predominantly positive. An investigation of the directional anisotropies, i.e. the counting rates of the sectors without taking into account the magnetic field vector

with respect to the spacecraft's spin plane, is not fully sufficient for this analysis. The reason is that a sector may sample the positive as well as the negative pitch-angle hemisphere, in the most unfortunate case, all sectors cover both hemispheres. Due to this ambiguity, the direction of an incoming particle can not be determined. Therefore, it is of importance to gain knowledge on the actual pitch-angle coverage of the particle telescope. In general, the directional anisotropy is a lower limit for the pitch-angle anisotropy, i.e. the latter one is expected to show a higher value.

Another examples to be discussed illustrates the ambiguity related to the determination of pitch angles. Fig. 8.4 shows the pitch-angle coverage and the corresponding normalized counting rates in the same manner as the previous Figures but for the two jets # Ea and Eb on day 101/2004. Both jets can be identified by an increase in flux. The center of anisotropy is sector 4, i.e. it is located in the positive pitch-angle hemisphere. For the opposite direction, sector 0, no flux enhancement is apparent. Focusing on sectors 2 and 7, also mainly covering the negative pitch-angle hemisphere, a small increase related to the Jovian jets is apparent. However, as can be seen by the pitch-angle coverage of this sectors, they also sample to some degree the positive pitch-angle hemisphere. In particular, this is the case if one considers the finite opening angle of the KET. As discussed before, it is not possible to judge if the electrons counting by these sectors come from the positive or negative hemisphere. Taking into account the vast increase of flux in sectors 3, 4, and 5, especially during the first event, it is most probable that the particles counted by sectors 3 and 7 are predominantly coming from the positive pitch-angle hemisphere. The degree of backscattered electrons is small or even absent. This situation is further emphasized in Fig. 8.5. Here, the normalized sum of a combination of several sectors was computed by

$$j(t)_{rel} = \frac{\sum_i s(t)_i}{\sum_i s_i^0}, \quad (8.2)$$

where  $j(t)_{rel}$  is the sum of a subset of sector counts  $s(t)_i$  with  $i \in [0, \dots, 7]$  normalized by a baseline given by sector counts  $s_i^0$ . The bottom panel of the Figure shows the normalized sum of sectors 3, 4, and 5. The two Jovian jets can clearly be identified. The top panel, on the other hand, shows the sum of sectors 0 and 1. During the first jet, the flux level does not exceed the  $2\sigma$  level and shows to significant variation with time. During the second event, between day 101.65 and 101.85, a small variation is evident to the eye resembling the flux profile of the positive pitch-angle hemisphere. Comparing the pitch-angle coverage, it becomes evident that the two sectors do not sample the positive pitch-angle hemisphere, i.e. the variation can be attributed to backscattered particles. However, the amplitude of this variation is very weak and in general does not exceed  $2\sigma$ . Finally, the middle panel contains the temporal evolution of the sum of sectors 2 and 7. As already discussed above, these sectors clearly show an increase in flux during the two Jovian jets with counting rates well above  $2\sigma$ . Both sectors, however, are expected to sample also the positive hemisphere to some degree (Fig. 8.4). This observations lead to the assumption that only a small fraction of electrons – if any – were backscattered during these events by pitch-angle diffusion

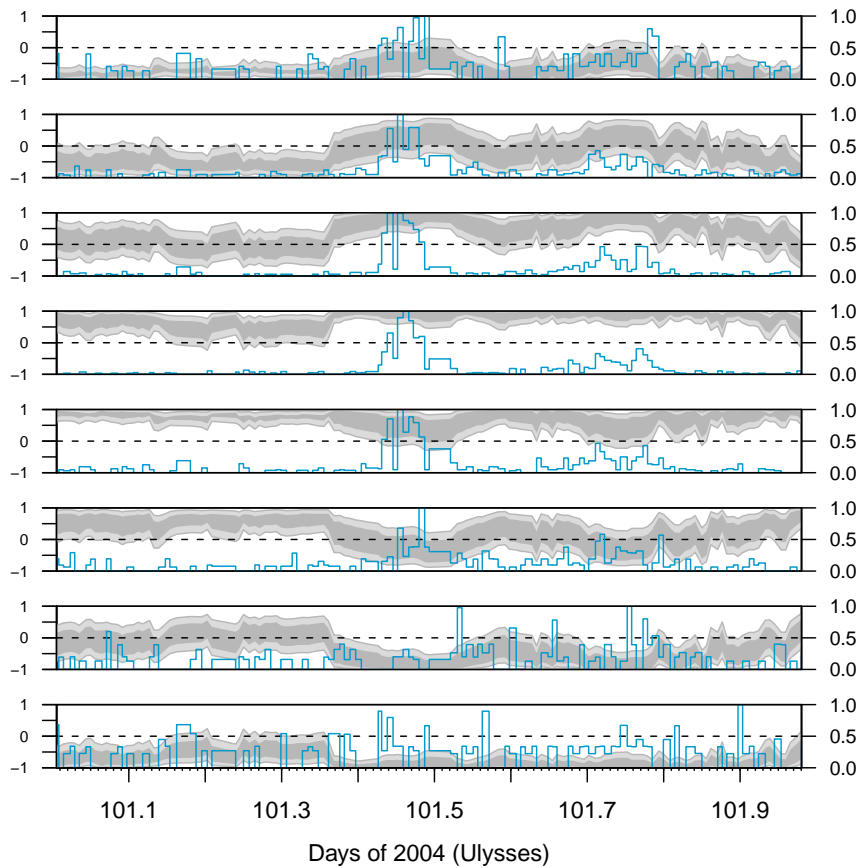


**Figure 8.4:** Like Fig. 8.2 and 8.3, this plot shows the pitch-angle coverage and the corresponding normalized sector counts. While there are clear flux increases in the positive pitch-angle hemisphere, indicating the jets #Ea and Eb, the negative hemisphere barely shows evidence for enhanced electron fluxes.

across  $\mu = 0$ . Consequently, the mean free path of the electrons is expected to be longer than the distance between Jupiter and the spacecraft during the time of measurement of 0.97 AU.

### 8.3 Jovian Jets And ICMEs

The observation of Jovian jets and their interpretation raises immediately the question what causes the significant deviations from the nominal Parker field required to establish a magnetic connection between the Jovian magnetosphere and the distant

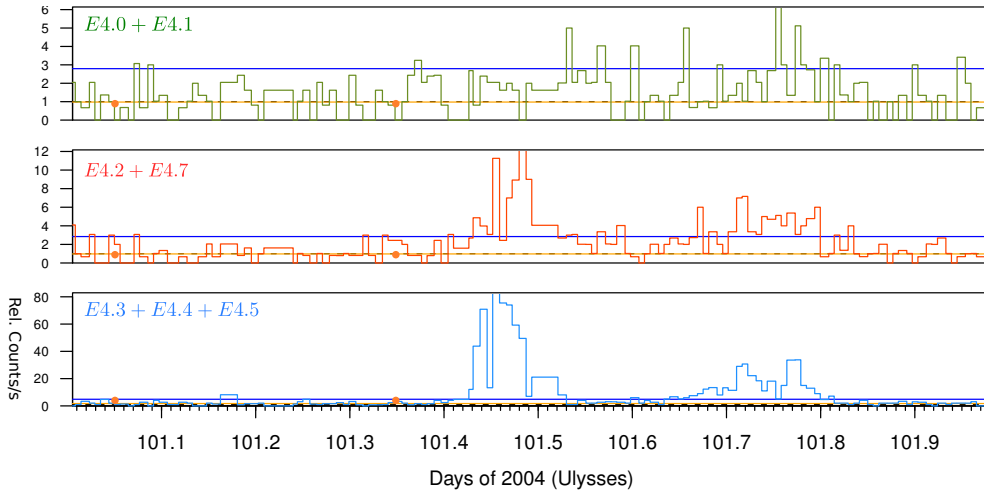


**Figure 8.5:** To illustrate the temporal behavior of several E4 sectors, this plot shows the evolution of the normalized sum of sectors 3, 4, and 5 (bottom), 2 and 3 (middle) and 0 and 1 (top). The orange lines denote the mean value of the flux taken between the two orange bullets, the blue line is the corresponding  $2\sigma$  level. While the top panel barely shows an flux increase related to the Jovian jets, sector 2 and 7 show a temporal evolution related to sectors 3, 4, and 5. See text for further discussion.

observer. It was already noted by McKibben et al. (2007) that the random walk of magnetic field lines on the solar surface (Jokipii and Parker, 1968) is not sufficient enough to explain the observed deviations. Furthermore, during the first Jovian flyby all 35 jets were observed up to a radial distance from Jupiter of 0.8 AU, while during the second flyby 15 events occurred within a range of 0.8 to 2.2 AU. Even though the trajectory of the spacecraft was not identical with respect to Jupiter during both time intervals, it may be suggested that there was a larger global rate of occurrence of Jovian jets out of the ecliptic during the latter time period. This conclusion can be drawn from the simple assumption that the probability of the detection of a jet decreases with the square of the radial distance from the source, i.e. the Jovian magnetosphere.

In the following, a connection between the observation of Jovian jets at high latitudes and the occurrence of ICMES will be proposed to account for the magnetic field excursions beyond the limits of the normal field-line random walk. The main argument for a temporal correlation between Jovian jets and ICMES is the fact that ICMES are known to cause large-scale disturbances in the IMF because of their topology (Forsyth et al., 2006). In particular, multi-spacecraft observations of ICMES (eg. Falkenberg et al. (2011) and Kilpua et al. (2011)) enhanced the understanding of global ICME topologies and their influence on the IMF.

Fig. 8.6 shows a sketch of the possible shape of an ICME approaching towards 1 AU and the surrounding IMF. Since the magnetic fields cannot intersect, the surrounding

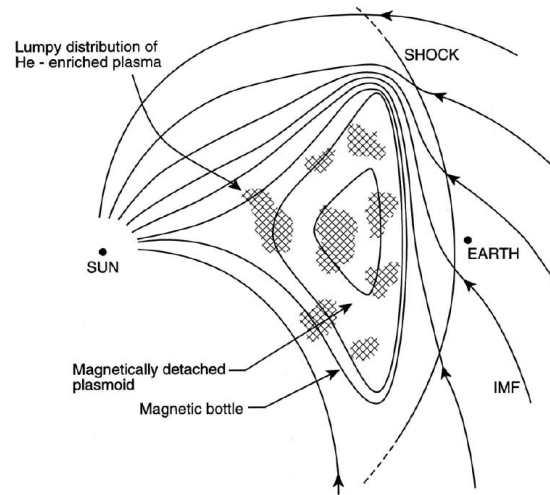


**Figure 8.6:** Hypothetical topology of an ICME. Because of the size of the ICME and the presence of a region magnetically disconnected from the Sun, large deviation from the nominal Parker field may be the results of a propagating ICME. Figure taken from McComas et al. (1998).

IMF is bent away by the propagating ICME. If the propagation speed of ICME is fast enough compared to the surrounding solar wind plasma, it may drive a shock wave as illustrated in the Figure. The development of a magnetic bottle configuration can be deduced from the observation of suprathermal, i.e. in a range of a few eV, electrons with bidirectional pitch-angle distributions.

To search for correlations between ICMEs and jet events along Ulysses' trajectory, the occurrence of both was plotted as a function of time in Figs. 8.7 and 8.8. For the creation of the Figures, the Ulysses ICME table of Du et al. (2010) (yellow bars) and the SWOOPS ICME table<sup>3</sup> (light blue) had been used in combination with the occurrences of Jovian jets indicated by red dots and the counting rates of  $\sim 2.5 - 7$  MeV electrons of the KET instrument. Note that the SWOOPS table starts after the Jupiter flyby, while the pre-flyby interval is included in the work of Du et al. (2010). It is obvious, however, that there are considerable differences between the number of observed ICMEs and their specific on- and offset times. The reasons for this are manifold and not at least it depends on the criteria used for the identification and interpretation of ICMEs. Du et al. (2010) e.g. focused mainly on the presence of abnormally low proton temperatures as a criteria, while the SWOOPS data are mainly based on the presence of bidirectional suprathermal electrons. However, since there is no unique parameter giving striking

<sup>3</sup>This table can be found at [http://swoops.lanl.gov/cme\\_list.html](http://swoops.lanl.gov/cme_list.html).

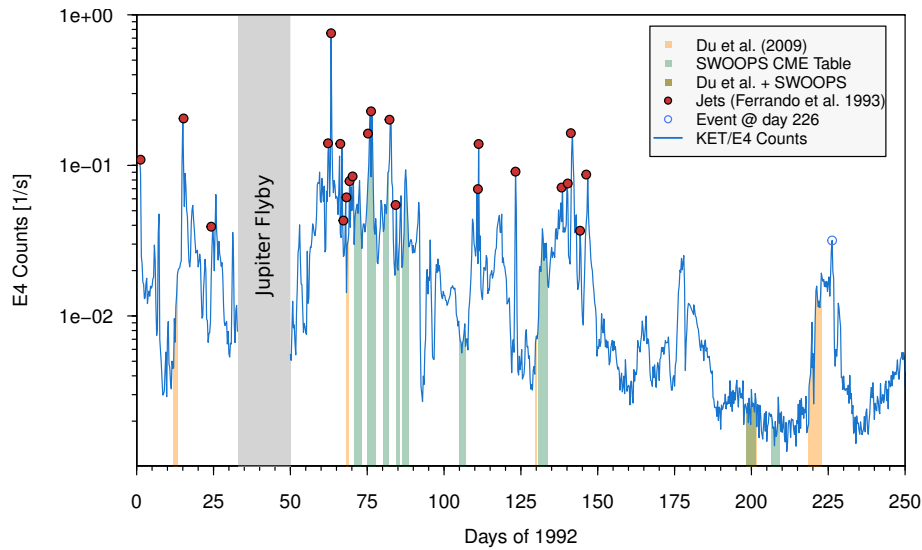


**Figure 8.7:** Distribution of ICMEs observed by Ulysses in the context of the occurrence of Jovian jets (red dots) and E4 counting rates (blue curve) for 1992. The shaded intervals correspond to ICMEs listed in the work of Du et al. (2010) and in the SWOOPS ICME table according to the legend.

evidence for the detection of an ICME, events list are somewhat different from each other. In particular beyond the orbit of the Earth, ICME signatures are often biased by the interaction with the ambient solar wind regime and the typical plasma properties do not necessarily occur simultaneous.

During the 1992 time interval, Jovian jets were generally observed during general enhancements of the E4 counting rate, in particular during the day 60-80 time period, where most of the jets of the first flyby were observed and the general counting rates were considerable higher than just before and after the Jupiter flyby, and between the days 135-145, where again a clumping of Jovian jets can be seen. Comparing these events with the occurrences of ICMEs, there is no immediate correlation between these two kinds of events. However, during the second half of the electron enhancement from day 60 to 80, there are several ICMEs listed in the SWOOPS table. An ICME is also reported by the authors of the table a few days before the jets on day 110 and 111 and before the onset of the series of jets after day 135. The event list compiled by Du et al. (2010), however, shows much fewer events observed at different time intervals. The first event observed by Du et al. (2010) in 1992 occurs just before the jet event observed on day 15, while the last ICME is somewhat correlated with the ICME of the SWOOPS list preceding the series of jets after day 135.

The second, more distant flyby of Ulysses is shown in Fig. 8.8, covering the last 90 days of 2003 (top) and day 1 to 325 of 2004. Comparing these time intervals with the 1992 data, the most eye-catching difference is that the number of ICMEs reported by

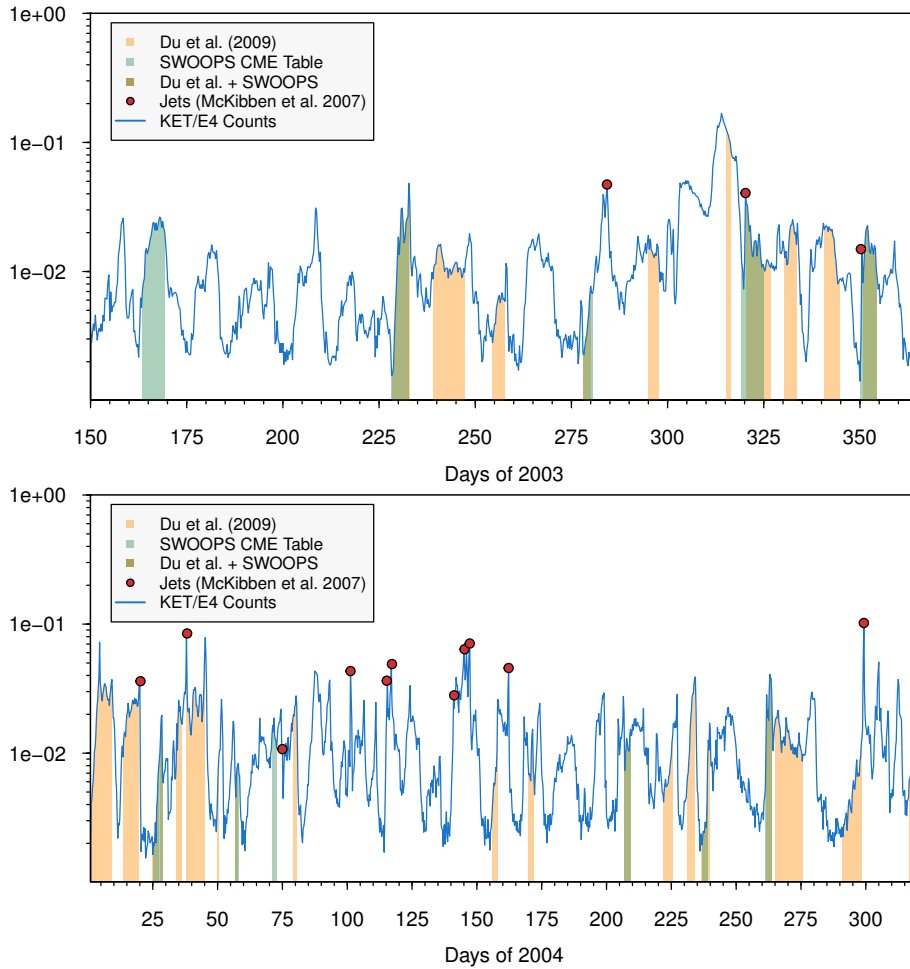


**Figure 8.8:** Same as Fig. 8.7 but for the last 90 days of 2003 (top) and year 2004 (bottom).

Du et al. (2010) is significantly increased compared to the number of events listed in the SWOOPS table. In 1992 the opposite was the case. However, the SWOOPS events are generally in good coincidence with the corresponding events of Du et al. (2010). Note that in mid-2004, Ulysses was located relatively close to the ecliptic (cf. Fig. 8.1), i.e. the perpendicular excursions of the magnetic field needed to establish magnetic connections to Jupiter are smaller than during the 2003 and late-2004 period. The very last Jovian electron jet seen by Ulysses, event 'L' of McKibben et al. (2007), was observed at a very large distance from Jupiter of 2.21 AU. The perpendicular distance between Jupiter and the spacecraft was about 0.6 AU and the event was a relatively long lasting one of  $\sim 7$  hours. Just before the onset of this event (day 299.2), Du et al. (2010) reported the occurrence of a magnetic cloud starting at day 293.88 and lasting for 4.375 days, i.e. Ulysses left this event at day 298.255 or one day before



the Jovian jet was observed. The ICME, showing the signature of a magnetic cloud (MC), traveled with a mean speed of  $\bar{v} = 372$  km/s and had an estimated width of 0.94 AU. Assuming a radial distance between Ulysses and Jupiter of 0.18 AU, a rough computation ( $\Delta r/\bar{v}$ ) results in 0.84 days for the travel time of the ICME's trailing edge from Ulysses to Jupiter. Interestingly, the estimated time when the ICME has passed Jupiter (day 299.1) is in some coincidence with the onset time of the Jovian jet at Ulysses (day 299.08). We interpret this as the result of a temporal disturbance of the interplanetary magnetic field caused by the ICME, resulting in a magnetic field condition that allows a straight propagation of Jovian electrons perpendicular to the mean magnetic field.

Together with parameters like the tilt angle of the heliospheric current sheet (HCS) and the number of sunspots, the rate of occurrence of CMEs and their interplanetary counterparts is used as a general indicator of solar activity (Webb and Howard, 1994), i.e. the CME occurrence rate is positively correlated with the sunspot number. While the sunspot number was almost equal in the 1992 and 2003/04 period, the ICME occurrence rates and the tilt angle of the HCS tend towards higher levels in 2003/04, giving rise to the assumption that the Sun was in a state of higher solar activity during this time. Following the argument that an enhanced rate of occurrence of ICMEs leads to an enhanced distortion of the nominal Parker field in the vicinity of the ICMEs, this further leads to the assumption that the observed Jovian jets at large joventric distances during the second flyby may be at least partially caused by this effect.

However, this does not rule out the influence of other major effects that may play a role. In addition, the possibility of an increased intrinsically injection of Jovian electrons into the IMF may taken into account. Beside what was discussed up to now, there are a couple of Jovian jets being observed not only in the vicinity of ICME but inside these structures. For example, the jet on day 320 in 2003 (see also McKibben et al. (2005)) occurred during the ICME discussed by de Koning et al. (2005). At this time, Ulysses was located at a radial distance of 1.03 AU from Jupiter, what was almost equal to the perpendicular distance to the ecliptic plane. The onset of the ICME was detected on day 319.85<sup>4</sup> by the observation of bidirectional suprathermal electrons and a smooth rotation of the magnetic field vector. The spacecraft left this structure about 5 days later on day 324.16. This ICME, classified as a magnetic cloud by the authors, was an unusual event because of the propagation speed exceeding 990 km/s and its comparatively large size. The radial width was determined to 2.0 – 2.5 AU. Fig. 8.9 shows Ulysses measurements covering the time interval from day 317 to 324 in 2003. The onset of the ICME/MC is indicated by the dot and the label "MC onset" in the upper panel. The three magnetic field components (red) show the typical smooth evolution. The MC is preceded by several shocks, two of which are indicated by the dash-dotted lines and are characterized by jumps in the solar wind speed (green) and

---

<sup>4</sup>In contrast to de Koning et al. (2005), Du et al. (2010) determined the onset of the ICME at day 319.16, while the SWOOPS list states 320.42 as the beginning of the event. Obviously, this difference is related to the used criteria to identify ICMEs.

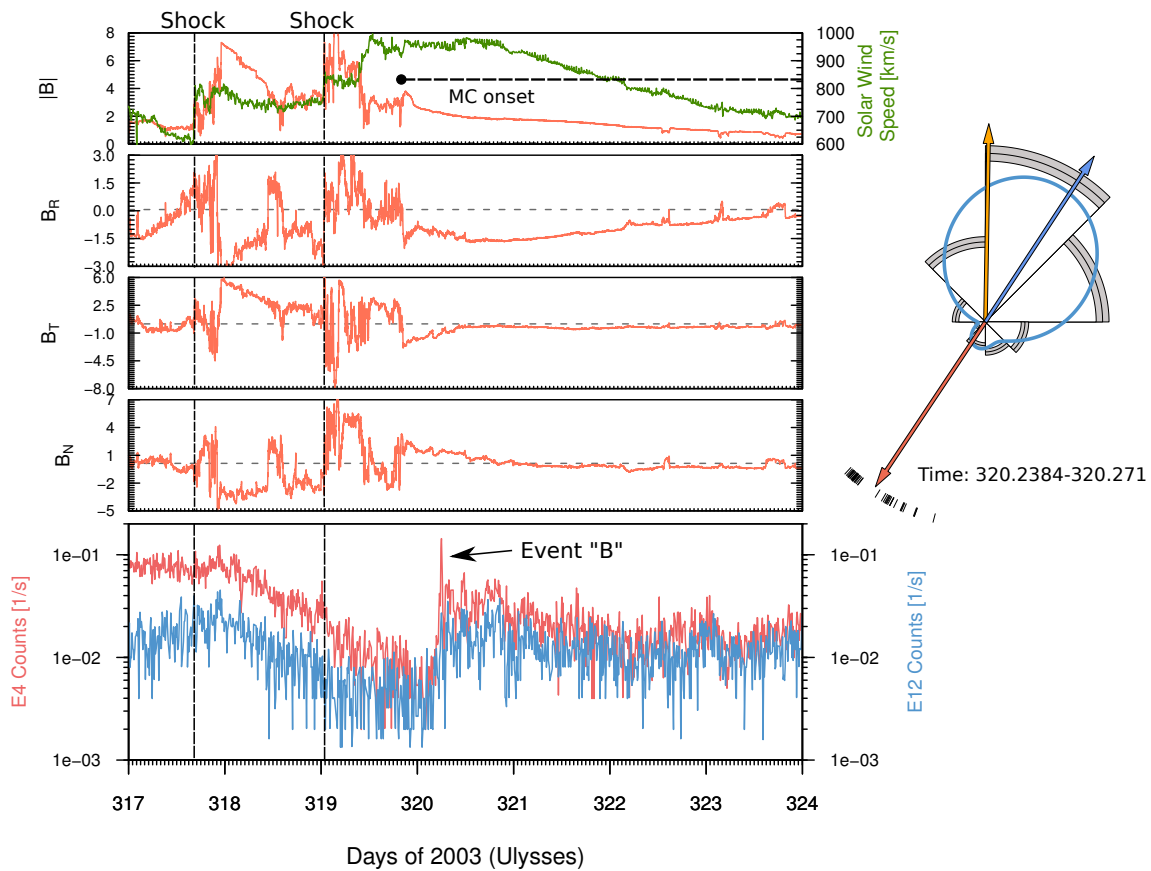


**Figure 8.9:** The Jovian event of day 320/2003 occurred inside an ICME. A sharp increase in the E4 counting rates is visible on day 320 (Event "B"). The sector diagram on the right shows of the accumulated E4 counts from day 320.238-320.271. The orange arrow indicates the direction to Jupiter, the red arrow indicates the mean magnetic field vector and the blue one the fitted axis of symmetry. The blue curve in the sector diagram is the fitted Fourier series.

in the magnetic field strength. The E4 counting rates decreases constantly until day 320. Around day 320.1, a substantial reincrease of electrons is observed culminating in the occurrence of a Jovian jet between day 320.2 and 320.3. The Figure's inlet shows a sector diagram of the E4 counting rates averaged from day 320.215 to 320.28. The orange arrow indicated the direction to Jupiter, the black arrow the magnetic field. As can clearly be seen there is a proper field-aligned anisotropy of particles coming from Jupiter's direction. The observation of a jet inside an ICME strongly suggest that source and observer were both located inside the ICME, what may also be supported by the general reincrease of electrons. This event emphasized the fact that an ICME shows a magnetic field structure quite different from the undisturbed Parker field. In particular the magnetic-cloud structure of this event requires a magnetic

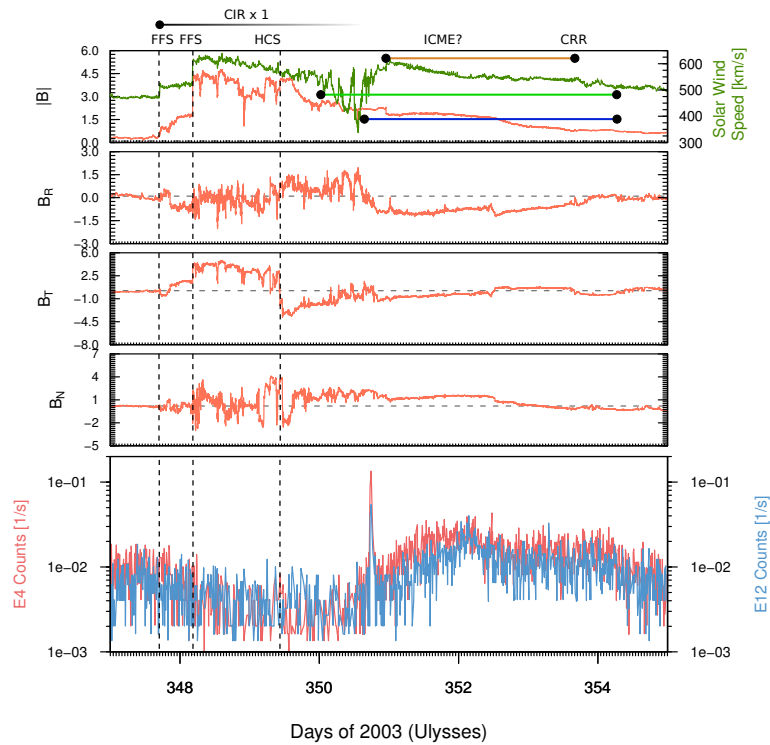


**Figure 8.10:** Ulysses measurements from day 347-355 in 2003. The magnetic field and solar wind data show the presence of a CIR starting with a fast forward shock (FFS) on day 347.708 and a second one on day 348.18. Ulysses crossed the heliospheric current sheet (HCS) on day 349.416. The corotating rarefaction region (CRR) trailing the CIR was detected from day 352.625-358.45. The Jovian jet can clearly be identified around day 350.75 by the increase of E4 counting rates by more than an order magnitude. Depending on the references, the jet occurred inside or a few hours before an ICME.

connection perpendicular to the ecliptic plane over a relatively large distance of 1 AU. Understanding the possibility to observe particles from a remote but well-known source as some kind of two-point measurement, the out-of-ecliptic extension of the ICME may be estimated. In the work of de Koning et al. (2005) it is argued that the ICME can be associated with the active region AR 0486 on the solar surface. This active region was located at  $-17^\circ$  with respect to the solar equator. During this time, Ulysses was located in the northern hemisphere. A lower limit of the extension of the ICME can be directly derived from the fact that Jupiter was also located inside the event, i.e. the width of the structure must be at least 1.03 AU. Assuming a mainly radial propagation of the ICME, its center is expected to cross the orbit of Jupiter in the southern ecliptic hemisphere. As stated before, the active region was at a solar latitude of  $-17^\circ$ , while Ulysses was located at a heliolatitude of  $5^\circ$  (corresponding to a Jupiter-Ulysses angle of

$\sim 11^\circ$ . Assuming a radial distance from the Sun of 5 AU and a latitudinal separation of the ICME's center and Ulysses of  $22^\circ$ , the perpendicular distance can be estimated to  $\sim 2$  AU, i.e. the minimal full-width of the ICME is about 4 AU.

This estimation, in combination with the radial width of 2.0 – 2.5 AU (de Koning et al., 2005), this emphasizes the large expansion of ICMEs in the heliosphere. Since shocks are driven by the ICME, the structure is faster than the surrounding medium, i.e. it acts as an obstacle for the ICME as it propagates away from the Sun, leading to a significant bending of the Parker field in the vicinity of the ICME and therefore allowing energetic particles to perform parallel propagation along highly non-Parkerian field lines.

Beside the jet on day 320/2003, there are some more jet events that might have occurred during ICMEs. According to the SWOOPS ICME table, an ICME convected past Ulysses from day 75.16 to 77.79 in 1992. During this time, four jets were found by Ferrando et al. (1993) when the spacecraft was still located relatively close to the planet ( $\sim 0.3$  AU). Du et al. (2010), however, found no evidence for the presence of an ICME during this time interval. On the other hand, Du et al. (2010) identified a non-MC event starting at day 37.88/2004, lasting for 168 hours. A few hours after the onset of the probable ICME, a Jovian jet was detected by the KET/HET instruments on day 38.15. In this case, no evidence for an ICME was found by SWOOPS.

A Jovian jet with remarkable features was detected on day 350.75/2003, i.e. 30 days after the event extensively discussed before. Fig. 8.10 covers the time interval from day 347 to 355 in 2003. The Jovian jet can clearly be identified by the sudden increase of the E4 counting rates by more than an order of magnitude. Roughly 2.5 days before the event, Ulysses encountered a CIR<sup>5</sup> by the detection of two fast forward shocks (FFS) at day 347.708 and 348.18, respectively. The heliospheric current sheet (HCS) was encountered by the spacecraft at day 349.416. The end of the CIR is hard to identify since there is no unambiguous reverse shock. Therefore, the time interval covered by the CIR is represented by the faded down bar on top of the Figure. As expected, the electron flux decreases after the occurrence of the first shock. The corotating rarefaction region (CRR) accompanying the CIR was detected from day 352.625-358.45. Promptly after the CIR, the table's composer suspect an ICME covering the time interval bounded by the horizontal orange bar (day 350.958-353.625). The previously used SWOOPS ICME table and the work of Du et al. (2010) also suggest the occurrence of an ICME during this time. However, both authors defined different on- and offset times. The green horizontal bar refers to the SWOOPS table, the blue one to Du et al. (2010). Consequently, the jet occurred just after the passage of a CIR and inside or shortly before an ICME. Note that a constant increase of MeV electrons is observed starting at day  $\sim 350.25$  up  $\sim 352.5$  resembling to some extent the profile of the counting rates during the day 320/2003 event. The shape of the magnetic

---

<sup>5</sup>The following dates had been taken from a table available at the JPL website [http://ulysses.jpl.nasa.gov/science/observed\\_data.html](http://ulysses.jpl.nasa.gov/science/observed_data.html). The CIR was named CIR x 1 by the compiler of the table, and refers to the first occurrence of CIR x.

field components, however, suggest that the onset time of the JPL table is in good agreement with the beginning of a smooth rotation of the magnetic field, identifying the ICME as a MC (see also Du et al., 2010). On the other hand, the E4 counting rates increase in a smooth manner, indicating that Ulysses and Jupiter were located in the same magnetic regime. This suggest that they are not separated by the CIR (cf. Conlon, 1978) or by the ICME structure. During this time interval, the radial distance between Jupiter and Ulysses was 0.9 AU, and the spacecraft was still located almost perpendicular to the planet (with respect to the ecliptic) with a perpendicular distance of 0.88 AU. The longitudinal separation between both objects was  $-1.7^\circ$ , i.e. it is expected that Ulysses sees the CIR a few hours before Jupiter.

The most prominent feature of this Jovian jet is its exceptional high degree of anisotropy.

## 8.4 Detection of the 10 h Periodicity

A challenging feature of the Jovian electron source is the observation that the modulation of the energy spectrum of Jovian electrons can occasionally be discovered in the interplanetary medium not too far away from Jupiter. What “far” means in this context will be discussed in the following.

While the method of building a phase histogram had been used by several authors to search for the 10 h periodicity (Schardt and Goertz, 1983; Ferrando et al., 1993), a different approach will be pursued here using the Lomb-Scargle algorithm as it has already been done for the analysis of Ulysses data inside the Jovian magnetosphere. The advantage of this kind of spectral analysis is that a wide range of periods can be investigated at a glance, allowing to search for possible frequency drifts in the data or a comparison of the main peak and the background frequencies. On the other hand, the Lomb-Scargle periodogram requires a time series that covers a time period at least equal to the periodicity under investigation. Thus, in practice the analyzed time series should cover a time interval  $> 2$  days. Consequently, the analysis stretches out over the time interval around the jets. This allows an investigation of the question if the 10 h periodicity can not only be recovered in jets but also during time periods where no extraordinary anisotropies are observed. The Lomb-Scargle algorithm is used in two different approaches. (i) The traditional frequency vs. power plot in combination with plots of the corresponding time series of the analyzed quantities and (ii) a sliding Lomb analysis allowing an investigation of the temporal evolution of the power spectrum as explained in section 5.6.

Not to solely rely on the results of the Lomb-Scargle algorithm, the time series of the spectral index is investigated visually by comparing it with a sine of a 10 h periodicity imposed on the data and ticks referring to a reference phase. In order to investigate the phase of the rocking modulation of the energy spectrum in the heliosphere, a point in time was chosen inside the Jovian magnetosphere used as a reference to track the 10 h periodicity. A useful reference system in this context is the

spacecraft's internal clock (SCET, spacecraft event time), counting the seconds since 01.01.1950. For the synodic rotation period of Jupiter we use  $9^h55^m33.12^s$  what refers to 35733.12 seconds. It is clear that it is hard to define the "optimal" point of reference. As it is discussed in section 7, the peaks in the energy spectrum often show a rather broad maximum with some variation in time with respect to the expected maximum. However, in the following we use the third peak observed by Ulysses during the inbound trajectory and define day 34.86820/1992 as the point of reference, equivalent to a SCET of 1328302208 s (cf. Fig. 8.11). As will be shown, differences between the spectral modulation in the heliosphere and the phase angle expected from the "clock" modulation are present in the data. During the 1992 time period, the continuation of the synodic periodicity of Jupiter stated above is precise enough, because of the relatively short time interval of  $\sim 110$  days between the direct flyby and the observation of the last jet. A systematic phase shift in the data is expected due to the uncertainties in the estimation of the sidereal periodicity of the planet and of its orbital period around the Sun is expected when extrapolating from the 1992 time period to 2003/2004. Allowing an uncertainty of the periodicity of  $\pm 1$  s, the deviation is about  $\pm 3$  h at the end of 2004. However, typical uncertainties in the sidereal period are  $< 10^{-2}$  s (cf. Yu and Russell, 2009), leading to phase differences of a few minutes. Simpson et al. (1975) could show that the spectral variation observed by Pioneer 11 was in good agreement with the prediction derived from Pioneer 10 measurements carried out one year earlier. This finding was verified by Voyager 1 (Schardt et al., 1981), showing a spectral index modulation in phase with Pioneer 10 results. Moreover, Rastoin (1995) claimed that the Ulysses observations are still in agreement with the Pioneer 10 predictions based on the synodic periodicity<sup>6</sup>.

We will start the investigation with the first Jupiter flyby of Ulysses. Ferrando et al. (1993) showed in their analysis that the 10 h periodicity of the energy spectra can be recovered at least up to 0.5 AU from the planet in 1992, analogous observations were reported by Simpson et al. (1993). An application of the analysis techniques used in this work to the first flyby allows a validation of the methods. In particular, this also allows a comparison of the KET and HET instrument with respect to their response to enhanced Jovian influence added to the background flux.

## 8.5 Reinvestigation of the 1992 Time Period

Fig. 8.12 shows the result of a sliding Lomb-Scargle analysis of KET & HET data (detrended E4/E12 and H6/H7 ratio) covering the time interval from days 55 to 115 in 1992 and a radial distance from Jupiter of  $\sim 0.1$  to  $\sim 0.6$  AU. Inside this range, 22 of the 35 observed Jovian jets are located. Four clusters of enhanced wave power at  $\sim 10$  h

---

<sup>6</sup> "Les Voyager arrivent, eux, quelques 5 ans après les Pioneer: la petite différence entre période de rotation et période sidérale induit alors une opposition de phase dans la modulation ( $\approx 5$  h). On peut donc choisir entre les deux périodes d'après les observation: la modulation montre la périodicité synodice. Ulysse confirme ce résultat." (Rastoin, 1995, p. 79)

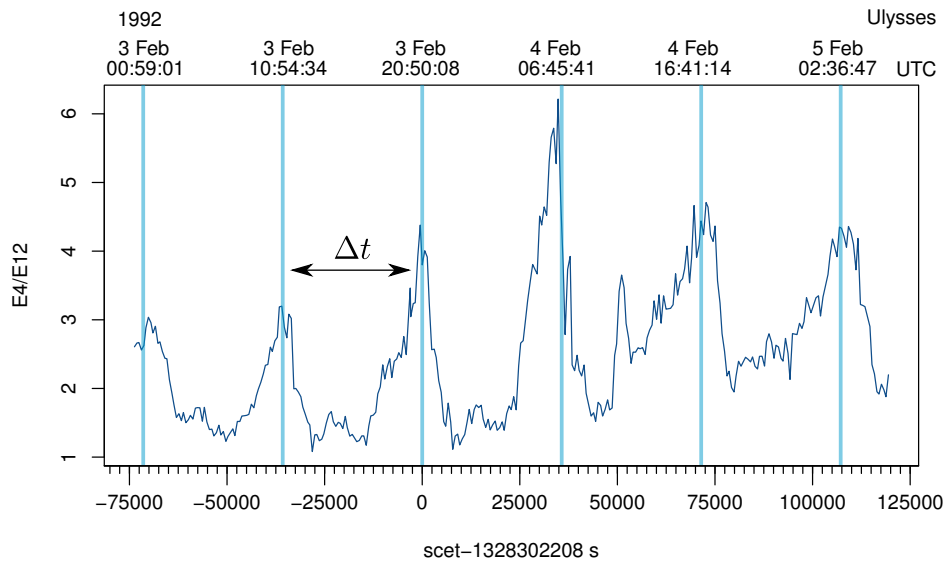


**Figure 8.11:** The E4/E12 ratio as a function of the relative SCET. For the definition of  $t_0$ , the third major peak of the E4/E12 ration had been used as a point of reference ( $t = 0$ ). The corresponding SCET is  $t_0 = 1328302208$  s. As can be seen, the single maxima do not exactly match the 10 h periodicity. Therefore, it is necessary to take into account an uncertainty of about  $\pm 30$  min. This uncertainty is of course related to the rather broad “active region”.

are clearly visible in the KET data in the first half of the plot, indicating a Jovian influenced spectral modulation of the electrons during these intervals. Comparing these intervals with the occurrences of Jovian jets reveals an unequivocal correlation as indicated by the intervals tagged with “JJs” and the respective index (consecutively numbered according to the table of Ferrando et al. (1993)) of the jets found in this time intervals.

The five white dots, on the other hand, represent jets that are not associated with a significant 10 h signal in the data. Note that the two jets that occurred on day 70 are of very short duration (15 and 26 minutes). The HET data, on the other hand, show a slightly different picture. While the 10 h periodicity is matched somewhat reasonably during the first series of jets (JJs #6-14), the following time intervals show the presence of enhanced wave power at expected dates, however with significant deviations from the expected periodicity (JJs #17-24). On the other hand, the HET (Fig. 8.13) shows the presence of a strong  $\sim 10$  h periodicity during days 110 and 111, while for the KET data any evidence for a periodic modulation is absent. Why is this the case?

To address this question, it is important to recall that the HET has a much larger opening angle compared to the KET. Consequently, the HET counts much more particles per time unit than the KET, expected to result in a different signal/noise ratio and response to background particles. To illustrate the difference between times of

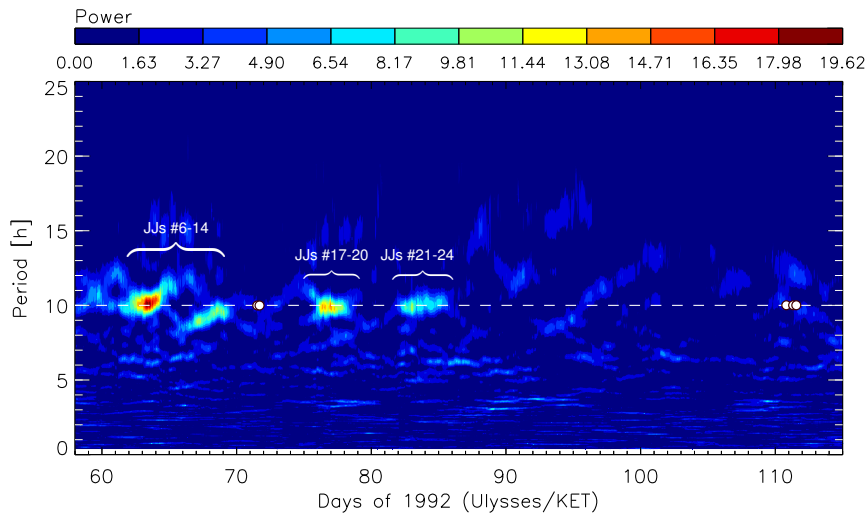


**Figure 8.12:** An overview of the periodicities present in the KET data during the post-flyby phase in 1992. The Jovian influence can be found in the data indicated by wave-power enhancements close to a periodicity of 10 h. A clear correlation between jet and the 10 h modulation is visible as indicated by the assignments of jets (JJs) according to a consecutive numbering of the events in Ferrando et al. (1993). Single dots indicate jets not associated with a 10 h periodicity.

low counts mainly due to ambient particles and times of significant influence of Jovian electrons, Figs 8.14, 8.15 and 8.16 display data of KET's E4 and E12 channel as well as sets of HET's H6/H7 and H8/H7 data. The top bottom always displays the channel of lower energy, subjacent the channel of higher energies is shown. The two bottom panels shows the detrended (green) as well as the undetrended (red) ratio of the two energy channels. On the right, the result of a Lomb-Scargle spectral analysis of the ratios measured during this time interval is displayed. During this specific time interval, covering days 62-65.5/1992, four Jovian jets occurred, all of which can clearly be identified in the time profiles of the counting rates and are numbered according to their occurrence in Ferrando et al. (1993). Looking at the detrended ratio of the E4 and E12 channels reveals a 10 h periodicity apparently visible to the eye during most of the time interval. This impression is further supported by the sine function of a periodicity equal to the Jovian periodicity (thick green curve) imposed on the data and by the result of the Lomb-Scargle analysis. Here, a clear peak at  $\sim 10$  h is present in the detrended as well as in the undetrended data. The deviation of the recovered periodicity from the expected one can be explained by the fact that phase of the data starts to drift off, beginning around day 64.5. Comparing the occurrence of the recurrent maxima in the E4/E12 channel with the predicted maxima based on the point of reference defined earlier, a systematic discrepancy is evident: the measured



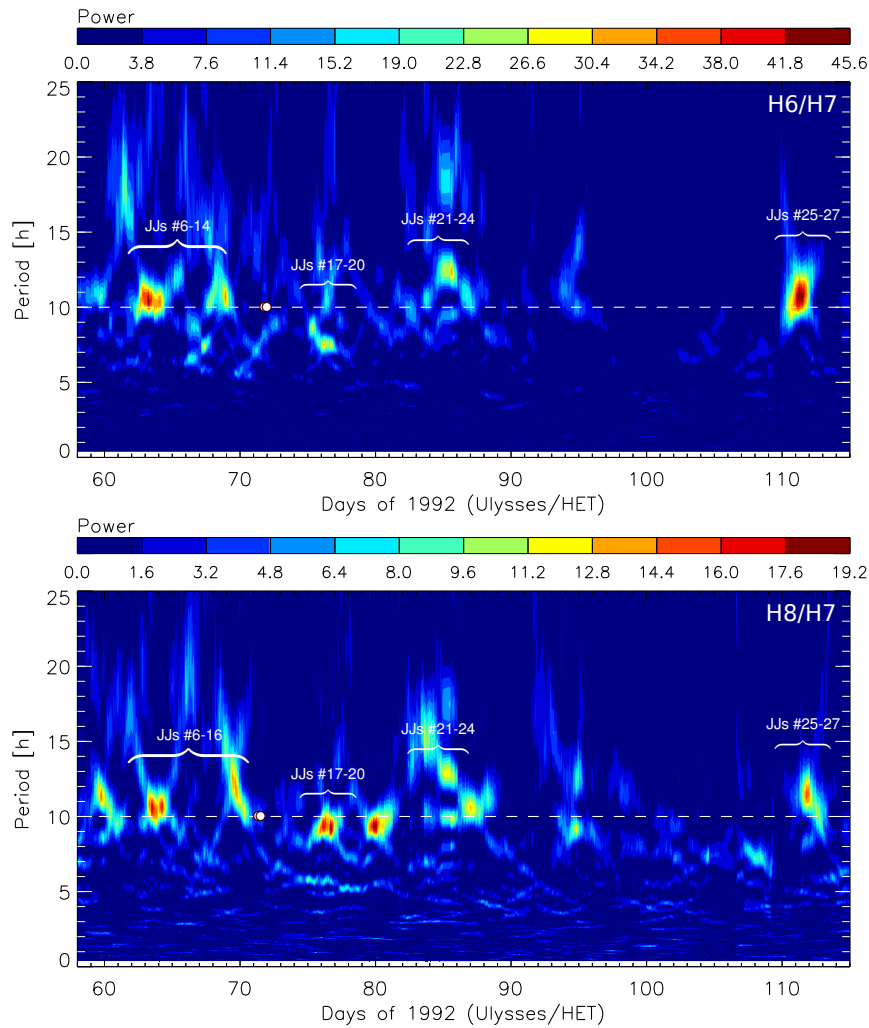


**Figure 8.13:** The same time interval as in Fig. 8.12 but for the H6/H7 (top) and H8/H7 (bottom) ratio.

maxima occur  $\sim 2$  h later than the expected maxima as indicated by the label. Given two charged particle instruments sensitive to similar energy ranges, it is expected to obtain comparable results. Fig. 8.15, however, showing HET's H6 and H7 data in the same format and for the same time interval as for the KET data, reveals a somewhat different result. A phase shift of  $\sim 4$  h is apparent in the H6/H7 ratio as already determined by Simpson et al. (1993) and used as an input parameter of an isotropic propagation model in order to estimate the diffusion coefficients of the electrons. For further investigations of this finding, the same analysis was performed on the H8/H7 ratio, i.e. a smaller energy interval. The result is displayed in Fig. 8.16. Compared to the H6/H8 ratio, the ratio shows a smoother temporal evolution and a somewhat “unsteady” behavior of the phase than the E4/E12 ratio. However, comparing H8/H7

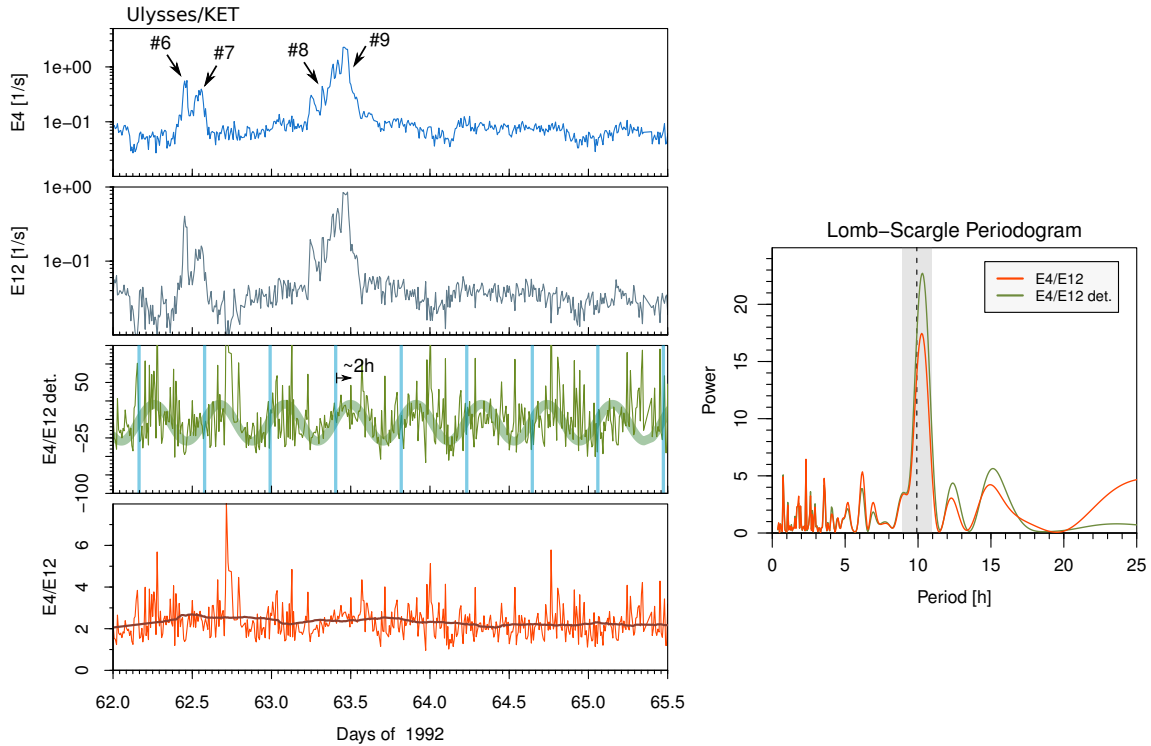


**Figure 8.14:** The E4 & E12 counting rates of the KET as well as the detrended and undetrended E4/E12 ratios is displayed for the time interval day 62-65.5 in 1992. Four Jovian jets are indicated by their order of occurrence in Ferrando et al. (1993). A 10 h periodicity is visible in the detrended and undetrended E4/E12 ratio, however, the detrended ratio is found to be better pronounced. The green, thick curve is a sinusoid put on top of the data for visual guidance. The solid lines in the same panel indicates the expected maximum according to the extrapolation described earlier. The gray shaded area indicates the interval  $9.91 \pm 1$  h.

and E4/E12, one finds a good agreement of the phase shifts, i.e. the H8/H7 data also reveal a shift of 2 h.

To understand the different behavior of H6/H7, one might note that the detrended as well as the undetrended ratio show significant drops when the counting rates increase because of the observation of Jovian jets. The notable depression of the H6/H7 ratio can be related to the background of the H6 channel: during quiet times, the fraction of background particles in the H6 channel is sufficiently higher than during Jovian jet events. The left panel of Fig. 8.17 shows a three dimensional scatterplot of  $\log(H6)$  and  $\log(H7)$  versus H6/H7 for the jet event #9 (indicated by brown dots) and the circumjacent time interval (light blue dots). To guide the eye, the three dimensional distribution is projected on the three planes spanned by the coordinate system. A clear

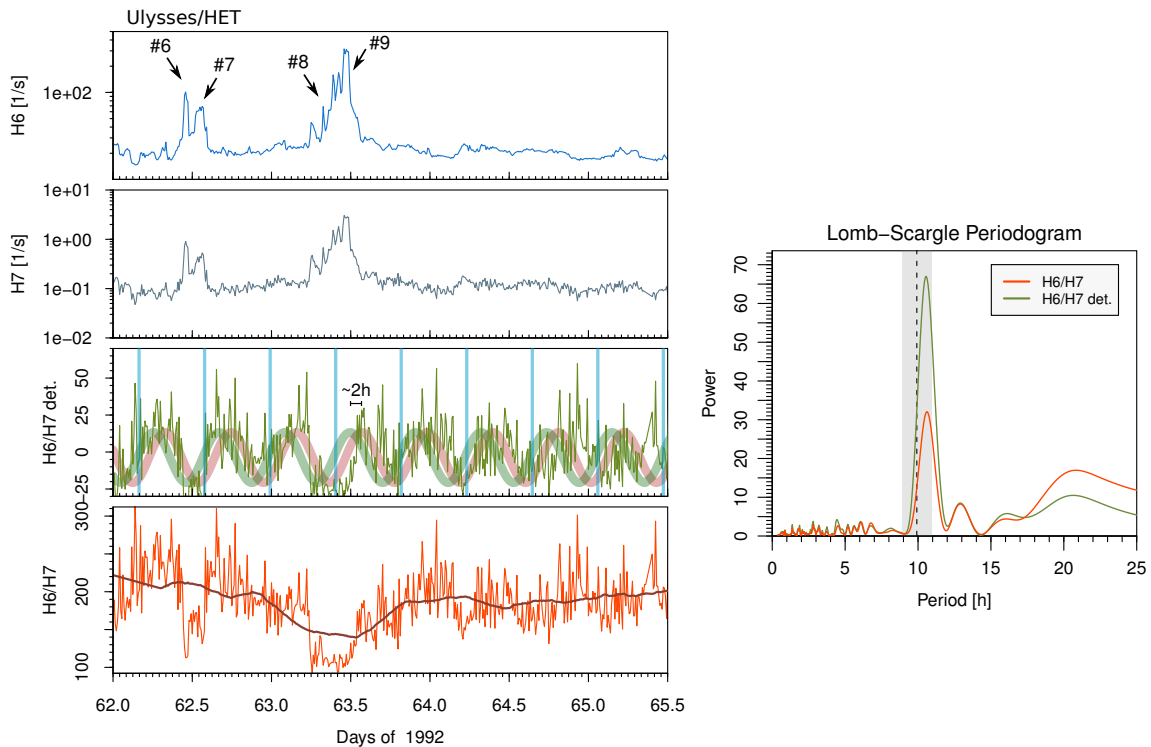


**Figure 8.15:** The same time interval as in Fig. 8.14 but for the HET instruments. While the counting rates of the the KET and HET show a similar behavior, the H6/H7 ratio is somewhat different compared to the E4/E12 ratio. An additional phase difference of 2 h is visible (red curve), leading to a total phase shift of 4 h with respect to the prediction.

difference in the distribution of the jet-related events and the ambient events. While the response of H6/H7 is relatively moderate for high values of  $\log(H6)$  and  $\log(H7)$ , H6/H7 is highly sensitive to variations of  $\log(H6)$  and  $\log(H7)$  at low counting rate levels, i.e. during time where ambient background flux dominates. From this it can be deduced that during quiet times, the relative value of background particles is high, but decreases rapidly during the occurrence of Jovian jets. This transition leads to the unsteady profile of the time series. The right panel of the Figure shows two dimensional scatter plots of  $\log(H6)$  vs.  $\log(H7)$  (top) and  $\log(H8)$  vs.  $\log(H7)$  (bottom) for the same time period. Both subsets of the electrons counts (jets, non-jets) were fitted independently using a linear regression model. While the two slopes of the linear models (indicate by “m”) in the bottom panel are almost the same, indicating a similar response of the detector over a wide range of energies, they differ in the case of H6/H7. Here, a kink in the distribution is visible around  $\log(H6) = 3.5$ , suggesting a different behavior of the instrument beyond this point. The most important result from this is the observation that  $m = \Delta \log(H7) / \Delta \log(H6)$  is larger for low counting rates. That

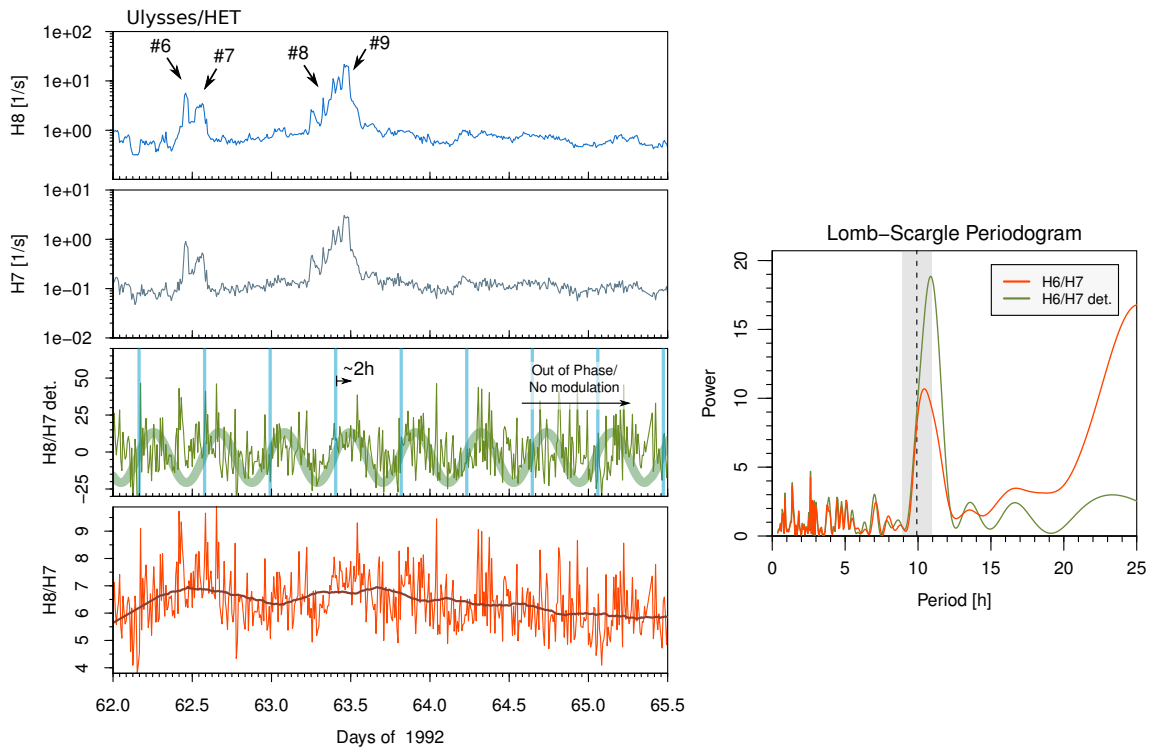


**Figure 8.16:** The same time interval as in Fig. 8.14 and 8.15 but for the HET’s H8 and H7 channel. This ratio shows a smoother behavior than the corresponding H6/H7 and is in good agreement with the KET data.

means, the H6 channel stays at a higher level when H7 decreases. This results in the high H6/H7 ratio displayed in the three dimensional scatter plot. During the transition from ambient fluxes to a Jovian jet event, the variation of the channel ratio due to the 10 h periodicity may be imposed by the instrumental effect. Depending on the time of the jet’s occurrence, both effects may annihilate to some extent, leading to distorted temporal evolution of the variations.

To come back to the events observed further away from the planet around days 110/112 in 1992, a pronounced signal near Jupiter’s rotation period is visible in the H6/H7 and H8/H7 ratios, although somewhat shifted with respect to the exact 10 h periodicity as shown in Fig. 8.13. A comparison with the corresponding KET analysis (Fig. 8.12) shows that no evidence for a  $\sim 10$  h periodicity can be found in the KET data in this overview plot. The time series shown in the left panel in Fig. 8.18 shows HET data, the right one KET data for this time interval. While the three Jovian jets are visible in the counting rates, a visual inspection of the E4/E12 ratio gives no evidence for the presence of the 10 h modulation. In H6/H7 ratio, however, a periodic variation is visible, in particular in the detrended ratio from day 110.5 to  $\sim 111.3$ . The related Lomb-Scargle periodograms reveals a surprisingly strong signal at  $P = 11$  h, i.e.

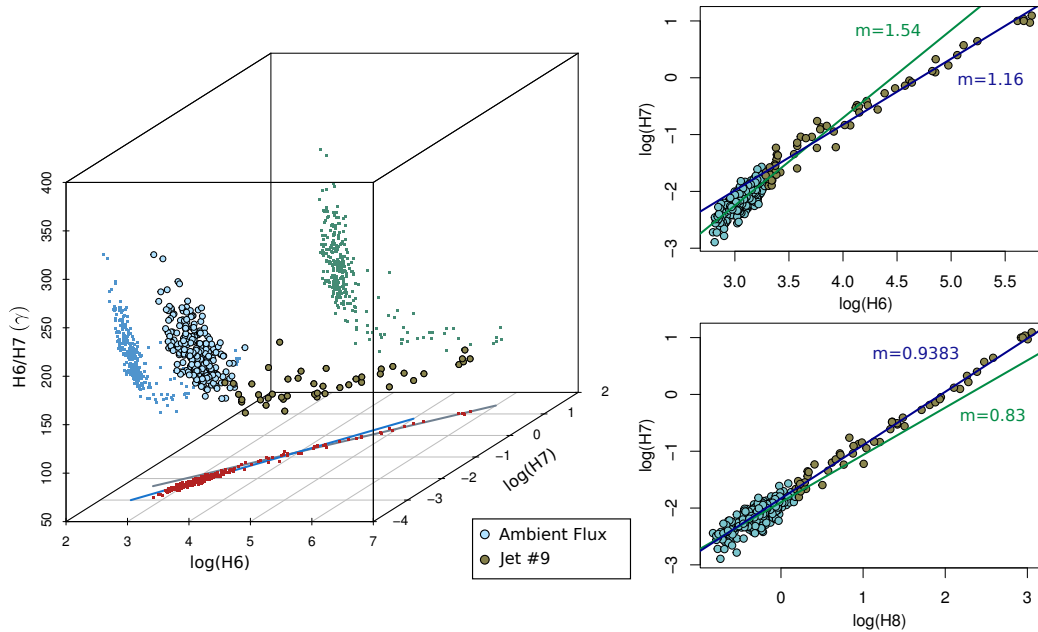


**Figure 8.17:** Left: the  $H6/H7$  ( $\gamma$ ) ratio as a function of the logarithms of the  $H6$  and  $H7$  counting rates. The brown dots indicate measurements during the occurrence of jet #9 of Ferrando et al. (1993), the cyan colored dots denote measurements of the ambient flux. As can be seen, the two samples show a different behavior in a way that the slope of  $\gamma(H6, H7)$  is much larger for the ambient flux than for the jet event. Right: scatter plots of  $\log(H6)$  vs.  $\log(H7)$  and  $\log(H8)$  vs.  $\log(H7)$ . While the slope of the distribution of ambient events is steeper than their jet-related counterparts for  $H6$  and  $H7$ , the slopes for the  $H8$  and  $H7$  distributions are more similar.

near Jupiter's periodicity. Interestingly, the finding of a periodicity of 11 h is confirmed by the periodogram of the KET data, albeit the signal strength is very weak compared to the HET data and the other events e.g. shown in Fig. 8.12. Indeed, superimposing a sine with a periodicity of 11 h on the data (thick red curve), shows a better fit to the HET data than assuming 10 h (thick green curve). A possible explanation for this observation are the rather low counting rates and the related noise level and the influence of background particles. In particular, a non-stationary background is expected disturbs the signal of interest. Furthermore, the electron enhancements around day 110.8 and 111.8 are rather broad and a clear assignment of random fluctuations and the 10 h spectral modulation is hard.

While the Lomb-Spectral analysis was found to be very helpful in detecting periodic patterns over a relatively long time interval, the results are of course not satisfying if the duration of the signal is too short to cover a full 10 h periodicity. Nevertheless, it is possible to find evidence for the presence of a Jupiter related periodicity in the

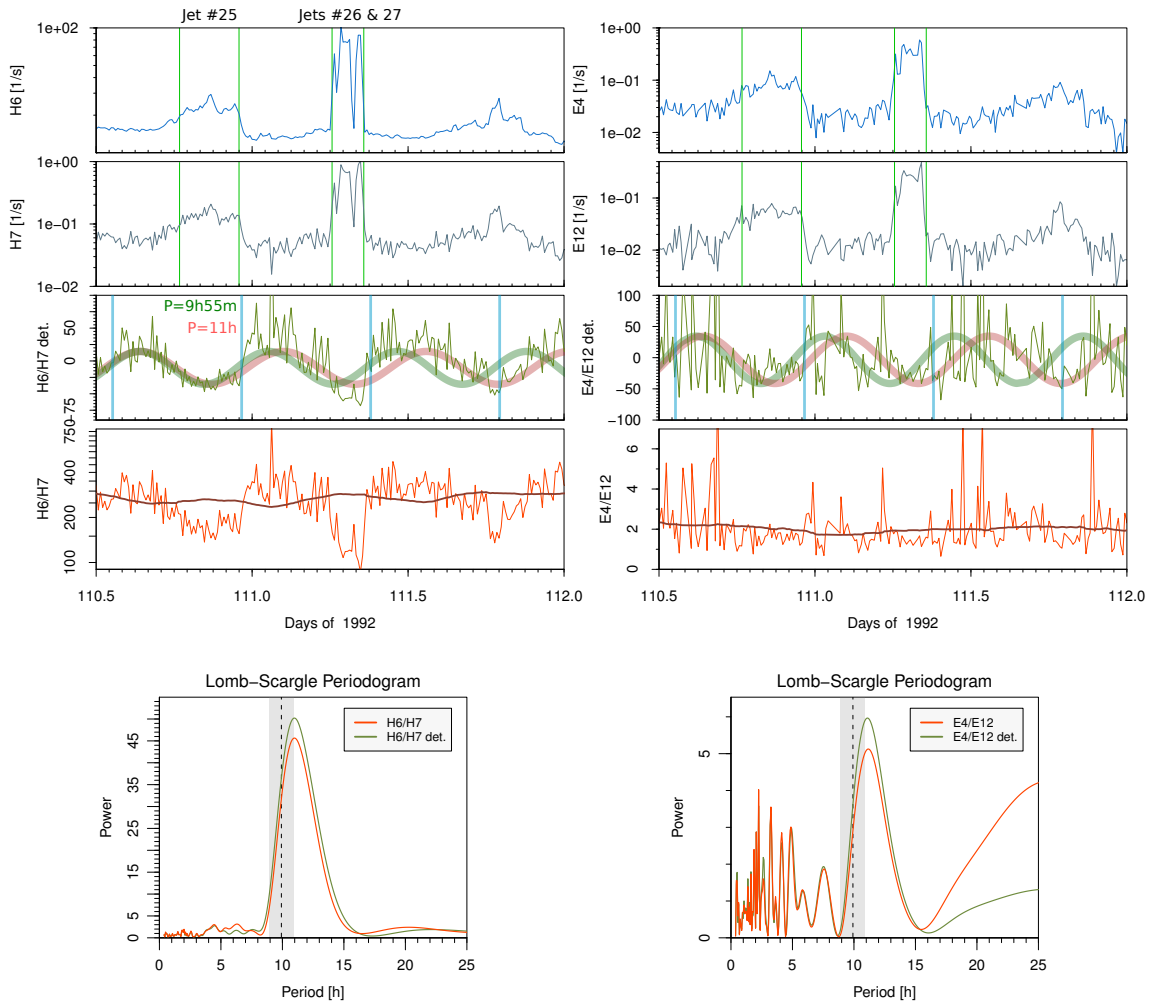


**Figure 8.18:** HET (left) and (KET) measurements covering day 110.5-112. A periodicity of 11 h is found in the HET as well as the KET data.

measurements by analyzing the time series with respect to typical features of the Jovian electron spectrum. In particular, the temporal evolution of spectral index is compared with a sine with periodicity of 10 h. Furthermore, an anticorrelation between counting rates and spectral index indicates the presence of an electron population carrying the spectral signature of the electrons in the Jovian magnetosphere. An example showing HET data of this is presented in the left panel of Fig. 8.19. The beginning of the Jovian jet (# 28, distance to Jupiter of 0.68 AU) is correlated with a jump in the magnetic field direction (red dashed line) and ends 80 mins later according to Ferrando et al. (1993) as indicated by the green solid line. However, it can be seen that the counting rates stay at a level significantly higher than the background up to day 123.8 with a local maxima at day 123.6, when a second jump in the IMF direction is observed.

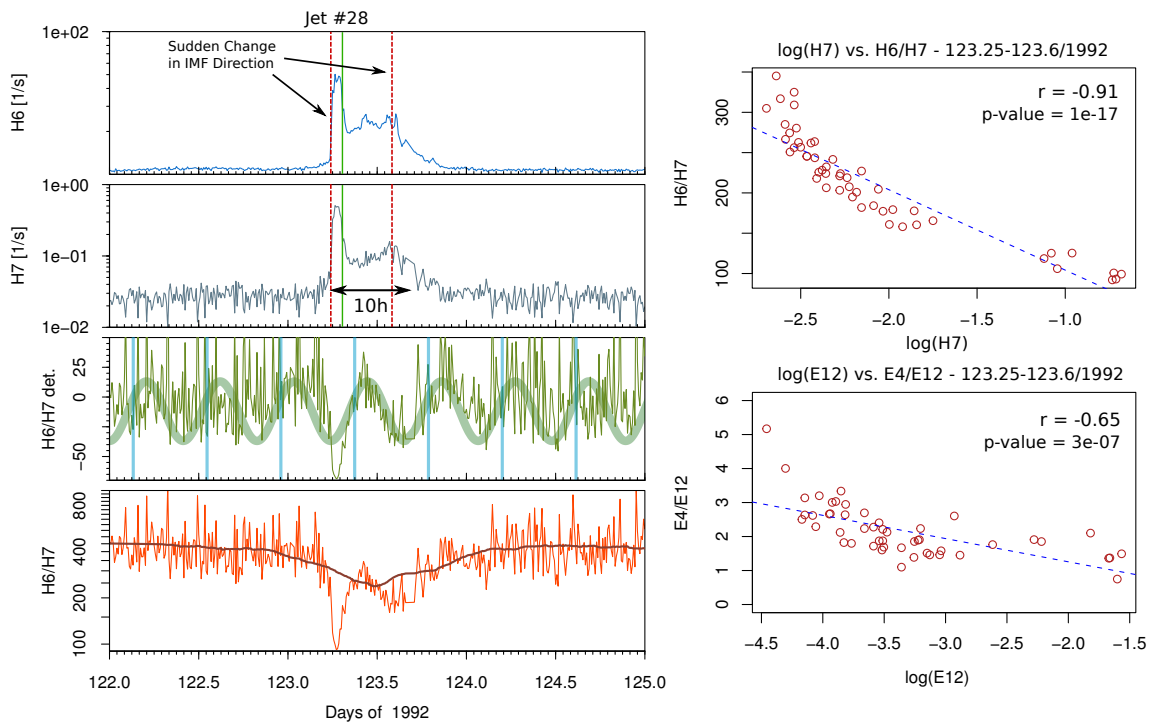


**Figure 8.19:** At almost 0.7 AU from Jupiter, Jovian jet # 28 shows evidence for a Jupiter-related spectral modulation, as illustrated by the HET data on the left side of the Figure. For about 12 h, an enhanced electron flux is visible, although only the first 80 mins (bounded by the left red and green vertical lines) had been classified as a Jovian jet by Ferrando et al. (1993). The H6/H7 ratio implies a spectral modulation with a periodicity of  $\sim 10$  h. The right panels show correlation plots of  $\log(\text{H7})$  vs. H6/H7 (top) and  $\log(\text{E12})$  vs. E4/E12. A significant anticorrelation is visible in both measurements. The  $r$  value is the correlation coefficient,  $p$ -value the corresponding confidence interval.

Looking at the H6/H7 ratio, an almost flat curve is visible until the onset of the jet, when a sudden drop in H6/H7 is visible, followed by periodic variation of about 10 h. This impression is supported by the green curve, showing a sine of that periodicity. This periodicity can be traced up to the end of day 123 and vanishes as the counting rates decrease. In addition, the undetrended H6/H7 ratio shows a gradual increase with time, indicating an increasing influence of background particles. The expected maxima of the spectral index (light blue lines) is in good agreement with the actually measured maxima, who lags by 1-1.5 h. The right top panel of the Figure shows a Pearson-correlation analysis of the logarithmic counting rates of the H7 energy channel and the H6/H7 ratio for the time period day 123.25-123.6. As can be seen, there's an unambiguous anticorrelation between both quantities ( $r = -0.91$ ). A similar result is found in the KET data. Here, the correlation coefficient is  $r = -0.65$ , resembling

the temporal evolution of MeV electrons in the Jovian magnetosphere. Based on this analysis, there is strong evidence that this Jovian electron jet (or burst, considering the extended event) still carries – previously not reported – the 10 h periodicity.

## 8.6 Ulysses' Second Flyby

### Overview of Spectral Modulation

The previous section showed that the previously reported occurrence of Jupiter's 10 h periodicity in space can effectively be recovered and extended using the Lomb-Scargle algorithm. This technique is now applied to the time period covering the second, more distant Jupiter flyby of Ulysses in 2003/04. Based on the findings from the 1992 time period, the presence of a 10 h modulation of the electrons's spectral index is expected during times of enhanced anisotropies, in particular during times classified as Jovian jets.

The 2004 time period from day 5 to 305 is shown in Figs. 8.20, 8.21 and 8.22, splitted into three subintervals of 100 days each. In the middle panel, day 105 to 205, two time periods of enhanced wavepower at  $\sim 10$  h can be identified. These time intervals are in coincidence with the occurrence of Jovian jets which are labeled according to the table in McKibben et al. (2007). Comparing the indications for

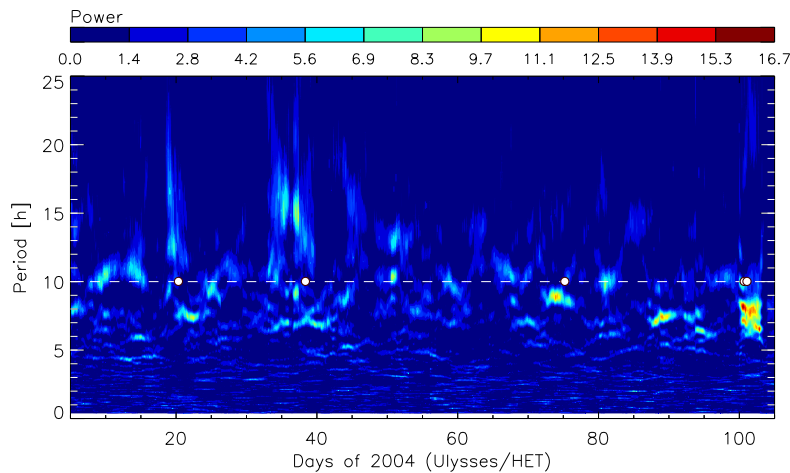


**Figure 8.20:** The "sliding" Lomb analysis for the detrended H6/H7 ratio from day 5 to 105 in 2004. During this time interval, no clear evidence for the 10 h periodicity related to Jovian jets (dots) exists.

the presence of a Jovian influence in the spectrogram for the first and second flyby, a general higher activity is evident for the first flyby. The most obvious interpretation is the fact that Ulysses was much further away from Jupiter during the second approach.



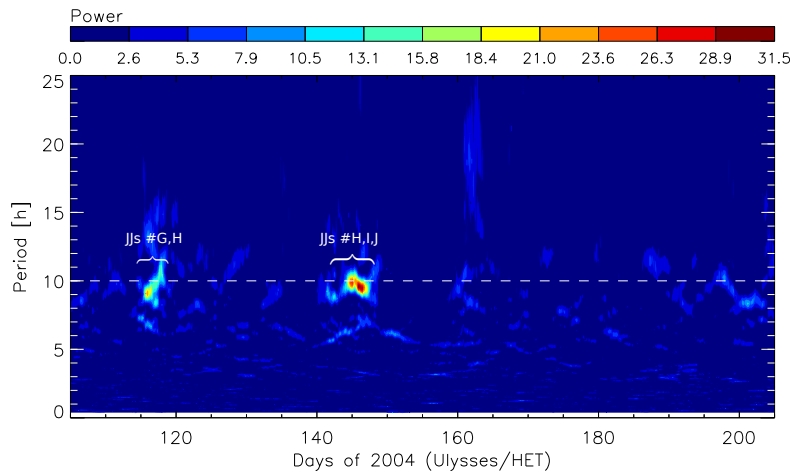


**Figure 8.21:** The "sliding" Lomb analysis for the detrended H6/H7 ratio from day 105 to 205 in 2004. Two time periods (around day 115 and 145) show a close correlation between the occurrence of Jovian jets (JJs) and enhanced wavepower at 10 h.

Indeed, while Ulysses did not come closer to the planet than 0.8 AU in 2003/04, all Jovian jets observed during the first flyby occurred within 0.8 AU.

### Spectral Variations of 10 h at $\sim 1.2$ AU From the Planet

The most striking evidence of a 10 h periodicity during the second flyby is observed between day 141 and 147 in 2004 when Ulysses was about 1.2 AU away from the planet. This time period is characterized by a general reincrease of Jovian electrons starting at day 140 after an interaction region has passed Ulysses as well as Jupiter and shows the presence of a continuous directional particle anisotropy of varying degree. During this time interval the Jovian periodicity can not only be recovered in the spectrum, but also in the counting rates themselves. This finding is in agreement with previous observations of Simpson et al. (1993), who found causal quasi-periodic peaks in the MeV-electron counting rates during the first Jupiter flyby but much closer to the planet ( $\leq 0.5$  AU). Fig. 8.23 gives an overview of the HET data collected during day 143.5 to 147. As in the previous Figures, the counting rates of two adjacent energy channels are plotted in the two top panels while their detrended and undetrended ratios are displayed in the bottom panels. The right panel displays the result of the Lomb-Scargle analysis for the respective time period. The result of this analysis, i.e. a clear 10 h signal in both the detrended and undetrended ratios, can unambiguously be recovered visually in the respective time series. Note that the periodic behavior is best pronounced when the counting rates are high, e.g. during the Jovian jet event labeled "I" because of the enhanced signal/noise ratio, in particular in the undetrended data.

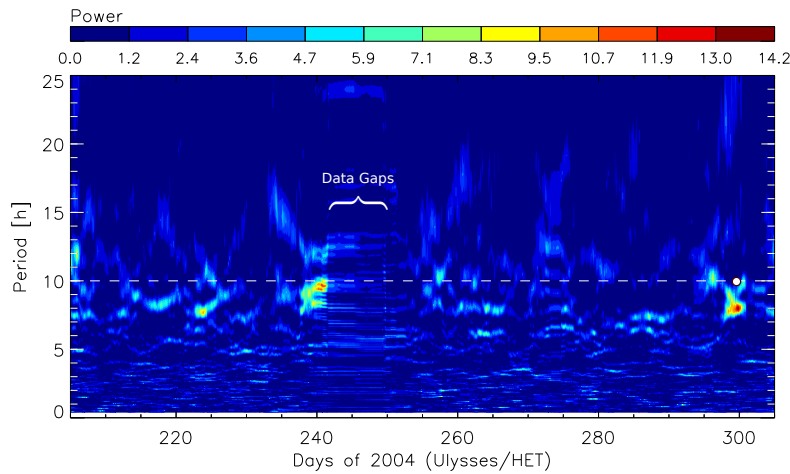


**Figure 8.22:** Wavepower versus time and period for days 205-305. During this time, only one Jovian jets was identified (day 299). An enhancement in wavepower is observed at  $\sim 8$  h, i.e. significantly shifted with respect to 10 h. Note that between day 240 and 250 considerable data gaps occurred, leading to a corrupted shape of the wavepower.

The sliding Lomb-Scargle representation of a time interval a little bit broader than in the previous Figure is shown in Fig. 8.24. Three Jovian jets are indicated by the labels #H, #I, and #J. Interestingly, an increase in wavepower at  $\sim 10$  h is evident during the first event, followed by a gap showing a decreasing wavepower at the Jovian periodicity. Around the beginning of day 144, however, the Jovian influence on the spectrum reincrease with a maximum during the occurrence of event #I and can be traced up to day 148, i.e. just after the occurrence of event #J. This example also shows that the Jovian rotation period can be recovered in the electron flux even during times where no flux enhancements qualifying as Jovian jets are detected. However, a further investigation reveals the existence of a persistent net flux of electrons coming from Jupiter, supporting the idea of a connection between particle anisotropy and the presence of the 10 h periodicity. To investigate the occurrence of long-lasting anisotropies, the sector plots alone are not sufficient, because they only contain the anisotropy information for a single time interval. A more appropriate way, however, is to plot the fitted anisotropy of first order as a function of time. For this task, a proper accumulation interval must be chosen, balancing the desire for enough counts to keep the error bars small and a resolution high enough that the anisotropy will not be smeared out. For Fig. 8.25, an accumulation time of 240 min had been chosen. The sectorized H7 data used for this analysis were fitted by a Fourier-series and the resulting first-order anisotropy coefficient  $A_1$  was then plotted as a function of time (gray solid line) including the uncertainty estimated by the fitting procedure (light gray region). Comparing this Figure with the corresponding sliding Lomb analysis, a correlation

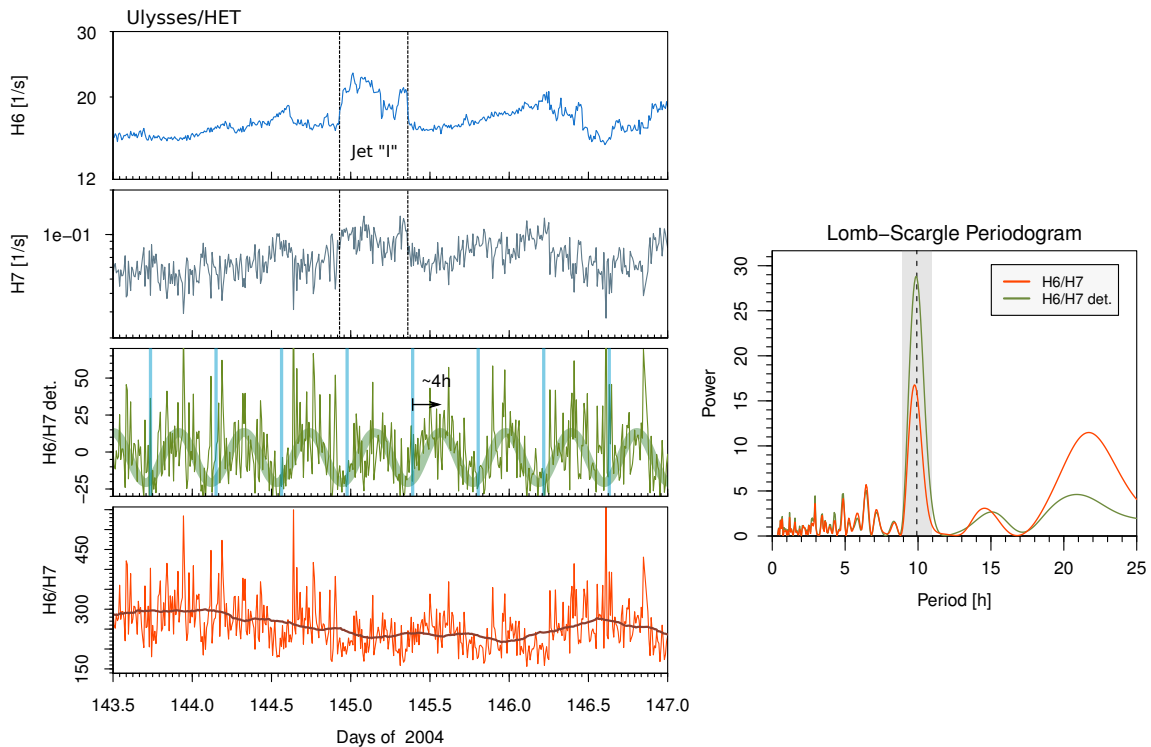


**Figure 8.23:** HET data covering day 143.5 to 147 in 2004 including event "I" of McKibben et al. (2007). A clear 10 h periodicity is visible throughout the plotted time interval being best pronounced in the detrended H6/H7 ratio. The result of the Lomb-Scargle analysis (left figure) verifies this observation: The Jovian periodicity is matched almost exactly.

between the presence of the 10 h and anisotropy is directly visible. The interval of enhanced anisotropy in Fig. 8.25 bounded by the dashed lines is congruent with the time interval where the 10 h periodicity is present. The relatively well pronounced events #I and #J can be identified by the peaks in the anisotropy while the weaker event #H does show an anisotropy above the enhanced level of anisotropy that is present for the  $\sim 6$  days bounded by the dashed lines. Note that the gap in the 10 h periodicity on day 142 is in coincidence with a significant decrease of the anisotropy, emphasizing the relation between both observable parameters.

The related sector plots are shown in Fig. 8.26 displaying on the sector distribution of the E4 channel for three time intervals. The middle panel shows the same sector distribution for the jet #I. The orange arrow points to Jupiter, the red one represents the mean magnetic field, while the blue arrow is the fitted axis of anisotropy of first order  $\phi_1$ . The individual magnetic field measurements (1 min averages) are represented by black stripes. Since the radius of the segments is proportional to the counting rates, the figure illustrates that the particles are streaming away from Jupiter during

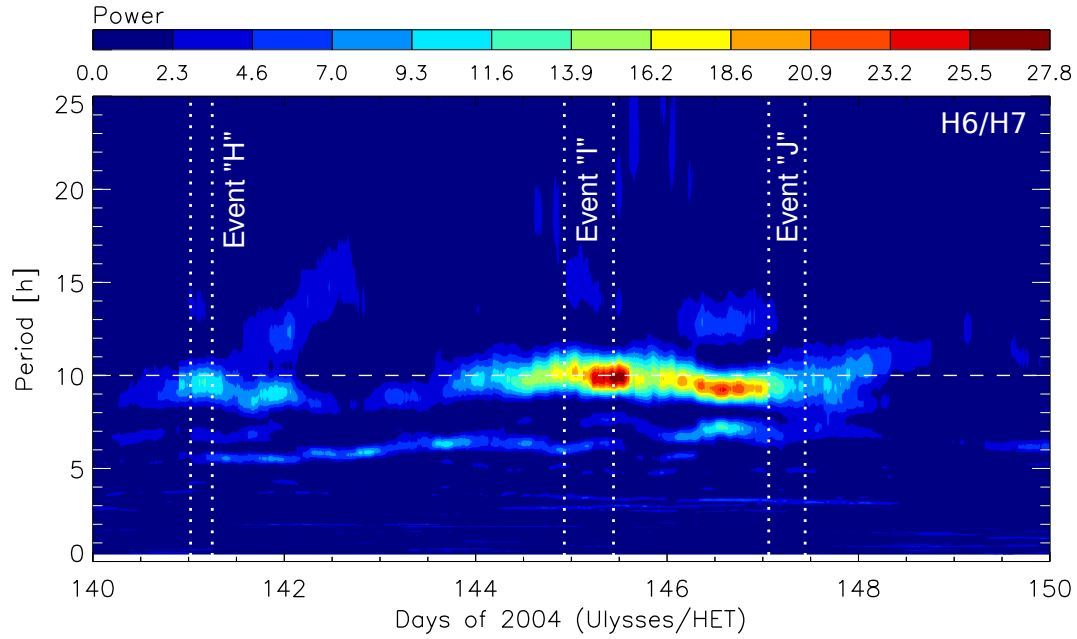


**Figure 8.24:** This plots shows the result of the sliding Lomb analysis applied to the detrended H6/H7 ratio covering the time interval from day 140 to 150 in 2004. A clear  $\sim 10$  h periodicity is visible in the appointed time interval. The three Jovian jets found in this time interval are bounded by dotted vertical lines and labeled according to table 1 in McKibben et al. (2007).

all times. The calculated anisotropies of the three time periods are  $A_1 = 14.6 \pm 2.8\%$  and  $34.2 \pm 5.7\%$  and  $20.3 \pm 1.0\%$ , respectively.

Another interesting fact that can be well observed during this time interval is the anticorrelation between H6/H7 and the counting rates, i.e. the spectral index decreases if the counting rates increase, according to the variation of the electrons trapped in the Jovian magnetic field. Consequently, the counting rates and the H6/H7 ratio are expected to be anticorrelated while the autocorrelation of the counting rates implies a periodic pattern. Both is true, at least for H7, as can be seen in the two panels of Fig. 8.27. The H7 channel shows a recurrent autocorrelation for multiples of a lag of 10 h, implying a increase and decrease of particle flux every 10 h. No such modulation, however, is evident for H6, except for an anticorrelation for a lag of  $\sim 5$  h. This may be related to the presence of background particles, resulting in a non-stationary distribution and a generally high level of fluctuations. Considering the cross correlation of H7 and H6/H7, a definite anticorrelation every  $n \cdot 10$  h with  $n \in \mathbb{N}$  is visible as well as a correlation every  $(n + \frac{1}{2}) \cdot 10$  h, i.e. the spectral index increases when the fluxes decrease and vice versa. During this time interval, the modulation seems to be mainly related to variations of the H7 energy channel.

In the Jovian magnetosphere, all energy channels show a significant temporal vari-

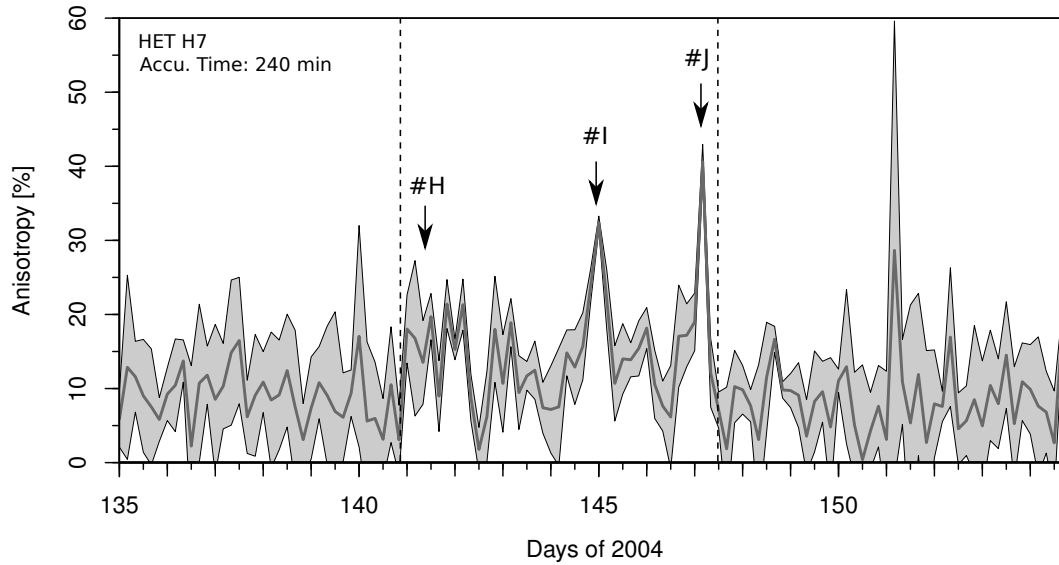


**Figure 8.25:** The  $A_1$  coefficient of the sectorized H7 data as a function of time for the time interval day 135-155/2004. During the interval bounded by the dashed lines, a persistent anisotropy well above the background is visible, suggesting a net flux of Jovian electrons from Jupiter for about 6 days.

ation. However, it can be shown (cf. chapter 7) that the strongest modulation is related to higher energies. In principal, a temporal variation would also be visible if only one of the two energy channels taken into account to calculate the spectral index shows a periodicity. The temporal variation of the higher energy channels with  $\sim 10$  h can convincingly be recovered in the respective timeseries as shown in Fig. 8.28. Here, the detrended H7 data are shown in gray, the green curve represent the smoothed detrended H7 data. The dashed vertical lines indicate the 10 h cycle. As can be seen, a periodic behaviour of the counting rates close to 10 h is evident, suggesting a periodic injection of Jovian electrons into the heliosphere.

The time interval from day 143 to 147 is the most distant one (1.2 AU) where the 10 h periodicity can be observed. Comparable results were reported by e.g. Chenette et al. (1974), Ferrando et al. (1993) and Simpson et al. (1993) who found the 10 h periodicity up to  $\sim 0.8$  AU in the data of the Pioneer and Ulysses Jupiter flyby, i.e. the observations shown here extend the limit of determination of the 10 h periodicity by a factor of  $\sim 1.5$ . However, in the chapter 8.6 after the next we discuss the presence of this periodicity even at 2.2 AU, even though not over a time interval of several days.

### A Weak Modulation at 1 AU From Jupiter

Another example to be discussed is the time period between days 115 and 118 in 2004. The result of the sliding spectral analysis reveals a prominent increase in wavepower

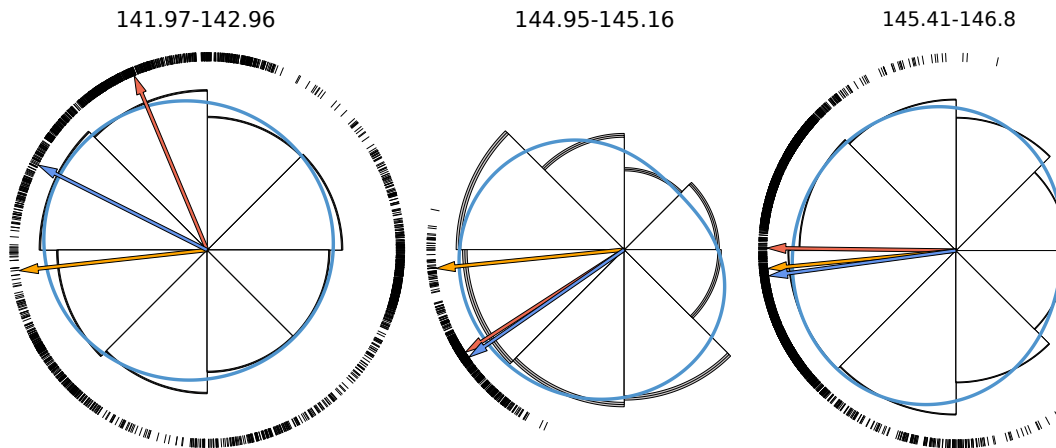


**Figure 8.26:** Three sector distributions of the E4 channel from day 141.97 to 142.96 (left), from day 144.95 to 145.16 during the jet #I (middle panel) and from day 145.41 to 146.8. See text for details.

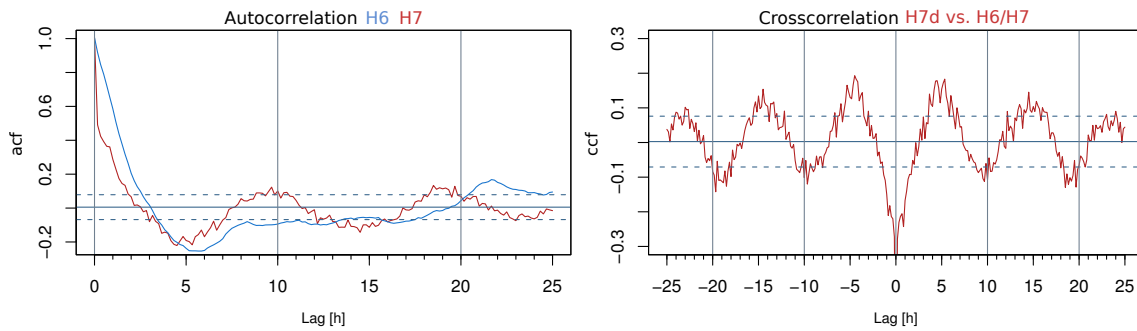


**Figure 8.27:** The left panel shows the autocorrelation of the H6 (blue) and H7 (red) channels, respectively. The right panel shows the crosscorrelation of H7 and H6/H7. The dashed horizontal lines indicate the 95% confidence level.

close to 10 h during this interval. Similar to the data analyzed before, there is no evidence for a 10 h periodicity before and after day 115-118. Note that the periodicity of maximal wave power does not exactly match the 10 h but is slightly below ( $\sim 9.5$  h) or above ( $\sim 10.8$  h). A possible explanation of this finding may be the fact that there is a discontinuity in the phase of the 10 h modulation as can be seen in Fig. 8.30. Here, the detrended H6/H7 ratio reveals the presence of the 10 h periodicity, however, the two sine functions added to the plot illustrate the discrepancy in phase of about 2 h. Similar phase shifts were also observed by Simpson et al. (1993) in 1992. Under the assumption of the “clock” hypotheses of the spectral modulation of electrons in the Jovian magnetosphere, stating that the spectral modulation is predominantly a function of time and not of position, the observed phase shift can be interpreted as a

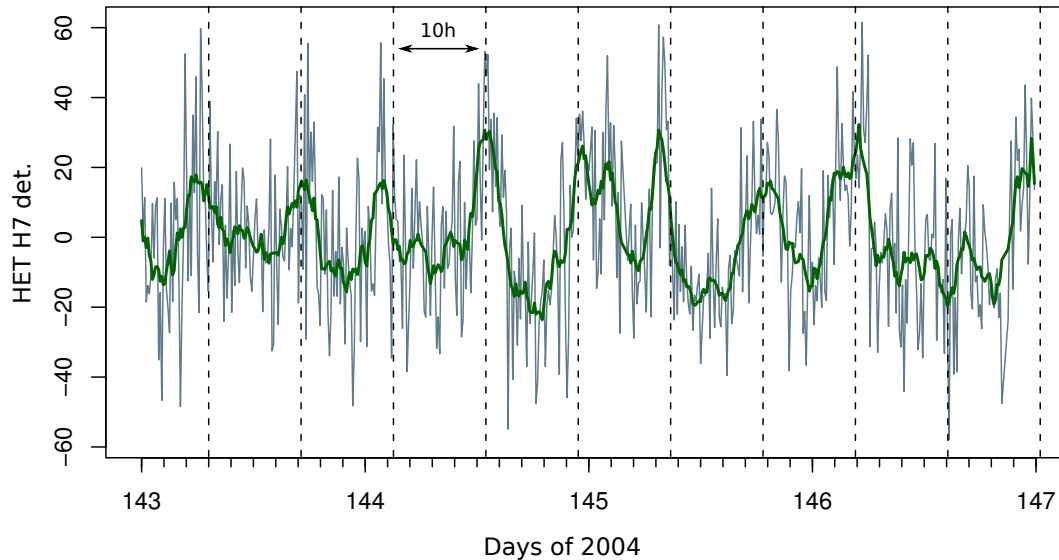


**Figure 8.28:** Detrended H7 counting rates and a smoothed version of the data. The dashed vertical lines are 10 h apart from each other. As can be seen, the counting rates show a 10 h periodicity.

propagation effect. The phase shift would then depend on the distance between the source and the observer as well as the mean parallel speed of the particles with respect to the magnetic field. The particles' mean parallel speed does not only depend on the initial pitch angle but also on the degree of scattering of the particles. Furthermore, the phase shift may be related to instrumental effects. This mainly addresses the influence of the  $\gamma$ -ray background to the HET and KET instruments in combination with a non stationarity of the background electron flux.

The calculated anisotropies derived from KET E4 are shown in the bottom panel of Fig. 8.29. The general degree of anisotropy within the time interval where the 10 h can be detected barely exceeds the background level, except for jet # G, that can clearly be identified by an increase in anisotropy. Concerning the KET data during this time interval, no evidence for a 10 h variation of the E4/E12 ratio could be found. This can be explained by the low counting rates of the KET during this time, and thus a lower statistics. During the time period day 143-147/2004, the background flux was twice the flux observed during this time period. The HET, however, benefits from its larger opening angle and higher counting rates. Sector plots for this time interval are shown in Fig. 8.31. During the two jets (inlet A and D), clear anisotropies are visible in the KET data. The time interval B shows no evidence for a net flux of particles, and the fitted axis of anisotropy is disaligned with respect to the magnetic field. During time interval C the axis of anisotropy matches the magnetic field line very well. The anisotropy, however, is weak ( $\approx 10\%$ ). A cross correlation analysis of the data between days 115 to 117/2004 (Fig. 8.32) also shows the presence of a periodic modulation

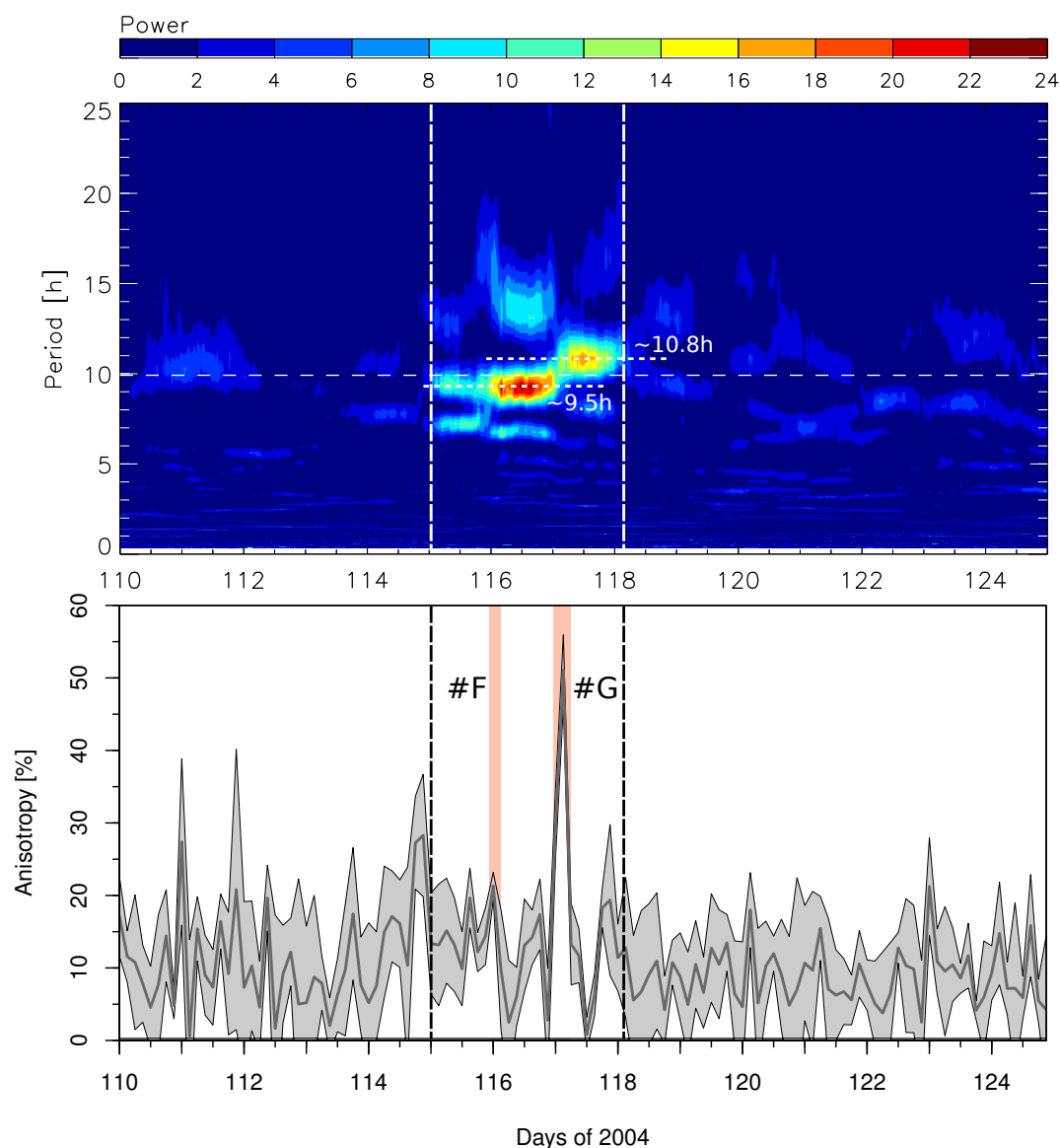


**Figure 8.29:** Top: “Sliding” spectral analysis from day 110 to 125 in 2004. Enhanced wavepower close to 10 h can be observed between days 115 and 118. The bottom panel shows the directional anisotropy. Note that the anisotropy is fairly weak.

of the detrended H7 counting rates and the spectral index according to the results discussed in the previous section.

### Evidence for the 10 h Periodicity at 2.21 AU?

The most distant Jovian jet observed so far occurred on day 299 in 2004. At this time, Ulysses was already 2.21 AU away from Jupiter on its way to the third solar polar



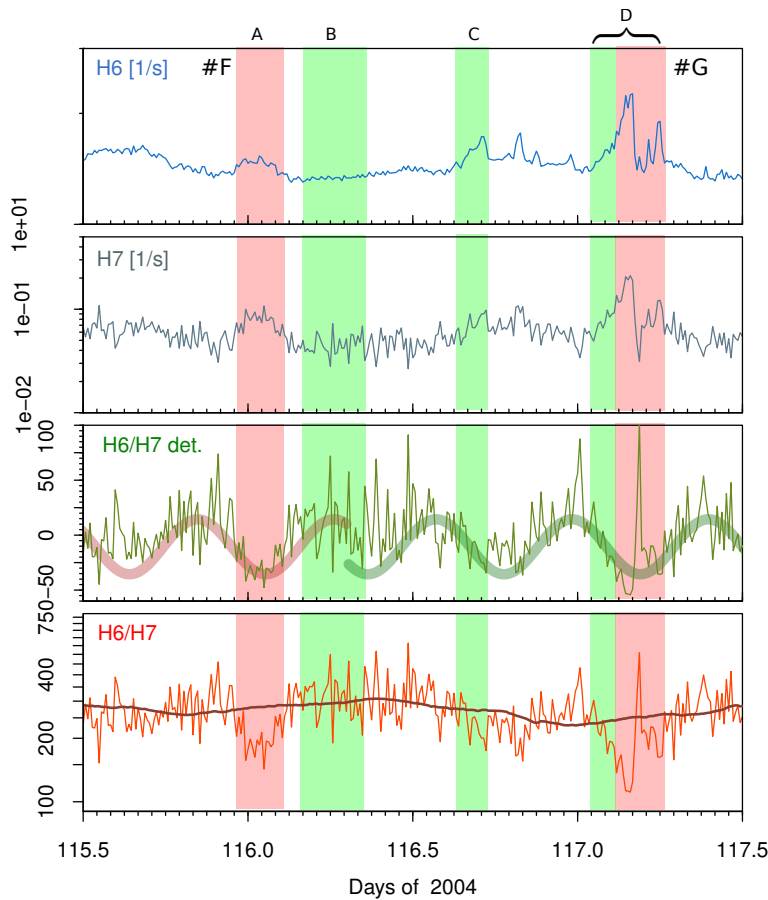


**Figure 8.30:** HET data for days 115.5-117.5/2004, including the jets # F & H (red shapes). The letters and the corresponding red or green shades refer to the sector diagrams in Fig. 8.31.

pass. In the last section the presence of the 10 h periodicity at distances of at least 1.2 AU away from Jupiter was discussed. In the following we will pursue the question if the Jupiter's periodicity is retained in the energy spectrum of jet electrons as far away as 2.2 AU.

Fig. 8.33 shows KET data of the mentioned Jovian jet. The inner dashed vertical lines indicate the on- and offset of the event. The blue lines in the panels showing the detrended  $E4/E12$  ratio indicates the predicted times of maxima based on the “clock” hypothesis.

A visual inspection of the KET data show that the detrended as well as the undetrended  $E4/E12$  ratio obtain a suspicious temporal evolution from day 299.1 to 299.5. This impression is fortified by the fact that the curve is in excellent agreements with the predicted maximum of the spectral index and the sine function plotted on top of the data.

To confirm or reject the visual impression using a more objective method, the data

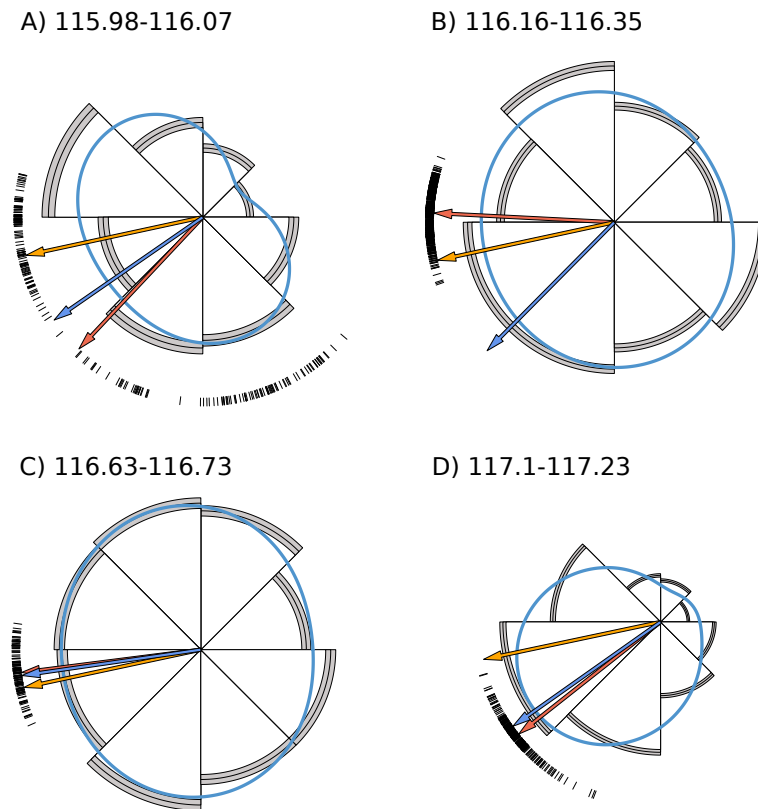


**Figure 8.31:** Sector diagram for the time interval marked in Fig. 8.30 in the same format as for Fig. 8.26. See text for discussion.

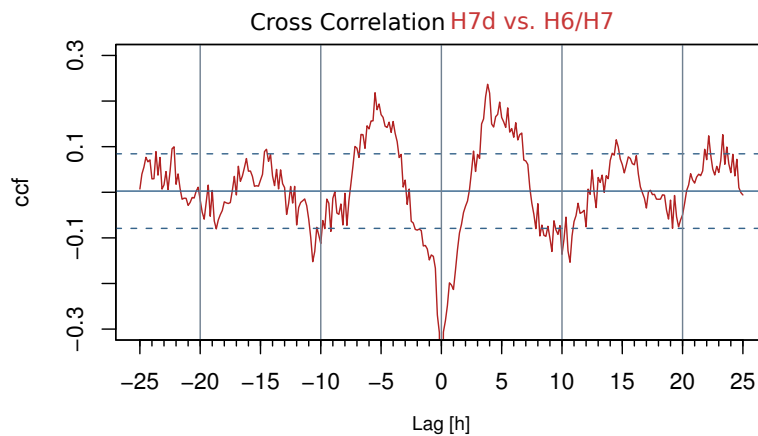


**Figure 8.32:** Cross correlation of H7 and H6/H7 as for days 143.5-147/2004. Albeit less pronounced, an anti correlation with a periodicity of  $\sim 10$  h is present.

will be fitted and tested against the hypothesis that they can be described by a 10 h periodicity. In particular, this technique is helpful if one investigates a time period that is too short to be analyzed with the Lomb-Scargle algorithm or the phase shift of

the periodic variation is different from a point of reference of a phase histogram. For the fitting procedure we used a cosine of the form

$$g_{fit} = a \cdot \cos\left(\frac{2\pi}{P}(t - t_0)\right) + c, \quad (8.3)$$

where  $a$  is the amplitude,  $P = 35733.12$  s is the periodicity,  $t$  is the time and  $t_0$  the phase while  $c$  represents the offset, i.e. we have three constraints and therefore  $d = n - 3$ , where  $d$  is the degree of freedom and  $n$  the number of bins used for the computation. Based on the  $\tilde{\chi}^2$  derived from the fitting procedure, the data set is tested against the hypothesis that it can indeed be described by a cosine, i.e. if it shows a periodic variation. However, it should be kept in mind that the reliability of a fit depends on the number of data points and, given a periodic function, the number of cycles covered by the data set. In order to find reasonable values for the weighting that enters the fitting procedure and affects the  $\tilde{\chi}^2$  test, it is necessary to derive the error of  $g_{data}$  that depends of the counting rates of two channels that are both affected by uncertainties. To determine this error, it is assumed that the counts accumulated by channel during an integration time underlies Poisson statistics, hence

$$\text{counts} = \overline{\text{counts}} \pm \sqrt{\text{counts}}, \quad (8.4)$$

where  $\overline{\text{counts}}$  denotes the mean counts, i.e. the actually measured counts. In Poisson statistics,  $\sqrt{\text{counts}}$  equals the standard deviation. The propagation of the uncertainty by computing the ratio of two channels can be calculated by (cf. Taylor, 1997, p. 52)

$$g_{data} = \frac{\text{counts}_1}{\text{counts}_2} \left( 1 \pm \underbrace{\left( \frac{\sqrt{\text{counts}_1}}{\text{counts}_1} + \frac{\sqrt{\text{counts}_2}}{\text{counts}_2} \right)}_{\text{fractional error}} \right). \quad (8.5)$$

The data were fitted using a nonlinear least-square method (Gauß-Newton algorithm) as well as a linear least-square method<sup>7</sup>. Both algorithms resulted in the same set of fitted parameters. Fig. 8.33 shows the results of the fit procedure. The bottom panel shows the counts of the KET's E4 and E12 channels for an accumulation interval of 600 s. The third panel shows the E4/E12 ratio while the panel on top displays the standard derivation as given by Eqn. (8.5). According to the previous plots, the dashed lines and the corresponding orange sinusoid in the middle panel show the times of maxima of the E4/E12 ratio derived from the "clock". The red curve segment bounded by the two dashed vertical bars is the result of the fit. As can be seen, the fit is in good agreement with the predicted temporal evolution of E4/E12. The fitted curve trails the model by about 30 min in phase. The value of  $\tilde{\chi}^2$  is 0.83. This is a

<sup>7</sup>A function of the form  $y(x) = a \cdot \cos(x + b)$  can be linearized by using the angle addition formula  $\cos(x \pm b) = \cos x \cos b \pm \sin x \sin b$  and by the substitutions  $\bar{x} = \cos x$ ,  $\tilde{x} = \sin x$  and  $\bar{b} = \cos b$ ,  $\tilde{b} = \sin b$ . The new function then reads  $y(\bar{x}, \tilde{x}) = \bar{b}\bar{x} + \tilde{b}\tilde{x}$ .

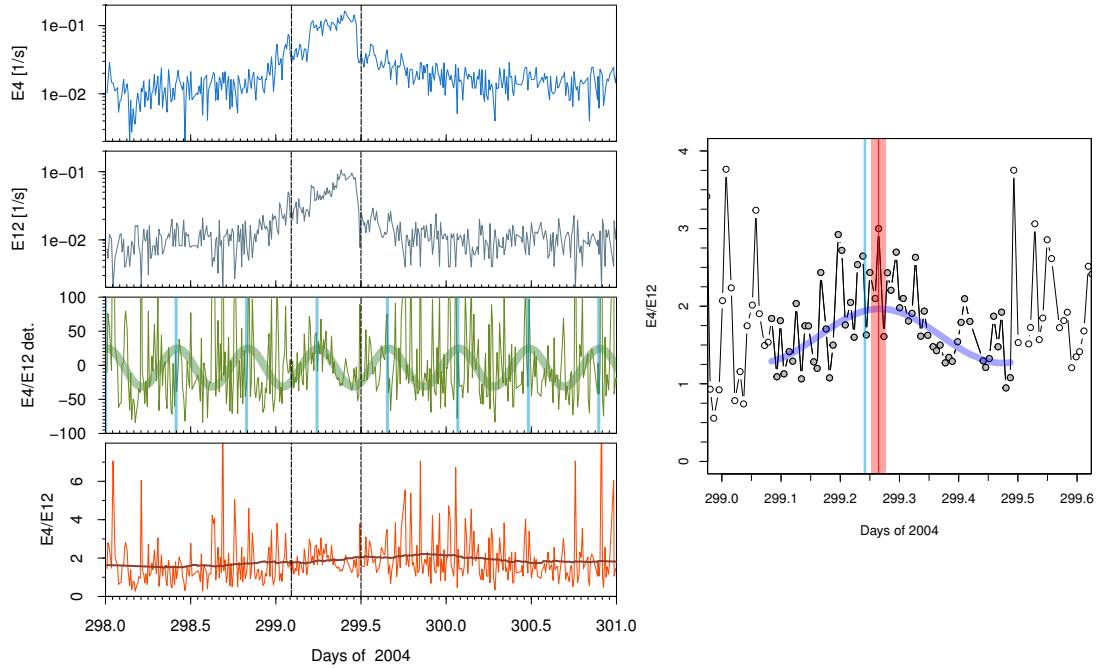


**Figure 8.33:** The left panel shows counting rates of KET’s E4 and E12 channel as well as their detrended and undetrended ratio. The interval bounded by the dashed lines gives the impression of a sine-like variation confirmed by a visual fit of a sine function with a period equal to the Jovian rotation period. The right panel shows the undetrended E4/E12 ratio in the time interval of interest.

surprisingly good result but has a sobering explanation: The standard deviation of the E4/E12 ratio that enters the computation of  $\tilde{\chi}^2$  is relatively high and of the order of  $\sim 0.5$ , reducing the reliability of the result<sup>8</sup>. It is also clear that it would make no sense to fit the temporal evolution of E4/E12 before and after the jet event because of the very high noise level. Nevertheless, the result of fitting the data emphasizes the visual expression of a spectral modulation of the Jovian electrons during this jet event 2.21 AU away from Jupiter. The fact that the phase shift between the ”clock“ model and the fitted data is very small indicated that the propagation of the electrons during this event was almost scatter free, i.e. the mean free path of the particles must be equal or larger than the distance between Jupiter and the observer. It is not surprising that the best pronounced periodic variation of the spectral index is observed when the counting rates are highest, since high counting rates refer to good statistics and therefore a good signal/noise ratio.

<sup>8</sup>This is a dilemma of the space-borne observation of high energetic particles: rather low counting rates and the generally unreproducible nature of measurements.

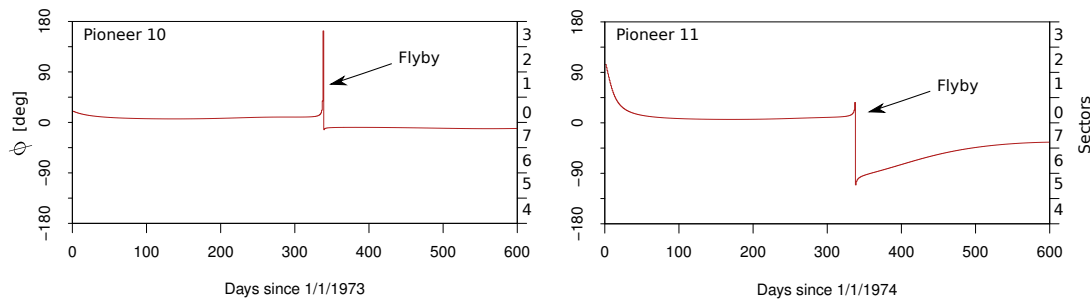


**Figure 8.34:** The red curve shows the location of the viewing direction from the spacecraft to Jupiter projected on the spin plane for the case of Pioneer 10 starting at 1973.0. The right ordinate indicates the location of the Pioneer 10/11-Jupiter connection with respect to the eight segments, the left ordinate the corresponding angle.

## 8.7 Jovian Jets Observed by Pioneer 10

Encouraged by the observations made by Ulysses, a reinvestigation of the Pioneer 10 data with respect to Jovian electron jets was performed and the results will be discussed in the following. In fact, it turned out that there are events in the Pioneer 10 data quiet similar to what was reported by Ferrando et al. (1993) and McKibben et al. (2007). Indeed, time intervals of enhanced transient Jovian electron fluxes with or without the presence of a 10 h rocking of the energy spectrum had already been copiously elaborated by Chenette et al. (1974). However, the authors generally computed the anisotropies of the measured electrons on rather long time intervals. As will be shown in the following almost all events that may be classified as “Jovian jet” are subsets of time intervals already noted by Chenette et al. (1974) to be of enhanced Jovian influence.

For the further analysis we made use of MeV-electron data obtained from measurements of the University of Chicago instruments (CPI) aboard the Pioneer 10 and 11 spacecraft (cf. chapter 5). In this work the sectorized counting rates of the D5N6 channels measuring electrons from 6-30 MeV (but also protons of energies from 29-67 MeV) and the ID4 and ID5 channels counting electrons in a range of energy from 2-7 and 6-30 MeV, respectively were used. The time resolution of the sectorized electron data is 30 minutes, that of the omnidirectional ID4 and ID5 counting rates is 15 minutes.

Figs. 8.34 and 8.35 show information on the orientation of the particle instrument close the Jupiter flyby. The red curves in the left and right panel in Fig. 8.34 show the projection of the direction to Jupiter on the spin plane for Pioneer 10 and 11, respectively (Pioneer 11 is shown for comparison). For the case of Pioneer 10, the direction to Jupiter is located in sectors 0 or 7, i.e. it is expected to find the axis of symmetry of electron anisotropies in this sectors. Fig. 8.35 shows a sketch of the view cone of the instrument (as seen from top) with respect to the spin axis of the spacecraft

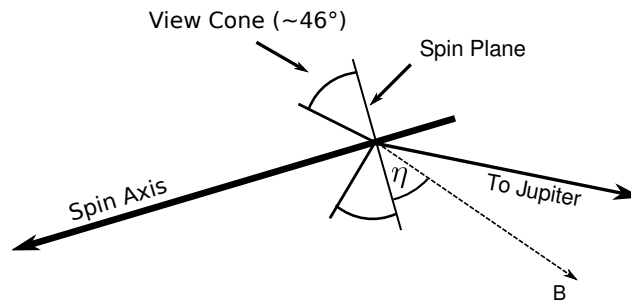


**Figure 8.35:** The orientation of the CPI aboard Pioneer 10 about 90 days before the Jupiter encounter adapted from Chenette et al. (1974). The half width of the instrument aperture cone for particles that triggers the D5N6 logic is  $\sim 23^\circ$  (McKibben, private communication; see also Hamilton (1977) for a sketch of the detector system).

pointing to Earth as well as the approximated direction to Jupiter.

Magnetic field data were obtained by the Vector Helium Magnetometer (VHM) described by Smith et al. (1975) and the solar wind data by the Plasma Analyser Instrument (Wolfe et al., 1974). The data we used in this work were provided by the National Space Science Data Center<sup>9</sup>.

We investigated the time period the first occurrence of quite time electrons (day  $\sim 100$  in 1973) to the end of 1974 for Pioneer 10. Jovian jets are identified by a significant increase in flux, an alignment between the magnetic field vector and Jupiter as projected on the spin plane as well as an notable increase in anisotropy. Because the time resolution of the available electron data is limited to 30 minutes, this leads to restrictions in the identification of jet events. The mean duration of the events reported by Ferrando et al. (1993) is about 30 minutes. This makes clear, that jets of a comparable duration are barely detectable because the time profile as well as the anisotropy is smeared out. Additionally, it is questionable whether or not a jump in flux and anisotropy in a single time bin can unambiguously be attributed to a jet event. Two neighboring jets separated by a gap close to the time resolution of the data may also lead to the fact, that some independent events are interpreted as a single event. Therefore, it is not surprising that the events presented here are of longer duration than the ones of Ferrando et al. (1993). Indeed, several events resemble long lasting jets seen by Ulysses, like the events on day 15 or 141/142 in 1992 with durations of 317 and 590 minutes, respectively. Furthermore, a low time resolution leads to generally flatter and less spiky jet structures. Some electron increases that can not unambiguously defined to be Jovian jets (e.g because of insufficient anisotropies or a misalignment of the magnetic field with respect to the detected anisotropies) were detected but not included in Tab. 8.1.

<sup>9</sup>[ftp://nssdcftp.gsfc.nasa.gov/spacecraft\\_data/pioneer/](ftp://nssdcftp.gsfc.nasa.gov/spacecraft_data/pioneer/)

Pioneer 11 data were also investigated. Beside several typical Jovian jet events, the data show the existence of two MeV electrons bursts of the duration of  $>2$  days (Conlon, 1978). These burst show a quasi-periodic time profile of 10 h in the counting rates as well as temporarily anisotropies. In addition, these bursts are accompanied by the presence of strong MHD waves (Smith et al., 1976). These events are not part of the present work.

When analyzing experimental data one is sometimes confronted with some ambiguity concerning the classification of events. As noted by Haggerty and Armstrong (1999) or McKibben et al. (2007), according to the worker's criteria, some events may not be counted as upstream events or Jovian jets, even if they strongly resemble those type of events. This may be also the case for the Pioneer data presented in this section. Therefore, Tab. 8.1 may either not be exhaustive or maybe contain events that other researchers with different criteria would have been dropped from their list. In the following the discussion is restricted to Pioneer 10 events as the Pioneer 11 data contain no fundamental new insights despite the presence of strong MHD waves during some events mentioned above. These events are beyond the scope of this work.

## 8.8 Overview of the Pioneer Events & the 10 h Modulation

Analogous to Fig 8.1, Fig. 8.36 shows the trajectory of Pioneer 10 close to Jupiter (pink curve) in combination with the occurrence of Jovian jets and the time intervals described by Chenette et al. (1974). The sense of the spacecraft's motion is indicated by the small arrows near the trajectory. The occurrences of Jovian jet events are labeled by the green circles. The Jovian magnetosphere is represented by the yellow shape assuming a sunward extension of  $100 R_J$ . The red curves indicate nominal Parker spirals for different typical solar wind speeds.

Similar to the Ulysses observations, the Pioneer events are not uniformly distributed along the trajectory but show some clustering. Indeed, as will be shown in the following, several events occur within a narrow time window. In total, 16 events entered Tab. 8.1 providing an overview of the detected Jovian jets. This table contains the consecutive number of the events, their starting time and duration as well as the degree of anisotropy and the distance from Jupiter. Compared to previous work (Dunzlaff et al., 2009), two events were added, two previously distinct events were merged and two were dropped from the compilation because of new insights gained from the analysis of the magnetic field not taken into account in the mentioned conference contribution. The anisotropies were derived in the same way as for the Ulysses data and are calculated for the entire duration of an event.

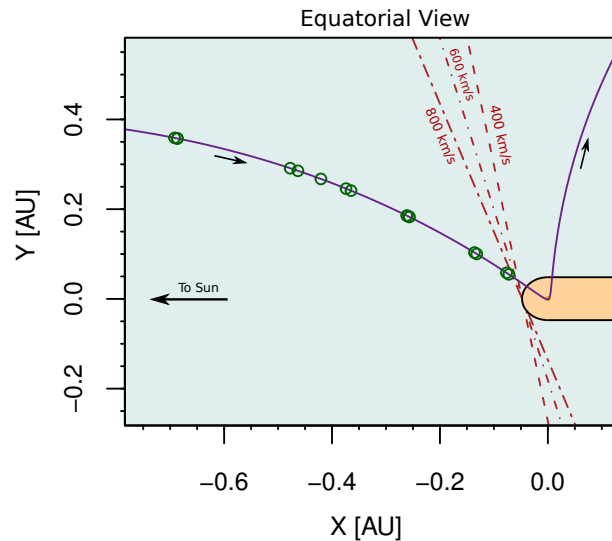


**Figure 8.36:** Trajectory of Pioneer 10 around the Jupiter flyby in a coordinate system in which the planet and the Sun are fixed. The green circles indicate Jovian jets. The red lines denote Parker spirals for typical solar wind speeds.

## 8.9 Short Lived Events in the Pioneer Data

The first event to be discussed in this section is a jet observed by Pioneer 10 that occurred on day 317 in 1973, i.e. 13 days before the contact with the Jovian magnetosphere. At this time, the spacecraft was already located relatively close to the planet with a distance of about  $268 R_J$ , i.e.  $\sim 160 R_J$  upstream from the bowshock.

Fig. 8.39 shows a time interval covering day 315 to 320 in a format according to the Ulysses plots. The three panels in the top show the magnetic field and the solar wind speed, the color-coded panel the sector distribution of the D5N6 (cf. section 5.3) coincidence as well as the projection of the magnetic field vector on the spin plane and the direction to Jupiter. The bottom panels displays the counting rates of the ID4 and ID5 channels. As can be seen, at day 317.1, a sudden increase of the electron flux is detected lasting for about one hour. This event is embedded in a smooth increase of electrons starting at day  $\sim 317.6$ . A good alignment of the direction of the magnetic field and center of the anisotropy is visible as well as a good correlation with the line-of-sight connection to Jupiter.

The corresponding sequence of sector plots is shown in Fig. 8.40. The sector plot showing the data integrated over the two time bins affected by the jet (a) reveals a strong first order anisotropy of  $\sim 72 \pm 9\%$  and a clear correlation between the fitted axis of symmetry of the distribution (blue arrow) and magnetic field vector (red arrow). Separate plots of the time bins, however, reveal a somewhat unexpected shape of the directional anisotropy: Sector 0, where the maximum of counts is expected



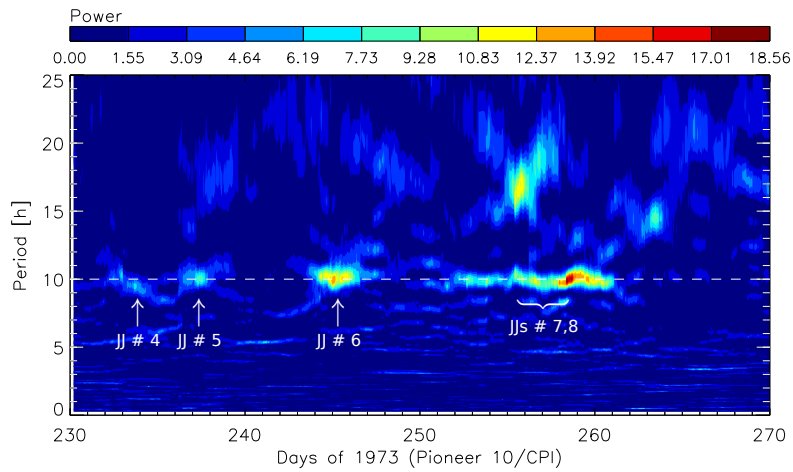


**Figure 8.37:** Sliding Lomb analysis of the time period from day 230-270 in 1973 (P10). The presence of the 10 h modulation is apparent and related to the occurrence of Jovian jets. The events are labeled by  $JJ \#$  followed by the jet's id according to Tab. 8.1.

shows a lower counter reading than the adjacent sector 1 and 7. At least two possible explanation for this observations exist. On the one hand the counting rate of D5N6 does not exceed 0.1 counts/s per sector during the event, resulting in a bad statistics reflected by the rather broad error bars of the sector plot. On the other hand, the observations has a more physical explanation if one takes into account the possibility of velocity dispersion of the particles according to their net speed  $\mu \cdot c$ . A general treatment of this effect will be part of the chapter on the numerical simulation of anisotropic Jovian electrons.

## 8.10 A Series of Events Seen by Pioneer 10

A quiet interesting time interval that deserves to be mentioned occurred between days 280 and 281 in 1973. During this time, four electron enhancements were detected by Pioneer 10 while at a distance of approx. 0.31 AU. This series of events is displayed in Fig. 8.41. The bottom panel shows the ID4 and ID5 electrons counts while the middle panels contains the sector counts of the D5N6 channel in the familiar way. Looking at events #6 and #7, a gap of  $\sim 10$  h between the counting rate maxima is visible. The corresponding sector plots, derived from exemplary subsets of the complete events, shows a moderate anisotropy for event #6, most likely related to the very large variance of the magnetic field vector during this time in a sense that it is unjustifiable to speak of a mean magnetic field direction. During the successive event #7, the magnetic field is much smoother and the anisotropy is better pronounced and the fitted axis of symmetry of the  $A_1$  coefficient and the mean magnetic field direction

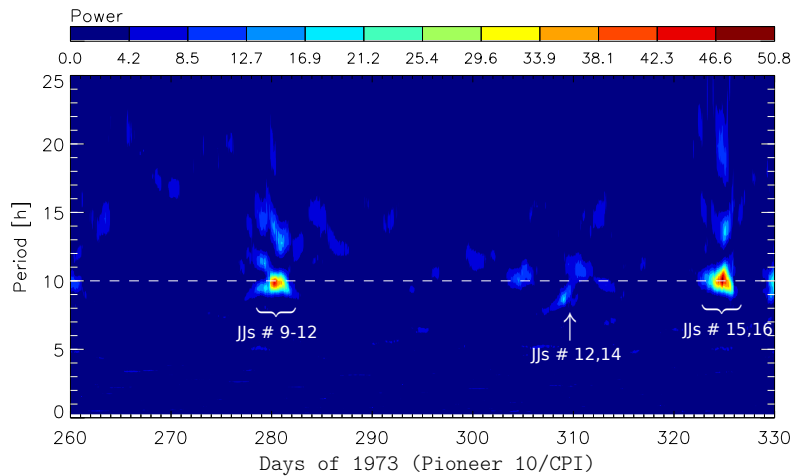


**Figure 8.38:** Same as Fig. 8.37 but for the time interval day 260-330 in 1973. Again, the occurrence of Jovian jets is related to the presence of the 10 h periodicity. Just before the end of the plotted interval, the 10 h modulation at the outer boundary of the magnetosphere is visible.

are in good agreement. Some 30 h, i.e. 3 Jovian rotations, before the occurrence of event #6, a minor electron event marked by the asterisk (\*) is visible. This event, not counted as a Jovian jet, also shows a clear correlation between the direction to Jupiter and the fitted and measured axis of symmetry, i.e. the magnetic field direction. Because of the low counting rates, the error bars are relatively high, but the fitting procedure reveals a significant first-order anisotropy of  $16 \pm 1\%$ . The most anisotropic events of this series are the two jets observed around day 281.5. These jets, events # 8 and #9, are separated by a gap of  $\sim 1$  h, where the counting rates fall down to the background level. Event #8, showing a prominent rise and decrease of particles, reveals a first-order anisotropy of  $74.7 \pm 4.3\%$  and a variation of the magnetic field vector comparable to event #7. Consequently, the magnetic field direction and the fitted axis of symmetry differ only by a few degrees. As can be seen in the Figure, #7 occurs about 3.5 h too “early“ relative to the phase predicted by the two previous events. This sequence of events is an example of a quasi-continuous emission of particles with considerable directional anisotropies, similar to the Ulysses observations discussed in Section 8.6. Therefore, the presence of the 10 h spectral modulation is expected in the data. Indeed, the Lomb-Scargle analysis of this time intervals supported the visual impression of a 10 h periodicity as shown in Fig. 8.38. Another noteworthy time interval revealing similarities to the series of events observed by Ulysses discussed in Section 8.6 was observed by Pioneer 10 between days 252 and 262 in 1973. This time interval is shown in Fig. 8.42. The bottom panels contains the counting rates of the ID4 and ID5 channels, the middle panel the color coded sector counts and the top panel the smoothed (37 h window) and detrended id4/id5 ratio (red curve)

#	Year	frac. Day	$\Delta t$	$A_1$ [%]	$d$ [AU]
1	1973	190.90	2.5	$18.4 \pm 0.9$	0.79
2	"	191.00	2.0	$24.9 \pm 1.0$	0.79
3	"	191.55	4.5	$36.2 \pm 1.8$	0.79
4	"	233.95	0.5	$12.6 \pm 1.6$	0.58
5	"	236.80	3.0	$20.1 \pm 0.47$	0.55
6	"	245.14	3.5	$58.1 \pm 3.7$	0.51
7	"	255.10	1.5	$13.1 \pm 4.7$	0.51
8	"	257.20	4.0	$17.8 \pm 1.2$	0.46
9	"	280.30	3.5	$13.6 \pm 6.8$	0.33
10	"	280.70	2.5	$14.9 \pm 0.4$	0.33
11	"	281.40	2.0	$74.7 \pm 4.3$	0.33
12	"	281.50	2.5	$44.4 \pm 5.2$	0.33
13	"	309.80	2.5	$11.8 \pm 2.8$	0.18
14	"	310.00	2.5	$10.3 \pm 1.8$	0.18
15	"	323.65	5.5	$24.8 \pm 2.3$	0.09
16	"	324.12	4.0	$14.3 \pm 2.5$	0.09

**Table 8.1:** Listing of the Jovian jet events found in the Pioneer 10 data. The events are numbered consecutively. The fractional day of occurrence and the duration underlie an uncertainty of  $\sim 30$  min because of the resolution of the data. The first order anisotropy  $A_1$  was calculated from the entire event. The distance from Jupiter  $d$  is given in AU.

imposed with a sine function with a periodicity of 10 h (blue). The two Jovian jets observed during this interval (# 8 & 9) are indicated by the vertical bars. Comparing the omnidirectional counting rates and the sector counts, the electron flux appears to be highly variable in anisotropy and flux level. The spectral index, i.e. the ratio of id4 and id5, shows the presence of a 10 h modulation starting around the beginning of day 252 in coincidence with the increase of the electron flux level. From day 252 to the beginning of day 260, the magnetic field direction (yellow and white dots in the middle panel) is well aligned with the direction to Jupiter. Consequently, the net flux of particles is predominantly coming from sectors 0 and 7. This can be seen by investigating the sector plots for several subintervals of Fig. 8.42 shown in the first three plots of Fig. 8.43. The single sector plots are numbered according to the sampled intervals (horizontal bars) of Fig. 8.42. Weak or moderate anisotropies were found with the axis of symmetry being in good agreement with the magnetic field direction and the position of Jupiter. Note that the anisotropy is most pronounced during the time period (2) including the Jovian jet # 9. This observation confirms the Ulysses observations that the presence of Jupiter's 10 h periodicity in the energy spectrum of Jovian electrons is related to the presence of a net flux of particles. At the beginning of day 262 a sudden change in the orientation of the magnetic field occurs as can be seen

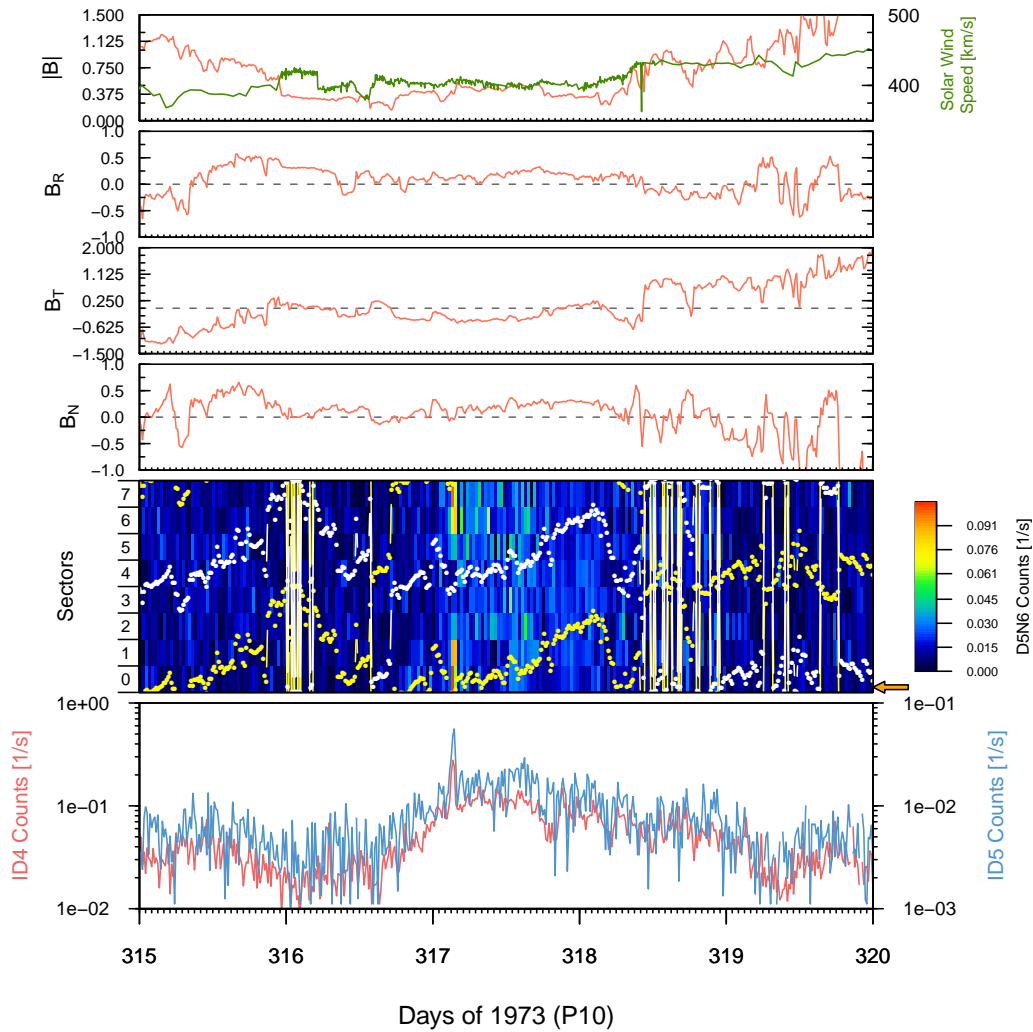


**Figure 8.39:** A Jovian jet observed by Pioneer 10 on day 317/1973. A sudden increase of electron flux as well as anisotropy is visible in the counting rates of the ID4 & ID5 channels and in the D5N6 sector counts. During the event, the direction to Jupiter (orange arrow) is well aligned with the magnetic field represented by the dots yellow and white dots (i.e. parallel and antiparallel magnetic field direction).

in the middle panel of Fig. 8.42. As mentioned before, the projection of the magnetic field vector on the spacecraft's spin plane is indicated by the yellow (parallel direction) and white dots (anti-parallel direction). Interestingly, the projection of the magnetic field flips by about  $180^\circ$ . The 10 h modulation is still present as well as an anisotropy. This anisotropy, however, indicates a net flux of particles from sectors 3 and 4 as can be seen in the fourth sector plot of Fig. 8.43. The degree of anisotropy of first order

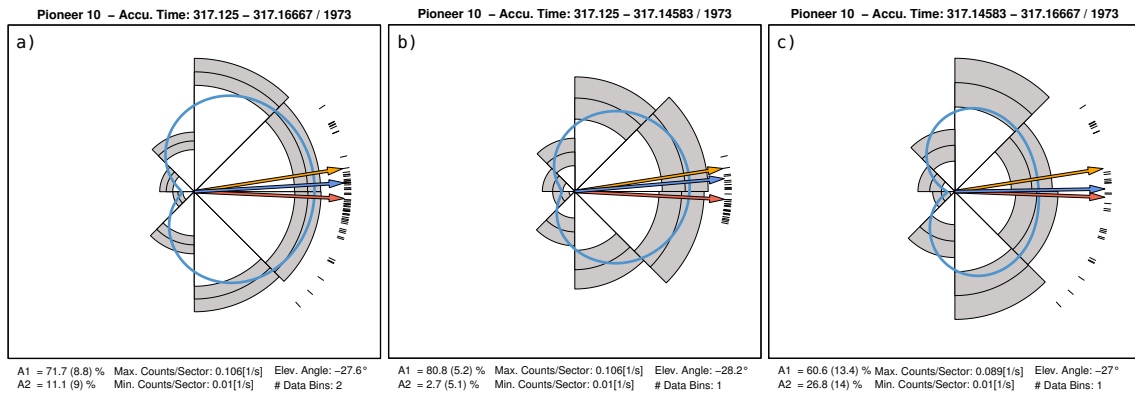


**Figure 8.40:** Sector plots of the Pioneer 10 event occurring on day 317/1973. Panel a) shows the accumulated counts over the complete event while b) and c) cover the first and second half of the event, respectively. The orange arrow is the direction to Jupiter, the red arrow the mean magnetic field and the blue one the fitted axis of anisotropy. The blue curve is the result of fitting the electron data using a Fourier series.

is very weak ( $A_1 = 3.7 \pm 0.6\%$ ) but visible to the eye. Relative to the anisotropy of first order, there is also a notable anisotropy of second order ( $A_2 = 3.2 \pm 0.6\%$ ), indicating a dumbbell distribution of particles. Indeed, a closer investigation of the sector plot reveals that the counting rates of sectors 0 and 7 slightly exceed that of sectors 1 and 6. To allow a closer look at the magnetic field topology, Fig. 8.44 shows from top to bottom the magnetic field magnitude and the R, T and N components of the magnetic field vector as well as the sector counts in the bottom panel for days 258 to 267 in 1973. The shaded area indicates the time interval bounded by jumps in the magnetic field vector (projected on the spacecraft’s spin plane). During this interval, the magnetic field is considerably smoother than before and after. The N component of the magnetic field vector moves from positive values at the beginning of day 260 to negative values at day  $\sim 265.5$  and back to positive value on day 262. Furthermore, the R component is positive or close to zero while the T component also points in the positive direction. In combination, the magnetic field vector is expected to be found in quadrant II in Fig. 8.46. As will be discussed in more deep in the following section, this magnetic field configuration strongly deviates from the nominal Parker-field. The overall configuration of the magnetic field suggest a CME-like (magnetic bottle) shape of the magnetic field during this time giving an explanation for the observed Jovian electron anisotropies of first and second order. This finding leads to observations made directly before Pioneer 10 entered the Jovian magnetosphere.

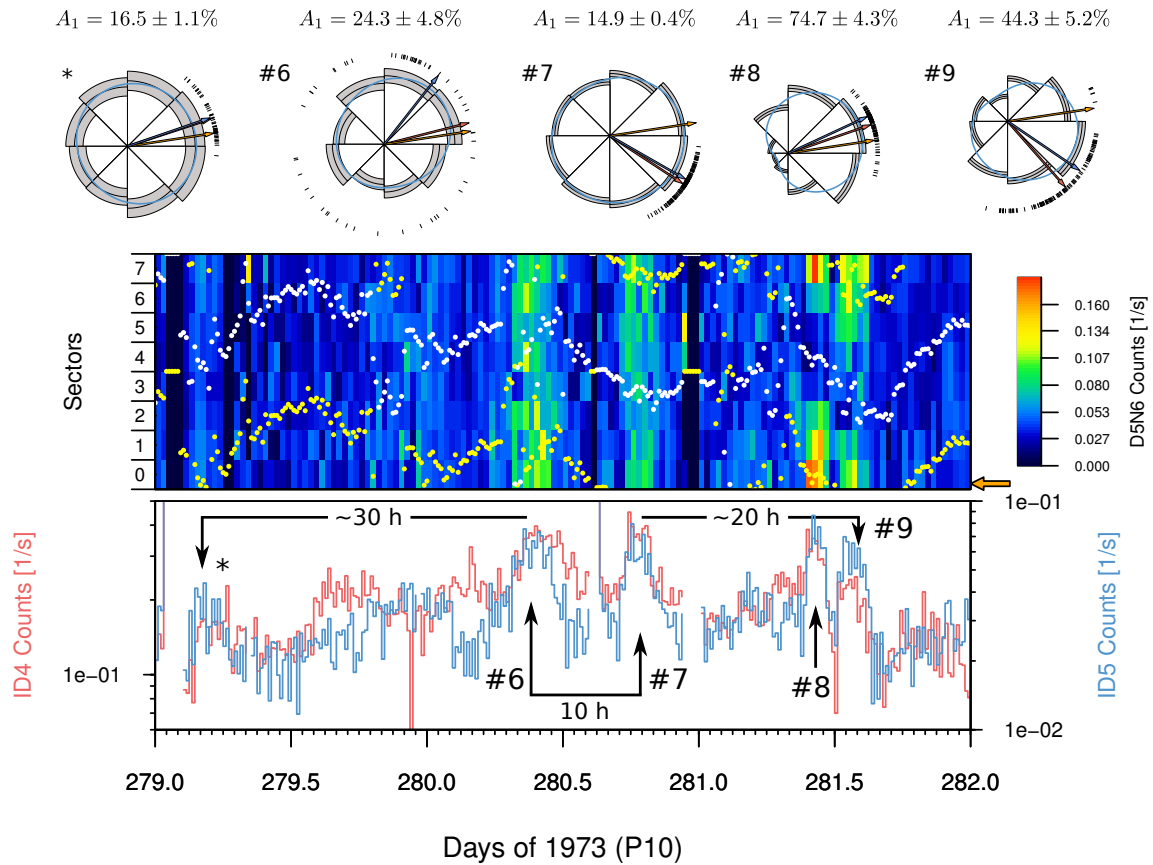


**Figure 8.41:** The time series of MeV electrons counts from day 279 to 281 show the presence of quasi-periodic events accompanied by particle anisotropies. The sector plots on top refer to time intervals indicated by the asterisk (\*) or jet number in the bottom panel.

## 8.11 Observation of “Reverse” Jovian Bursts?

An interesting finding is the occurrence of electron events that seem to propagate perpendicular to the nominal field or towards Jupiter instead of away from it. An example of this behavior as shown in Fig. 8.45 when Pioneer 10 was located very close to the planet ( $\sim 0.08$  AU).

This Figure shows the time period from day 322 and 326 in 1973. During this time, the spacecraft was about  $80 R_J$  away from the bow shock, assuming a bow shock radius of  $100 R_J$ . It was shown before that this time interval is strongly affected by the presence of the 10 h periodicity. This is a clear evidence that the electrons are indeed of Jovian origin.

The Jovian electron enhancement is somewhat different from the time profile e.g. shown in Fig. 8.41, because the flux increase is primarily gradual and lacks clear

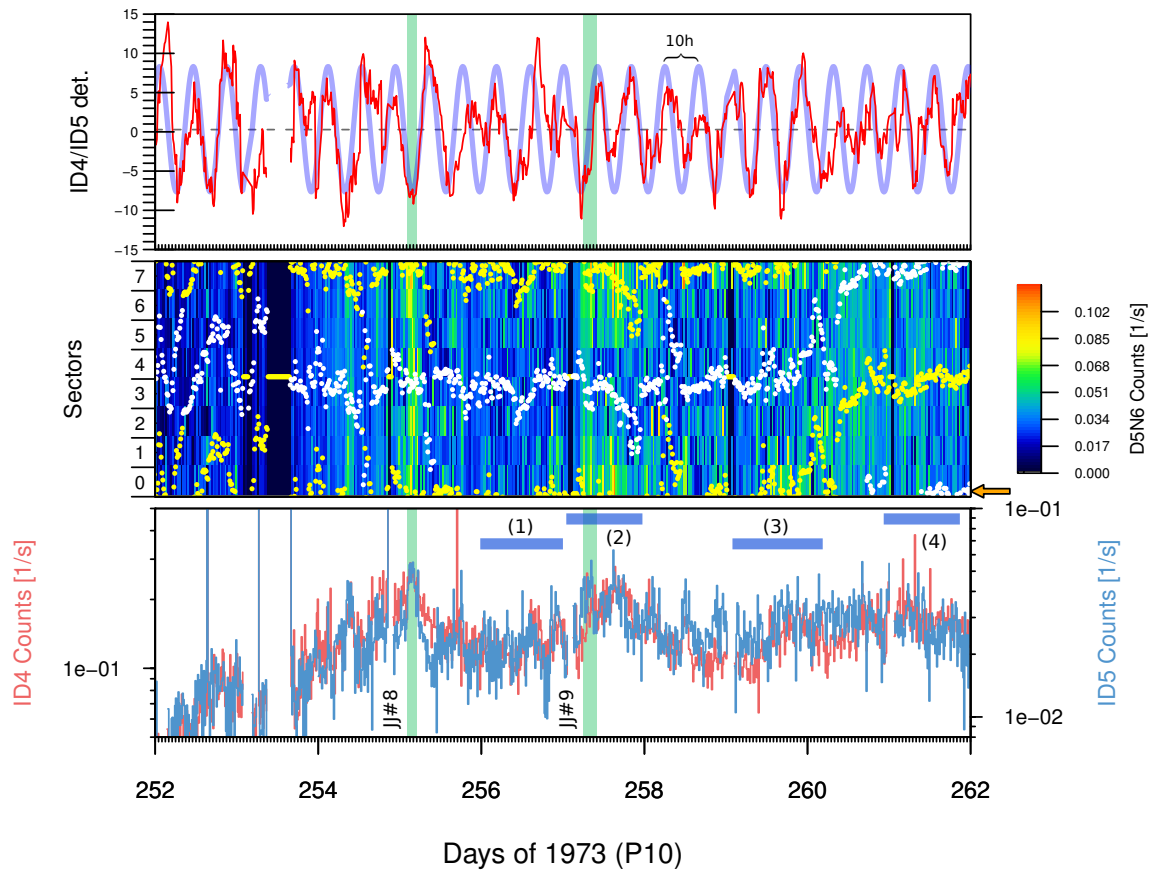


**Figure 8.42:** Time series of MeV-electron data from day 252 to 262 in 1973 (bottom) and the corresponding sector data including the magnetic field (middle panel). The top panel shows the detrended id4/id5 ratio (red curve) imposed by a sine function with a period of 10 h. Most of the time, a periodic variation in the spectral index is apparent. Two jets that occur during this time are indicated by the green bars. The blue horizontal bars indicate the sub intervals from which the sector plots in Fig. 8.43 were derived.

intermittencies in the electron counting rates and anisotropies. In this respect, the shown electron enhancement is similar to the Ulysses multiple jet events found at day 15/1992 and 141/1992. Although the Ulysses events are of shorter duration ( $\sim 5$  and  $\sim 10$ h, respectively), they are also characterized by a smooth increase of the electron counting rates and Jovian jet being located inside a general Jovian electron enhancement.

In order to interpret the observed flux direction, it is necessary to investigate the magnetic field structure related to the flux increases. During the first event (day 323.65 to 323.91), the T-component of the magnetic field vector has a negative or more or less vanishing value during the first and second event, respectively, indicated in

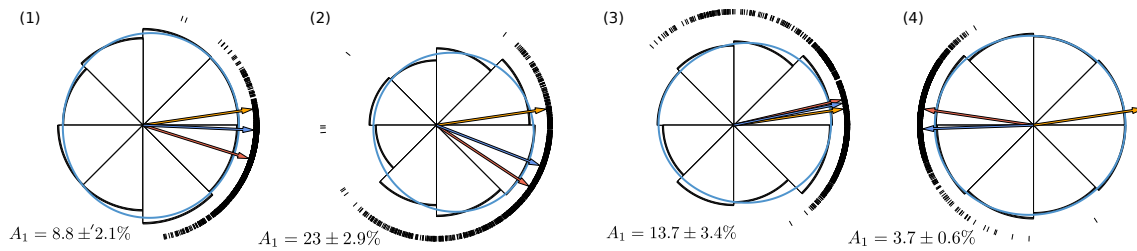


**Figure 8.43:** Sector plots of the time intervals indicated by the blue horizontal bars in Fig. 8.42. Albeit not overwhelming, anisotropies are present in the time intervals 1 to 3.

Fig. 8.45. The R-component also shows a negative value. Since a nominal Parker spiral is only given if the T-component (R-component) is positive and the R-component (T-component) negative, this indicates a temporarily disturbed magnetic field structure. Fig. 8.46 schematically shows the principal direction of the magnetic field vector. The close distance to the Jovian magnetosphere and the fact that the Jovian magnetosphere is a substantial barrier for the solar wind and the accompanying magnetic field may lead to an disturbance of the IMF close to the planet resulting in the observations shown in Fig.8.45. During the following events (starting around day 325.0), the magnetic field is in agreement with a Parker-field geometry. Because of a N-component of the magnetic field of a similar magnitude compared to the R- and T-component, the center of the anisotropy is located in sector 2, i.e. the streaming of the electrons has a strong component perpendicular to the ecliptic plane. This resembles the strong deviations from the nominal Parker-field geometry required to establish a magnetic connection between Jupiter and Ulysses during the spacecraft’s observation of jets.

This conclusion is in agreement with observations of several upstream events seen at Earth’s orbit where a strong twisting or looping of magnetic field lines may be taken into account to explain the streaming direction of the particles (cf. Stansberry et al., 1988; Haggerty et al., 2000; Klassen et al., 2009).

While the event discussed in this section was observed close to the Jovian magnetosphere and shows a long lasting increase in flux as well as in anisotropies, this event may be seen as a major release of electrons previously trapped in the Jovian magnetosphere. In combination with the observation of a non-uniform magnetic field structure, a rapid spread of electrons in the IMF resulting in a cascading of the long lasting events into Jovian jet events of short durations may be expected.

The reanalysis of the Pioneer data showed that in the light of the Ulysses results presented by Ferrando et al. (1993), Simpson et al. (1993) and in this work, a clear agreement of the properties of the Jovian “bursts” discussed by Chenette et al. (1974) and “jets” is evident. Indeed, it could be shown in the previous section that several Jovian “bursts” can be identified as Jovian “jets” following the nomenclature of Ferrando et al. (1993) and McKibben et al. (2007).



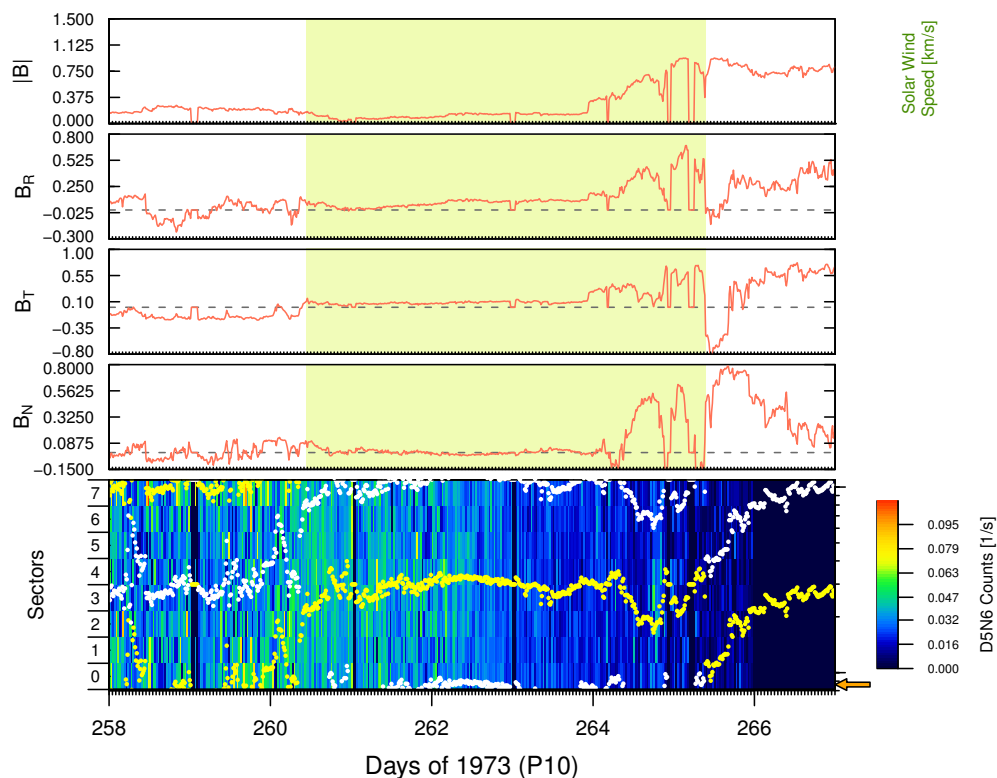


**Figure 8.44:** The magnitude and the three components of the magnetic field in the RTN coordinate system and the sectorized counting rates. The shaded area indicates the time interval bounded by  $\sim 180^\circ$  jumps of the magnetic field. During this time, a weak anisotropy of electrons coming from sectors 3 and 4 is observed in combination with some evidence for particles coming from sectors 0 and 7. The temporal evolution of the magnetic field suggest a CME-like geometry of the magnetic field.

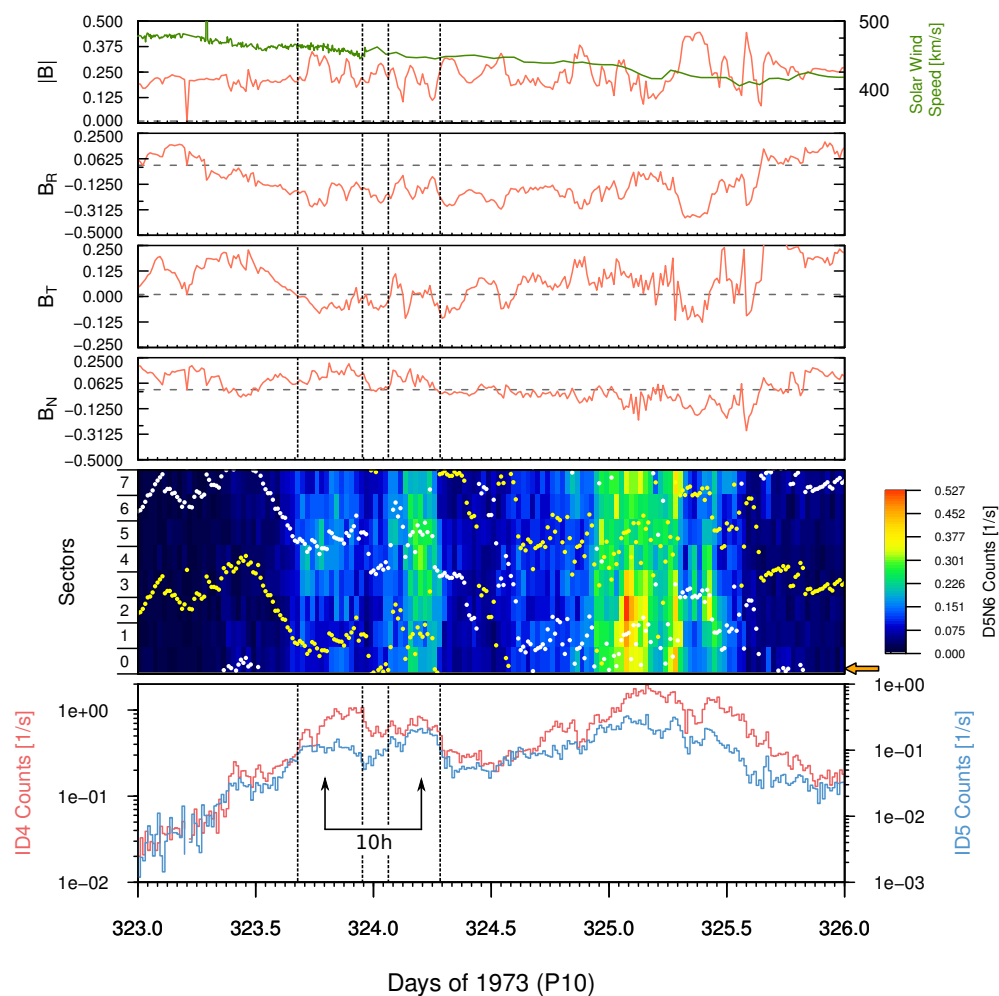


**Figure 8.45:** From day 322 and 326 in 1973, Pioneer 10 detected several MeV-electron flux and anisotropy increases as shown in the plot. Somewhat puzzling, however, is the finding that the electrons of the two first increases seem to stream towards the planet instead of away from it. The analysis of the magnetic field during this events, however, reveals strong deviations from a nominal Parker-like magnetic field line.

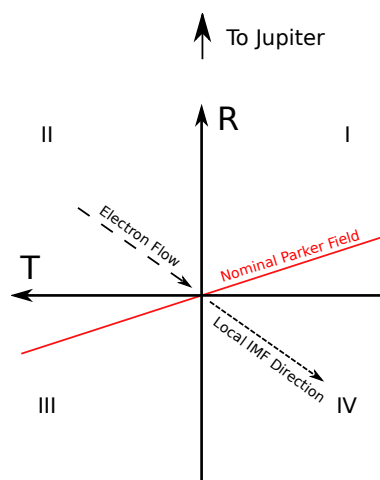


**Figure 8.46:** A nominal Parker-spiral is expected to be located in quadrant I or III, depending on the polarity of the magnetic field. During the “reverse” events, however, the magnetic field vector is temporarily located in quadrant II or IV indicating a deviation from the expected IMF direction. This configuration can explain the observed flow of anisotropy.



# Chapter 9

## A FPE Based Jovian Electron Burst Transport Model

We balance probabilities and choose the most likely. It is the scientific use of the imagination.

---

Arthur Conan Doyle -  
The Hound of the Baskervilles

The previous chapter illustrated that Jovian electrons jets are bursts of Jovian electrons emerging from the Jovian magnetosphere that propagate in the interplanetary medium parallel to the local magnetic field. This propagation was found to be dependent on the pitch angle of the particles, i.e. the assumption of an isotropic pitch angle distribution is not valid. Consequently, for this type of events, a treatment in terms of Parker's transport equation is not justified. This is also the case for solar flare particles observed at Earth, making it necessary to use a pitch-angle dependent form of the transport equation. This so-called focused-transport equation has been introduced in section 4.4. The transport of relativistic or nearly relativistic electrons during solar flare events had been successfully modeled by Kallenrode (1993) (Helios observations of  $\sim 1$  MeV electrons) and Agueda (2008) (ACE observation of  $\leq 312$  keV electrons) using the focused transport equation. It must be noted that the following sections are not exhausting but are reduced to the basic properties of the numerical description of the pitch-angle dependent transport of Jovian electrons. A more detailed discussion will be the subject of further studies.

### 9.1 Setup of the Simulation

The purpose of this chapter is the investigation of pitch-angle dependent Jovian electron fluxes along magnetic flux tubes. The requirements for the transport equation read as follows:

- The mean interplanetary magnetic field has the shape of an Archimedean spiral, i.e. charged particles coming from the outer heliosphere do not travel along straight lines towards the Sun but along this spiral. Therefore, the spatial dimension in the simulation belongs to the arclength  $z$  of the Parker spiral. A special case, however, is the assumption of an unbended magnetic flux tube. In this case, the arclength between the source and the observer is identical to the radial distance. This study is restricted to the case of a straight, homogenous flux tube.
- Perpendicular diffusion is neglected in the model, i.e.  $z$  is the only spatial dimension.
- The process of focusing or defocusing is implemented in the model to take into account the systematic change in pitch angle due to the diverging heliospheric magnetic field. However, focusing may also be switched off to simulate particle transport along a flux tube with a constant diameter, i.e. a constant magnetic field strength. Indeed, this work only discusses the propagation of particles in a homogeneous flux tube.
- Energy changes are not included in the code, i.e. it is assumed that particles do not lose or gain energy by systematic effect nor by momentum diffusion related to random electric fields. A discussion of pitch-angle dependent adiabatic energy losses of solar cosmic rays can be found in Ruffolo (1995).
- The spectral index in the diffusion coefficient was set to the  $q = 5/3$  for the simulation runs, i.e. the value for Kolmogorov's turbulence, in good agreement with observations in the inner heliosphere by Hedgecock (1975). It is clear, however, that there exists some variation in the value of  $q$  in the range from  $\sim 1.3 - 1.9$  (see references in Schwenn and Marsch, 1991). However, as pointed out by Goldstein (2001), the mean value of  $q$  stays fairly constant up to several AU, i.e. it may be justified to choose the cited value of  $q$  for the interplanetary medium at Jupiter. However, it is of course of interest to study the diffusion of particles as a function of  $q$ .
- The particle source, i.e. the Jovian magnetosphere is a rather limited region. Therefore, the injection region on the numerical grid should be reasonable small. In numerical calculations, spatial quantities like the length of a bundle of magnetic field lines are finite. The boundary condition for the  $z$  dimension has been chosen that particles reaching the boundary (either  $z_{min}$  or  $z_{max}$ ) are lost, i.e. they will not come back.
- Convection of the particles by the solar wind is neglected. This restriction is founded on the fact that the speed of relativistic electrons ( $v \approx c$ ) is much larger than the solar wind speed ( $u_{sw} \approx 400 \dots 800$  km/s) and the assumption that

the time scale under investigation are too small to make solar wind convection important.

- Finally, the particles are considered as “test particles” in a given magnetic field configuration. Consequently, wave-particle interactions are fairly beyond the scope of the model. Furthermore, we neglect systematic or random changes in the momentum/energy of the particles.

The points noted above lead to a principal model as it is illustrated in Fig. 9.1. The two dimensional domain  $[-1, 1] \times [z_{min}, z_{max}]$  defined by the pitch-angle space and the length of the field line  $z$  is given by the gray box. The abscissa is  $z$  and the ordinate corresponds to the pitch-angle space  $\mu$ . The dashed line indicates the location where  $\mu = 0$ . Three influences act on the particles. The convection is related to the motion of the particles due to the component of their velocity parallel to the magnetic field, the sense of motion therefore depends on the actual sign of  $\mu$ . Pitch-angle diffusion acts only in the pitch-angle domain and principally leads to a spreading of particles in this domain. The effect of focusing also acts in the pitch-angle domain. However, focusing only acts in one direction defined by the direction of the diverging magnetic field. In this Figure, the cross section of a flux tube increases with increasing distance  $z$ .

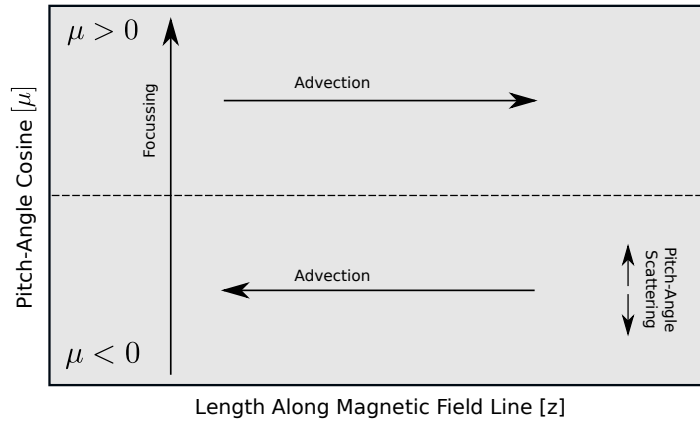


**Figure 9.1:** To illustrate the different influences acting on the particles and their directions, this figure shows the two dimensional space defined by the distance along the magnetic field line  $z$ , with  $z \in [z_{min}, z_{max}]$  and the pitch-angle domain  $\mu$ , with  $\mu \in [-1, 1]$ . While the advection leads to a displacement of the particle in  $z$  according to the actual sign of  $\mu$ , pitch-angle scattering is a typical diffusion process. The focusing term acts only in one direction.

## 9.2 Propagation in a Homogeneous Fluxtube

The simplest case for pitch-angle dependent transport is the propagation of particles along a flux tube of constant cross section. According to Maxwell's laws, the magnetic field strength is constant along the flux tube and no focusing has to be taken into account. For Jovian jets and the often strong deviations from the mean magnetic field, it is not possible to deduce the exact shape of the magnetic flux tube between the source and the observer. Therefore, the degree of focusing/defocusing can not be determined. For this reason, the shapes of Jovian jet flux tubes will be assumed as of constant cross section. Furthermore, the effect of focusing is not very weak with respect to the distances from the source at which Jovian electrons were detected. Since the numerical model is capable of taking into account the effect of focusing, this is a further task to be discussed in the future. The idea behind the effect of focusing on Jovian electrons was described in chapter 6.

### Basic Properties

In what follows, the temporal evolutions of particle injections with a fixed mean free path of  $\lambda = 1.0$  AU (that enters the diffusion coefficient) but different injection profiles in the pitch-angle domain will be investigated.

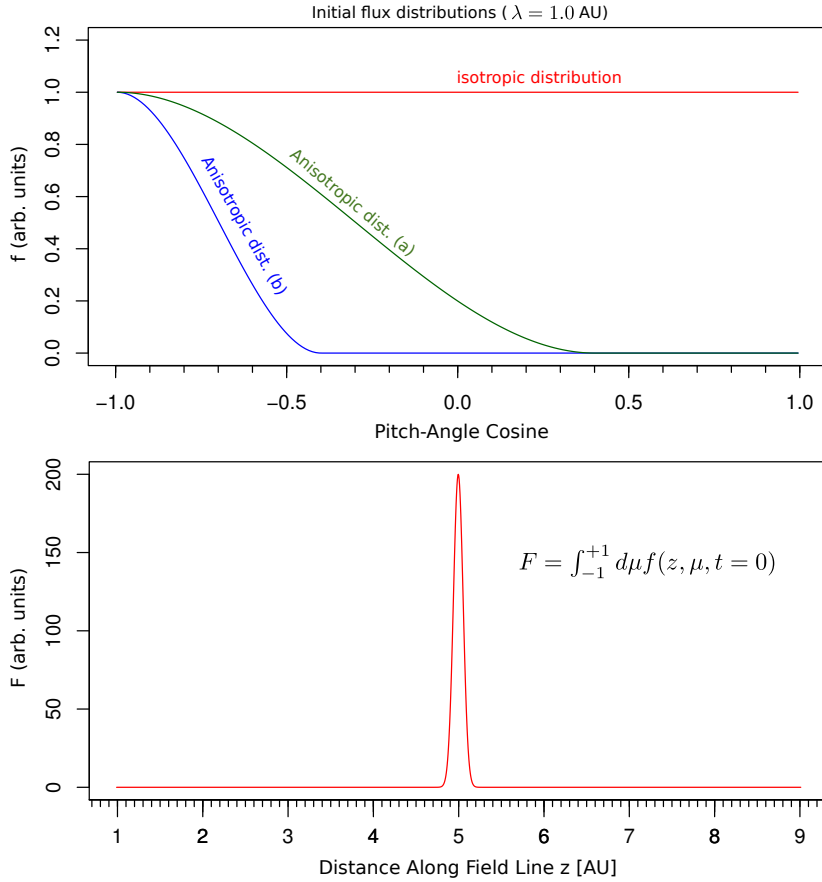
The center of the injection is located at  $z = 5$  AU. The numerical boundaries are at 1 and 9 AU. The spectral index was set to  $q = 5/3$  while the isotropic scattering parameter  $h$  was set to zero. The first case to be studied is that of an isotropic pitch-angle distribution, i.e.  $\partial f(\mu, z, t = 0)/\partial \mu = 0$ .

Fig. 9.2 shows the initial flux distributions for three different cases in the pitch-angle and spatial domain. The red curve in the top panel represents an isotropic distribution, the green and the blue one that of different degrees of anisotropy realized by a polynomial of third degree between  $\mu = -1$  and  $\mu = +0.4$  and  $-0.4$ , respectively.

The temporal evolution of the isotropic initial distribution (Fig. 9.3) is characterized by two maxima moving away from the place of injection in both directions. As time proceeds, the amplitudes of these maxima decrease and finally disappear. After the disappearance of these maxima, the maximum of the distribution is located at the place of the original particle injection.

The symmetry of the temporal evolution follows directly from the isotropic injection and the non-directional dependence of the transport, i.e. the absence of focusing and a spatially homogenous diffusion coefficient. The particles with a pitch-angle cosine close to  $\pm 1$  experience the largest net displacement along the magnetic field line because of the term  $\mu v$  and the small influence of diffusion because of the special shape of the diffusion coefficient for values of  $q > 1$  (cf. Fig. 4.2). On the other hand, particles located around  $\mu = 0.5$  experience a high degree of scattering, while for  $\mu = 0$  this influence is small in combination with a rather small displacement along the field line. The time profile of the isotropic initial pitch-angle distribution for later times can be understood by comparing the result with pure spatial diffusion. Since the particles are





**Figure 9.2:** Top: Three different initial pitch-angle distributions. The red curve represents a fully isotropic distribution, the other ones smooth polynomials from  $\mu = -1$  to  $\mu = +0.4$  (a) and  $\mu = -0.4$  (b), respectively. (Bottom): The spatial profile of the injection function shown here for the isotropic case. For all three injections, the spatial profile was realized by a Gaussian one. Note that the shown curve represents the flux integrated over the pitch-angle domain.

distributed homogeneously in the pitch-angle domain, their propagation in the parallel and anti parallel pitch-angle hemispheres is symmetric and differs only in the sign of the propagation term  $\mu v$ . Consequently, the net shift of particles in the parallel and anti parallel pitch-angle hemisphere balance each other: The center of the particle distribution is located at the place of injection. This is similar to the behavior of the above-mentioned spatial diffusion (for a  $\delta$ -injection in time and space)

$$f(z_0, z, t) = \frac{1}{\sqrt{4\pi Dt}} e^{-(z-z_0)^2/4Dt}, \quad (9.1)$$

where  $t$  is the time,  $D$  the spatial diffusion coefficient and  $z_0$  the place of injection. The maximum of the flux stays at  $z_0$  as time proceeds and no net motion of the

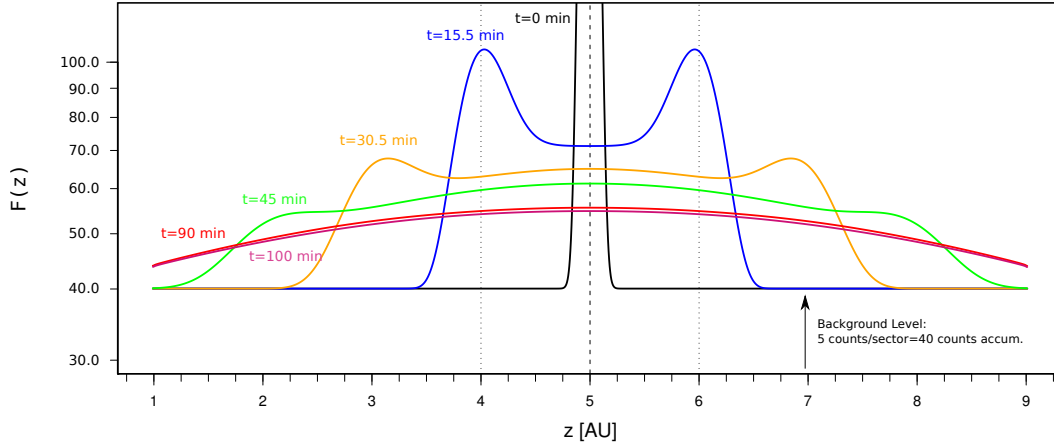


**Figure 9.3:** Profile of a particle injection at  $z=5$  AU with an isotropic initial pitch-angle distribution and  $\lambda = 1.0$  AU for different times. Because of the isotropic injection the behavior is symmetric with respect to the place of injection. As time increases, the distribution approaches a Gaussian-like shape with the maximum of flux at the place of injection.

ensemble occurs. As already mentioned, the two “humps” that can be observed are the result of the form of the pitch-angle diffusion coefficient in combination with the velocity dispersion ( $\mu v$ ) of the particles. These humps decay as time proceeds and the ensemble converges to isotropy<sup>1</sup>.

Given the case of a non-isotropic initial pitch-angle distribution (Fig. 9.4), the symmetry is broken, i.e. one pitch-angle hemisphere is populated with more particles than the opposite hemisphere. In this case, the center of the particle ensemble is shifted along the magnetic field line because of the global net flux of particles. The degree of the displacement depends on the degree of initial anisotropy. The displacement is zero for the already discussed isotropic initial distribution and approached the mean free path  $\lambda$  that indirectly enters the computation in the form of the scattering frequency  $\nu_0$  (cf. Eqn. 4.27). This behavior can be understood by keeping in mind that the meaning of the mean free path is that this is the typical length a particle propagates until is scattered by  $90^\circ$  from its initial position. For a particle injection with a narrow pitch-angle distribution close to  $\mu = 1$  it follows that at a distance from the source close to the mean free path, just half of the particles were scattered across  $\mu = 0$ . In this moment the net shift of the ensemble reached its final point. Fig. 9.5 shows the spatial profile for the initial pitch-angle distribution (b) in Fig. 9.2. Again, the flux  $F(z)$  is plotted for several times with an isotropic background flux added to the data. Compared to Fig. 9.4, the differences are barely visible, i.e. the influence of the different injection

<sup>1</sup>It is important to note in this context that isotropy indicates the state of no *global* net flux. For a given point in space, there is always at least some small portion of *local* anisotropy in the pitch-angle domain in a numerical setup that allows the particle to escape.

functions is small. In Fig. 9.6 the temporal evolutions of the positions of the maxima of the two anisotropic distributions are compared. Here, the location of the maximum is defined by the largest value of the pitch-angle integrated flux  $F$ . It can be seen that the motion of the anisotropic peak is almost identical for both distribution. At about  $t = 40$  mins, however, the “isotropic” part of the distributions, i.e. the maximum of the distribution if its approaches a symmetric profile, dominates. The locations of the isotropic maxima differ: for the more anisotropic injection function (i.e. case (b)), the location of the “isotropic” maximum is further away from the source than is the case for the other injection.

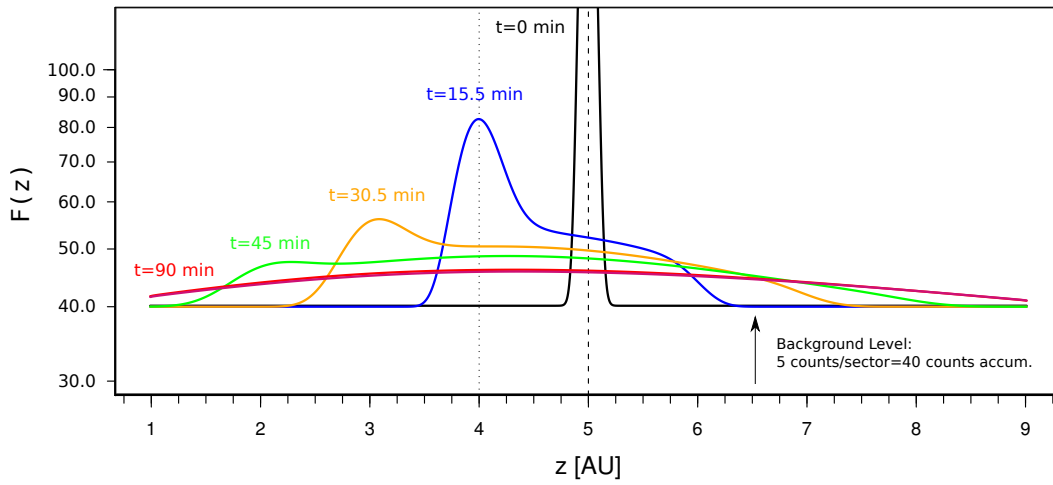


**Figure 9.4:** Profile of a particle injection at  $z=5$  AU with the initial pitch-angle distribution (a) in Fig. 9.2 for several times, i.e. the initial distribution extends from  $\mu = -1$  to  $\mu = +0.4$ . Due to the anisotropic injection, the center of mass of the distribution moves to the left because of the contribution of the term  $\mu v$ . In addition, the initial distribution becomes blurred because of pitch-angle scattering. Note that the maxima of distribution decreases while approaching a symmetric shape indicating a global state of isotropy.

Fig. 9.7 shows for a longer time interval ( $t_{max} = 140$  min) the location of the global maximum as a function of time for the injection function (a). The mean free path is set to  $\lambda = 1.0$  AU. For late times ( $t > 100$  min) the location of the maximum moves back towards the center of the computational domain. This can be explained by considering that the distribution  $f$  has a steeper gradient at the left side of the spatial domain with respect to the right side resulting in an enhanced diffusion current across the numerical boundary on the left side, i.e. the distribution tends towards an equilibrium. This behavior is therefore caused by the boundary condition.

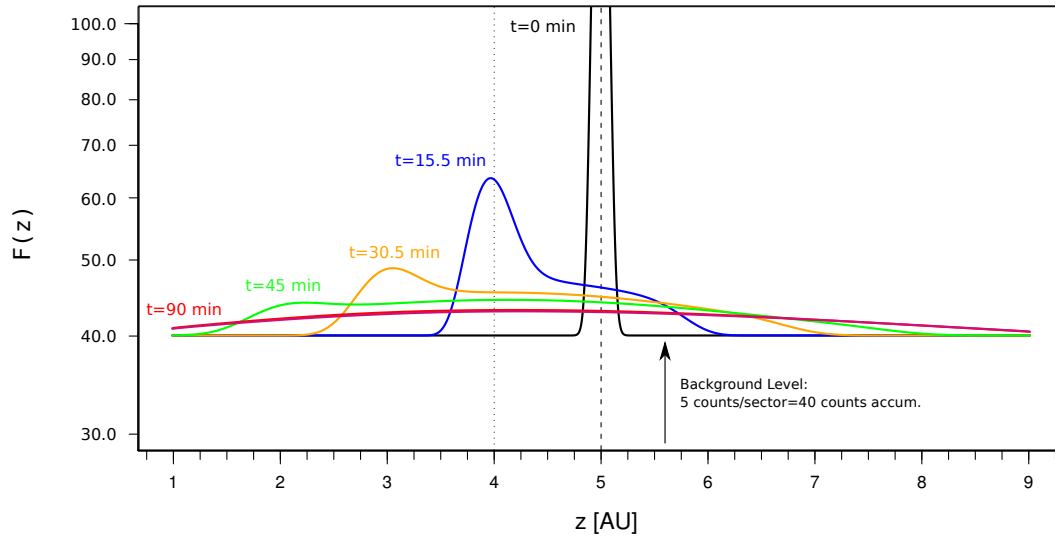


**Figure 9.5:** Same as Fig. 9.3 and Fig 9.4 but for the injection function (b) in Fig. 9.2, i.e. the initial distribution extends from  $\mu = -1$  to  $\mu = -0.4$ . The difference in the profile compared to the case where the initial pitch-angle distribution extends from  $\mu = -1$  to  $\mu = +0.4$  is barely visible.

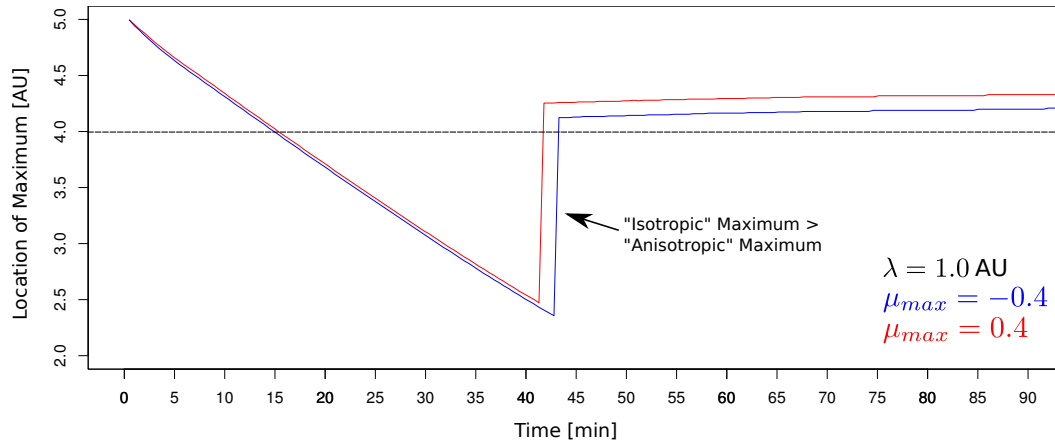


**Figure 9.6:** Location of the global maxima of the initial pitch-angle distribution (a) (red curve) and (b) (blue curve) for a mean free path of  $\lambda = 1.0$  AU. The discontinuity just after  $t = 40$  min is caused by the fact that the isotropic part of the distribution becomes larger than the anisotropic one. As can be seen, the motion of the anisotropic peak is almost identical for both distributions. The locations of the isotropic maxima, however, differs.

## Investigations of Anisotropies

Beside a plain background flux, the results of the numerical model can be superimposed by a certain level of noise to mimic the uncertainty nature of the process of measuring

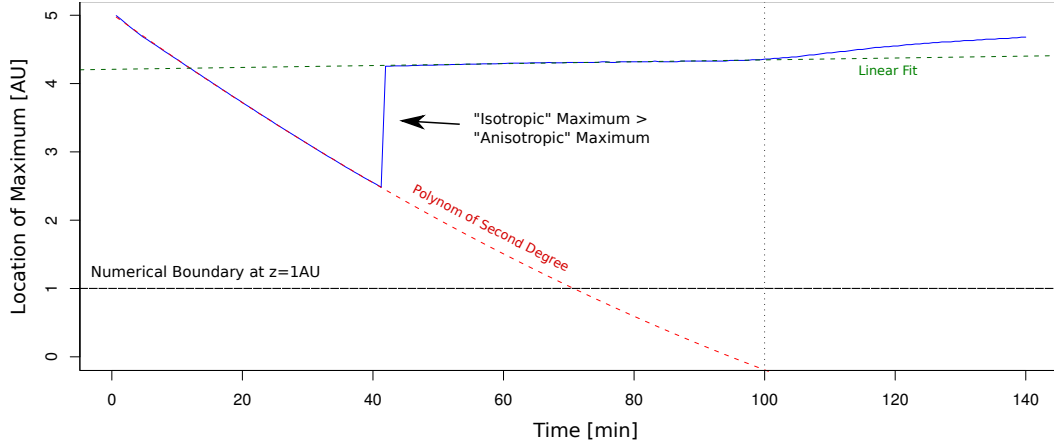


**Figure 9.7:** Location of the global maximum of the particle distribution as a function of time for a mean free path of  $\lambda = 1.0$  AU. At  $t \approx 40$  min the maximum of the anisotropic part becomes smaller than that of the isotropic part. The red curve is an extrapolation of the trace of the anisotropic maximum. At  $t \approx 100$  min, the maximum moves back towards the source. An explanation is the steeper gradient of  $f$  at the left side of the spatial domain with respect to the right side resulting in an enhanced diffusion current across the numerical boundary on the left side, i.e. the distribution tends towards an equilibrium with a maximum at the center of the spatial computational domain for  $t \rightarrow \infty$ .

and that of the particle ensemble itself. This is realized by computing random numbers following a Poisson distribution  $\text{Pois}(\Lambda)$  according to the value of the background flux, where  $\Lambda$  is the level of the background flux (see e.g. Press et al., 1992)<sup>2</sup>. A Poisson-like noise distribution was chosen because of the fairly low level of counts per accumulation interval of the KET/HET, say  $< 100$  events in 10 minutes. For very high counter readings, i.e. large values of  $\Lambda$ , the Poisson distribution approaches the Gaussian (normal) distribution. It is clear that the level of background flux and the attendant noise has implications on the traceability of the signal (i.e. the injected particle distribution): if the background is high, the traces of the signal will get lost in the noise much faster than for a rather low level of background flux.

To make the numerical results comparable with observations, the data were processed in order to derive sector plots as they had been discussed in the previous chapter. The original model data were binned to eight sectors and accumulated. Furthermore, we will assume a “perfect” detector, i.e. instrumental effects leading to a bias of the flux according to the angle of incidence will be neglected. In addition, the magnetic field line taken to be identical with the border of sectors 0 and 7. Another issue to consider is the conceptual difference of the sector plots and the numerical model. The latter

<sup>2</sup>Instead of the common practice of writing  $\lambda$  for the expectation value, we will use  $\Lambda$  since the mean free path is already denoted  $\lambda$ .

one takes the flux or counting rates as a function of the pitch-angle cosine ( $\mu = \cos \varphi$ ) using an equidistant grid. An instrument like the KET, however, scans the spin plane of the spacecraft at a constant rate  $\Delta\alpha/\Delta t$ , where  $\alpha$  is the phase angle as introduced in section 5.5 and under the mentioned setup equals  $\varphi$ . Due to the non-equidistant relation between  $\mu$  and  $\varphi$ , the accumulated numerical data were normalized by taking into account the actual density of data points in the interval.

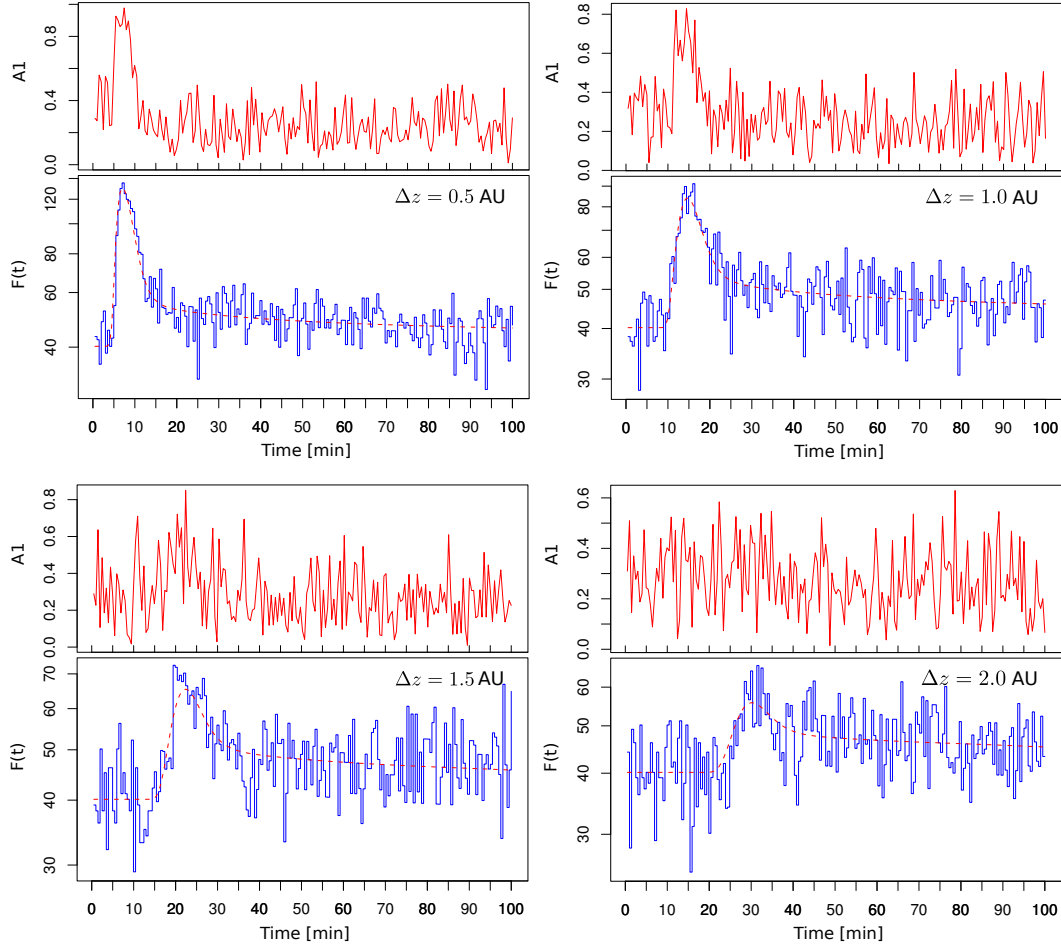


**Figure 9.8:** Time profiles of a particle injection observed at several distances  $\Delta z$  from the source. Again, the mean free path is 1.0 AU, the center of the injection is  $z = 5$  AU. The bottom panels show the flux imposed by Poisson noise background with an expectation value of 5 counts/sector, i.e. a total background of 40 counts. The dashed red curve shows the original flux. The top panels show the associated degree of anisotropy  $A_1$ .

Fig. 9.8 shows the typical temporal evolution of an anisotropic  $\delta$ -injection in time at several distances from the source. Here, the percentage of the noise level is 5% with respect to the highest sector counting rate at the time of injection. According to the

finite propagation time of the particle, the maximum of the distribution arrive at the remote location with a time lag. Simultaneously, the amplitude of the distribution decreases in response to diffusion and is barely visible at a distance from the source of 2 AU (bottom right panel). The same is true for the anisotropy. For close distances ( $\Delta z = 0.5$  AU or  $\Delta z = 1$  AU), a prominent peak in the anisotropy is evident in correlation with the maximum of the counting rates. While still evident at 1.5 AU, the anisotropy does not exceed the background level at 2 AU. This means, the anisotropy vanishes at about the same distance, a clear maximum in the counting rates can be identified. This is in good agreement with the observations.

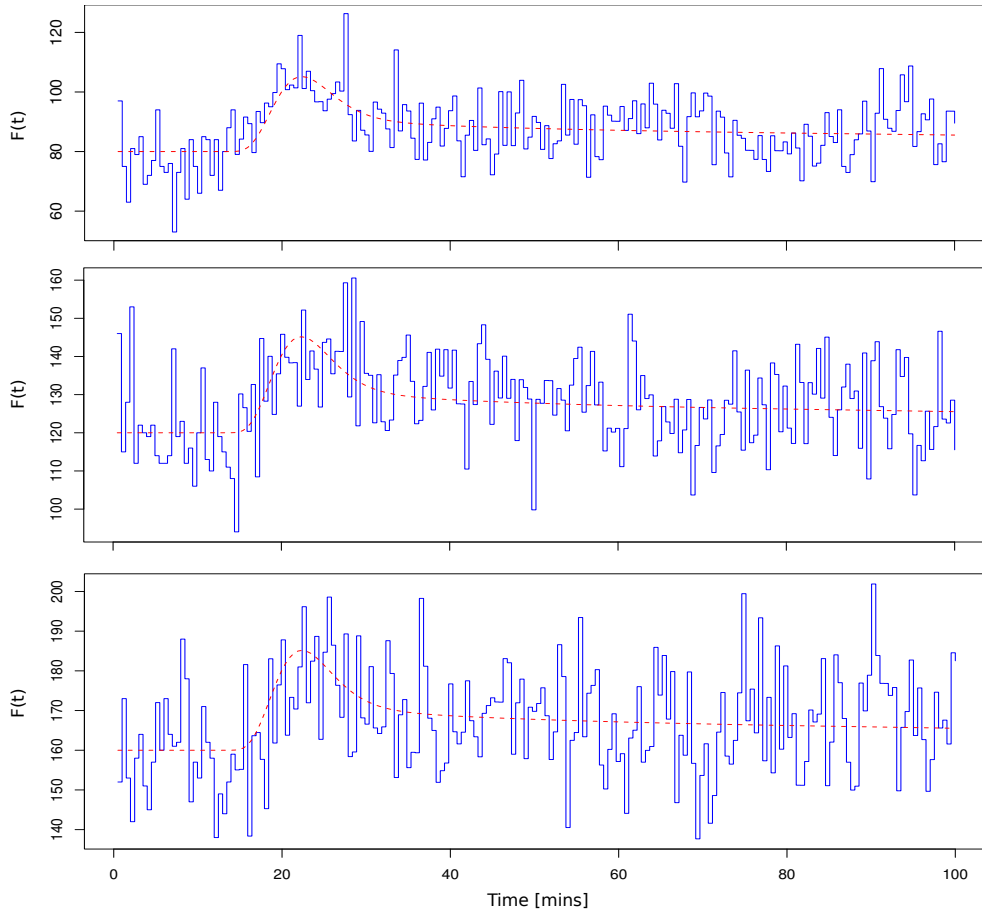
In real observations shown in the previous parts of this work the background anisotropies are generally lower. The reason for that is that the sector data of the particle instrument were accumulated over a relatively large time interval, e.g. 2 h, in order to enhance the statistics. Consequently, the measurements are accumulated over a wide range of different magnetic field vectors leading to a blurring of the anisotropy. On the one hand, this is generally leads to an underestimation of the real anisotropy. On the other hand, however, this helps to cancel out the undesired influence of anisotropies of the background flux.

Fig. 9.9 shows the time profiles of a particle injection observed at a distance of  $\Delta z = 1.5$  AU from the source but with different degrees of noise added to the data. From top to bottom a noise level of 10, 15 and 20% was used. As expected, the traceability of the particle burst decreases with an increase of the noise level.

Based on the results discussed so far the question for the implication of a pitch-angle dependent treatment of the Jovian electron source with respect to Parker's transport model arises. One of the main differences between both approaches is the location of the center of the distribution. As shown, the net displacement of the center of the injected particles depends on the degree of initial anisotropy and is zero for the case of isotropic injection. Depending on the degree of initial anisotropy, the displacement of the distribution maximum  $\Delta z_{max}$  for late times is  $\leq \lambda$ . If  $\Delta z_{max}$  is reached, the particles can be described by Parker's transport equation. While the displacement of the distribution's center and the time needed is of importance for the propagation of Jovian electrons on small spatial and temporal scales, it is not of major importance on heliospheric scales. The propagation of Jovian electrons from Jupiter to the orbit of the Earth, for example, incorporates spatial scales of  $\sim 15$  AU (i.e. the length of the Parker spiral) and times of several days depending on the mean free path of the particles.

## The 10 h Periodicity in the Heliosphere

An interesting topic concerning the propagation of Jovian electrons is the question, if a simple pitch-angle dependent propagation model is able to explain the occasionally observation of the 10 h periodicity of the energy spectra (or counting rates) of the particles. This question – and its answer – may allow important insights into the transport of Jovian electrons not directly accessible by models considering only the



**Figure 9.9:** Time profiles of a particle injection observed at a distance of  $\Delta z = 1.5$  AU from the source but with different degrees of noise added to the data. From top to bottom a noise level of 10, 15 and 20% was used. The signature of the particle injection decreases with increasing noise level.

spatial diffusion and systematic energy changes over large scale like Parker's model. If the 10 h periodicity can not be explained properly by an energy-independent model with pure pitch-angle scattering and advection, other effects like momentum diffusion or significant wave-particle interactions that change the particle's energy must be taken into account in the existing models. In principal, the following processes may account for the vanishing of the 10 h periodicity:

- The 10 h variation is present in the energy spectrum (approximated by the ratio of two adjacent energy channels). This means that at least one of the channels must show a periodic variation in its counting rates what can be seen for example in Fig. 8.28. This periodic variation is expected to vanish if scattering is strong enough to blur it.



- The ratio of the signal and the background & noise becomes to small.
- Given the case that pitch-angle scattering is absent (or very weak), the particles experience velocity dispersion because of the  $\mu$ -dependent parallel velocity. This effect, however, should not play a significant role in the propagation of relativistic electrons.

The contributions of different phases of the periodicity (or the injection of particles at different times) can be investigated by using the principle of superposition of the solution of a (partial) differential equation, i.e. the total phase space density  $F(z, \mu, t)$  at time  $t$  is given by

$$F(z, \mu, t) = \int_0^t f(\tau|z, \mu, t) d\tau, \quad (9.2)$$

where  $f(\tau|z, \mu, t)$  accounts for particles injected at time  $\tau$  and are observed at the remote distance  $z$  at time  $t$ . Thus, a continuous injection in time can be realized by a series of  $\delta$ -injections. This method was also applied by Tsuchiya et al. (1999) for the investigation of the modulation of Jovian electrons at CIRs using the diffusion equation found by Conlon (1978). The physical interpretation of the latter equation is that the observed particle flux at a given distance and time is the sum of all particles that had been injected in the past and reach the observer. Note that this is only applicable for linear problems. If the strength of the diffusion would depend on the magnitude of the particle flux, this assumption is not valid.

The requirement for observing a periodicity in a quantity is  $f(t) = f(t + P)$ , where  $P$  is the periodicity. That means that a recurrent variation must be identifiable. For the Jovian electron bursts this means that the particles injected at a given time, i.e. a given phase, must show a corresponding feature in the measured time series of an observer at a remote location. This is the case if the signal of the injected particles can be distinguished from the ambient background flux. As shown in the previous section this depends on the distance from the source and in particular from the noise level. It can be concluded that the 10 h periodicity can be detected at a remote location as long as each single signature of the injections can be identified. Of importance, however, is the particle's mean free path and the signal to noise/background ratio. For the case of a mean free path of  $\lambda = 1$  AU and a noise level of 5% (Fig. 9.8), the 10 h periodicity would be observed up to about 1.5 AU.

In addition, the results of the numerical model are in agreement with the observations that the presence of the 10 h periodicity is related to the presence of a measurable anisotropy.

Fig. 9.10 shows the result of applying Eqn.(9.2) for the example of a particle injection every 30 mins at the source. Here, the observer is 1 AU away from the source and the mean free path was set to 1 AU and a noise level of 5% was used. A periodicity of 30 mins can be identified. Note the general increase of the total flux level with time.

One observation the model can not directly explain with the transport parameter used above are the shifts in the phase between the 10 h periodicity observed in situ

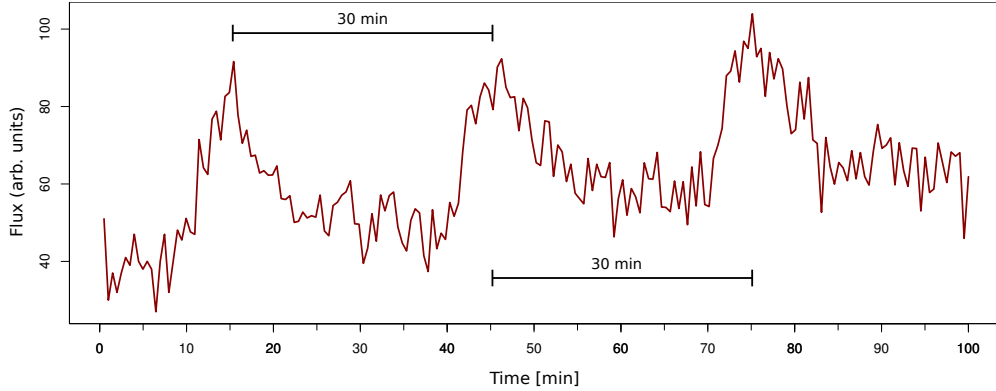


**Figure 9.10:** Result of applying Eqn. (9.2) for the case of a particle injection every 30 mins observed at a distance of 1 AU. Again, the mean free path is  $\lambda = 1$  AU and a noise level of 5% was used. Under these conditions, the periodic variation of the source can be observed at this remote location.

and the predictions of the “Jovian clock”. As shown in the chapter on observations of Jovian jets, phase shifts of up to 4 h were frequently observed. The time shifts estimated from the numerical model are smaller (cf. Fig. 9.8). Assuming a distance between the source and the observer of 1.2 AU as in the case of the observations around day 145 in 2004, the mean pitch-angle cosine of the particles can be calculated as

$$\langle \mu \rangle = \frac{s}{v_0 \Delta t}, \quad (9.3)$$

where  $s = 1.2$  AU is the distance,  $v_0 \approx c$  the speed of the particles and  $\Delta t = 4$  h is the phase shift. Using this values one obtains  $\langle \mu \rangle \approx 0.0416$ , i.e. a mean pitch angle of  $\approx 87.6^\circ$ . This contradicts the observations of the large anisotropies during Jovian jet events.

What are possible reasons for this discrepancy? Instrumental effect were shown to play a role as discussed in chapter 8. The influence of background fluxes in combination with the sudden increase of flux during jet events affects the detectability of the 10 h periodicity. The assumption of a straight magnetic connection between the source and the observer may not always be valid. A longer distance than the line-of-sight connection leads to a longer travel time of the electrons. Local focusing or defocusing effects must also be taken into account. Not at least there may be effects not taken into account yet, e.g. the wave-particle interactions.

# Chapter 10

## Summary & Outlook

And now for something  
completely different.

---

Monty Python's Flying Circus

### Résumé

In the early 1970's, the Jovian magnetosphere was identified as a considerable source of MeV electrons in the heliosphere by the Pioneer 10 and 11 spacecraft. Since then, these so-called Jovian electrons were under investigation by experimental and theoretical means. The propagation of Jovian electrons was successfully described by Parker's transport model, a diffusion-convection equation including adiabatic energy changes. This model, however, does not take into account the pitch-angle of the electrons, hence it only describes the spatial diffusion of particles. While this assumption is justified for the description of the global propagation of Jovian electrons, there is a class of Jovian electron events called Jovian Bursts or Jovian jets, where Parker's model is not applicable. These events are characterized by sudden increases and decreases with respect to the ambient electron flux, a notable anisotropy of the particles with respect to the local magnetic field and frequently show a period modulation of the electron's spectral index related to Jupiter's diurnal rotation period of approx. 10 h, similar to the electrons observed inside the Jovian magnetosphere.

The main results of this work can be summarized as follows:

- A reinvestigation of the Ulysses and Pioneer 10/11 data in the Jovian magnetosphere revealed the existence of a second recurrent variation in the energy spectrum of MeV electron can be identified beside the well-known "clock" modulation during Ulysses' inbound trajectory. While this observations lacks a coherent discussion in the literature, a comprehensive analysis of these variation was part of this work. Based on Ulysses observations this second modulation is manifested

by small maxima (coined “minor peaks”) in the particle spectral index trailing the larger “clock” peaks by about 3.25 h. These minor peaks in the spectral index are accompanied by local minima in the electron counting rates. These peaks were found to occur at subsolar longitudes of  $\lambda_{III} = 45 - 100^\circ$ . A comparison with Pioneer 10 data showed that these minor peaks were also present and show similar properties as the Ulysses events, e.g. the correlation with counting rates and the temporal distance to the major peaks, albeit the minor peaks were not present throughout the entire inbound trajectory. The Pioneer 11 data, however, show no evidence for this additional modulation. An investigation of the spacecraft’s distance from the magnetospheric current sheet as a function of the subsolar longitude lead to the suggestion that the minor peaks are a feature of low magnetic latitudes. The fact that Ulysses was located close to the magnetic equator when the longitudes  $\lambda_{III} = 45 - 100^\circ$  were facing the subsolar point while Pioneer 10 and 11 were much further away is interpreted as the explanation for the good observability of the minor peaks by Ulysses. Furthermore, previous results of the HI-SCALE instrument aboard Ulysses concerning the existence of a so-called high-latitude boundary layer, i.e. a reservoir of energetic particles at high magnetic latitudes linked to the “clock” modulation could be verified by means of an analysis of KET data for MeV electron data.

- For the first time the pitch-angle distributions of jets were analyzed in order to answer the question if Jovian jets show evidence for scattering across  $\mu = 0$ . Several examples were discussed showing that strong backscattering can be observed as well as a complete absence of scattering across  $\mu = 0$ . This finding has important impact on the understanding of the connection between the isotropic Jovian electron flux and anisotropic jets event. The presence of jets showing significant backscattering as well as (almost) scatterfree events illustrates the highly variable transport conditions in the interplanetary magnetic field at the orbit of Jupiter. Scattering across  $\mu = 0$  leads to an isotropization of the particle distribution, thus Jovian electron jets are assumed to contribute to the global Jovian electron flux in the heliosphere.
- A connection between the occurrence of Jovian jets and interplanetary coronal mass ejections (ICMEs) was discussed. While the overall picture shows no convincing correlation between both kinds of events, several events were discussed where Jovian jets can be related to the occurrence of ICMEs.
- Based on a three-dimensional (time, periodicity, power) spectral analysis of the ratio of two adjacent energy channels of the electron counting rates of the HET and KET instruments as well as a comparison of these data with the expected temporal evolution, it was possible to find clear evidence that the Jovian 10 h periodicity can be recovered up to distance of  $\sim 1.2$  AU from the planet during Jovian bursts or jets. During this times, persistent anisotropies of MeV electrons are observed, indicating effective transport of these particles parallel to the local

magnetic field. While the observation of the 10 h periodicity at 1.2 AU from the planet is the most distant and convincing observation of this feature so far, there is even evidence that the last Jovian jet observed by Ulysses in 2004 about  $\sim 2.2$  AU away from Jupiter still features the periodic variation of the energy spectrum. Another important finding is the connection between the observation of the 10 h periodicity and the detection of particle anisotropies. The presence of the 10 h periodicity is always accompanied by anisotropies in the electron flux. From this it can be concluded that the 10 h periodicity vanishes when the anisotropy of an injected electron ensemble vanishes.

- A careful reinvestigation of the Pioneer 10 MeV-electron data with respect to the magnetic field direction and particle anisotropies showed that many events already discussed by Chenette et al. (1974) can be subdivided to Jovian jet events according to the Ulysses observations of Ferrando et al. (1993) and McKibben et al. (2007). In agreement with the Ulysses findings presented in this work, a close correlation between the occurrence of anisotropies and the observation of the 10 h periodicity could be found. This emphasizes the fact that short-lived and anisotropic electron events are a common feature of the Jovian electron source and must be taken into account for a comprehensive description of Jovian electrons.
- As discussed in the latter point, the pitch-angle dependent transport of Jovian electrons is of importance for the understanding of their propagation. Based on the focused-transport model (also known as Roelof's equation), a numerical model was developed to describe the pitch-angle dependent propagation of Jovian electrons. This model contains pitch-angle diffusion as well as systematic changes of the pitch angle. For an assumed mean free path of the particles of  $\lambda = 1$  AU it was shown that the model is able to describe the basic properties of Jovian jets. Albeit more work is required, one question may be answered: What is a Jovian jet? Based on the observations and numerical computation presented in this work, a Jovian jet event can be interpreted as Jovian electrons injected into interplanetary space and observed at times before the mean free path of the particles allowed a cumulative scattering strong enough to let their anisotropy vanish.

## Outlook

Of course, the present work raised further questions<sup>1</sup> that could not yet be answered and motivate for the further application of novel techniques in the data analysis and numerical modeling. Furthermore, some work that had been done but did not enter the thesis needs to be mentioned. Some of these ideas are outlined in the following.

---

<sup>1</sup>The purpose of science is to find answers to questions raised by science.

As it was shown, the HET instrument, in particular the H6 channel, is affected by background radiation. A subtraction of this background would provide an enhancement of the signature of Jovian electrons detected by the instrument and a better comparability with the KET instrument.

Based on the calculation of the pitch-angle coverage of the KET and HET instruments it becomes possible to investigate the question if a persistent net flux of electrons away from Jupiter can be observed even during times where no jet-like events are present. This would involve a sophisticated treatment of the highly variable magnetic field direction with respect to the viewing direction of the particle instrument by means of statistical methods.

Beside the MeV-electron data measured by the KET/HET, the Jovian influence on the particle population in the vicinity of the planet can also be found in the low energetic electron and ion data of HI-SCALE and EPAC. A comprehensive comparison of these data might enhance the knowledge of the interplay of the interplanetary magnetic field and particles from some keV up to some MeV.

While the presented model for the Jovian jets turned out to be able to principally describe the observed data, more detailed insights could be derived by using stochastic differential equations (SDEs). This method allows the calculation of single particle trajectories, while "traditional" models compute the probability density function. The study of single particle trajectories is of highest interest for the study of the 10 h periodicity since every particle can be assigned to its phase within the 10 h cycle during the time of injection.

# Appendix A

## The System III (1965) Coordinate System

The definition of a coordinate system to identify points on a planetary surface, for example, requires the definition of a point of reference. For the Earth, the longitude is defined via the zero meridian (zero longitude), crossing the observatory in Greenwich, UK. The latitude is defined by the equator and the poles of the Earth. This definition is relatively easy, because it is assumed that the point of reference stays constant over time. For Jupiter, however, the definition of a point of reference is much more complicated because there is no solid surface visible to the observer due to the non-uniform motion of Jupiter's cloud layers. Over time, three different reference systems have been developed. The first and second ones, System I & II, were defined by the rotation rate of cloud features at different latitudes. When Jupiter was identified as a radio source in the late 1950's, however, it became convenient and necessary to establish a third coordinate system, called System III (1957), based on the radio emission of Jupiter. The coordinate system that is commonly used today is called System III (1965) is a more precise version of System III (1957)<sup>1</sup>. The convention of the System III (1965) coordinates can be seen in Fig. A.1. The center of the coordinate system is the location of Jupiter, and  $\Omega_J$  is the angular speed. If observed from the North pole, the planet rotates counter clockwise, so does the prime meridian (i.e.  $\lambda_{III} = 0^\circ$ ). As a consequence, for a spacecraft (s/c) located at a fixed position with respect to the subsolar point, the System III (1965) longitude increase with time, i.e. the coordinate system is left-handed. Once the System III (1965) longitude  $\lambda_{III}$  of a spacecraft at a given time is known, one is often also interested in the latitude of the spacecraft with respect to magnetic equator. To solve this question, one needs to know how Jupiter's magnetic dipole is tilted with respect to the System III (1965) convention. It was estimated that the northern end of the dipole is tilted about  $9.6^\circ$  towards  $\lambda_{III} = 20 \pm 3^\circ$ . Therefore, the magnetic and jovigraphic equators intersect at

---

<sup>1</sup>Indeed, the only difference between System I, II and III is the value of Jupiter's angular speed,  $\Omega_J$ , being used.

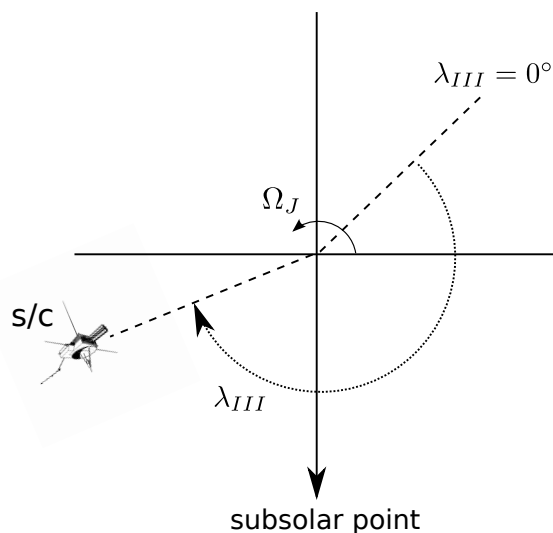


**Figure A.1:** Definition of the  $\lambda_{III}$  coordinate system as seen from above the north pole. While the planet rotates counter clockwise, the  $\lambda_{III}$  longitude of a spacecraft increases with time.

$\lambda_{III} = 110^\circ$  and  $\lambda_{III} = 290^\circ$ , respectively. The latitudinal distance from the magnetic equator can therefore be calculated by

$$\vartheta_m = 9.6^\circ \sin(\lambda_{III} - 110^\circ) + \vartheta. \quad (\text{A.1})$$

Here,  $\vartheta_m$  is the latitude of the spacecraft with respect to the magnetic equator,  $\vartheta$  is the jovigraphic latitude and  $\lambda_{III}$  indicates the respective longitude in System III (1965). Eqn. A.1 has been used in this study to calculate the magnetic latitude of Pioneer 10 and 11.



# Appendix B

## Numerical Solution of the Transport Model

In this work, the so-called Roelof equation for charged particles in a magnetic field including systematic and stochastic changes in the pitch angle was used to study the pitch-angle depended propagation of Jovian electrons along the interplanetary magnetic field. The equation reads

$$\frac{\partial f}{\partial t} + \mu v \frac{\partial f}{\partial z} + \frac{v(1-\mu^2)}{2L} \frac{\partial f}{\partial \mu} = \frac{\partial}{\partial \mu} \left( D_{\mu\mu} \frac{\partial f}{\partial \mu} \right) + Q(z, \mu, t), \quad (\text{B.1})$$

as described in Section 4.4. This equation, however, is not flux conserving if the diameter of the flux tube under investigation is not constant. This is the case if the magnetic field changes with distance because of the conservation of the magnetic flux

$$\int \vec{B} \cdot d\vec{A} = \text{const.} \quad (\text{B.2})$$

This can be expressed as

$$B_0 A_0 = B(z) A(z), \quad (\text{B.3})$$

where  $B_0$  and  $A_0$  is the magnetic field strength and the flux tube diameter at  $z_0$ . To make sure that the phase space density in Eqn. (B.1) is conserved, it must be multiplied with the flux tube's diameter (Ng and Wong, 1979), i.e.

$$F(z, \mu, t) = A(z) f(z, \mu, t). \quad (\text{B.4})$$

The conservative form of the transport equation can now be written as

$$\frac{\partial F}{\partial t} + \frac{\partial (\mu v F)}{\partial z} + \frac{\partial}{\partial \mu} \left( \frac{v(1-\mu^2)}{2L} F \right) = \frac{\partial}{\partial \mu} \left( D_{\mu\mu} \frac{\partial F}{\partial \mu} \right) + \tilde{Q}(z, \mu, t), \quad (\text{B.5})$$

with  $\tilde{Q}(z, \mu, t) = A(z) Q(z, \mu, t)$ . Eqn. (B.5) is the equation being actually solved.

## B.1 Numerical Setup

Most physical problems are expressed as ordinary (ODEs) or partial differential equation (PDEs), e.g. Newton's law of motion or the diffusion equation. Unfortunately, for many problems, general solutions of the corresponding equations are not known, e.g. for Parker's transport equation or Roelof's equation described in chapter 4.4. In this case, it is necessary to approach the exact solution by means of numerical calculations. In order to do so, the PDE has to be transformed to a finite differences equation (FDE) to achieve an algebraic expression that can be solved by a computing machine (e.g. Anderson et al., 1997; Fletcher, 2000).

This transformation is, of course, related to the mathematical definition of the derivative of a function  $f(x)$ , e.g.

$$\frac{\partial f(x)}{\partial x} = \lim_{\Delta x \rightarrow 0} \frac{f(x_0 + \Delta x, y_0) - f(x_0, y_0)}{\Delta x}. \quad (\text{B.6})$$

Using a computer to calculate the derivative,  $\Delta x$  can not be infinitely small, what unavoidably leads to truncation errors. A Taylor-series expansion of  $f(x)$  at  $(x_0, y_0)$  leads to

$$f(x_0 + \Delta x) = f(x_0) + \frac{\partial f}{\partial x} \Big|_0 \Delta x + \underbrace{\frac{\partial^2 f}{\partial x^2} \Big|_0 \frac{(\Delta x)^2}{2!} + \dots}_{\text{Truncation Error } O(\Delta x)}, \quad (\text{B.7})$$

where the terms indicated by  $O(\Delta x)$  refers to the truncations error that occurs if the calculation stops after the second term on the right side. In terms of Eqn. (B.6), the first derivative can be written as

$$\frac{\partial f}{\partial x} \Big|_{x_0} = \frac{f(x_0 + \Delta x) - f(x_0)}{\Delta x} + O(\Delta x), \quad (\text{B.8})$$

where  $O(\Delta x)$  denotes the truncation error of first order as indicated in Eqn. (B.7). Defining a one-dimensional equidistant grid with nodes  $i \in \mathbf{N}_0$  so that  $\Delta x = x_{j+1} - x_j = \text{const.}$  (see Fig. B.1), the latter equation can be rewritten as

$$\frac{\partial f}{\partial x} \Big|_{x_j} = \frac{f_{j+1} - f_j}{\Delta x} + O(\Delta x). \quad (\text{B.9})$$

This is a so-called forward difference scheme. The corresponding backward difference scheme reads

$$\frac{\partial f}{\partial x} \Big|_{x_j} = \frac{f_j - f_{j-1}}{\Delta x} + O(\Delta x). \quad (\text{B.10})$$

A central-difference scheme can be obtained by taking the average of the forward and backward schemes so that

$$\frac{\partial f}{\partial x} \Big|_{x_j} = \frac{f_{j+1} - f_{j-1}}{2\Delta x} + O(\Delta x^2). \quad (\text{B.11})$$

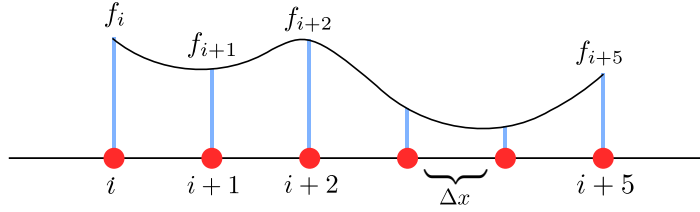


**Figure B.1:** A simple one-dimensional equally spaced numerical grid. The distance between two nodes is defined as  $\Delta x$ . The discrete values of the phase space density  $f_j$  belonging to the nodes  $j$  are the numerical representation of the continuous quantity.

The fact that this scheme is of second-order accuracy can be shown by subtracting the Taylor series expansion of the forward difference from that of the backward one. Over the last decades a variety of methods to discretize and solve PDEs were developed that differ in the number of grid points being involved, numerical stability and the truncation error.

## The DuFort-Frankel & Leapfrog Schemes

Consider the one-dimensional diffusion equation with an constant convection term  $v$

$$\frac{\partial f}{\partial t} + v \frac{\partial f}{\partial x} = \frac{\partial}{\partial x} \left( D \frac{\partial f}{\partial x} \right). \quad (\text{B.12})$$

There are several ways to give an algebraic expression for the first and second order derivatives in Eqn. (B.12) extensively discussed in text books (e.g. Anderson et al., 1997; Fletcher, 2000). Assuming constant diffusion and convection coefficients, the discretization of this equation using the leapfrog method reads

$$\frac{f_j^{n+1} - f_j^{n-1}}{2\Delta t} + v \frac{f_{j+1}^n - f_{j-1}^n}{2\Delta x} - D \frac{f_{j-1}^n - 2f_j^n + f_{j+1}^n}{\Delta x^2} = 0, \quad (\text{B.13})$$

where  $j$  and  $n$  are nodes in the spatial and time domains, respectively, and can be resolved to give an explicit algebraic expression for  $f_j^{n+1}$ . DuFort and Frankel (1953), however, noted that because of the shape of the second derivative (known as Richardson's method, Richardson (1910)) this expression is unconditionally unstable (see also Fletcher, 2000; Chung, 2002). However, substituting  $f_j^n$  by  $(f_j^{n+1} + f_j^{n-1})/2$  results<sup>1</sup> in the DuFort-Frankel scheme<sup>2</sup>

$$\frac{f_j^{n+1} - f_j^{n-1}}{2\Delta t} + v \frac{f_{j+1}^n - f_{j-1}^n}{2\Delta x} - D \frac{f_{j-1}^n - (f_j^{n-1} + f_j^{n+1}) + f_{j+1}^n}{\Delta x^2} = 0, \quad (\text{B.14})$$

<sup>1</sup>This is simply the temporal interpolation of  $f_j^n$  by using the two neighboring nodes in the time domain.

<sup>2</sup>In the original work the convection term was not taken into account, i.e.  $v = 0$ .

that is found to be unconditionally stable. Again, this algebraic equation can explicitly be rearranged to derive an expression

$$f_j^{n+1} = ((1 - \beta) f_j^{n-1} - \alpha (f_{j+1}^n - f_{j-1}^n) + \beta (f_{j+1}^n + f_{j-1}^n)) / (1 + \beta), \quad (\text{B.15})$$

with  $\alpha = v\Delta t/\Delta x$  and  $\beta = 2D\Delta t/\Delta x^2$ . It should be noted, however, that in the Taylor expansion of the DuFort-Frankel scheme the term

$$-D \frac{\partial^2 f}{\partial t^2} \Big|_{n,j} \left( \frac{\Delta t}{\Delta x} \right)^2 \quad (\text{B.16})$$

appears. Given the case that  $\Delta t$  is not sufficiently smaller than  $\Delta x$ , i.e.

$$\lim_{\Delta t, \Delta x \rightarrow 0} \left( \frac{\Delta t}{\Delta x} \right)^2 \neq 0, \quad (\text{B.17})$$

the DuFort-Frankel scheme actually solves the partial differential equation

$$\frac{\partial f}{\partial t} + \alpha^2 D \frac{\partial^2 f}{\partial t^2} = D \frac{\partial^2 f}{\partial x^2}, \quad (\text{B.18})$$

with  $\alpha = \Delta t/\Delta x$ . While the DuFort-Frankel scheme is still stable, it is not consistent with the original diffusion equation (cf. Anderson et al., 1997).

Since the DuFort-Frankel method only affects the second derivative, Eqn. (B.14) may be seen as a combination of the DuFort-Frankel and leapfrog methods. Fig. B.2 shows a comparison of the DuFort-Frankel and leapfrog schemes for the second derivative. The nodes in the spatial domain (horizontal direction) are indicated by  $j$ 's, the time domain (vertical direction) by the  $n$ 's. The filled red dots represent nodes being used for the computation of  $f_j^{n+1}$ , represented by the filled blue dots. For the DuFort-Frankel method the node  $f_j^{n+1}$  also appears in the second spatial derivative.

However, being a second-order scheme, the DuFort-Frankel/leapfrog algorithm requires two time steps to calculate the next one, namely the nodes  $n$  and  $n - 1$ . For the very first time step, the  $f$  at the node  $n - 1$  is not defined. To circumvent this problem, another algorithm may be used for the first step of integration while for all other time steps, the DuFort-Frankel/leapfrog method is used. A possible first time step can be realized by implementing the FTCS (full-time central-space) algorithm (Roache, 1972; Strikwerda, 2004)

$$\frac{f_j^{n+1} - f_j^n}{\Delta t} + v \frac{f_{j+1}^n - f_{j-1}^n}{2\Delta x} - D \frac{f_{j-1}^n - 2f_j^n + f_{j+1}^n}{\Delta x^2} = 0. \quad (\text{B.19})$$

Note that the temporal derivative incorporates two nodes, i.e.  $n$  and  $n + 1$ , i.e. Eqn. (B.19) is a one-step scheme what makes it usable for the first time step.

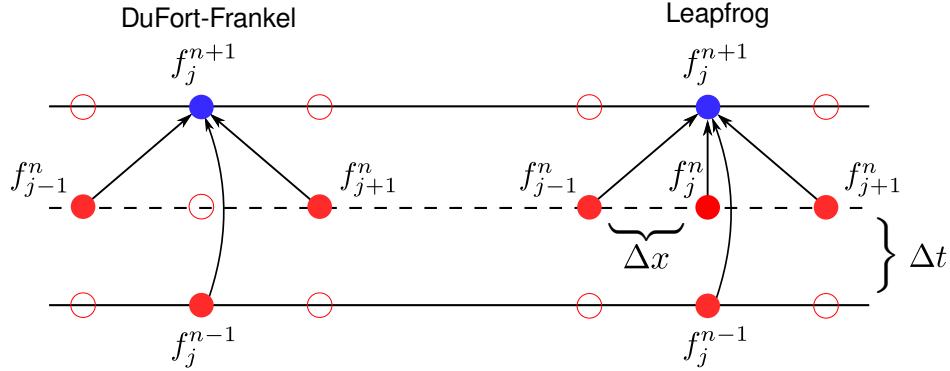


**Figure B.2:** Comparison of the stencils of the DuFort-Frankel and leapfrog discretization schemes for the second derivative assuming a constant diffusion coefficient. The filled red dots indicate the grid points used to calculate the grid point  $f_j^{n+1}$ , indicated by the blue dots.

### Modified Schemes for Focusing & Diffusion

In the case of our transport equation, the diffusion coefficient is not a constant, but depends on  $\mu$ . The same applies to the focusing term being a function of  $\mu$  as well. Starting with the focusing term and keeping in mind that the leapfrog scheme is a central difference scheme we may write

$$\frac{\partial}{\partial \mu} \left( \frac{v(1 - \mu^2)}{2L} f \right) \Big|_{\mu=\mu_j} \approx \frac{L_{j+1/2}^* \frac{(f_{j+1}^n + f_j^n)}{2} - L_{j-1/2}^* \frac{(f_j^n + f_{j-1}^n)}{2}}{\Delta \mu}. \quad (\text{B.20})$$

Here,  $L_{j\pm 1/2}^*$  represents the complete focusing term  $v(1 - \mu_{j\pm 1/2}^2)/(2L)$ . Note that the grid points  $j \pm 1/2$  are located half-way between the grid points  $j \pm 1$  and the corresponding values of  $L^*$  control the flux across the boundary of the two adjacent grid points. This type of discretization has already been used by Ng and Wong (1979). It is clear that we obtain the above form of the leapfrog scheme if  $L_{j+1/2}^* = L_{j-1/2}^*$  for all  $j$ . The  $\approx$  appears because of the truncation error of the finite difference scheme.

The discretization of the diffusion term with variable diffusion coefficient using the DuFort-Frankel scheme can be obtained in a similar way and reads (see also chapter 6 of Randall (2009) for the DuFort-Frankel scheme or chapter 6 of Strikwerda (2004) for an application of the FTCS scheme to this problem)

$$\frac{\partial}{\partial \mu} \left( D_{\mu\mu} \frac{\partial f}{\partial \mu} \right) \Big|_{\mu=\mu_j} \approx \frac{1}{(\Delta \mu)^2} [D_{j+1/2} (f_{j+1}^n - f_j^{n+1}) - D_{j-1/2} (f_j^{n-1} - f_{j-1}^n)], \quad (\text{B.21})$$

where the values of the diffusion coefficient are defined in the same way as in the case of the convection term. However, concerning the assignment of the diffusion coefficients  $D_{j\pm 1/2}$  and the phase space densities  $f_j^{n\pm 1}$ , this stencil is found to be somewhat

arbitrarily. Alternatively, one may also write

$$\frac{\partial}{\partial \mu} \left( D_{\mu\mu} \frac{\partial f}{\partial \mu} \right) \Big|_{\mu=\mu_j} \approx \frac{1}{(\Delta\mu)^2} [D_{j+1/2} (f_{j+1}^n - f_j^{n-1}) - D_{j-1/2} (f_j^{n+1} - f_{j-1}^n)]. \quad (\text{B.22})$$

Numerical tests showed that an algorithm that uses one of the two possible forms fails to conserve the phase space density over time as an algorithm does that makes use of both algorithm in an alternating way (e.g. Eqn. (B.21) for even time steps, Eqn (B.22) for uneven time-steps). Another alternative, however, is to combine the stencils of the two schemes. This can be achieved by substituting  $f_i^{n\pm 1}$  by the average  $(f_i^{n+1} + f_i^{n-1})/2$ . Consequently, we write

$$\begin{aligned} \frac{\partial}{\partial \mu} \left( D_{\mu\mu} \frac{\partial f}{\partial \mu} \right) \Big|_{\mu=\mu_j} \approx & \frac{1}{(\Delta\mu)^2} D_{j+1/2} \left( f_{j+1}^n - \frac{f_j^{n+1} + f_j^{n-1}}{2} \right) \\ & - \frac{1}{(\Delta\mu)^2} D_{j-1/2} \left( \frac{f_j^{n+1} + f_j^{n-1}}{2} - f_{j-1}^n \right). \end{aligned} \quad (\text{B.23})$$

This is the finite difference scheme for the pitch-angle diffusion term actually being used in this work, because it was found that this scheme shows a much better performance and stability as well as a much better conservation of the phase space density (conservation of mass).

The use of two staggered grids also has a reasonable physical interpretation: consider two basins each filled with a solution of different concentrations separated by a membrane. The diffusion current across the membrane is determined by its permeability and the concentration of the solutions in the two basins.

### A Convection Scheme of Fourth Order Accuracy

The general leapfrog scheme is of second order accuracy. The fourth-order difference scheme for the first derivative reads

$$\frac{\partial f}{\partial z} \Big|_{z=z_i} = \frac{-f_{i+2}^n + 8f_{i+1}^n - 8f_{i-1}^n + f_{i-2}^n}{12\Delta z} + O(\Delta z^4), \quad (\text{B.24})$$

and can be derived by analyzing the Taylor series of the function as shown e.g. by Strikwerda (2004, p. 80). This scheme was used in this work to discretize the convection of particles along the magnetic field line because of the higher accuracy of the scheme compared to the basic leapfrog scheme. The drawback of this scheme, however, is the lowered level of numerical stability.

### Grid Generation & Boundary Conditions

An important subject in the solution of PDEs is the formulation of a so-called well-posed problem. As discussed by Fletcher (2000) and Mattheij et al. (2005), a problem

is well posed if a unique (computational) solution exists and the solution depends continuously on the initial problem and the boundary conditions. In particular, the latter point is of importance for numerical calculations because it emphasizes the importance of stability (see also Salsa, 2008). Therefore, well-posed problems strongly depend on the correct formulation of initial and boundary conditions. There are basically three types of boundary conditions as briefly discussed in the following.

### Dirichlet Conditions

The Dirichlet boundary condition is the most straight-forward way to implement boundary conditions. Dirichlet conditions have the form

$$f = u \text{ on } \partial R \quad u \in \mathbf{R}, \quad (\text{B.25})$$

where  $u$  may either be a constant or a function of time and  $\partial R$  denotes the boundary of the grid. A typical application of Dirichlet conditions may be heat transfer along a rod, which ends are held at constant temperatures.

### Neumann Conditions

In contrast to Dirichlet conditions, Neumann conditions do not determine the value of  $f$  at the boundary but its derivative, i.e.

$$\partial f / \partial n = u \text{ on } \partial R \quad u \in \mathbf{R}. \quad (\text{B.26})$$

Again,  $u$  may be constant or variable in time, and  $\partial / \partial n$  is the normal derivative.

### Periodic Conditions

Periodic boundary conditions may apply if the numerical boundaries actually represent the same physical location. An example of such a system may be the heat transport in a closed iron ring with a given initial heat distribution. In addition, periodic boundary conditions are also useful for test purposes. For a quantity  $f(x, t)$  on the interval  $x \in [a, b]$ , periodic boundary conditions read

$$f(a, t) = f(b, t). \quad (\text{B.27})$$

That means that what “leaves” the domain at one side, “comes in” at the opposite side.

In addition, a fourth type of boundary condition may be constructed by a combination of Dirichlet and Neumann conditions, called Robin condition (e.g. Fletcher, 2000). In this case, the boundary is defined by the sum of a Dirichlet and a Neumann term, i.e.  $\frac{\partial f}{\partial n} + bf = u$ , where  $b$  and  $u$  may be functions of time.

The boundary conditions of the transport equation depend on the physical meaning of the boundaries and practical considerations. For the two physical domains, the following boundary conditions must be considered.

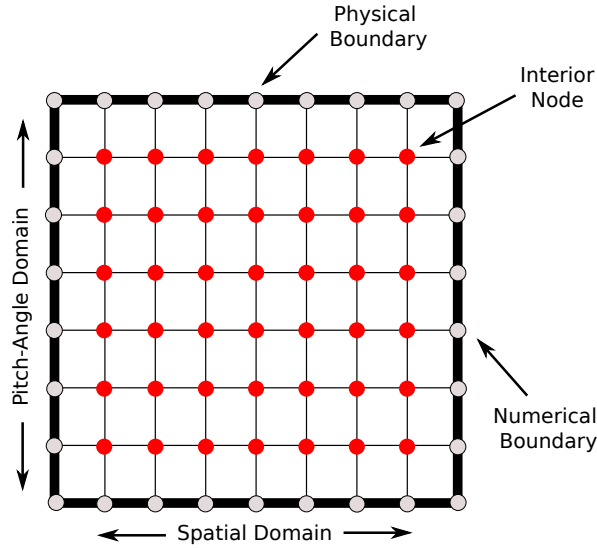


**Figure B.3:** A two dimensional numerical grid representing a spatial domain (abscissa) and the pitch-angle domain (ordinate). The red dots represent the nodes in the interior of the computational domain, the light shaded dots are boundary points. With respect to the physical conditions, the boundary conditions that apply in the spatial domain are numerical, while the boundary condition in pitch-angle space must fulfill a well defined physical meaning.

### Boundary Conditions for the Spatial Domain

In the numerical model it is necessary to consider a finite interval of a magnetic field line. There are several ways to implement boundary conditions for the spatial domain. Hatzky (1996) applied reflecting conditions to the inner boundary (i.e. near the solar surface) and open boundary conditions at the outer boundary. Owens and Gombosi (1981) and Kóta et al. (1982) used absorbing (Dirichlet) conditions by setting the flux to zero at the inner and outer spatial boundary. The model presented in this work incorporates von Neumann boundary conditions that allow the particles to leave the boundaries of the computational domain with a minimum of disturbances generated at the boundary and the interior in order to minimize the influence of the numerical boundary on the physical processes in the domain.

Strikwerda (2004, chapter 11) discusses several possible boundary conditions for numerical representation of hyperbolic partial differential equation of the form

$$\frac{\partial f}{\partial t} + a \frac{\partial f}{\partial x} = 0$$

using the leapfrog scheme with respect to their stability. The author shows that a suitable boundary condition for this scheme is

$$f_0^{n+1} = f_0^n + \alpha (f_1^n - f_0^n), \quad (\text{B.28})$$



where  $\alpha = a\Delta t/\Delta x$  with  $a > 0$ . The index 0 refers to the boundary point on the “left”. In the model used in this study, however, a central difference scheme of fourth-order accuracy (leapfrog of fourth order) is used for the convection of particles along the magnetic field line. That means there are two numerical boundary points at each side of the spatial domain ( $f_0, f_1$  and  $f_{i_{max}}, f_{i_{max}-1}$ ). During the development of the transport model, it was found that the boundary condition Eqn. (B.28) can directly be used to the fourth-order difference scheme if the condition is applied to each boundary point separately, i.e.

$$f_1^{n+1} = f_1^n + \alpha (f_2^n - f_1^n),$$

and

$$f_0^{n+1} = f_0^n + \alpha (f_1^n - f_0^n).$$

The boundary condition for the “right” side of the computational domain follows accordingly.

### Boundary Conditions for the Pitch-Angle Domain

Since particles are not allowed to be scattered or convected across  $\mu = \pm 1$ , the flux  $S_\mu$  in the pitch angle domain must vanish at the boundaries (e.g. Earl et al., 1995; Hatzky, 1996). Therefore, the phase space density is not defined beyond this boundaries. To illustrate this, consider again the one-dimensional diffusion or heat transport equation with variable diffusion coefficient

$$\frac{\partial f}{\partial t} = \frac{\partial}{\partial x} \underbrace{\left( D(x) \frac{\partial f}{\partial x} \right)}_{S_x}, \quad (\text{B.29})$$

where  $S_x$  denotes the diffusion or heat flux, respectively. Depending on the boundary conditions, two principal physical situations may be constructed. In the first case, we apply the diffusion equation to an iron rod which two ends are held at fixed temperatures  $T_1$  and  $T_2$  as it is shown on the left side of Fig. B.4. Independent of the initial solution (dashed curve), the temperature distribution will approach the steady state solution (solid line) as time proceeds. Apparently, the boundary conditions are Dirichlet conditions. If  $T_0 \neq T_1$ , the diffusion current along the rod is non-zero, i.e. heat is transported from one end to the other. As can be seen, however, the derivative of the diffusion flux vanishes as does the time derivative. In the second case, illustrated by the sketch on the right side of Fig. B.4, the ends of the rod are isolated, i.e. no heat (i.e. energy) is allowed to leave or enter the volume. Therefore, Neumann conditions apply since there is no flux across the boundary, i.e.  $\partial f/\partial x = 0$  on  $\partial R$ . In this case, the steady state solution is given by the solid line, i.e. the steady state condition is an isothermal distribution along the iron rod and the diffusion current is zero, i.e. there is no net transport of heat along the rod.

Concerning the transport of particles in the pitch-angle domain, we are facing a similar boundary condition as for the case of the isolated rod: Particles are not allowed

to be scattered or convected across  $\mu = \pm 1$ . Interestingly, these (Neumann) boundary condition is met automatically because of the term  $(1 - \mu^2)$  in both the focusing and diffusion coefficient. Therefore, it is convenient to define the grid so that the grid points

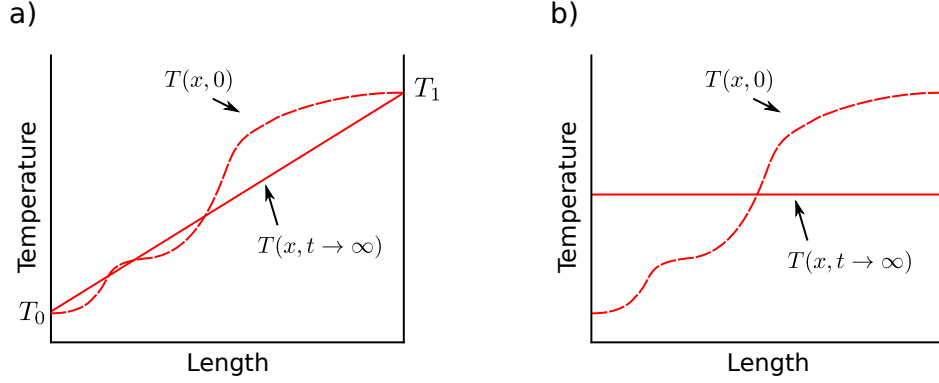


**Figure B.4:** Two typical examples of diffusion or heat transport are shown. Panel a) may represent an iron rod with an initial spatial temperature distribution  $T(x, 0)$  (dashed line), which two ends are hold at fixed temperatures  $T_1$  and  $T_2$ . The steady state solution is given by the solid line. Panel b) accounts the case of a fully isolated rod, i.e. the energy of the system is conserved. Again, the dashed line represents the initial distribution and the solid line the steady state solution. In both cases, the derivative of the diffusion current vanishes when the steady state configuration is reached.

$\mu_{-1/2}$  and  $\mu_{j_{max}+1/2}$  represent  $\mu = \pm 1$ . Consequently, the diffusion and focusing fluxes become exactly zero at these grid points because of the factor  $(1 - \mu^2)$ . Therefore, using Eqn. (B.21) the derivative of the diffusion term at the first and last grid point, respectively, read

$$\left. \frac{\partial}{\partial \mu} \left( D_{\mu\mu} \frac{\partial f}{\partial \mu} \right) \right|_{\mu=\mu_0} \approx \frac{D_{1/2}}{(\Delta\mu)^2} (f_1^n - f_0^{n+1}) \quad \text{if } j = 0, \quad (\text{B.30})$$

and

$$\left. \frac{\partial}{\partial \mu} \left( D_{\mu\mu} \frac{\partial f}{\partial \mu} \right) \right|_{\mu=\mu_{j_{max}}} \approx \frac{-D_{j_{max}-1/2}}{(\Delta\mu)^2} (f_j^{n-1} - f_{j_{max}-1}^n) \quad \text{if } j = j_{max}. \quad (\text{B.31})$$

The derivation of the boundary values for the scheme given in Eqn. (B.22) follows accordingly. The boundary values for the time-averaged scheme (Eqn. (B.23)) are given by

$$\left. \frac{\partial}{\partial \mu} \left( D_{\mu\mu} \frac{\partial f}{\partial \mu} \right) \right|_{\mu=\mu_0} \approx \frac{D_{1/2}}{(\Delta\mu)^2} \left( f_1^n - \frac{f_0^{n+1} + f_0^{n-1}}{2} \right) \quad (\text{B.32})$$

and

$$\left. \frac{\partial}{\partial \mu} \left( D_{\mu\mu} \frac{\partial f}{\partial \mu} \right) \right|_{\mu=\mu_{j_{max}}} \approx -\frac{D_{j_{max}-1/2}}{(\Delta\mu)^2} \left( \frac{f_{j_{max}}^{n+1} + f_{j_{max}}^{n-1}}{2} - f_{j_{max}-1}^n \right) \quad (\text{B.33})$$

The expressions for the focusing term at the boundary are derived in a similar way and read

$$\left. \frac{\partial f}{\partial \mu} \right|_{\mu=\mu_0} \approx L_{1/2}^* \frac{(f_1^n - f_0^n)}{2\Delta\mu} \quad \text{at } j = 0, \quad (\text{B.34})$$

and

$$\left. \frac{\partial f}{\partial \mu} \right|_{\mu=\mu_0} \approx -L_{j_{max}-1/2}^* \frac{(f_{j_{max}}^n - f_{j_{max}-1}^n)}{2\Delta\mu} \quad \text{at } j = j_{max}. \quad (\text{B.35})$$

As the result of this conditions, the transport parameter for the pitch-angle domain

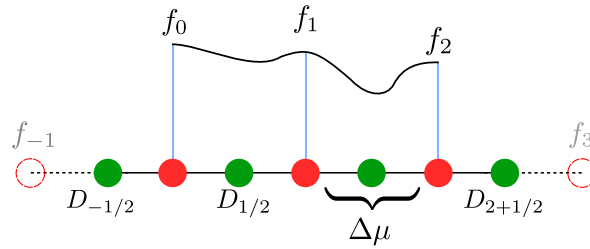


**Figure B.5:** An extension of the grid shown in Fig. B.1 to take into account  $\mu$ -dependent coefficients, e.g. the pitch-angle scattering coefficient  $D_{\mu\mu}$ . Because the grid has been defined in a way that  $D_{-1/2} = D_{\mu\mu}(\mu = -1)$  and  $D_{2+1/2} = D_{\mu\mu}(\mu = 1)$  become zero, the nodes  $f_{-1}$  and  $f_3$  never appear in the algorithm. This leads to closed boundary conditions with no flux across the  $\mu \pm 1$  boundary.

are defined so that

$$D_{\mu\mu}, v(1 - \mu^2)/(2L) \in [-1, 1],$$

For the phase-space density, in contrast, we write

$$f(z, \mu, t) \in (-1, 1).$$

That means, the value of the phase-space density at  $\mu = \pm 1$  can not be calculated. This is a well known (Earl et al., 1995), but not all to awkward limitation of numerical schemes since with a reasonable fine grid (say  $> 51$  nodes), the first and the last grid point are very close to  $|\mu| = 1$ .

## B.2 The Discretization of the Transport Equation

After having discussed the basics of the discretization scheme, we are now in the position to derive a discretized version of the full transport equation. Applying the DuFort-Frankel/leapfrog scheme for the  $\mu$ -transport and the fourth-order scheme for

the convection along the field line to the full Eqn. (B.5) leads to

$$\begin{aligned}
\frac{f_{i,j}^{n+1} - f_{i,j}^{n-1}}{2\Delta t} &= -\frac{v\mu_j}{12\Delta z} [-f_{i+2,j}^n + 8f_{i+1,j}^n - 8f_{i-1,j}^n + f_{i-2,j}^n] \\
&\quad -\frac{1}{2\Delta\mu} [L_{i,j+1/2}^* (f_{i,j+1}^n + f_{i,j}^n) + L_{i,j-1/2}^* (f_{i,j}^n + f_{i,j-1}^n)] \\
&\quad +\frac{1}{(\Delta\mu)^2} \left[ D_{i,j+1/2} \left( f_{i,j+1}^n - \frac{f_{i,j}^{n+1} + f_{i,j}^{n-1}}{2} \right) \right. \\
&\quad \left. - D_{i,j-1/2} \left( \frac{f_{i,j}^{n-1} + f_{i,j}^{n+1}}{2} - f_{i,j-1}^n \right) \right] \\
&\quad + Q_{i,j}^n,
\end{aligned}$$

where  $i$  and  $j$  represent the nodes in  $z$  and  $\mu$ , respectively.  $D_{i,j\pm 1/2}$  is the pitch-angle diffusion coefficient and corresponds to the value of  $D_{\mu\mu}$  between the nodes  $j$  and  $j\pm 1$ , respectively (cf. Fig. B.5). The same applies to  $L_{i,j\pm 1/2}^*$ . By rearranging the third term (the diffusion term) it can be substituted by

$$\frac{1}{(\Delta\mu)^2} \left( D_{i,j+1/2} f_{i,j+1}^n + D_{i,j-1/2} f_{i,j-1}^n - \hat{D}_{i,j} (f_{i,j}^{n+1} + f_{i,j}^{n-1}) \right),$$

with

$$\hat{D}_{i,j} = \frac{D_{i,j+1/2} + D_{i,j-1/2}}{2} \tag{B.36}$$

We define the following coefficients

$$\begin{aligned}
\zeta_j &= \frac{v\mu_j\Delta t}{6\Delta z} \\
\alpha_{i,j+1/2}^+ &= \frac{\Delta t L_{i,j+1/2}^*}{\Delta\mu} \\
\alpha_{i,j-1/2}^- &= \frac{\Delta t L_{i,j-1/2}^*}{\Delta\mu} \\
\beta_{i,j+1/2}^+ &= \frac{2\Delta t D_{i,j+1/2}}{(\Delta\mu)^2} \\
\beta_{i,j-1/2}^- &= \frac{2\Delta t D_{i,j-1/2}}{(\Delta\mu)^2} \\
\hat{\beta}_{i,j} &= \frac{2\Delta t \hat{D}_{i,j}}{(\Delta\mu)^2} \\
\gamma_{i,j}^+ &= 1 + \hat{\beta}_{i,j} \\
\gamma_{i,j}^- &= 1 - \hat{\beta}_{i,j} \\
\sigma_{i,j}^n &= 2\Delta t Q_{i,j}^n
\end{aligned}$$

and find the scheme

$$\begin{aligned}
f_{i,j}^{n+1} = & \left( \gamma_{i,j}^- f_i^{n-1} \right. \\
& - \zeta_j \left[ -f_{i+2,j}^n + 8f_{i+1,j}^n - 8f_{i-1,j}^n + f_{i-2,j}^n \right] \\
& - \alpha_{i,j+1/2}^+ (f_{i,j+1}^n + f_{i,j}^n) - \alpha_{i,j-1/2}^- (f_{i,j}^n + f_{i,j-1}^n) \\
& + \beta_{i,j+1/2}^+ f_{i,j+1}^n + \beta_{i,j-1/2}^- f_{i,j-1}^n \\
& \left. + \sigma_{i,j}^n \right) / \gamma_{i,j}^+.
\end{aligned} \tag{B.37}$$

Eqn. (B.37) is an expression that allows a calculation of the values  $f_{i,j}^{n+1}$  from the two preceding time-steps  $n-$  and  $n$ . In combination with the scheme for the first time-step and the numerical realization of the boundary conditions, this expression is the core of the simulation.

### Treatment of Flux Streaming Across $\mu = 0$

The Fokker-Planck coefficient for pitch-angle scattering used in this work becomes zero at  $\mu = 0$  for  $q < 2$  if  $h = 0$ . The integral

$$\kappa_{zz} = \frac{v^2}{4} \int_{-1}^{+1} d\mu \frac{1 - \mu^2}{\nu_0 |\mu|^{q-1}}, \tag{B.38}$$

however, results in a finite spatial diffusion coefficient and therefore in a finite mean free path. That means, particles are able to scatter across  $\mu = 0$ . If  $q \geq 2$ , the gap at  $\mu = 0$  becomes too large and the mean free path is infinite, i.e. particles can not leave their initial hemisphere in the pitch-angle domain<sup>3</sup>. In the numerical implementation, however, the flux across  $\mu = 0$  vanishes as already noted by Ng and Wong (1979) and further elaborated e.g. by Hatzky (1996). Therefore, it is necessary to find a finite value for  $D_{\mu\mu}(0)$  to allow the particles to scatter across the two hemispheres. In this work, we follow the solution of Hatzky (1996, Eqn 3.72) and assume

$$D_{\mu\mu}(0) \approx \frac{\nu_0}{2} (2 - q) \left( \frac{\Delta\mu}{2} \right)^{q-1} \tag{B.39}$$

to obtain a finite value at  $\mu = 0$  for  $q < 2$ . Note that for the case of isotropic scattering, i.e.  $q = 1$ , this expression is identical to the result of Eqn. (4.22) at  $\mu = 0$  if  $h = 0$ .

## B.3 Convergence & Stability Considerations

A crucial issue of the application of numerical schemes to solve PDEs is the stability of the scheme. Basically speaking, the ratio of the time step  $\Delta t$  and the step in the

<sup>3</sup>This behavior can easily be studied by evaluating the integral in Eqn. (B.38) as a function of  $q$  with computational software programs like *Mathematica* or *Maple*.

spatial domains may not be chosen arbitrarily but must fulfill requirements that can be derived from a so-called stability analysis. According to Potter (1973), “*a numerical method is stable if a small error at any stage produces a smaller cumulative error*”. Therefore, after a discussion of the so-called CFL condition, a von Neumann analysis will be applied to the numerical scheme to figure out the conditions for numerical stability.

## The CFL Condition

The analysis of the numerical solutions of the one-dimensional hyperbolic PDE

$$\frac{\partial f}{\partial t} + a \frac{\partial f}{\partial x} = 0, \quad (\text{B.40})$$

which describes the physical process of convection, reveals that

$$|a\lambda| \leq 1, \quad (\text{B.41})$$

with  $\lambda = \Delta t / \Delta x$  is a necessary condition for stability, given the (constant) coefficient  $a$ . This condition is in compliance with the Courant-Friedrichs-Lewy (CFL) condition. The CFL condition can be interpreted in a way that the speed of propagation of the numerical scheme must be greater or at least equal to the speed of propagation given by the physical problem. Given the case that a numerical scheme does not propagate the solution faster than the analytical solution of the differential equation, the numerical scheme does not solve the differential equation. Note, however, that the CFL condition not automatically implies numerical stability.

## Von Neumann Analysis

A general approach to the investigation of the stability of numerical schemes is the von Neumann stability analysis founded on Fourier analysis (e.g. Strikwerda, 2004). The *ansatz* is the Fourier inversion formula for  $f_j^n$  that reads

$$f_j^n = \sum \varphi_k (g_k)^n e^{ikx_j}. \quad (\text{B.42})$$

Here,  $\varphi_k$  is the Fourier coefficient belonging to the wavenumber  $k$  and  $(g_k)^n$  is the amplification factor. Note that the superscript of  $g$  is a power, not an index. The factor  $g$  corresponds to the magnitude of amplification (or decay) of each frequency. For amplification factors  $|g| = \sqrt{gg^*} > 1$ , the algorithm is unstable. On the other hand,  $|g| \leq 1$  implies a stable algorithm. Focusing on a single wavenumber  $k$  (due to the linearity of the problem, all wavenumbers can be expressed in terms of linear combinations), we obtain

$$f_j^n = \hat{f} g^n e^{ikx_j}, \quad (\text{B.43})$$

and in particular

$$f_j^{n+1} = \hat{f} g^{n+1} e^{ikx_j}. \quad (\text{B.44})$$

and consequently

$$g = \frac{f_j^{n+1}}{f_j^n}. \quad (\text{B.45})$$

This expression is derived by keeping in mind that  $g^{n+1} = g^n g$  and inserting Eqn. (B.43) into Eqn. (B.44). After having found the expression for amplification from  $n$  to  $n+1$ , i.e. in the time domain, a similar expression can be derived for the spatial domain. Since  $x_{j\pm 1} = x_j \pm \Delta x$ , we find

$$f_{j\pm 1}^n = \hat{f} g^n e^{ikx_j \pm \Delta x} \quad (\text{B.46})$$

and

$$f_{j\pm 2}^n = \hat{f} g^n e^{ikx_j \pm 2\Delta x}. \quad (\text{B.47})$$

### Leapfrog of 4th Order

In the next step, we will apply the von Neumann analysis to the convection scheme of fourth order (see section B.1). Inserting the Fourier representations into Eqn. (B.24) leads to

$$g^2 = 1 - \frac{g\alpha}{6} (-e^{2ik\Delta x} + 8e^{ik\Delta x} - 8e^{-ik\Delta x} + e^{-2ik\Delta x}), \quad (\text{B.48})$$

where  $\alpha = v\Delta t/\Delta x$ . Using the identities

$$\sin \varphi = \frac{e^{i\varphi} - e^{-i\varphi}}{2i} \quad (\text{B.49})$$

and

$$2i \sin \varphi \cos \varphi = \frac{e^{2i\varphi} - e^{-2i\varphi}}{2}, \quad (\text{B.50})$$

with  $\varphi = k\Delta x$ , one finds

$$g^2 + \frac{2}{3}ig\alpha \sin(\varphi) (4 - \cos(\varphi)) - 1 = 0. \quad (\text{B.51})$$

The solutions read

$$g_{\pm} = -\frac{1}{6}i \left( 8\alpha \sin(\varphi) - 2\alpha \sin(\varphi) \cos(\varphi) \pm \sqrt{16\alpha^2 \sin(\varphi)^2 - 8\alpha^2 \sin(\varphi)^2 \cos(\varphi) + \alpha^2 \varphi \sin(\varphi)^2 \cos(\varphi)^2 - 9} \right).$$

Numerical evaluation of the absolute value  $\sqrt{gg^*}$  for a set of possible values for  $\varphi$  and  $\alpha$  finally leads to a stability of the scheme if  $\alpha \leq 0.72$ . The graph of the amplification factor is shown in Fig. B.6 for the case of  $\phi = \pi/2$ .

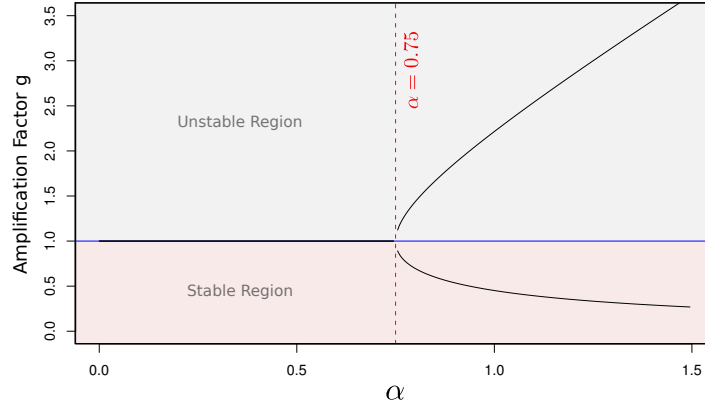


**Figure B.6:** The amplification factor  $g$  (black curve) as a function of  $\alpha$  for  $\phi = \pi/2$ . For this case, up to values for  $\alpha$  of 0.75,  $g$  equals unity. Above  $\alpha = 0.75$ ,  $g$  splits into two branches, one being always above  $g = 1$ . The minimal value of  $g$  as a function is  $\alpha$  and  $\phi$  is  $\sim 0.72$ .

### The Diffusion Term

Similar to the convection term, the diffusion term Eqn. (B.23) including the time dependent term  $(f_j^{n+1} - f_j^{n-1})/2\Delta t$  on the left hand side will be evaluated in what follows. We define  $\alpha_1 = D_{i,j+1/2}\Delta t/\Delta\mu^2$  and  $\alpha_2 = D_{i,j-1/2}\Delta t/\Delta\mu^2$  and obtain

$$\begin{aligned} f_j^{n+1} &= f_j^{n-1} + 2\alpha_1 f_{j+1}^n - \alpha_1 f_j^{n+1} - \alpha_1 f_j^{n-1} \\ &\quad - \alpha_2 f_j^{n-1} - \alpha_2 f_j^{n+1} + 2\alpha_2 f_{j-1}^n. \end{aligned}$$

Rearranging this expression leads to

$$f_j^{n+1}(1 + \alpha_1 + \alpha_2) = f_j^{n-1} + 2\alpha_1 f_{j+1}^n + 2\alpha_2 f_{j-1}^n - \alpha_1 f_j^{n-1} - \alpha_2 f_j^{n-1}. \quad (\text{B.52})$$

If we assume a constant diffusion coefficient, i.e.  $\alpha_1 = \alpha_2 = \alpha$ , this equation simplifies to the well-known DuFort-Frankel scheme

$$f_j^{n+1}(1 + 2\alpha) = f_j^{n-1} + 2\alpha (f_{j+1}^n + f_{j-1}^n - f_j^{n-1}). \quad (\text{B.53})$$

Applying the *ansatz* of Eqn. (B.42), we get for the amplification factor

$$(1 + 2\alpha)g^2 - 4g\alpha(\cos(\varphi)) + 2\alpha - 1 = 0, \quad (\text{B.54})$$

i.e.

$$g = \frac{2\alpha \cos \varphi \pm \sqrt{1 - 4\alpha^2 \sin^2 \varphi}}{1 + 2\alpha}. \quad (\text{B.55})$$

An investigation of this equation shows that  $g \leq 1$  for  $\alpha > 0$ . Therefore, this scheme is unconditionally stable. The case of a non-constant diffusion coefficient  $D_{j\pm 1/2}$ , however,



is more complex. A possibility to study the stability of this scheme is to introduce (A. Kopp, private communication)

$$D_{j\pm 1/2} = D_0 e^{\pm ik \frac{\Delta x}{2}}. \quad (\text{B.56})$$

Here,  $\Delta x/2$  is used because the grid for the diffusion coefficient is shifted by a half grid step with respect to the grid for  $f_j^n$ . In combination with the previously used

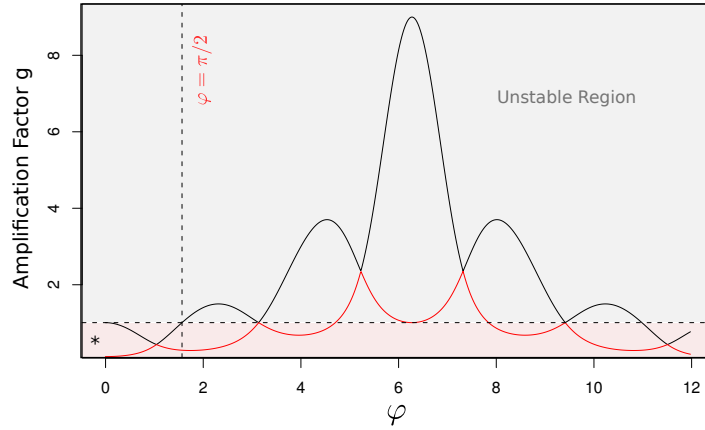


**Figure B.7:** The amplification factor  $g$  (black and red curve) as a function of  $\phi = \pi/2$ , while  $\alpha = 0.8$ . For  $\phi > \pi/2$ , the schemes is unstable independent of  $\alpha$ , but stable in the region marked by the asterisk in the left bottom corner. Interpreting this finding in terms of the wave vector, the condition  $k \leq \pi/(2\Delta x)$  must be fulfilled.

expressions, Eqn. (B.23) leads to an amplification factor  $g$  of

$$g_{\pm} = \left( \alpha e^{2ik\Delta x} + \alpha e^{-ik\Delta x} \pm e^{-ik\Delta x} \sqrt{\alpha^2 e^{6ik\Delta x} + \alpha^2 - \alpha^2 e^{4ik\Delta x} + 4e^{3ik\Delta x} - \alpha^2 e^{2ik\Delta x}} \right) / (\alpha e^{ik\Delta x} + e^{ik\Delta x/2} + \alpha).$$

The magnitude of  $g$  is plotted as a function of  $\varphi = k\Delta x$  in Fig.B.7 for  $\alpha = 0.8$ . Stability is governed for  $\varphi \leq \pi/2$ . Since  $\varphi = k\Delta x$  and  $k = 2\pi/\lambda$ , the wavelengths of distortions may not exceed  $4\Delta x$ . The value of  $\phi = \pi/2$  was found to be independent on the value of  $\alpha$ . While testing the algorithm, it turned out that the restriction mentioned above does not lead to an unstable runtime behavior of the code for typical setups of the diffusion coefficient as well as diffusion coefficients showing a very high variability with wavelength close to the  $\Delta x$ .

## B.4 Testing the Code

As already mentioned, general analytical solutions of the transport equation are not known. It is, however, possible to find analytical solutions for some special cases of the transport equation. These solutions can be compared with numerical results obtained by the realization of the algorithm (called JJTM for Jovian Jet Transport Model) in order to verify the correctness of the numerical calculations.

### The Convection Term

The first special case to study neglects the focusing as well as the diffusion term and assumes that there are no sources. The transport equation therefore simply describes the shifting of an initial function along the  $z$ -axis and reads

$$\frac{\partial F}{\partial t} + \frac{\partial(\mu v F)}{\partial z} = 0 \quad \text{with } F(z, 0) = F_0(z). \quad (\text{B.57})$$

This is a first-order partial differential equation describing the convection of a profile along  $z$  with speed  $\mu v$ . The solution of this equation is

$$F(t, z) = F_0(z - \mu v t), \quad (\text{B.58})$$

where  $F_0$  is an arbitrary function representing the starting solution. The physical meaning of the solution of this transport equation is the simple streaming of particles along  $z$  with a velocity  $v(\mu) = \mu v$ . For the validation of the code, an initial function of the form  $\exp(-(|z - z_0|/z_d)^2)$  had been chosen, where  $z_0$  and  $z_d$  are constants. The result is shown in Fig. B.8 for several time. The open red circles correspond to the numerical solution, while the blue solid line is the analytical solution. Here,  $\mu$  was set to 1. As expected, the profile given by  $F_0$  propagates corresponding to the factor  $\mu v$ .

### The Focusing Term

The focusing term of the conservative transport equation can be tested by neglecting diffusion as well as convection. Setting  $v/(2L) = 1$ , the resulting equation is a hyperbolic partial differential equation with a variable coefficient and reads

$$\frac{\partial F}{\partial t} + \frac{\partial(1 - \mu^2)F}{\partial \mu} = 0, \quad (\text{B.59})$$

with the solution given by Hatzky (1996)<sup>4</sup>

$$F(\mu, t) = F_0 \left( t - \frac{1}{2} \ln \left( \frac{1 + \mu}{1 - \mu} \right) \right), \quad (\text{B.60})$$

---

<sup>4</sup>Note that the solution given by Hatzky (1996) is only valid for the non-conservative form of the equation and has to be divided by  $(1 - \mu^2)$  to obtain the solution of the conservative form.

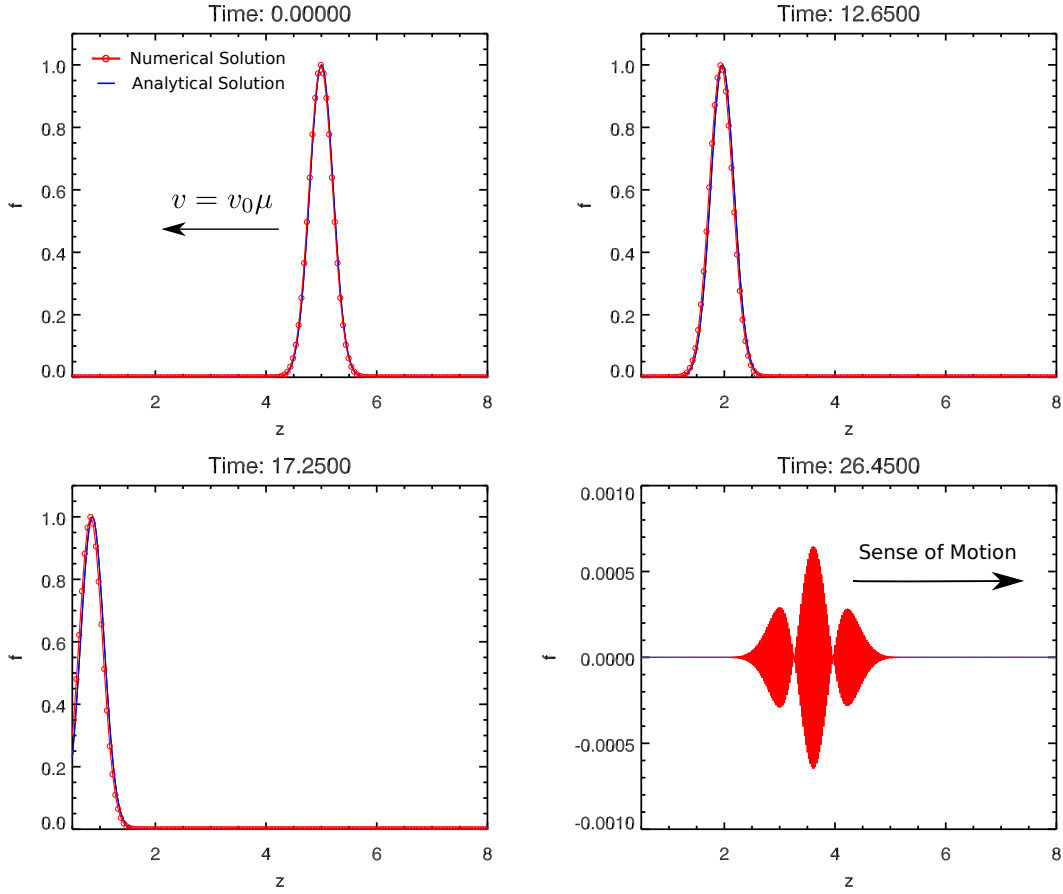


**Figure B.8:** Transport of particles injected with a Gaussian injection profile and a propagation speed  $\mu v$ . The red dots correspond the numerical solution of the corresponding partial differential equation, while the blue solid curve shows the analytical solution of the problem. The bottom right Figure shows a distortion moving in the opposite direction generated by the convection of the initial function across the numerical boundary. Note that the scale of the ordinate had been changed significantly.

where  $F_0$  is an arbitrary function. Here,  $F_0$  was set to

$$F(\mu, t) = \exp\left(-5.2\left(t - \frac{1}{2}\ln\left(\frac{1+\mu}{1-\mu}\right)\right)\right) / (1 - \mu^2). \quad (\text{B.61})$$

The physical meaning of Eqn. (B.60) is the pitch-angle focusing of the particles, i.e. it reflects the fact that the pitch angle cosine of a particle increases as it moves from a regime of a high magnetic field strength to a regime of a low magnetic field strength and vice versa. Considering Eqn. (4.7), a particle that has an initial pitch-angle cosine of  $\pm 1$  will never be shifted to other pitch-angle cosines. A particle with a pitch-angle cosine  $\mu \neq 1$  will never be shifted to exactly  $\mu = 1$ , but will approach this values as

time proceeds, or to be more specific

$$\lim_{t \rightarrow \infty} f(\mu, t) = \delta(\mu - 1),$$

i.e. the probability to find all particles concentrated at  $\mu = 1$  is exactly 1 ( $\delta$ -function) for  $f(\mu, t_0) \in (-1, 1]$ . It is clear that a numerical scheme can not totally account this strict behavior, because of the representation of the pitch-angle domain as a discrete grid and the fact that the points  $\mu = \pm 1$  are excluded from the calculation. Consequently, the particles will accumulate at  $\mu(j_{max})$ , i.e. at a value of  $\mu$  close but not equal to 1, depending on the resolution of the grid. For typical grids, however, the deviation from the analytical solution is fairly small as can be seen in Fig. B.9. This Figure shows a comparison of the analytical and numerical solutions for several time steps. As can be seen, both solutions are in good agreement unless the numerical solution becomes too steep, resulting in an oscillating behavior. This is a consequence of the used numerical solution. However, given the purpose of the simulation, pencil-like pitch-angle propagation are not expected.

## The Diffusion Term

If convection and focusing is neglected by setting  $v = 0$  and  $1/(2L) = 0$ , the resulting partial differential equation reads

$$\frac{\partial F}{\partial t} = \frac{\partial}{\partial \mu} \left( D_{\mu\mu} \frac{\partial F}{\partial \mu} \right). \quad (\text{B.62})$$

Given that  $D_{\mu\mu}$  is a constant, Eqn. (B.62) results in the well-known equation of heat conduction. However, the pitch-angle diffusion coefficient used here is a function of  $\mu$ . Setting  $\nu_0 = 2$ ,  $q = 1$  and  $\epsilon = 0$  in Eqn. (4.22), the transport equation simplifies to

$$\frac{\partial F}{\partial t} = \frac{\partial}{\partial \mu} \left( (1 - \mu^2) \frac{\partial F}{\partial \mu} \right). \quad (\text{B.63})$$

The exact solution of this equation was already given by Hatzky (1996), but without a proper derivation. Therefore, in what follows, the derivation of the analytic solution of Eqn. (B.63) will be given prior to the results of the comparison with the numerical solution will be presented.

We start with the method of separation of variables, i.e. we assume

$$F(\mu, t) = g(\mu)h(t). \quad (\text{B.64})$$

Inserting in B.63 and dividing by  $g(\mu)h(t)$  leads to

$$\frac{1}{h} \frac{\partial h}{\partial t} = \frac{1}{g} \left( \frac{\partial}{\partial \mu} \left( (1 - \mu^2) \frac{\partial g}{\partial \mu} \right) \right). \quad (\text{B.65})$$

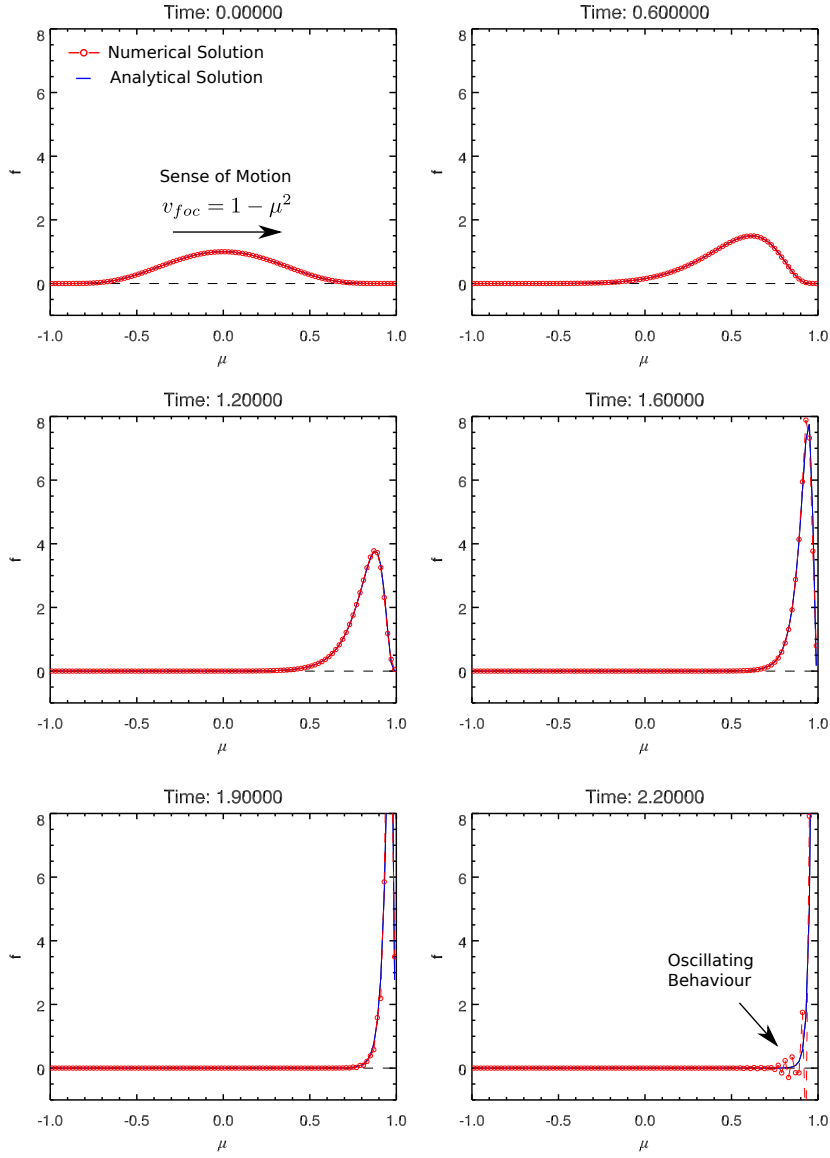


**Figure B.9:** Numerical vs. analytic solution of the temporal evolution of Eqn (B.59) with the initial condition given by Eqn. (B.61) for several times. As can be seen, the numerical and the analytic solution are in good agreement unless the slope of  $f$  becomes too steep.

Setting the left side of this equation to a constant  $\alpha$ , we derive

$$\frac{1}{h} \frac{\partial h}{\partial t} = \alpha, \tag{B.66}$$

with the solution

$$h(t) = e^{\alpha t}. \tag{B.67}$$

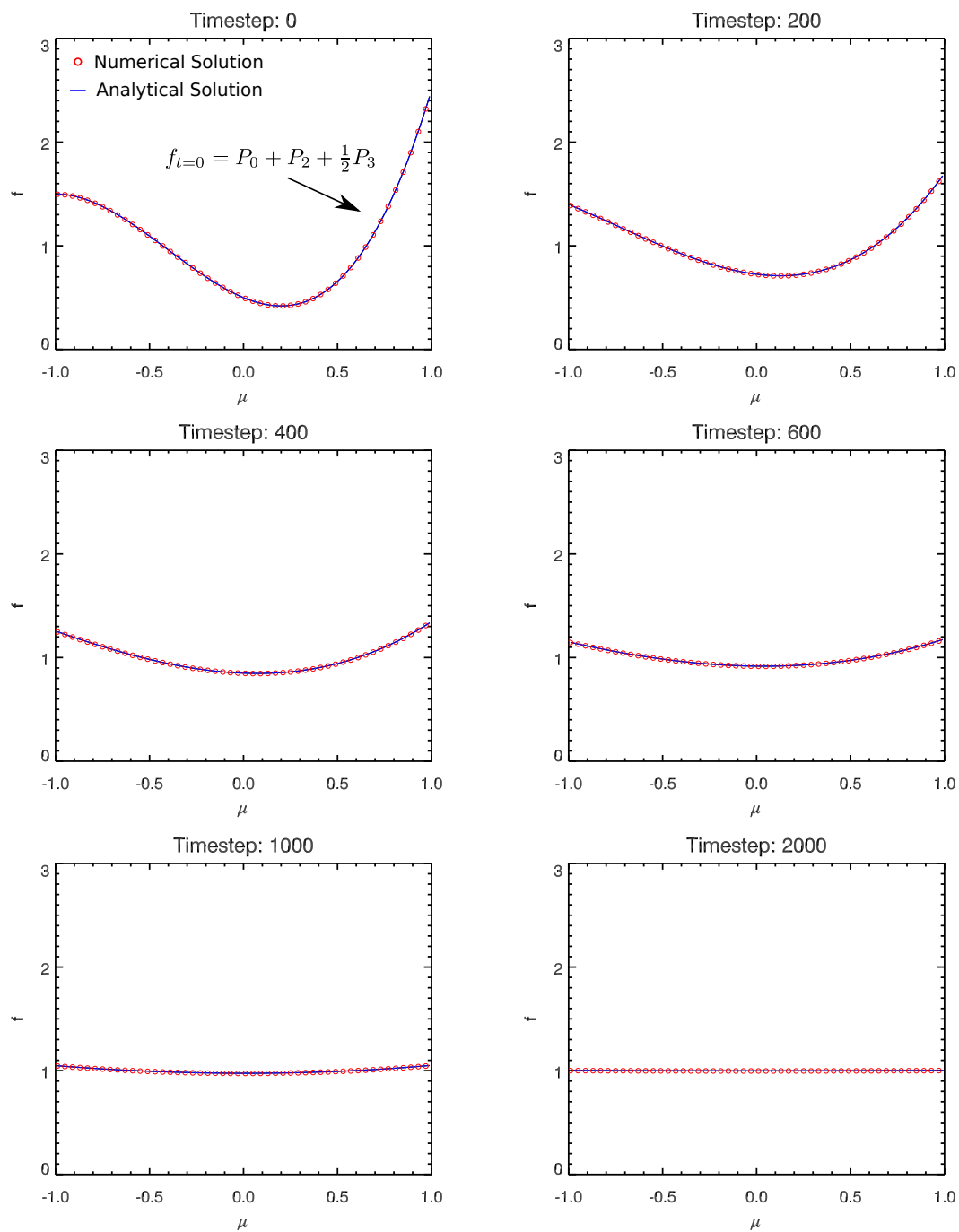


**Figure B.10:** Numerical vs. analytic solution of the temporal evolution of the initial solution given by Eqn. (B.72) for different times. The numerical and the analytic solution are in good agreement and the phase space density  $f$  finally reaches a steady state configuration.

Accordingly,

$$\alpha = \frac{1}{g} \left( \frac{\partial}{\partial \mu} \left( (1 - \mu^2) \frac{\partial g}{\partial \mu} \right) \right), \quad (\text{B.68})$$

what can be rewritten as

$$\alpha g = \frac{\partial}{\partial \mu} \left( (1 - \mu^2) \frac{\partial g}{\partial \mu} \right). \quad (\text{B.69})$$

The latter equation is identical to Legendre's differential equation (Arfken, 1985) if  $\alpha = -n(n+1)$ , with  $n \in \mathbf{N}_0$ . The solutions of Legendre's differential equation are linear combinations of the Legendre polynomials  $P_n(\mu)$ . The full solution of  $F$  is therefore

$$F(\mu, t) = \sum_n a_n P_n(\mu) e^{-n(n+1)t}, \quad (\text{B.70})$$

where  $a_n \in \mathbf{R}$  is a scaling factor.

Now, the numerical solution of Eqn. (B.62) will be compared with the exact solution given by Eqn. (B.70) for the initial solutions

$$F(\mu, t_0 = 0) = \underbrace{1}_{P_0} + \underbrace{\frac{1}{2}(3\mu^2 - 1)}_{P_2} + \underbrace{\frac{1}{4}(5\mu^3 - 3\mu)}_{\frac{1}{2}P_3} \quad (\text{B.71})$$

and

$$F(\mu, t) = 1 + \frac{1}{2}(3\mu^2 - 1)e^{-6t} + \frac{1}{4}(5\mu^3 - 3\mu)e^{-12t} \quad (\text{B.72})$$

for  $t > t_0$ . Fig. B.10 shows the result of the numerical solution (open red circles) and the analytic solution (blue solid curve) for several integration steps. Note that only every fifth data point of the actual computed data points were used to create the plot.





# Bibliography

- N. Agueda. *Near-relativistic electron events. Monte Carlo simulations of solar injection and interplanetary transport*. PhD thesis, Universitat de Barcelona, 2008.
- F. Aharonian and the HESS consortium. A detailed spectral and morphological study of the gamma-ray supernova remnant RX J1713.7-3946 with HESS. *Astronomy & Astrophysics*, 449:223–242, April 2006.
- H. Alfvén. *Electric current in cosmic plasmas*. 1977.
- G. C. Anagnostopoulos, P. K. Marhavilas, E. T. Sarris, I. Karanikola, and A. Balogh. Energetic ion populations and periodicities near Jupiter. *J. Geophys. Res.*, 103: 20055–20074, September 1998.
- G. C. Anagnostopoulos, I. Karanikola, and P. Marhavilas. Large-scale energetic particle layers in the high latitude Jovian magnetosphere. *Plan. Space Sci.*, 49:1049–1065, August 2001.
- D. A. Anderson, J. H. Tannehill, and R. H. Pletcher. *Computational Fluid Mechanics and Heat Transfer*. Taylor & Francis, 2. edition, 1997.
- G. Arfken. *Mathematical methods for physicists*. Academic Press, 3 edition, 1985.
- Markus J. Aschwanden. *Physics of the solar corona*. Springer-Praxis Books in Astronomy and Planetary Sciences. Springer, 2009.
- F. Bagenal, T. E. Dowling, and W. B. McKinnon. *Jupiter*. Cambridge University Press, nov 2004.
- A. Balogh, T. J. Beek, R. J. Forsyth, P. C. Hedgecock, R. J. Marquedant, E. J. Smith, D. J. Southwood, and B. T. Tsurutani. The magnetic field investigation on the ULYSSES mission - Instrumentation and preliminary scientific results. *Astron. Astrophys. Suppl. Ser.*, 92:221–236, January 1992.
- S. J. Bame, D. J. McComas, B. L. Barraclough, J. L. Phillips, K. J. Sofaly, J. C. Chavez, B. E. Goldstein, and R. K. Sakurai. The ULYSSES solar wind plasma experiment. *Astron. Astrophys. Suppl. Ser.*, 92:237–265, January 1992.

- C. Bandt. Ordinal time series analysis. *Ecological Modelling*, 182:229–235, 2005.
- J. W. Bieber and W. H. Matthaeus. Perpendicular Diffusion and Drift at Intermediate Cosmic-Ray Energies. *Astrophysical Journal*, 485:655, August 1997.
- J. W. Bieber, P. Evenson, and W. H. Matthaeus. Magnetic helicity of the IMF and the solar modulation of cosmic rays. *Geophys. Res. Lett.*, 14:864–867, August 1987.
- J. W. Bieber, W. H. Matthaeus, A. Shalchi, and G. Qin. Nonlinear guiding center theory of perpendicular diffusion: General properties and comparison with observation. *Geophys. Res. Lett.*, 31:10805, May 2004.
- T. J. M. Boyd and J. J. Sanderson. *Plasma Dynamics*. Thomas Nelson and Sons, 1969.
- A. L. Broadfoot, B. R. Sandel, D. E. Shemansky, J. C. McConnell, G. R. Smith, J. B. Holberg, S. K. Atreya, T. M. Donahue, D. F. Strobel, and J. L. Bertaux. Overview of the Voyager ultraviolet spectrometry results through Jupiter encounter. *J. Geophys. Res.*, 86:8259–8284, September 1981.
- I. N. Bronstein, K. A. Semendjajew, G. Musiol, and H. Mühlig. *Taschenbuch der Mathematik*. Harri Deutsch, 5 edition, 2001.
- B. F. Burke and K. L. Franklin. "iau symposium". In H. C. van de Hulst, editor, *Radio astronomy*, volume 4, page 394, 1957.
- L. F. Burlaga. Interplanetary stream interfaces. *J. Geophys. Res.*, 79:3717–3725, 1974.
- I. Büsching and M. S. Potgieter. The variability of the proton cosmic ray flux on the Sun's way around the galactic center. *Advances in Space Research*, 42:504–509, August 2008.
- I. Büsching, C. Venter, and O. C. de Jager. Contributions from nearby pulsars to the local cosmic ray electron spectrum. *Advances in Space Research*, 42:497–503, August 2008.
- F. Busse. Theory of planetary dynamos. In Kennel, C. F. and Lanzerotti, L. J. and Parker, E. N., editor, *Solar System Plasma Physics, Vol II*, pages 293–317. North Holland, Amsterdam, 1979.
- J. F. Carbary, D. G. Mitchell, S. M. Krimigis, D. C. Hamilton, and N. Krupp. Spin-period effects in magnetospheres with no axial tilt. *Geophys. Res. Lett.*, 34:L18107, September 2007.
- S. Chandrasekhar. Stochastic problems in physics and astronomy. *Rev. Mod. Phys.*, 15(1):1–89, Jan 1943.

- D. L. Chenette. The propagation of Jovian electrons to earth. *J. Geophys. Res.*, 85: 2243–2256, May 1980.
- D. L. Chenette, T. F. Conlon, and J. A. Simpson. Bursts of relativistic electrons from jupiter observed in interplanetary space with the time variation of the planetary rotation period. *J. Geophys. Res.*, 79(25):3551–3558, 1974.
- T. J. Chung. *Computational Fluid Dynamics*. Cambridge University Press, 2002.
- T. F. Conlon. The interplanetary modulation and transport of Jovian electrons. *J. Geophys. Res.*, 83:541–552, February 1978.
- T. F. Conlon and J. A. Simpson. Modulation of Jovian electron intensity in interplanetary space by corotating interaction regions. *Astrophysical Journal Letters*, 211: L45–L49, January 1977.
- C. A. de Koning, J. T. Steinberg, J. T. Gosling, D. B. Reisenfeld, R. M. Skoug, O. C. St. Cyr, M. L. Malayeri, A. Balogh, A. Rees, and D. J. McComas. An unusually fast interplanetary coronal mass ejection observed by Ulysses at 5 AU on 15 November 2003. *J. Geophys. Res.*, 110:A01102, January 2005.
- A. J. Dessler. *Physics of the Jovian Magnetosphere*. Cambridge University Press, 1983.
- A. J. Dessler and T. W. Hill. High-order magnetic multipoles as a source of gross asymmetry in the distant Jovian magnetosphere. *Geophys. Res. Lett.*, 2:567–570, December 1975.
- G. Dilmaghani, I. C. Henry, P. Soonthornnonda, E. R. Christensen, and R. C. Henry. Harmonic analysis of environmental time series with missing data or irregular sample spacing. *Environ. Sci. Technol.*, pages 7030–7038, October 2007.
- W. Dröge. Probing Heliospheric Diffusion Coefficients with Solar Energetic Particles. In *35th COSPAR Scientific Assembly*, volume 35 of *COSPAR, Plenary Meeting*, page 804, 2004.
- W. Dröge and Y. Y. Kartavykh. Testing Transport Theories with Solar Energetic Particles. *Astrophysical Journal*, 693:69–74, March 2009.
- D. Du, P. B. Zuo, and X. X. Zhang. Interplanetary Coronal Mass Ejections Observed by Ulysses Through Its Three Solar Orbits. *Solar Phys.*, 262:171–190, March 2010.
- E. C. DuFort and S. P. Frankel. Stability conditions in the numerical treatment of parabolic differential equations. *M.T.A.C.*, 7:135–152, 1953.
- P. Dunzlaff. Jupiterelektronen in der Inneren Heliosphäre. Master’s thesis, Christian-Albrechts-Universität Kiel, 2007.

- P. Dunzlaff, Kopp A., B. Heber, and O. Sternal. Comparison of Jovian jets observed by Ulysses and Pioneer 10. In *International Cosmic Ray Conference*, International Cosmic Ray Conference, 2009.
- J. A. Earl. The diffusive idealization of charged-particle transport in random magnetic fields. *Astrophysical Journal*, 193:231–242, October 1974.
- J. A. Earl, D. Ruffolo, H. L. Pauls, and J. W. Bieber. Comparison of Three Numerical Treatments of Charged Particle Transport. *Astrophysical Journal*, 454:749, December 1995.
- A. Einstein. Über die von der molekularkinetischen Theorie der Wärme geforderte Bewegung von in ruhenden Flüssigkeiten suspendierten Teilchen. *Annalen der Physik*, 322:549–560, 1905.
- J. H. Eraker and J. A. Simpson. Jovian electron propagation close to the sun /at about 0.5 AU/. *Astrophysical Journal Letters*, 232:L131–L134, September 1979.
- T. V. Falkenberg, S. Vennerstrom, D. A. Brain, G. Delory, and A. Taktakishvili. Multipoint observations of coronal mass ejection and solar energetic particle events on Mars and Earth during November 2001. *J. Geophys. Res.*, 116:A06104, June 2011.
- P. Ferrando, R. Ducros, C. Rastoin, and A. Raviart. Jovian electron jets in interplanetary space. *Planetary and Space Science*, 41:839–849, nov 1993. doi: 10.1016/0032-0633(93)90091-F.
- S. E. S. Ferreira. The transport of galactic and jovian cosmic ray electrons in the heliosphere. *Advances in Space Research*, 35:586–596, 2005.
- R. W. Fillius, C. E. McIlwain, and A. Mogro-Campero. Radiation belts of Jupiter - A second look. *Science*, 188:465–467, May 1975.
- C. A. J. Fletcher. *Computational Techniques for Fluid Dynamics*, volume 1. Springer-Verlag, 2. edition, 2000.
- R. J. Forsyth, V. Bothmer, C. Cid, N. U. Crooker, T. S. Horbury, K. Kecskemety, B. Klecker, J. A. Linker, D. Odstrcil, M. J. Reiner, I. G. Richardson, J. Rodriguez-Pacheco, J. M. Schmidt, and R. F. Wimmer-Schweingruber. ICMEs in the Inner Heliosphere: Origin, Evolution and Propagation Effects. Report of Working Group G. *Space Sci. Rev.*, 123:383–416, March 2006.
- N. Friedman. *The Naval Institute guide to world naval weapon systems*. Naval Institute Press, 2006.
- G. J. Fulks. Solar modulation of galactic cosmic ray electrons, protons, and alphas. *J. Geophys. Res.*, 80:1701–1714, May 1975.

- H. B. Garrett, S. M. Levin, S. J. Bolton, R. W. Evans, and B. Bhattacharya. A revised model of Jupiter's inner electron belts: Updating the Divine radiation model. *Geophys. Res. Kett.*, 32:4104, February 2005.
- T. Gehrels and M.S. Matthews. *Jupiter: studies of the interior, atmosphere, magnetosphere, and satellites*. University of Arizona Press, 1976.
- V. L. Ginzburg and S. I. Syrovatskii. *The Origin of Cosmic Rays*. 1964.
- G. Gloeckler, J. Geiss, H. Balsiger, P. Bedini, J. C. Cain, J. Fisher, L. A. Fisk, A. B. Galvin, F. Gliem, and D. C. Hamilton. The Solar Wind Ion Composition Spectrometer. *Astron. Astrophys. Suppl. Ser.*, 92:267–289, January 1992.
- T. Gold. Motions in the Magnetosphere of the Earth. *J. Geophys. Res.*, 64:1219–1224, September 1959.
- M. L. Goldstein. Major Unsolved Problems in Space Plasma Physics. *Astrophys. and Space Sci.*, 277:349–369, June 2001.
- D. Grodent, B. Bonfond, J.-C. Gérard, A. Radioti, J. Gustin, J. T. Clarke, J. Nichols, and J. E. P. Connerney. Auroral evidence of a localized magnetic anomaly in Jupiter's northern hemisphere. *J. Geophys. Res.*, 113:A09201, September 2008.
- C. Grupen. *Teilchendetektoren*. BI Wissenschaftsverlag, 1993.
- D. Haggerty and T. P. Armstrong. Observations of Jovian upstream events by Ulysses. *J. Geophys. Res.*, 104:4629–4642, March 1999.
- D. K. Haggerty, E. C. Roelof, C. W. Smith, N. F. Ness, R. L. Tokar, and R. M. Skoug. Interplanetary magnetic field connection to the L1 Lagrangian orbit during upstream energetic ion events. *J. Geophys. Res.*, 105:25123–25132, November 2000.
- D. C. Hamilton. The radial transport of energetic solar flare particles from 1 to 6 AU. *J. Geophys. Res.*, 82:2157–2169, June 1977.
- R. Hatzky. Systematische Analyse von Pitchwinkelverteilungen energiereicher Teilchen: Am Beispiel der Raumsonde Ulysses. Master's thesis, Christian-Albrechts-Universität Kiel, 1993.
- R. Hatzky. *Winkelverteilung energiereicher geladener Teilchen und die Streueigenschaften des interplanetaren Mediums*. PhD thesis, Christian-Albrechts-Universität zu Kiel, 1996.
- B. Heber. *Modulation galaktischer kosmischer Protonen und  $\alpha$ -Teilchen in der inneren dreidimensionalen Heliosphäre - Band B: Technische Aspekte*. PhD thesis, Christian-Albrechts-Universität zu Kiel, 1997.

- B. Heber, H. Fichtner, and K. Scherer. Solar and Heliospheric Modulation of Galactic Cosmic Rays. *Space Sci. Rev.*, 125:81–93, August 2006.
- B. Heber, M. S. Potgieter, S. E. S. Ferreira, S. Dalla, H. Kunow, R. Müller-Mellin, G. Wibberenz, C. Paizis, G. Sarri, R. G. Marsden, R. B. McKibben, and M. Zhang. An overview of Jovian electrons during the distant Ulysses Jupiter flyby. *Planet. and Space Sci.*, 55:1–11, January 2007.
- P. C. Hedgecock. Measurements of the interplanetary magnetic field in relation to the modulation of cosmic rays. *Solar Phys.*, 42:497–527, June 1975.
- G. Hernandez. Time series, periodograms, and significance. *J. Geophys. Res.*, 104:10355–10368, May 1999.
- C. Ho. Motion of relativistic charges in an increasing magnetic field. *Mon. Nor. R. astr. Soc.*, 221:523–536, August 1986.
- J. D. Jackson. *Classical Electrodynamics*. John Wiley & Sons, 1962.
- J. R. Jokipii. Propagation of cosmic rays in the solar wind. *Reviews of Geophysics and Space Physics*, 9:27–87, 1971.
- J. R. Jokipii and E. N. Parker. Random Walk of Magnetic Lines of Force in Astrophysics. *Physical Review Letters*, 21:44–47, July 1968.
- S. P. Joy, M. G. Kivelson, R. J. Walker, K. K. Khurana, C. T. Russell, and T. Ogino. Probabilistic models of the Jovian magnetopause and bow shock locations. *J. Geophys. Res.*, 107:1309, October 2002.
- M.-B. Kallenrode. Particle propagation in the inner heliosphere. *J. Geophys. Res.*, 98:19037, November 1993.
- S. G. Kanekal, D. N. Baker, J. B. Blake, M. D. Looper, R. A. Mewaldt, and C. A. Lopate. Modulation of Jovian electrons at 1 AU during solar cycles 22-23. *Geophys. Res. Lett.*, 30(15):1795, August 2003.
- K. K. Khurana, M. G. Kivelson, V.M. Vasyliunas, N. Krupp, A. Woch, A. Lagg, B. H. Mauk, and W. S. Kurth. The Configuration of Jupiter’s Magnetosphere. In Bagenal, F. and Dowling, T. and McKinnon, W., editor, *Jupiter. The Planet, Satellites and Magnetosphere*, pages 593–616. Cambridge University Press, 2004.
- E. K. J. Kilpua, L. K. Jian, Y. Li, J. G. Luhmann, and C. T. Russell. Multipoint ICME encounters: Pre-STEREO and STEREO observations. *Journal of Atmospheric and Solar-Terrestrial Physics*, 73:1228–1241, June 2011.
- C. Kittel. *Introduction to Solid State Physics*. Wiley John & Sons, 2004.

- A. Klassen, R. Gómez-Herrero, E. Böhm, R. Müller-Mellin, B. Heber, and R. Wimmer-Schweingruber. COSTEP/SOHO observations of energetic electrons far upstream of the Earth's bow-shock. *Annales Geophysicae*, 26:905–912, May 2008.
- A. Klassen, R. Gómez-Herrero, R. Müller-Mellin, S. Böttcher, B. Heber, Wimmer-Schweingruber R., and G. M. Mason. Observations of Upstream Particle Events: Almost Monoenergetic ion beams. *Ann. Geophys.*, 27:2077–2085, 2009.
- J. Kóta, E. Merenyi, J. R. Jokipii, D. A. Kopriva, T. I. Gombosi, and A. J. Owens. A numerical study of the pitch-angle scattering of cosmic rays. *Astrophysical Journal*, 254:398–404, March 1982.
- S. M. Krimigis. Voyager energetic particle observations at interplanetary shocks and upstream of planetary bow shocks - 1977-1990. *Space Sci. Rev.*, 59:167–201, January 1992.
- N. Krupp, E. Keppler, A. Korth, M. Fränz, A. Balogh, and M. K. Dougherty. Three-dimensional particle anisotropies in and near the plasma sheet of Jupiter observed by the EPAC experiment onboard the Ulysses spacecraft. *Planet. Space Sci.*, 41: 953–966, November 1993.
- N. Krupp, M. K. Dougherty, J. Woch, R. Seidel, and E. Keppler. Energetic particles in the duskside Jovian magnetosphere. *J. Geophys. Res.*, 104:14767–14780, July 1999.
- H. Kunow, G. Wibberenz, G. Green, R. Müller-Melling, and M. Kallenrode. Energetic Particles in the Inner Solar System. In Schwenn, R. & Marsch, E., editor, *Physics of the Inner Heliosphere II. Particles, Waves and Turbulence*. Springer-Verlag, 1991.
- L. J. Lanzerotti, T. P. Armstrong, C. G. MacLennan, G. M. Simnett, A. F. Cheng, R. E. Gold, D. J. Thomson, S. M. Krimigis, K. A. Anderson, S. E. Hawkins, M. Pick, E. C. Roelof, E. T. Sarris, and S. J. Tappin. Measurements of hot plasmas in the magnetosphere of Jupiter. *Planet. Space Sci.*, 41:893–917, November 1993.
- G. A. Lentz, J. McCarthy, J. J. O’Gallagher, and J. A. Simpson. Anisotropies of Galactic Cosmic Rays Outside the Orbit of Earth Measured on Pioneer 10. In *International Cosmic Ray Conference*, volume 5 of *International Cosmic Ray Conference*, page 3145, 1973.
- N. R. Lomb. Least-squares frequency analysis of unequally spaced data. *Astrophysics and Space Science*, 39:447–462, February 1976.
- M. S. Longair. *High Energy Astrophysics*, volume 1. Cambridge University Press, 1992.
- M. S. Longair. *High Energy Astrophysics*, volume 2. Cambridge University Press, 1994.
- C. Lopate. Jovian and Galactic Electrons (2-30 MeV) in the Heliosphere from 1 to 50AU. In *International Cosmic Ray Conference*, volume 2 of *International Cosmic Ray Conference*, page 149, August 1991.

- P. K. Marhavilas, G. C. Anagnostopoulos, and E. T. Sarris. On a systematic spectral variation of energetic ions in the Jovian outer magnetosphere: HI-SCALE/Ulysses observations. *Plan. Space Sci.*, 52:561–572, April 2004.
- G. M. Mason, R. von Steiger, R. B. Decker, M. I. Desai, J. R. Dwyer, L. A. Fisk, G. Gloeckler, J. T. Gosling, M. Hilchenbach, R. Kallenbach, E. Keppler, B. Klecker, H. Kunow, G. Mann, I. G. Richardson, T. R. Sanderson, G. M. Simnett, Y.-M. Wang, R. F. Wimmer-Schweingruber, M. Fränz, and J. E. Mazur. Origin, Injection, and Acceleration of CIR Particles: Observations Report of Working Group 6. *Space Science Reviews*, 89:327–367, July 1999.
- R. M. M Mattheij, S. W. Rienstra, and J. H. M ten Thijs Boonkcamp. *Partial Differential Equations - Modeling, Analysis, Computation*. SIAM - Society for Industrial Mathematics, 2005.
- J. McCarthy and J. J. Ogallagher. The time and spatial behavior of solar flare proton anisotropies observed in deep space on Pioneers 10 and 11. In *International Cosmic Ray Conference*, volume 4 of *International Cosmic Ray Conference*, pages 1526–1531, August 1975.
- D. J. McComas, S. J. Bame, P. Barker, W. C. Feldman, J. L. Phillips, P. Riley, and J. W. Griffée. Solar Wind Electron Proton Alpha Monitor (SWEPAM) for the Advanced Composition Explorer. *Space Sci. Rev.*, 86:563–612, July 1998.
- D. J. McComas, B. L. Barraclough, H. O. Funsten, J. T. Gosling, E. Santiago-Muñoz, R. M. Skoug, B. E. Goldstein, M. Neugebauer, P. Riley, and A. Balogh. Solar wind observations over Ulysses' first full polar orbit. *J. Geophys. Res.*, 105:10419–10434, May 2000.
- D. J. McComas, D. Alexashov, M. Bzowski, H. Fahr, J. Heerikhuisen, V. Izmodenov, M. A. Lee, E. Möbius, N. Pogorelov, N. A. Schwadron, and G. P. Zank. The heliosphere's interstellar interaction: No bow shock. *Science*, 2012.
- A. S. McEwen, M. J. S. Belton, H. H. Breneman, S. A. Fagents, P. Geissler, R. Greeley, J. W. Head, G. Hoppa, W. L. Jaeger, T. V. Johnson, L. Keszthelyi, K. P. Klaasen, R. Lopes-Gautier, K. P. Magee, M. P. Milazzo, J. M. Moore, R. T. Pappalardo, C. B. Phillips, J. Radebaugh, G. Schubert, P. Schuster, D. P. Simonelli, R. Sullivan, P. C. Thomas, E. P. Turtle, and D. A. Williams. Galileo at Io: Results from High-Resolution Imaging. *Science*, 288:1193–1198, May 2000.
- R. B. McKibben and J. A. Simpson. Evidence from charged particle studies for the distortion of the Jovian magnetosphere. *J. Geophys. Res.*, 79:3545–3549, 1974.
- R. B. McKibben, J. D. Anglin, J. J. Connell, S. Dalla, B. Heber, H. Kunow, C. Lopate, R. G. Marsden, T. R. Sanderson, and M. Zhang. Energetic particle observations from the Ulysses COSPIN instruments obtained during the October-November 2003 events. *J. Geophys. Res.*, 110:A09S19, September 2005.



- R. B. McKibben, M. Zhang, B. Heber, H. Kunow, and T. R. Sanderson. Localized Jets of Jovian electrons observed during Ulysses distant Jupiter flyby in 2003 2004. *Planet. and Space Sci.*, 55:21–31, January 2007.
- D. Meschede. *Gerthsen Physik*. Springer, Berlin, 24. edition, 2010.
- N. Meyer-Vernet. *Basic of the solar wind*. Cambridge University Press, 2007.
- F. M. Neubauer. Die Magnetosphären anderer Planeten im Sonnensystem. In K. H. Glassmeier and M. Scholer, editor, *Plasmaphysik im Sonnensystem*, pages 185–206. BI Wissenschaftsverlag, 1991.
- C. K. Ng and K. Y. Wong. Solar particle propagation under the influence of pitch-angle diffusion and collimation in the interplanetary magnetic field. In *International Cosmic Ray Conference*, volume 5, page 252, 1979.
- T. G. Northrop, C. K. Goertz, and M. F. Thomsen. The magnetosphere of Jupiter as observed with Pioneer 10. 2. Nonrigid rotation of the magnetodisc. *J. Geophys. Res.*, 79:3579–3582, 1974.
- A. J. Owens and T. I. Gombosi. The inapplicability of spatial diffusion models for solar cosmic rays. *Astrophysical Journal*, 245:328–334, April 1981.
- E. N. Parker. Dynamics of the interplanetary gas and magnetic fields. *Astrophysical Journal*, 128:664, nov 1958. doi: 10.1086/146579.
- E. N. Parker. The passage of energetic charged particles through interplanetary space. *Planet. Space Sci.*, 13:9, January 1965.
- K. I. Paularena. An investigation into solar wind plasma periodicities. *J. Geophys. Res.*, 101:27533–27542, December 1996.
- F. Perrin. Étude mathématique du mouvement brownien de roation. *Annales scientifiques de l'É.N.S. 3<sup>e</sup> série*, 3:1–51, 1928.
- M. S. Potgieter. Solar cycle variations and cosmic rays. *Journal of Atmospheric and Solar-Terrestrial Physics*, 70:207–218, February 2008.
- M. S. Potgieter. The dynamic heliosphere, solar activity, and cosmic rays. *Advances in Space Research*, 46:402–412, August 2010.
- D.E. Potter. *Computational physics*. Wiley-Interscience publication. J. Wiley, 1973.
- W. H. Press, S. A. Teukolsky, W. T. Vetterling, and B. P. Flannery. *Numerical Recipes in Fortran – The Art of Scientific Computing*. Cambridge University Press, 2 edition, 1992.
- G. Prölss. *Physik des erdnahen Weltraums*. Springer Verlag, 2001.

- K. R. Pyle and J. A. Simpson. The jovian relativistic electron distribution in interplanetary space from 1 to 11 au - evidence for a continuously emitting 'point' source. *The Astrophysical Journal*, 215:–89, jul 1977.
- D. A. Randall. An Introduction to Atmospheric Modeling, 2009. URL <http://kiwi.atmos.colostate.edu/group/dave/at604.html>.
- C. Rastoin. *Les électrons de Jupiter et de la Galaxie dans l'héliosphère d'après l'expérience KET à bord de la sonde spatiale ULYSSE*. PhD thesis, Université Paris VII-Denis Diderot, 1995.
- L. F. Richardson. The Approximate Arithmetical Solution by Finite Differences of Physical Problems Involving Differential Equations, with an Application to the Stresses in a Mansory Dam. *Philos. Trans. R. Soc. London*, 210:307–357, 1910.
- P. J. Roache. *Computational Fluid Dynamics*. Hermosa, Albuquerque, New Mexico, 1972.
- E. C. Roelof. Propagation of solar cosmic rays in the interplanetary magnetic field. In H. Ögelman and J. R. Wayland, editors, *Lectures in High-Energy Astrophysics*, page 111, 1969.
- D. Ruffolo. Effect of adiabatic deceleration on the focused transport of solar cosmic rays. *Astrophysical Journal*, 442:861–874, April 1995.
- S. Salsa. *Partial Differential Equations in Action*. Springer-Verlag, 2008.
- A. Sánchez-Lavega, G. S. Orton, R. Hueso, E. García-Melendo, S. Pérez-Hoyos, A. Simon-Miller, J. F. Rojas, J. M. Gómez, P. Yanamandra-Fisher, L. Fletcher, J. Joels, J. Kemerer, J. Hora, E. Karkoschka, I. de Pater, M. H. Wong, P. S. Marcus, N. Pinilla-Alonso, F. Carvalho, C. Go, D. Parker, M. Salway, M. Valimberti, A. Wesley, and Z. Pujic. Depth of a strong jovian jet from a planetary-scale disturbance driven by storms. *Nature*, 451:437–440, January 2008.
- J. D. Scargle. Studies in astronomical time series analysis. II - Statistical aspects of spectral analysis of unevenly spaced data. *Astrophysical Journal*, 263:835–853, December 1982.
- A. W. Schardt and C. K. Goertz. High-Energy Particles. In Dessler, A. J., editor, *Physics of the Jovian Magnetosphere*, pages 157–196. Cambridge University Press, 1983.
- A. W. Schardt, F. B. McDonald, and J. H. Trainor. Energetic particles in the predawn magnetotail of Jupiter. *J. Geophys. Res.*, 86:8413–8428, September 1981.
- R. Schlickeiser. *Cosmic Ray Astrophysics*. Springer-Verlag, 2002.

- R. Schlickeiser and A. Shalchi. Cosmic-Ray Diffusion Approximation with Weak Adiabatic Focusing. *Astrophysical Journal*, 686:292–302, October 2008.
- R. Schwenn and E. Marsch. *Physics of the Inner Heliosphere I. Large-Scale Phenomena*. Springer-Verlag, 1990.
- R. Schwenn and E. Marsch. *Physics of the Inner Heliosphere II. Particles, Waves and Turbulence*. 1991.
- P. K. Seidelmann, B. A. Archinal, M. F. A’Hearn, A. Conrad, G. J. Consolmagno, D. Hestroffer, J. L. Hilton, G. A. Krasinsky, G. Neumann, J. Oberst, P. Stooke, E. F. Tedesco, D. J. Tholen, P. C. Thomas, and I. P. Williams. Report of the IAU/IAG Working Group on cartographic coordinates and rotational elements: 2006. *Celestial Mechanics and Dynamical Astronomy*, 98:155–180, July 2007.
- A. Shalchi. *Nonlinear Cosmic Ray Diffusion Theories*. Springer Verlag, 2009.
- H. Sierks. Auswertung der Eichmessungen der Kieler Elektronenteleskops zur Erstellung von Energiespektren an Bord der Raumsonde Ulysses (International Solar Polar Mission). Master’s thesis, Christian Albrechts Universität Kiel, 1988.
- J. A. Simpson, B. Rossi, A. R. Hibbs, R. Jastrow, F. L. Whipple, Parker E., N. Christofilos, and J. A. Van Allen. Memorandum of round table discussion. *J. Geophys. Res.*, 64:1691, 1959.
- J. A. Simpson, D. C. Hamilton, G. A. Lentz, R. B. McKibben, M. Perkins, K. R. Pyle, A. J. Tuzzolino, and J. J. Ogallagher. Jupiter revisited - First results from the University of Chicago charged particle experiment on Pioneer 11. *Science*, 188:455–459, May 1975.
- J. A. Simpson, J. D. Anglin, A. Balogh, M. Bercovitch, J. M. Bouman, E. E. Budzinski, J. R. Burrows, R. Carvell, J. J. Connell, R. Ducros, P. Ferrando, J. Firth, M. Garcia-Munoz, J. Henrion, R. J. Hynds, B. Iwers, R. Jacquet, H. Kunow, G. Lentz, R. G. Marsden, R. B. McKibben, R. Müller-Mellin, D. E. Page, M. Perkins, A. Raviart, T. R. Sanderson, H. Sierks, L. Treguer, A. J. Tuzzolino, K. P. Wenzel, and G. Wibberenz. The ULYSSES Cosmic Ray and Solar Particle Investigation. *Astron. Astrophys. Suppl. Ser.*, 92:365–399, January 1992a.
- J. A. Simpson, J. D. Anglin, A. Balogh, J. R. Burrows, S. W. H. Cowley, P. Ferrando, B. Heber, R. J. Hynds, H. Kunow, and R. G. Marsden. Energetic charged-particle phenomena in the Jovian magnetosphere - First results from the ULYSSES COSPIN collaboration. *Science*, 257:1543–1550, September 1992b.
- J. A. Simpson, D. A. Smith, and M. Zhang. Jovian electron propagation in three dimensions of the heliosphere: The ULYSSES investigations. *J. Geophys. Res.*, 98:21129, December 1993.

- E. J. Smith, B. V. Connor, and G. T. Foster, Jr. Measuring the magnetic fields of Jupiter and the outer solar system. *IEEE Transactions on Magnetism*, 11:962–980, July 1975.
- E. J. Smith, B. T. Tsurutani, D. L. Chenette, T. F. Conlon, and J. A. Simpson. Jovian electron bursts - Correlation with the interplanetary field direction and hydromagnetic waves. *J. Geophys. Res.*, 81:65–72, January 1976.
- P. Sprent and N.C. Smeeton. *Applied nonparametric statistical methods*. Texts in statistical science. Chapman & Hall/CRC, 2007.
- J. A. Stansberry, J. T. Gosling, M. F. Thomsen, S. J. Bame, and E. J. Smith. Interplanetary magnetic field orientations associated with bidirectional electron heat fluxes detected at ISEE 3. *J. Geophys. Res.*, 93:1975–1980, March 1988.
- O. Sternal, N. E. Engelbrecht, R. A. Burger, S. E. S. Ferreira, H. Fichtner, B. Heber, A. Kopp, M. S. Potgieter, and K. Scherer. Possible Evidence for a Fisk-type Heliospheric Magnetic Field. I. Analyzing Ulysses/KET Electron Observations. *Astrophysical Journal*, 741:23, November 2011.
- R. D. Strauss, M. S. Potgieter, I. Büsching, and A. Kopp. Modeling the Modulation of Galactic and Jovian Electrons by Stochastic Processes. *Astrophysical Journal*, 735:83, July 2011.
- R. D. Strauss, M. S. Potgieter, I. Büsching, and A. Kopp. Modelling heliospheric current sheet drift in stochastic cosmic ray transport models. *Astrophys. Space Sci.*, 339:223–236, June 2012.
- J. C. Strikwerda. *Finite Difference Schemes and Partial Differential Equations*. SIAM - Society for Industrial Mathematics, 2. edition, 2004.
- J. D. Sullivan. Geometrical factor and directional response of single and multi-element particle telescopes. *Nuclear Instruments and Methods*, 95:5, 1971.
- J. R. Taylor. *Error Analysis*. University Science Books, 1997.
- B. J. Teegarden, F. B. McDonald, J. H. Trainor, W. R. Webber, and E. C. Roelof. Interplanetary MeV electrons of Jovian origin. *J. Geophys. Res.*, 79:3615–3622, 1974.
- N. Thomas, F. Bagenal, T. W. Hill, and J. K. Wilson. The Io Neutral Clouds and Plasma Torus. In Bagenal, F. and Dowling, T. and McKinnon, W., editor, *Jupiter. The Planet, Satellites and Magnetosphere*, pages 561–591. Cambridge University Press, 2004.
- F. Tsuchiya, A. Morioka, and H. Misawa. Jovian electron modulations by the solar wind interaction with the magnetosphere. *Earth, Planets, and Space*, 51:987–996, September 1999.

- J. A. van Allen, D. N. Baker, B. A. Randall, and D. D. Sentman. The magnetosphere of Jupiter as observed with Pioneer 10. 1. Instrument and principal findings. *J. Geophys. Res.*, 79:3559–3577, 1974.
- V. M. Vasyliunas. Modulation of Jovian interplanetary electrons and the longitude variation of decametric emissions. *Geophys. Res. Lett.*, 2:87, March 1975.
- V. M. Vasyliunas and A. J. Dessler. The magnetic-anomaly model of the Jovian magnetosphere - A post-Voyager assessment. *J. Geophys. Res.*, 86:8435–8446, September 1981.
- R. von Steiger and T. H. Zurbuchen. Composition signatures of interplanetary coronal mass ejections. In A. Wilson, editor, *Solar Variability as an Input to the Earth's Environment*, volume 535 of *ESA Special Publication*, pages 835–840, September 2003.
- D. F. Webb and R. A. Howard. The solar cycle variation of coronal mass ejections and the solar wind flux. *J. Geophys. Res.*, 99:4201–4220, March 1994.
- R. F. Wimmer-Schweingruber, R. von Steiger, and R. Paerli. Solar wind stream interfaces in corotating interaction regions: SWICS/Ulysses results. *J. Geophys. Res.*, 102:17407–17418, August 1997.
- J. H. Wolfe, J. D. Mihalov, H. R. Collard, D. D. McKibbin, L. A. Frank, and D. S. Intriligator. Pioneer 10 observations of the solar wind interaction with Jupiter. *J. Geophys. Res.*, 79:3489, 1974.
- Z. J. Yu and C. T. Russell. Rotation period of Jupiter from the observation of its magnetic field. *Geophys. Res. Lett.*, 36:20202, October 2009.
- M. Zhang, G. Qin, H. Rassoul, B. McKibben, C. Lopate, and B. Heber. Ulysses observations of Jovian relativistic electrons in the interplanetary space near Jupiter: Determination of perpendicular particle transport coefficients and their energy dependence. *Planet. and Space Sci.*, 55:12–20, January 2007.



# Acknowledgments

Was thaten wir, als wir diese  
Erde von ihrer Sonne  
losketteten? Wohin bewegt sie  
sich nun? Wohin bewegen wir  
uns?

---

Friedrich Nietzsche

First and foremost I like to thank my supervisor Prof. Dr. Bernd Heber for his enduring support, encouragements and assistance of my work.

I would also like to thank:

Dr. Andreas Kopp (Universität Kiel) for his tireless help e.g. in approaching the mysteries of numerical computing, his hospitality during my stays in Bochum and conversations not only restricted to physics.

Dr. Marius Potgieter (North-West University, South Africa) for interesting discussions on the propagation of energetic particles in the heliosphere and for his hospitality during my stays in South Africa.

Dr. R. Bruce McKibben (University of New Hampshire, USA) for providing the Pioneer data used in this work and for valuable advices and discussions.

Dr. Wolfgang Dröge (Universität Würzburg) for giving me the possibility to participate at the workshop “Transport of Energetic Particles in the Inner Heliosphere” held at the International Space Science Institute (ISSI), Switzerland.

Dipl. Phys. Reinhold Müller-Mellin (Universität Kiel) for valuable discussions on the KET instrument.

All members of the division for space physics/heliospheric astroparticle physics at the University of Kiel.

I would also like to express my gratitude to all the people – scientists, technicians, engineers, administrative authorities – that make spacecraft fly.





# Eidesstattliche Versicherung

Hiermit versichere ich an Eides Statt, dass ich die vorliegende Arbeit abgesehen vom Rat meiner akademischen Lehrer ohne fremde Hilfe und lediglich unter der Verwendung der angegebenen Literatur sowie den bekannten Nachschlagewerken der Naturwissenschaften angefertigt habe, und sie nach Inhalt und Form meine eigene ist. Diese Arbeit ist unter Einhaltung der Regeln guter wissenschaftlicher Praxis entstanden. Des weiteren versichere ich, dass diese Arbeit weder ganz noch teilweise an anderer Stelle zur Prüfung vorlag. Frühere Promotionsversuche wurden von mir nicht vorgenommen.

Während dieses Promotionsvorhabens wurden folgenden Artikel in wissenschaftlichen Zeitschriften unter meiner Mitwirkung veröffentlicht:

- i.) Dunzlaff, P.; Kopp, A.; Heber, B., *Propagation of Jovian electron jets in heliospheric flux tube structures*, Journal of Geophysical Research, 115, A14, 10106, 2010.
- ii.) Dunzlaff, P.; Heber, B.; Kopp, A.; Rother, O.; Müller-Mellin, R.; Klassen, A.; Gómez-Herrero, R.; Wimmer-Schweingruber, R., *Observations of recurrent cosmic ray decreases during solar cycles 22 and 23*, Annales Geophysicae, 26, 3127-3138, 2008.
- iii.) Heber, B.; Gieseler, J.; Dunzlaff, P.; Gómez-Herrero, R.; Klassen, A.; Müller-Mellin, R.; Mewaldt, R. A.; Potgieter, M. S.; Ferreira, S. E. S., *Latitudinal Gradients of Galactic Cosmic Rays during the 2007 Solar Minimum*, The Astrophysical Journal, 689, 1443-1447, 2008.

Kiel, den

---

Phillip Dunzlaff



# Lebenslauf

Name: Phillip Dunzloff  
Wohnort: Gutenbergstrasse 48, 24118 Kiel  
Geboren: 14.4.1981 in Itzehoe  
Familienstand: Ledig  
Staatsangehörigkeit: Deutsch

Schulbildung : 1987 - 1991 Grundschule Wewelsfleth  
1991 - 1997 Realschule Wilster  
1997 - 2000 Kreisberufsschule d. Kreises Steinburg,  
Fachgymnasium (Wirtschaftlicher Zweig), Itzehoe  
Abschluß: Allgemeine Hochschulreife

Studium : 2001 - 2007 Studium der Physik an der Christian-  
Albrechts Universität zu Kiel,  
Diplomnote : gut  
Diplomarbeit  
"Jupiterelektronen in der Inneren Heliosphäre"  
Betreuer: Prof. Dr. B. Heber

Berufstätigkeit : Seit 2007 Wissenschaftlicher Mitarbeiter der  
Arbeitsgruppe Prof. Dr. B. Heber am Institut  
für Experimentelle und Angewandte  
Physik der Christian-Albrechts-  
Universität zu Kiel